Guidance and robust control methods for the approach phase between two orbital vehicles with coupling between translational and rotational motions

Laura Sofia Urbina

To cite this version:

Laura Sofia Urbina. Guidance and robust control methods for the approach phase between two orbital vehicles with coupling between translational and rotational motions. Automatic. Université Paul Sabatier (Toulouse 3), 2017. English. NNT : . tel-01591851v1

HAL Id: tel-01591851
https://laas.hal.science/tel-01591851v1

Submitted on 22 Sep 2017 (v1), last revised 22 Oct 2018 (v2)

THÈSE

En vue de l'obtention du

DOCTORAT DE L'UNIVERSITÉ DE TOULOUSE

Délivré par : *l'Université Toulouse 3 Paul Sabatier (UT3 Paul Sabatier)*

Présentée et soutenue le *22/06/17* **par :**

Laura Sofía URBINA IGLESIAS

Guidance and robust control methods for the approach phase between two orbital vehicles with coupling between translational and rotational motions

---

JURY

Yann LABIT	Professeur, U. P. Sabatier	Président du Jury
Hélène PIET-LAHANIER	Adjointe scientifique, ONERA	Rapporteur
David HENRY	Professeur, U. Bordeaux	Rapporteur
Denis ARZELIER	Directeur de Recherche, CNRS	Examinateur
Christophe LOUEMBET	M. de Conférences, U. P. Sabatier	Examinateur
Yassine ARIBA	M. de Conférences, ICAM	Examinateur
Javier CRESPO	Profesor, U. Politécnica Madrid	Examinateur
Rafael VÁZQUEZ	Profesor, U. Sevilla	Examinateur
Jean-Claude BERGES	Ingénieur, CNES	Membre invité
Damiana LOSA	Ingénieur de recherche, TAS	Membre invité

École doctorale et spécialité :
EDSYS : Automatique 4200046
Unité de Recherche :
Laboratoire d'Analyse et d'Architecture des Systèmes du CNRS
Directeur(s) de Thèse :
Denis ARZELIER, Christophe LOUEMBET et *Yassine ARIBA*
Rapporteurs :
Hélène PIET-LAHANIER et *David HENRY*

Acknowledgements

I would like to thank my supervisors Denis Arzelier and Christophe Louembet for your patience all along this thesis. It was not easy, and you were there, mainly during the hard last months. I am deeply grateful for all your help, both professionally and personally.

Thanks also to Jean-Claude Berges and Pierre Labourdette from the Centre National d'Études Spatiales (CNES) for your precious help and implication. Thanks as well to the CNES, Thales Alenia Space and Région Midi-Pyrénées for funding the research culminating in this thesis.

I would also like to thank the MAC group, and specially Laura Dal Col, Alicia Arce, Paulo Arantes and Sabrina Hadjeras, who became real friends inside and outside the lab. Gracias por todos los momentos pasados juntas y por todos los que tienen que llegar. Os quiero, y el haberos conocido es una de las mejores experiencias que me llevo de estos años. Paulo, muito obrigada por tudo bro.

Je tiens à remercier très sincerement tout l'équipe pedagogique du département EEA à l'Université Paul Sabatier, pour toutes les heures passées ensemble, et pour tout ce que vous m'avez appris. Un grand merci très spéciale à Frédéric Gouaisbaut, Yann Labit, Sylvain Durola, Euriell Le Corronc, Pauline Ribot, Christophe Louembet et Denis Arzelier. Je n'oublierai jamais tout ce que vous avez fait pour moi. Je pourrai écrire toute une autre thèse pour vous remercier, c'est grâce à vous tous que j'ai réussi à finir cette thèse dans les conditions que vous connaisez. De coeur, merci.

Merci *coach* pour toutes les "séances" passées ensemble, pour me faire plus forte dans mon igloo, pour faire que ma motivation revienne et pour croire en moi même quand je n'y croyais plus. Sans tes conseils j'aurai quitté la thèse il y a longtemps. Merci pour ton temps et ta dédication.

Thanks to the bellydance art for bringing me back to life. À mes profs de danse Maya et Mariam, et à toutes les filles qui m'ont fait oublier les problèmes de la thèse pendant les longues heures d'entraînement: Chantal, Christelle, Sehem et Anyssa. Je vous adore toutes. Vous m'avez fait un vrai *reset*, et m'avez donné l'envie de me battre encore et encore.

A mis padres, familia y sobre todo a mi abuela. Te fuiste sin verme terminar la tesis, pero te lo prometí. Esto es para ti.

E grazie mille finalmente a Matt, per essere sempre vicino a me e ascoltarmi sempre, per il tuo aiuto ogni volta che te l'ho chiesto e per il tuo supporto fisico e psicologico. Grazie per avermi fatto sorridere quando solo avevo voglia di piangere. Grazie, grazie ed ancora grazie.

When you want to give up remember why you started.

Unknown.

DISCLAIMER: All images appearing on this manuscript have been created by me using *Inkscape* open source software. Otherwise, the credits are specified within the caption.

Résumé

Les techniques liées au vol en formation et aux opérations de proximité de satellites autonomes font partie des technologies opérationnelles spatiales les plus marquantes et les plus ambitieuses de ces dernières années. En particulier, cela nécessite la complète maitrise des phases de rendez-vous proche et de survol par un satellite actif avec un satellite, une station ou un débris passif. Le développement de systèmes GNC (Guidage Navigation Contrôle) associés performants et sûrs repose sur la connaissance d'un modèle dynamique réalisant un bon compromis entre faible complexité et prise en compte suffisante des principales caractéristiques dynamiques et cinématiques de ce type de systèmes.

La première partie de cette thèse est consacrée au développement d'une modélisation unifiée de la dynamique relative couplée entre un satellite coopératif chasseur et un satellite cible non coopérative. En effet, lorsque deux satellites sont proches l'un de l'autre, ils ne peuvent plus être traités comme des masses ponctuelles, car leur forme et leur taille affectent le mouvement relatif entre les points de masse décentralisés, conduisant à un couplage des mouvements de translation et de rotation. Ce développement est abordé de manière progressive: le mouvement de translation relatif non linéaire est décrit sous hypothèses képlériennes dans le repère orbital de la cible ainsi que le modèle linéarisé associé. Ensuite, le modèle non linéaire d'attitude relative est présenté au moyen des paramètres d'Euler-Rodrigues. Enfin, le formalisme des quaternions duaux est utilisé afin d'obtenir le modèle relatif couplé en translation et en attitude. La phase de modélisation du mouvement relatif linéaire de translation a ainsi permis de mettre en évidence certaines transformations de coordonnées conduisant à une caractérisation intéressante des trajectoires périodiques du chasseur et ainsi de proposer un premier type de loi de contrôle de guidage pour la phase d'approche et de survol.

Dans l'ensemble de notre travail, nous considérons un chasseur équipé de propulseurs chimiques et l'hypothèse classique des poussées impulsionnelles. Ce type de systèmes dynamiques conciliant dynamique continue et contrôle impulsionnel se définit naturellement comme une classe particulière de systèmes dynamiques hybrides. Plusieurs lois de contrôle hybrides sont alors proposées afin de stabiliser le chasseur sur une trajectoire de référence périodique proche de la cible. Les propriétés de stabilité et de convergence de ces différentes lois sont analysées et de nombreuses simulations numériques montrent les forces et les faiblesses de chaque contrôleur en termes d'indices de performance comme le temps de convergence, la consommation ainsi que des contraintes de sécurité.

Dans un second temps, des contraintes opérationnelles supplémentaires (contraintes de visibilité *par exemple) sont prises en considération en imposant une direction d'approche rectiligne (glideslope) au chasseur. Cette trajectoire impose au satellite chasseur de suivre une droite dans n'importe quelle direction du repère local reliant l'emplacement courant du chasseur à sa destination finale. Sous l'hypothèse de propulsion impulsionnelle, les résultats existant dans la littérature pour ce type d'approche ont été généralisés aux orbites elliptiques en identifiant une nouvelle formulation du problème comprenant des degrés de liberté utiles qui permettent de minimiser la consommation de carburant tout en contrôlant l'excursion de la trajectoire libre en dehors de la droite de glideslope en la confinant dans un couloir d'approche défini par l'utilisateur. La synthèse des lois de guidage ainsi obtenues repose sur la résolution de problèmes d'optimisation SDP dans le cas général ou linéaire pour les cas plus simples d'approche standards du type V-bar ou R-bar.*

Abstract

The techniques related to formation flying and proximity operations of autonomous satellites belong to the most significant and challenging operational space technologies of the last years. In particular, they require full mastery of the close-range rendezvous and observation phases by an active satellite with a passive satellite, station or debris. The development of efficient and safe associated Guidance, Navigation and Control (GNC) systems relies on the knowledge of a dynamic model that achieves a good trade-off between low complexity and sufficient inclusion of the main dynamic and kinematic characteristics of this type of systems.

The first part of this thesis is devoted to the development of a unified modeling of the relative coupled dynamics between a cooperative chaser satellite and a non-cooperative target satellite. Indeed, when two satellites are close to each other, they can no longer be treated as point masses because their shape and size affect the relative motion between the decentralized points, leading to a translational-attitude motions coupling. This development is addressed in a progressive way: the relative nonlinear translational motion is described under Keplerian assumptions in the target's orbital reference frame, as well as the associated linearized model. Then, the nonlinear relative attitude model is presented by means of the Euler-Rodrigues parameters. Finally, the dual quaternion formalism is used to obtain the relative translational and attitude coupled model. The modeling phase concerning the linear relative translational motion has allowed us to highlight certain coordinates transformations leading to an interesting characterization of the chaser's periodic trajectories and thus, to propose a first type of control law for the close-phase rendezvous and observation phases.

All along this work, we consider a chaser satellite equipped with chemical thrusters under the classical hypothesis of impulsive thrusts. This type of dynamic systems gathering continuous dynamics and impulsive control naturally belongs to a particular class of dynamical hybrid systems. Several hybrid control laws are then proposed in order to stabilize the chaser on a periodic reference trajectory close to the target. The stability and convergence properties of these different laws are analysed and several numerical simulations show the strengths and weaknesses of each controller in terms of performance indices such as convergence time, consumption and safety constraints.

In a second step, additional operational constraints (line-of-sight constraints for example) are taken into account by imposing a rectilinear (glideslope) direction to the chaser. This trajectory requires the chaser satellite to follow a straight line in any direction of the local reference frame and connecting the current location of the chaser to its final destination. Under the impulsive propulsion assumptions, the results in the literature for this type of approach have been generalized to elliptic orbits by identifying a new formulation of the problem including useful degrees of freedom, which allow minimizing the fuel consumption while controlling the humps of the trajectory outside the glideslope line by enclosing it in a user-defined approach corridor. Guidance laws are therefore synthetized via the solution of an SDP optimisation problem in the general case and via a linear programming when considering standard cases like the V-bar or R-bar approaches.

Contents

4 Approach phase via a glideslope method 109

List of Figures

Notations

Reference frames

- $\mathcal{I}$: pseudo-inertial reference frame;
- $B_i = [\vec{X}_i, \vec{Y}_i, \vec{Z}_i]$: basis vectors associated to reference frame $\mathcal{I}$;
- $\mathcal{O}_{\#}$: Local Vertical Local Horizontal (LVLH) orbital reference frame attached to the satellite $\#$;
- $B_{o\#} = [\vec{X}_{o\#}, \vec{Y}_{o\#}, \vec{Z}_{o\#}]$: basis vectors associated to the LVLH reference frame $\mathcal{O}_{\#}$;
- $\mathcal{B}_{\#}$: reference frame attached to the body of satellite $\#$;
- $B_{b\#} = [\vec{X}_{b\#}, \vec{Y}_{b\#}, \vec{Z}_{b\#}]$: basis vectors associated to the body reference frame $\mathcal{B}_{\#}$;
- $\left(\dfrac{d\vec{v}}{dt}\right)_{B_r}$: time derivative of vector $\vec{v}$ in basis B attached to reference frame $\mathcal{R}$;

Vectors

Geometric vectors will be represented with an arrow (except in Chapter 3, where all arrows have been removed), while algebraic vectors or vectors corresponding to the state-space representations will be represented without the arrow.

- v : algebraic or state-space vector ;
- $\vec{v}^{\,\mathcal{F}}$: geometric vector v expressed in the basis $B_f = [\vec{X}_f, \vec{Y}_f, \vec{Z}_f]$ attached to reference frame $\mathcal{F}$:
    - $\vec{v} = a\,\vec{X}_f + b\,\vec{Y}_f + c\,\vec{Z}_f$, or
    - $\vec{v}^{\,\mathcal{F}} = [a \quad b \quad c]^T$.

Constants and notations of orbital mechanics

- $\mu = GM_{\oplus} = 3.9860047\ 10^{14}\ \mathrm{m^3 s^{-2}}$: Earth standard gravitational parameter calculated from the american potential model GEM-T1 ;

- $J_2 = 1.081874\ 10^{-3}$: second degree harmonic parameter calculated from the Reference Earth Model - WGS84;
- $\vec{\rho}$: chaser's relative position vector with respect to the target ;
- $\vec{v}$: chaser's relative velocity vector with respect to the target ;
- $\vec{r}_{\#}$: position vector of the satellite $\#$;
- $\vec{\omega}$: angular velocity ;
- $\vec{\alpha}$: angular acceleration ;
- $\vec{h}$: orbital kinetic moment ;
- p : satellite's trajectory conical parameter ;
- n : mean orbital motion ;
- t_p : perigee transition date ;
- T_{sat} : orbital period ;

Orbital elements

- a : semi-major axis of an elliptical orbit ;
- Ω : Right Ascension of the Ascending Node (RAAN) ;
- ω : argument of perigee ;
- i : inclination of the satellite's orbit ;
- e : eccentricity of the satellite's orbit ;
- ν : true anomaly ;
- M : mean anomaly ;
- E : eccentric anomaly ;

General mathematics

Sets

- $\mathbb{N}$: set of natural numbers ;
- $\mathbb{Z}$: set of integer numbers ;
- $\mathbb{Z}_n^+$: set of positive or null integer numbers ;
- $\mathbb{H}$: set of quaternions ;
- $\mathcal{H}$: hybrid dynamical system ;
- $\mathbb{D}$: set of dual numbers ;
- $\mathbb{H}(\mathbb{D})$: set of dual quaternions ;

- $SO(3)$: special Lie orthogonal group of vectorial rotations in space ;
- $\mathcal{A} \cup \mathcal{B}$: union of sets $\mathcal{A}$ and $\mathcal{B}$;
- $\mathcal{A} \cap \mathcal{B}$: intersection of sets $\mathcal{A}$ and $\mathcal{B}$;
- $\mathcal{A} \setminus \mathcal{B}$: set of all elements that are members of $\mathcal{A}$ but not members of $\mathcal{B}$;
- $\overline{\mathcal{A}}$: complement of set $\mathcal{A}$;

Operators

- $|\cdot|$: absolute value ;
- $\|\cdot\|$: Euclidean norm for vectors, induced norm for matrices ;
- $\dot{(\cdot)}$: derivative of $(\cdot)$ with respect to time, t ;
- $\ddot{(\cdot)}$: second derivative of $(\cdot)$ with respect to time, t ;

Matrices

- M_{ij} : either an arbitrary element of M or the component in the ith row, jth column ;
- $M_{\rightarrow i}$: ith row of matrix M ;
- $M_{\downarrow j}$: jth column of matrix M ;
- $|M|$: determinant of matrix M ;
- M^T : transpose of matrix M ;
- M^{-1} : inverse of matrix M ;
- M^{-T} : transposed inverse of matrix M ;
- $M \succeq 0$: positive semi-definitness of symmetric real matrix $M \in \mathbb{R}^{n \times n}$;
- $M \preceq 0$: negative semi-definitness of symmetric real matrix $M \in \mathbb{R}^{n \times n}$;
- $0_{n \times m}$: null matrix of dimensions $n \times m$;
- $\mathbb{1}_n$: vector of n ones ;
- I_n : identity matrix of dimension n ;
- M^+ : $M^+ \in \mathbb{R}^{m \times n}$ pseudo-inverse matrix of $M \in \mathbb{R}^{n \times m}$;
- M^L : left pseudo-inverse matrix of M ;
- M^R : right pseudo-inverse matrix of M ;
- $M_1 \otimes M_2$: Kronecker product between matrices M_1 and M_2 ;
- $\vec{u} \cdot \vec{v}$ or $\langle \vec{u}, \vec{v} \rangle$: dot product between vectors $\vec{u}$ and $\vec{v} \in \mathbb{R}^n$;
- $\vec{u} \wedge \vec{v}$: cross product between vectors $\vec{u}$ and $\vec{v} \in \mathbb{R}^n$;

- $u^\times$: skew-symmetric matrix defined by $u^\times\vec{v} = \vec{u} \wedge \vec{v}$, for vectors $\vec{u}$ and $\vec{v}$;

$$u^\times = \begin{bmatrix} 0 & -u_z & u_y \\ u_z & 0 & -u_x \\ -u_y & u_x & 0 \end{bmatrix}$$

Quaternions

- $\mathbf{i}, \mathbf{j}, \mathbf{k}$: hyper complex numbers, square roots of -1, that allow defining the quaternions and dual quaternions ;
- ϵ : nilpotent operator ($\epsilon^2 = 0$ and $\epsilon \neq 0$) that allows defining the dual numbers and dual quaternions;
- $\hat{z} = x + \epsilon y$: dual number, $x, \ y \in \mathbb{R}$;
- $\hat{\vec{z}} = \vec{x} + \epsilon\vec{y}$: dual vector, $\vec{x}, \ \vec{y} \in \mathbb{R}^n$;
- q : quaternion $q = q_1\mathbf{i} + q_2\mathbf{j} + q_3\mathbf{k} + q_4$ where the scalar part is given by q_4 and the vectorial part by $\vec{q} = q_1\mathbf{i} + q_2\mathbf{j} + q_3\mathbf{k}$;
- q^* : conjugate of quaternion q, $q^* = -q_1\mathbf{i} - q_2\mathbf{j} - q_3\mathbf{k} + q_4$;
- q^{-1} : inverse of quaternion q, $q^{-1} = \dfrac{q^*}{\|q\|^2} = \dfrac{q^*}{q_4^2 + q_1^2 + q_2^2 + q_3^2}$;
- $\hat{q}$: versor (or unitary quaternion) of quaternion q, $\hat{q} = \dfrac{q}{\|q\|}$;
- $M_l(q_a)$: orthogonal matrix used to multiply two quaternions $q_a \odot q_b$ when the left quaternion is taken first ;
- $M_r(q_b)$: orthogonal matrix used to multiply two quaternions $q_a \odot q_b$ when the right quaternion is taken first ;
- Q : matrix of quaternions ;

$$Q(q) = \begin{bmatrix} q_4 & -q_3 & q_2 \\ q_3 & q_4 & -q_1 \\ -q_2 & q_1 & q_4 \\ -q_1 & -q_2 & -q_3 \end{bmatrix} = \begin{bmatrix} q_4\mathbb{1}_3 + q^\times \\ -\vec{q}^{\,T} \end{bmatrix}$$

- $\hat{q} = q_0 + \epsilon q_1$: dual quaternion, $q_0, \ q_1 \in \mathbb{H}$;
- $\odot$: product between two quaternions or two dual quaternions ;
- $\cdot$: scalar product between two quaternions or two dual quaternions ;
- $\times$: cross product between two quaternions or two dual quaternions ;
- $\hat{q}_a \circ \hat{q}_b$: dual product between two dual quaternions ;
- $M * q$: product between a matrix $M \in \mathbb{R}^{4\times4}$ and a quaternion $q \in \mathbb{H}$;
- $M \star \hat{q}$: product between a matrix $M \in \mathbb{R}^{8\times8}$ and a dual quaternion $\hat{q} \in \mathbb{H}(\mathbb{D})$;

Subscripts

- 0 : instant $t = 0$;
- b : relative to the satellite's body ;
- c : relative to the chaser spacecraft C ;
- ext : external ;
- h : relative to the Hill's reference frame ;
- lvlh : relative to the LVLH reference frame ;
- i : relative to the Earth-centered inertial reference frame ;
- o : relative to the orbital frame ;
- t : relative to the target spacecraft, T ;

Other symbols

- ♈ : vernal equinox ;
- $\oplus$: Earth ;
- $\odot$: Sun ;
- ☊ : ascending node ;
- ☋ : descending node ;

Acronyms

ADR	Active Debris Removal
ATV	Automated Transfer Vehicle
ATV-CC	Automated Transfer Vehicle Control Centre
CNES	Centre National D'Études Spatiales
CoM	Center of Mass
CW	Clohessy Wiltshire
DLR	Deutsche Zentrum für Luft- und Raumfahrt
DoF	Degrees of Freedom
DTU	Danmarks Tekniske Universitet
ESA	European Space Agency
FFIORD	Formation Flying In Orbit Ranging Demonstration
FoV	Field of View
GNC	Guidance, Navigation and Control
HCW	Hill-Clohessy-Wiltshire
HTV	H-II Transfer Vehicle
ISS	International Space Station
LoS	Line of Sight
LP	Linear Programming
LTI	Linear Time-Invariant
LTV	Linear Time-Variant
LVLH	Local Vertical Local Horizontal
MPAD	Mission Planning and Analysis Division
MPC	Model Predictive Control
NASA	National Aeronautics and Space Administration
OOS	On-Orbit Servicing
PRISMA	Prototype Research Instruments and Space Mission technology Advancement
RAAN	Right Ascension of the Ascending Node
SDP	Semidefinite Programming
SFF	Satellite Formation Flying
SNSB	Swedish National Space Board
SSC	Swedish Space Corporation

CHAPTER 1

INTRODUCTION

Contents

1.1. Context and motivations

1.1.1. Satellite formation flying and rendezvous

Many future space missions depend on the formation flying technologies involving more than one spacecraft. During the last decades, the concept of Satellite Formation Flying (SFF) has retained the space scientists' attention.

In the past, many space missions relied on a single satellite performing all the required scientific tasks. The new technologies that soon became available demanded more on-board capabilities: larger structures for Earth observation missions, greater resolution for telescopes or new capacities allowing debris removal. Soon, these single satellites showed limited capabilities to achieve these new scientific challenges.

The development of other types of technologies overcoming these limitations was naturally imposed. There, the concept of SFF appeared, defined by NASA's Goddard Space Flight Center as *the tracking or maintenance of a desired relative separation, orientation or position between or among spacecraft* whose objective is to work together in a group to accomplish *science measurement, data acquisition, processing, analysis and distribution*.

SFF allows scientists to obtain unique measurements by combining data from several satellites rather than flying all the instruments on one costly satellite. These measurements lead to obtain comprehensive information about various key scientific processes. Combining the information from several sources gives a more complete answer to many questions than would be possible from any single satellite taken by itself.

The use of small satellites flying in precise formations is used to enhance or enable a number of space missions [73]. Small satellites flying in formation present a more efficient and affordable way of achieving the same or better performance than a single large satellite because of their many benefits [79], including:

- need of a single launcher to deliver several satellites at once;
- lower production and replacement costs;
- simpler designs and shorter development cycles;
- distribution of risk across formation elements to reduce catastrophic failures (redundancy);
- mission flexibility through adaptive formations;
- view of targets from multiple angles or at multiple times with higher resolution.

In addition to maintaining a given geometry of a satellites constellation, the concept of SFF defined in its broadest sense also covers the rendezvous phase between two vehicles and proximity operations such as inspection of a (non-)cooperative target, repairing a damaged satellite, replacing equipment, refueling or collecting space debris.

As defined in [38], *the rendezvous process consists of a series of orbital maneuvers and controlled trajectories, which successively bring the active vehicle (chaser) into the vicinity of, and eventually into contact with the passive vehicle (target)*.

Several phases are considered for the rendezvous process [38], whose main features are:

- launch: the chaser satellite stabilizes in the target's orbital plane;
- phasing: the phase angle between chaser and target decreases;
- far-range: intermediate phase appearing just after the phasing and that transfers the chaser to the first holding point in the vicinity of the target;
- close-range: transfer performed from the first holding point up to the capture point;
- docking: structural connection between spacecraft.

Three common examples of rendezvous are Active Debris Removal (ADR) missions — where the target is a space debris —, an On-Orbit Servicing (OOS) mission, where the target is a satellite waiting to be repaired or the rendezvous with the International Space Station (ISS) for refueling, reorbiting or providing several services.

According to the objectives and needs of the mission, we distinguish three types of phases:

- an approach phase, considered as the previous close-range stage, during which the chaser is steered from several kilometers to a few hundreds of meters near the target and prepares its entry into the final approach corridor (closing) [39];
- an observation or inspection phase in the vicinity of the target, where the chaser flights over the target with the objective of acquiring information (attitude, etc); and
- a manipulation or operation phase involving the docking of both spacecraft.

Among all possible approaches, the choice will be done according to safety reasons, fuel budget or different constraints affecting the mission, such as observability (LoS), velocity requirements, collision avoidance or lightning features. This thesis is dedicated to the study of both the approach and observation phases.

Rendezvous between two spacecraft is still one of the most salient operational technologies since its first manual achievement in the sixties between a Gemini vehicle and an unmanned target vehicle.

Within the context of autonomous formation flying applications, two particular space missions may be pointed out: the ESA's Automated Transfer Vehicle (ATV) program, and the cooperation between the French Centre National D'Études Spatiales (CNES), the German Deutsche Zentrum für Luft- und

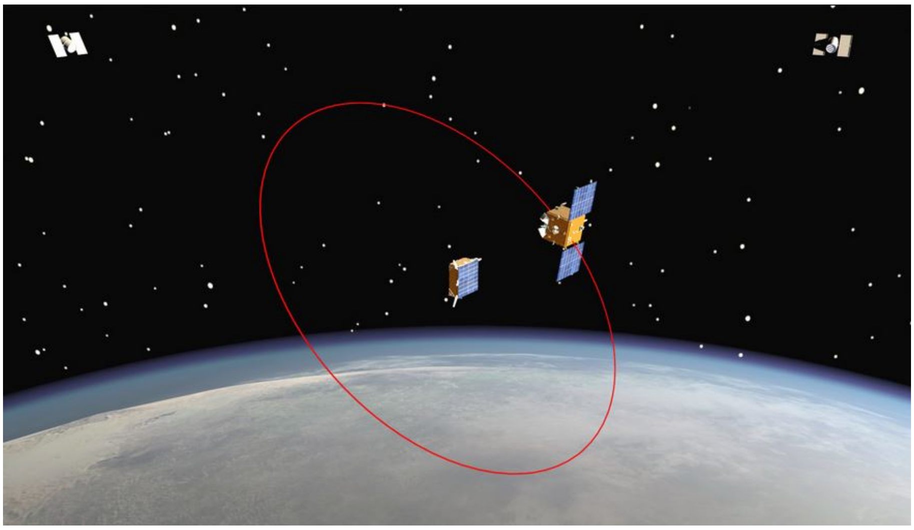

Figure 1.1: PRISMA mission program. Photo courtesy of CNES.

Raumfahrt (DLR) and the Danish Danmarks Tekniske Universitet (DTU) resulting in the PRISMA mission (c.f. Figure 1.1).

The PRISMA mission was intended to test in-orbit guidance schemes (particularly autonomous orbit control) for formation flying and rendezvous technologies [26]. In the mission, the chaser satellite Mango (whose movements were controlled by navigation and guidance algorithms developed by CNES) repeatedly approached and receded from the Tango target satellite autonomously. We distinguish the Formation Flying In Orbit Ranging Demonstration (FFIORD) experiment, designed to validate manoeuvres for satellite separation distances from 10 km down to 50 m.

The diverse range of operations performed by PRISMA and the FFIORD experiment has significantly advanced in-orbit validation of SFF and orbital rendezvous techniques, working within very tight schedules and cost constraints.

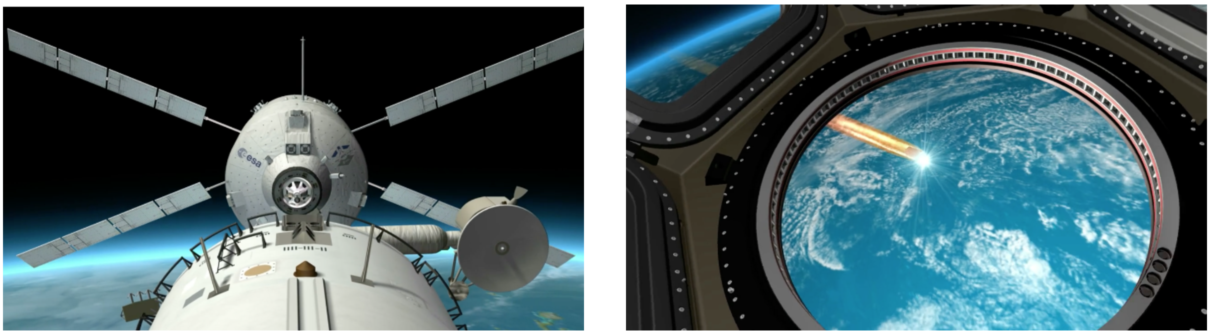

(a) Docking to the ISS.

(b) Re-entry into the atmosphere.

Figure 1.2: ATV-4. Photos courtesy of CNES.

The Europe's ATV was a semi-automated spacecraft developed by ESA to resupply the ISS, with enough capacity for up to 8 tonnes of equipment, oxygen, fuel, water, food and scientific experiments [25]. It allowed automatic docking with the station under the supervision of the Automated Transfer Vehicle Control Centre (ATV-CC) (c.f. Figure 1.2a). Once docked, the carrier's cargo was transferred to the station, after which it was filled with waste. The ATV could remain docked to the ISS for up to 6 months, eventually using its own thrusters to boost the station's orbit. After its stay in orbit, the ATV undocked from the station, burning up when re-entering the Earth's atmosphere (c.f. Figure 1.2b).

There have been five flights between 2008 and 2015: ATV *Jules Verne*, launched on March 2008 followed by ATV-2 *Johannes Kepler* in 2011, ATV-3 *Edoardo Amaldi* in 2012, ATV-4 *Albert Einstein* in 2013 and ATV-5 *Georges Lemaître* in 2014.

1.1.2. Challenges in rendezvous missions

The spacecraft autonomy becomes then one of the most desirable features regarding close-range rendezvous operations. The full mastery of this rendezvous phase is only possible when highly efficient control algorithms and measurement systems are used, with a particular interest in reducing fuel consumption and improving control accuracy in this terminal phase.

The strong constraints associated to the inspection and/or manipulation missions of a target vehicle explain the need for more accurate relative models, allowing the synthesis of more efficient and safer GNC algorithms, which play an important role in the success of SFF and rendezvous missions. The development of such GNC systems relies on the knowledge of a dynamic model that achieves a good trade-off between its complexity and sufficient inclusion of the main dynamic and kinematic characteristics of this type of systems.

This is a very challenging task due to the nonlinear nature of satellite dynamics. The knowledge of an accurate relative motion mathematical model concerning both the kinematics and dynamics of SFF is an important foundation in developing a control system, becoming of vital importance in close proximity maneuvering.

1.1.2.1. Relative models

In SFF, we consider two or more spacecraft: the *chief* and the *deputies*. An alternative terminology designates one of the satellites as *leader*, and the others as *followers*. In the context of orbital rendezvous, one of the satellites is usually referred to as *target*, and the other is called *chaser* [3]. This last designation is used all along this dissertation.

Along this manuscript, the target is considered passive or non-cooperative, while assuming that the chaser is equipped with chemical thrusters and is therefore fully actuated. The notion of relative motion is used to describe the chaser's relative state with respect to the target, applicable for both translation and attitude motions.

The works on the relative translational motion modeling between two space vehicles has been extensively treated in the literature during the last 50 years. Their origin goes back to the article by Clohessy and Wiltshire [23], giving for the first time a linear Keplerian model of the rendezvous problem assuming a circular reference orbit in cartesian coordinates. These initial works have been extended to the elliptic case with various orbital perturbations. Later achievements include nonlinear models as presented in e.g. Pan and Kapila (2001), Wang and Hadaegh (1996) and Yan, Yang, Kapila, and de Queiroz (2000), derived for arbitrary orbital eccentricity and with added terms for orbital perturbations [71]. In all these works, space vehicles involved in the rendezvous phase are assumed to be point masses with 3 Degrees of Freedom (DoF).

The description of the relative attitude motion modeling has also been subject of several works in the literature, developed by Euler, Jacobi, Hamilton, Cayley and Rodrigues among others [99]. The orientation of spacecraft can be completely described by means of different attitude parameters as shown in reference [5], where Euler angles were used; rotation matrices in reference [61], [77] or Euler-Rodrigues parameters that form a quaternion in [92], [2], [68], [82] and [76]. These attitude models are also considered as 3 DoF models.

In general, rigid-body dynamics can be represented as both the translation and rotation about the Center of Mass (CoM). When spacecraft are close to each other, such as in the final phase of rendezvous, or in the docking phase, they can no longer be treated as point masses because the shape and size of the spacecraft affects the relative motion between the off CoM points.

When a point on a spacecraft does not coincide with the spacecraft's CoM, a kinematic coupling between the translational and rotational dynamics is generated [75]. Orbital-attitude coupling is induced when a non-symmetrical spacecraft in orbit is disturbed by means of active maneuvers or by external disturbances. Direct contributing factors to the coupled dynamics include the orbital radius, the gravitational parameter and the orbital angular velocity.

This effect is accentuated as the distance between the two spacecraft becomes closer, meaning that models considering either the translation or the attitude motions independently — known as 3 DoF models — are not sufficient in order to achieve a high degree of precision for close maneuvers. In order to account for the effects that the translation has over the attitude and viceversa, it becomes necessary to model both motions at the same time, commonly known as 6 DoF models or coupled models. The relative motion between the target and the chaser is therefore a 6 DoF motion which represents the coupling of the relative translational motion with the rotational one [29].

Two different kinds of couplings have been differentiated in the last years. One is originated by external torques such as the gravity-gradient torque which is the most obvious example and depends on the altitude. The other is created by internal torque, and is incurred regardless of external perturbation torque. By comparing propagated trajectories using the new coupled relative equations of motion and the Clohessy Wiltshire (CW) relative equations of motion, [102] show that this kinematic coupling effect is the key for high precision modeling of tight SFF and rendezvous. However, the linear CW relative equation model can result in considerable errors in the modeling of relative spacecraft translational motion [75].

In current literature, there are a few publications in coupled control of SFF. Main contributors on this specific field include authors like: Pan, Wong, and Kapila on nonlinear coupled dynamics control, [71] on 6 DoF integrator control, as well as [4] on the basis of coupled dynamics fundamentals [44]. In [136] a relative position and attitude estimation approach for SFF was investigated, where coupled relative translational dynamics is derived to represent orbital motion of arbitrary feature points on the chaser, and the relative attitude motion is formulated by rotational dynamics for non-gyro satellites.

1.1.2.2. Guidance algorithms

Once a dynamic model of the relative motion has been derived, it is necessary to design guidance and control laws complying to safety, operational and performance requirements for the approach and inspection phases. This design phase is heavily dependent upon the nature of the propulsion system used for actuation of the chaser satellite. Spacecraft may be equipped with electric and/or chemical thrusters. Even if electric propulsion is nowadays becoming a valid option for some missions, chemical propulsion remains largely the commonly used system for reducing the range to a target in the closing phase of a space rendezvous. Though widely studied for many decades, the problem of designing impulsive hopping maneuvers during the close-range rendezvous phase is still an active area of research.

In particular, if the impulsive idealization of the thrust introduces a simplified abstraction of the control problem, it generates in return some theoretical difficulties regarding the existence of solutions and their nature to the minimum-fuel rendezvous problem [90]. In fact, with this assumption, the relative dynamics gather continuous dynamics and impulsive control functions requiring specific tools for the design of optimal maneuvers. One way to address this difficulty is to immerse this model into the particular class of dynamical hybrid systems.

Hybrid dynamical systems have attracted important research efforts over the recent years as an emerging discipline within the dynamical systems theory and control [57] to develop a systematic framework for the analysis and design of complex engineering systems, as can be found in aerospace systems [78].

According to the authors in [57], a hybrid system is an interacting countable collection of dynamical systems involving a mixture of continuous-time dynamics and discrete events that includes among others, impulsive dynamical systems.

We focus on the rendezvous phase as an impulsive hybrid dynamical system, considering a chaser satellite equipped with chemical thrusters, such that the associated control problem falls into the class of impulsive hybrid control problems. Under the impulsive hybrid systems formalism, the satellite's approach phase can be modeled as a continuous-time system while no control input is applied on the satellite, and as a discrete-time system when the control inputs are applied at a given time. Furthermore, hybrid systems theory offers a formal framework for studying the asymptotic stability of these systems.

In this dissertation, a first type of guidance algorithms based on several hybrid control laws are proposed in order to stabilize the chaser on a periodic reference trajectory close to the target, analysing their stability and convergence properties.

Another challenge regarding the close-range rendezvous phase concerns the operational constraints associated to this flight phase. The close-range rendezvous phase is one of the stages of the global rendezvous process during which the chaser spacecraft prepares its entry into the final approach corridor and eventually performs the docking action with the target satellite [39].

Depending on various operational and safety constraints, various closing phase strategies may be envisioned and proposed to perform the proximal rendezvous. In the literature, the most common type of approaches are performed in order to ensure LoS operational constraints (c.f. Figure 1.3). This type of constraint refers generally to the straight line between two objects. Regarding the rendezvous problem, the LoS does not refer exactly to the straight line between chaser and target, but to the cone of visibility of one of the spacecraft's sensor. This means that one spacecraft should be inside the sensor's visibility cone — or FoV — of the other spacecraft to guarantee LoS.

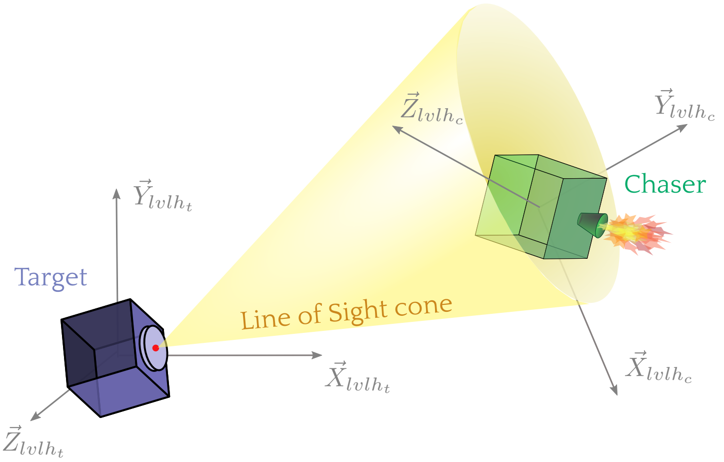

Figure 1.3: Example of LoS constraint within the FoV of the target.

Within the considered guidance algorithms that are proposed in this dissertation, additional operational constraints regarding LoS constraints are taken into account by imposing a rectilinear direction to the chaser, commonly referred to as *glideslope* approach. These type of trajectories require the chaser satellite to follow a straight line in any direction of the local reference frame and connecting the current location of the chaser to its final destination.

The glideslope concept was developed by the Mission Planning and Analysis Division (MPAD) at the National Aeronautics and Space Administration (NASA) Johnson Space Center, as a part of the design activities for the Space Shuttle in 1983. It is possible to get to reference [93] for history, motivation and a brief technical analysis of the development of this technique in the context of the American Space Shuttle program. Therein, only a relative trajectory in the orbital plane is studied, parametrized under the assumptions that the front and rear Space Shuttle's engines have a given angle with respect to the Shuttle's axis.

Glideslope trajectories were also used for terminal approaches during ATV cargo missions [46] and H-II Transfer Vehicle (HTV) [122] to the ISS. In these last cases, glideslope is essentially one of the conventional approaches in proximity operations, following the R-bar ($\vec{Z}$ axis of the Local Vertical Local Horizontal (LVLH) frame) or V-bar ($\vec{X}$ axis of the LVLH frame) directions, which are recalled in detail in [39].

The preliminary works in [93] have been extended and generalized for any direction in space in [56], [124], preserving the linearization hypothesis around a circular orbit, leading to the use of the Hill-Clohessy-Wiltshire (HCW) equations, and for elliptic reference orbit in [91]. Indeed, the results presented in [56] are well-known and constitute the reference on the subject and define the classical glideslope algorithm as usually described in the literature. However, the results in [56] are limited to circular reference orbits, and the consumption is not optimized. In addition, the real trajectory of the chaser will not be strictly along the straight line but will exhibit humps between the impulsive maneuvers.

Under the impulsive propulsion assumptions, these classical glideslope results have been generalized in this manuscript to elliptic orbits by identifying a new formulation of the guidance problem including useful degrees of freedom, which allow minimizing the fuel consumption while controlling the humps of the trajectory outside the glideslope line by enclosing it in a user-defined approach corridor.

1.2. Thesis organization

There are two main objectives within this manuscript. The first one deals with the relative motion modeling, while the second one proposes different controllers for the satellite guidance schemes.

Chapter 2 is devoted to the development of a general, uniform and homogeneous model of the relative coupled dynamics between an actuated chaser and a non-cooperative target, able to describe both approach and observation phases of a space mission. This development is done progressively, starting from the relative nonlinear translational motion equations under Keplerian assumptions. The nonlinear model is then linearized with respect to the elliptic target's orbit.

We address the nonlinear relative attitude model by means of the Euler-Rodrigues parameters that form a quaternion.

Finally, we use the dual quaternions formalism to provide the coupled modeling of both the translational and attitude model, i.e. the 6 DoF model. The complexity of the relative motion model, however, may vary depending on the needs of each rendezvous phase (approach, observation and manipulation), meaning that it will not be necessary to use the 6 DoF model for every phase. The approach phase, for example, has much simpler needs than the manipulation one. This is why a translational model is sufficient in this case. On the other hand, the complete model with 6 DoF would become necessary in an eventual operation phase.

The modeling of the linear relative translational motion allows us to feature four coordinate transformations that characterizes periodic chaser trajectories. We exploit these transformations to propose a first type of control laws for the close-phase rendezvous and observation phases. Based on the impulsive abstraction of the actuators, in Chapter 3 we address the chaser stabilization problem on a reference periodic trajectory by means of different controllers based on dynamical hybrid systems. The hybrid systems theory allows to prove stability and convergence properties of the different controllers, evaluating their performances by means of consumption and convergence indices.

In Chapter 4, we consider additional constraints over the chaser's trajectory, forced to follow a straight path or glideslope approach. The results in the literature for this type of approach have been generalized to elliptic orbits, where new degrees of freedom are integrated in two new algorithms, synthetized via the solution of an SDP optimisation problem in the general case and via a linear programming when considering standard cases like the V-bar or R-bar approaches. These two new controllers become able to minimize the fuel consumption while controlling the humps of the trajectory outside the glideslope line by enclosing it in a user-defined approach corridor.

CHAPTER 2

TRANSLATIONAL AND ROTATIONAL RELATIVE COUPLED MODELS

Contents

Résumé

La nécessité de modèles plus précis pour le vol relatif entre deux véhicules spatiaux est essentiellement issue du développement, durant les 20 dernières années, de la problématique du vol en formation. Outre le maintien dans une formation de géométrie donnée d'un ensemble de satellites, la notion de vol en formation définie au sens large recouvre également la phase de rendezvous entre deux véhicules et les opérations de proximité (inspection d'une cible coopérative ou non, réparation d'un satellite endommagé, remplacement d'un équipement, ravitaillement, ramassage d'un débris spatial). C'est dans le cadre de la phase de rendezvous proximal et d'opérations de proximité que se situe cette étude.

Les travaux consacrés à la modélisation du mouvement orbital différentiel en translation entre deux véhicules spatiaux (une cible passive et un chasseur actionné) ont été très abondants ces 50 dernières années. Leur origine remonte à l'article précurseur de Clohessy et Wiltshire, donnant pour la première fois un modèle képlérien du problème de rendezvous en supposant une orbite de référence circulaire [23]. Depuis, ces travaux initiaux ont été étendus au cas elliptique [74], [17], [47], [18], [84], [64], [139] ou/et à la prise en compte de divers perturbations orbitales [51], [20], pour ne citer que quelques références parmi les nombreuses que l'on peut trouver dans la littérature. Une étude détaillant l'obtention des différents modèles et des hypothèses associées a été proposée dans le rapport [9].

Dans l'ensemble de ces résultats, les véhicules spatiaux impliqués dans la phase de rendezvous sont supposés être des masses ponctuelles à 3 degrés de liberté. Quand les deux satellites sont très proches l'un de l'autre, comme dans le cas de la phase terminale d'un rendezvous, la phase d'inspection ou la phase précédant celle d'une intervention sur le satellite cible, ils ne peuvent plus être considérés comme des masses ponctuelles du fait que la forme et la taille de chacun des satellites peuvent affecter le mouvement de translation des points hors Centre de Masse (CdM).

Ce phénomène est en général accentué par la diminution de la distance inter-satellites. Dans le but d'assurer le repositionnement, la ré-orientation ou l'inspection éventuels d'un satellite cible dont l'attitude peut ne plus être maitrisée, par un satellite chasseur, la modélisation précise du mouvement relatif en translation et en attitude est nécessaire. En effet, dans ce cas, la modélisation indépendante des mouvements relatifs en translation et en rotation n'est plus suffisante et il est nécessaire de recourir à une modélisation couplée du mouvement relatif à 6 degrés de liberté (ddl). Depuis les premiers travaux de Pan [92], l'intérêt porté à cette thématique de la modélisation à 6 degrés de liberté a très largement augmenté dans la littérature ces dernières années, comme en témoigne la liste de références suivantes [69], [72], [128], [137], [95], [45], [28], [27], [67]. Les contraintes fortes associées aux missions d'inspection et de manipulation d'un véhicule cible expliquent le besoin de modèles relatifs plus précis et couplés, permettant la synthèse d'algorithmes de GNC plus performants et plus sûrs. Á titre d'exemple, nous pouvons mentionner les contraintes sur les trajectoires d'approches :

- *Evitement de collision ;*
- *Contraintes d'orientation sur la poussée pour le contrôle d'orbite [87], [128] ;*
- *Contraintes d'attitude induites par l'orientation des capteurs (satellite cible toujours en vue du satellite chasseur (cf. Figure 2.1), zone interdite pour le satellite chasseur dans le champ de vision du satellite cible, la distance d'inspection devant satisfaire une condition de résolution des informations capteurs, angle minimal d'inspection) [95], [128] ;*
- *Synchronisation de l'attitude du chasseur sur l'attitude de la cible pour une éventuelle manipulation (débris, docking) [135], [98], [141] ;*
- *Vérification d'une condition de docking (le port de docking du satellite chasseur doit pointer vers le port de docking du satellite cible) [45], [98].*

Dans ce rapport, la modélisation du mouvement relatif couplé est abordée de manière systématique et progressive. Dans un premier temps, les modèles relatifs non linéaires en translation et en attitude sont définis indépendament. Puis, le couplage entre les deux dynamiques est ensuite étudié dans un cadre non linéaire. Les modèles linéarisés associés aux modèles en translation sont également calculés. Les modèles à 6 degrés de liberté sont généralement utilisés hors de la plage de validité des hypothèses de linéarisation des modèles relatifs en rotation comme il sera justifié plus loin dans le rapport. C'est pour cela que ces modèles linéaires ne sont pas inclus.

Nous nous sommes efforcés de préciser le plus clairement possible les hypothèses utilisées, les référentiels dans lesquels sont écrites les équations dynamiques et cinématiques dans un cadre de notations unifiées.

2.1. Introduction

The need for more accurate models concerning the relative flight between two orbital vehicles is the consequence of the development of the formation flying problem over the last 20 years. Besides station keeping for a given set of satellites' geometry, the broadly defined concept of formation flying includes the rendezvous phase between two vehicles as well as space proximity operations (inspection of a (non-)cooperative target, repair of a damaged satellite, replacement of equipment, refuelling, collection of space debris). This study is placed in the context of the close rendezvous and proximity operations.

Dedicated works on the modeling of the translational differential orbital relative motion between two spacecraft (a passive target and an actuated chaser) have been very abundant over the past 50 years. The origin dates back to the Clohessy and Wiltshire's seminal article, providing a first Keplerian linearized model of the rendezvous problem assuming a circular reference orbit [23]. Since then, these initial studies have been extended to the elliptical case [74], [17], [47], [18], [84], [64], [139], and/or to the consideration of various orbital perturbations [51], [20], to cite few references among the numerous that can be found in the literature. A study detailing the various ways to obtain the different models and the associated assumptions was proposed in [9].

Within these results, space vehicles involved in the rendezvous phase are supposed to be point masses with 3 DoF. When the two satellites are very close to one another, as in the case of the terminal phase of a rendezvous, the inspection phase or the previous stage to an intervention on the target satellite, they can no longer be considered as point masses since the shape and size of each satellite can affect the translational motion of points out of the CoM.

This phenomenon is in general emphasized by the decrease of the inter-satellite distance. In order to ensure the repositioning, reorientation or inspection of a target satellite whose attitude cannot be mastered by a chaser satellite, an accurate modeling of the relative translational and attitude motion becomes necessary. Indeed, in this case, the independent modeling of relative motions in translation and in rotation is not sufficient any more and it becomes necessary to use a modeling of the coupled relative motion with 6 DoF. Since the early work of Pan [92], the interest over the 6 DoF modeling has largely increased in the literature in recent years, as evidenced by the following references list [69], [72], [128], [137], [95], [45], [28], [27], [67]. The strong constraints associated to the inspection and manipulation missions of a target vehicle explain the need for more accurate and coupled relative models, allowing the synthesis of more efficient and safer GNC algorithms. As an example, it is possible to mention the constraints over the approach trajectories, graphically synthetised in Figure 2.1:

- collision avoidance;
- restricted areas where the chaser's instruments cannot point at (concealment avoidance, for example) [128];
- thrust orientation constraints for control over the orbit [87], [128];
- attitude constraints induced by the orientation of the sensors (target satellite always visible by the chaser, see Figure 2.1, forbidden area for the chaser in the target's field of view, LoS, the inspection distance having to satisfy the sensor's resolution capabilities, minimum angle of inspection) [95];
- synchronization of the chaser's attitude for target manipulation (debris, docking) [135], [98], [141];
- checking docking condition (chaser's docking port must point to the target's docking port) [45], [98].

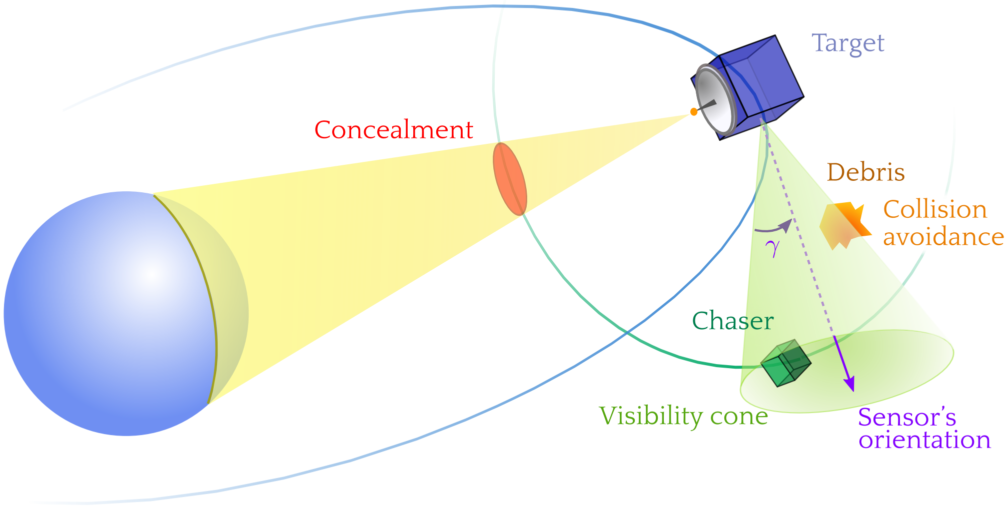

Figure 2.1: Example of various types of constraints [95], [131].

In this dissertation, the modeling of coupled relative motion is addressed in a systematic and progressive way by the independent definition, firstly, of the nonlinear relative translational and rotational motions. The coupling between the two dynamics is then tackled within a nonlinear framework. The linearized models associated to the translational models are also derived. The 6 DoF models are generally used outside the validity range of the linearizing hypothesis for the rotational relative models, as it will be proved later. This is the reason why these linear models have not been included.

A special effort has been done to specify as clearly as possible the used assumptions, the reference frames for both the dynamic and kinematic equations within a unified notation framework.

2.2. Nonlinear relative translational dynamics

The main purpose of this section is to develop the nonlinear dynamic equations of the translational relative motion under a Keplerian general framework without the associated linearization assumptions and for any orbit eccentricity $e \in [0,1)$. This development is made using local Cartesian coordinates expressed in the LVLH reference frame, in contrast with the models based on orbital differential parameters that will not be addressed in this study. We recall that a study of such models was produced in the note [9]. This section aims at unifying the modeling and the notations from different references, such as [65] in the case of a circular target orbit, or [100], [104], [116], in the case of elliptical target orbits.

All the different reference frames are defined in Appendix B. The relative position vector between the chaser and the target is a function of their relative position vectors, respectively:

$$\vec{\rho} = \vec{r}_c(t) - \vec{r}_t(t). \tag{2.1}$$

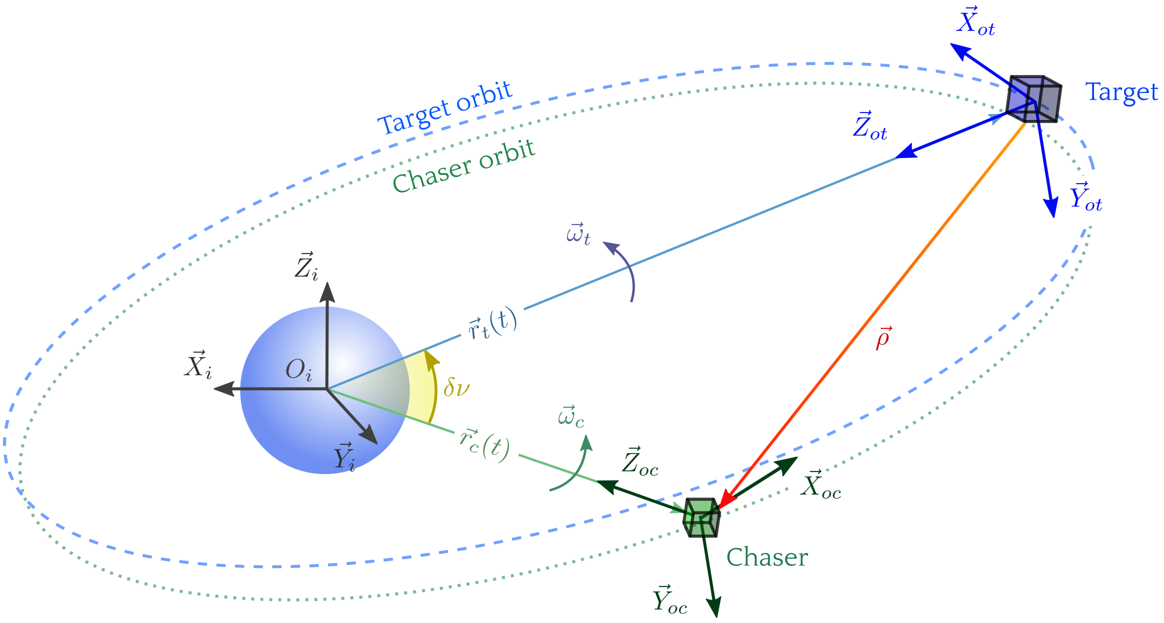

Figure 2.2: Translational relative motion.

$\mathcal{I}$ is the pseudo-inertial reference frame, B_i is its orthonormal basis, $\mathcal{O}_t$ is the local orbital frame (LVLH) attached to the target and B_{ot} is its basis (cf. Figure 2.2).

In general, the dynamics of a point P of mass m (assumed constant) in the inertial reference frame $\mathcal{I}$, subject to the Earth's gravity field $\vec{g}(\cdot)$, to external forces $\vec{F}_{ext}$ —included any other forces than the gravity one— and to a propulsion force $\vec{F}_{prop}$ is governed by the equation:

$$m\,\ddot{\overrightarrow{O_iP}}^{\,\mathcal{I}} = m\,\vec{g}(P)^{\,\mathcal{I}} + \vec{F}_{ext}^{\,\mathcal{I}} + \vec{F}_{prop}^{\,\mathcal{I}}, \tag{2.2}$$

or:

$$\left(\frac{d^2\overrightarrow{O_iP}}{dt^2}\right)_{B_i} = \vec{g}(P) + \frac{\vec{F}_{ext}}{m} + \frac{\vec{F}_{prop}}{m}. \tag{2.3}$$

Therefore, the equations of motion for the target $P = T$ or chaser $P = C$ satellites in the inertial reference frame $\mathcal{I}$ are:

$$\begin{cases} \left(\dfrac{d^2\overrightarrow{O_iT}}{dt^2}\right)_{B_i} = \left(\dfrac{d^2\vec{r}_t(t)}{dt^2}\right)_{B_i} = \vec{g}(T) + \dfrac{\vec{F}_{ext_t}}{m_t} + \dfrac{\vec{F}_{prop_t}}{m_t} \\ \left(\dfrac{d^2\overrightarrow{O_iC}}{dt^2}\right)_{B_i} = \left(\dfrac{d^2\vec{r}_c(t)}{dt^2}\right)_{B_i} = \vec{g}(C) + \dfrac{\vec{F}_{ext_c}}{m_c} + \dfrac{\vec{F}_{prop_c}}{m_c}. \end{cases} \tag{2.4}$$

Since the relative position in the inertial frame of reference is defined by Equation (2.1), the relative acceleration is directly given by the expression:

$$\ddot{\vec{\rho}}^{\,\mathcal{I}} = \ddot{\vec{r}}_c - \ddot{\vec{r}}_t, \tag{2.5}$$

from which we can get:

$$\left(\frac{d^2\overrightarrow{TC}}{dt^2}\right)_{B_i} = \vec{g}(C) - \vec{g}(T) + \frac{\vec{F}_{ext_c}}{m_c} - \frac{\vec{F}_{ext_t}}{m_t} + \frac{\vec{F}_{prop_c}}{m_c} - \frac{\vec{F}_{prop_t}}{m_t}, \tag{2.6}$$

that is:

$$\left(\frac{d^2\vec{\rho}}{dt^2}\right)_{B_i} = \Delta\vec{g} + \frac{\vec{F}_{ext_c}}{m_c} - \frac{\vec{F}_{ext_t}}{m_t} + \frac{\vec{F}_{prop_c}}{m_c} - \frac{\vec{F}_{prop_t}}{m_t}, \tag{2.7}$$

with

$$\Delta\vec{g} = \vec{g}(C) - \vec{g}(T).$$

In the sequel of this dissertation, the target satellite is considered as passive (non-actuated).

✣ **ASSUMPTION 1:**

The target is not actuated:

$$\vec{F}_{prop_t} = \vec{0}. \tag{2.8}$$

✣ **ASSUMPTION 2** (Two-body problem, Keplerian assumptions—2BPKE)**:**

1- *Neither the target nor the chaser undergo external orbital disturbances:*

$$\vec{F}_{ext_t} = \vec{0}, \qquad\qquad \vec{F}_{ext_c} = \vec{0}. \tag{2.9}$$

2- *Only the attraction forces of the simplified two body problem are taken into account.*

3- *The central body is spherical and homogeneous. The gravity potential is then:*

$$U(M) = U_s(M) = \frac{\mu}{r_t}. \tag{2.10}$$

4- *The target's orbit is elliptical:*

$$r_t = \frac{p}{\kappa(\nu)} = \frac{a\,(1-e^2)}{(1+e\,\cos\nu)}. \tag{2.11}$$

The usual set of orbital parameters of a given satellite is recalled in Appendix A: semi-major axis a, eccentricity e, inclination i, Right Ascension of the Ascending Node (RAAN) Ω, argument of perigee ω and true anomaly ν.

The general equation of the relative motion is therefore given by:

$$\left(\frac{d^2\vec{\rho}}{dt^2}\right)_{B_i} = \Delta\vec{g} + \frac{\vec{F}_{prop_c}}{m_c}, \tag{2.12}$$

or

$$\left(\frac{d^2\vec{r}_c(t)}{dt^2} - \frac{d^2\vec{r}_t(t)}{dt^2}\right)_{B_i} = \vec{g}(C) - \vec{g}(T) + \frac{\vec{F}_{prop_c}}{m_c}. \tag{2.13}$$

The general methodology therefore consists of writing the different terms $\frac{d^2\vec{r}_c(t)}{dt^2}$, $\frac{d^2\vec{r}_t(t)}{dt^2}$, $\vec{g}(C)$, $\vec{g}(T)$, of this equation in the target local reference frame $\mathcal{O}_t$. In case Keplerian assumptions are made on the reference, the computation is relatively straightforward since it involves the law of composition of the accelerations.

$$\left(\frac{d^2\vec{\rho}}{dt^2}\right)_{B_i} = \left(\frac{d^2\vec{\rho}}{dt^2}\right)_{B_{ot}} + \vec{\omega}_t \wedge (\vec{\omega}_t \wedge \vec{\rho}) + \left(\frac{d\vec{\omega}_t}{dt}\right)_{B_{ot}} \wedge \vec{\rho} + 2\vec{\omega}_t \wedge \left(\frac{d\vec{\rho}}{dt}\right)_{B_{ot}}, \tag{2.14}$$

where

- $\left(\frac{d^2\vec{\rho}}{dt^2}\right)_{B_{ot}} = \ddot{\vec{\rho}}^{\,\mathcal{O}_t}$ is the acceleration in the target's LVLH reference frame;
- $\vec{\omega}_t \wedge (\vec{\omega}_t \times \vec{\rho})$ is the centrifugal acceleration;
- $\left(\frac{d\vec{\omega}_t}{dt}\right)_{B_{ot}} \wedge \vec{\rho} = \dot{\vec{\omega}}_t \wedge \vec{\rho}$ is the Euler acceleration;
- $2\vec{\omega}_t \wedge \left(\frac{d\vec{\rho}}{dt}\right)_{B_{ot}} = 2\vec{\omega}_t \times \dot{\vec{\rho}}$ is the Coriolis acceleration.

The development of each acceleration expression is recalled in Appendix C.
From Figure 2.2, we can define the vectors of the local basis associated to the target's LVLH reference frame, $B_{ot} = [\vec{X}_{ot}, \vec{Y}_{ot}, \vec{Z}_{ot}]$ and deduce the positions of the chaser and the target and the target's angular rotation vector $\vec{\omega}_t$.

The chaser's position is given by the expression:

$$\vec{r}_c(t) = \vec{r}_t(t) + \vec{\rho}. \tag{2.15}$$

This allows us to write the equations of the target T and the chaser C in the local orbital reference frame $\mathcal{O}_t$:

$$\vec{r}_t(t) = -r_t\vec{Z}_{ot}, \tag{2.16a}$$

$$\vec{r}_c(t) = x\vec{X}_{ot} + y\vec{Y}_{ot} + (z - r_t)\vec{Z}_{ot}. \tag{2.16b}$$

The angular rotation vector of the LVLH frame associated to the target satellite with respect to the inertial frame is given by:

$$\vec{\omega}_t = -\dot{\nu}\vec{Y}_{ot}. \tag{2.17}$$

The vectors of the local orbital reference frame verify the following definition and derivation rules:

$$\begin{aligned}
\vec{X}_{ot} &= \vec{Y}_{ot} \times \vec{Z}_{ot}, & \frac{d\vec{X}_{ot}}{dt} &= \vec{\omega}_t \times \vec{X}_{ot} = \dot{\nu}\vec{Z}_{ot}, \\
\vec{Y}_{ot} &= -\frac{\vec{h}_t}{h_t}, & \frac{d\vec{Y}_{ot}}{dt} &= 0, \\
\vec{Z}_{ot} &= -\frac{\vec{r}_t}{r_t}, & \frac{d\vec{Z}_{ot}}{dt} &= \vec{\omega}_t \times \vec{Z}_{ot} = -\dot{\nu}\vec{X}_{ot}.
\end{aligned} \tag{2.18}$$

2.2.1. Expression of the different terms in the local basis $\mathcal{O}_t$

2.2.1.1. Expression of $\vec{g}(T)$

Considering the Keplerian Assumptions 2 and the fact that $\vec{r}(t) = -r_t\,\vec{Z}_{ot}$, the formulation of the central attraction term applied to the target satellite straightly comes out as:

$$\vec{g}(T) = -\mu\frac{\vec{r}_t^{\,\mathcal{O}_t}}{\|\vec{r}_t\|^3}, \qquad \vec{g}(T)^{\mathcal{O}_t} = \begin{bmatrix} 0 \\ 0 \\ \dfrac{\mu}{r_t^2} \end{bmatrix}. \tag{2.19}$$

2.2.1.2. Expression of $\vec{g}(C)$

Recalling that the position vector for the chaser satellite is given by Equation (2.16b), the current chaser's radius is given by:

$$\|\vec{r}_c\| = r_c = \sqrt{x^2 + y^2 + (z - r_t)^2}. \tag{2.20}$$

The gravitational acceleration applied on the chaser satellite and expressed in the LVLH local orbital frame becomes:

$$\vec{g}(C) = -\mu\frac{\vec{r}_c^{\,\mathcal{O}_t}}{\|\vec{r}_c\|^3}, \qquad \vec{g}(C)^{\mathcal{O}_t} = -\frac{\mu}{r_c^3}\begin{bmatrix} x \\ y \\ z - r_t \end{bmatrix}. \tag{2.21}$$

2.2.1.3. Expression of $\left(\frac{d^2\vec{r}_t(t)}{dt^2}\right)_{B_{ot}}$

Deriving Expression (2.16a), we get:

$$\dot{\vec{r}}_t = r_t\,\dot{\nu}\,\vec{X}_{ot} - \dot{r}_t\,\vec{Z}_{ot}. \tag{2.22}$$

Let us define the angular momentum associated to the target orbit as a function of the orbital parameters of this orbit:

$$\vec{h}_t = \vec{r}_t \times \dot{\vec{r}}_t = -r_t^2\,\dot{\nu}\,\vec{Y}_{ot}, \tag{2.23}$$

therefore obtained as:

$$h_t = r_t^2\dot{\nu}. \tag{2.24}$$

Due to the Keplerian Assumptions 2, the target's orbit angular momentum $\vec{h}_t^{\,\mathcal{O}_t}$ is constant and its time derivative is therefore zero. Deriving Equation (2.23), it is possible to obtain the following relations:

$$\dot{\vec{h}}_t = 0 = -(2r_t\dot{r}_t\dot{\nu} + r_t^2\ddot{\nu})\,\vec{Y}_{ot} \Rightarrow 2\dot{r}_t\dot{\nu} = -r_t\ddot{\nu}. \tag{2.25}$$

The acceleration vector of the target satellite in the LVLH reference frame is calculated and simplified using (2.25) as follows:

$$\ddot{\vec{r}}_t = (r_t\ddot{\nu} + 2\dot{r}_t\dot{\nu})\vec{X}_{ot} + (r_t\dot{\nu}^2 - \ddot{r}_t)\vec{Z}_{ot} = (r_t\ddot{\nu} - r_t\ddot{\nu})\vec{X}_{ot} + (r_t\dot{\nu}^2 - \ddot{r}_t)\vec{Z}_{ot} = (r_t\dot{\nu}^2 - \ddot{r}_t)\vec{Z}_{ot}. \tag{2.26}$$

Finally, from Equations (2.16a), (2.23) and (2.26) in a vector form, we have obtained:

$$\vec{r}_t^{\,\mathcal{O}_t} = \begin{bmatrix} 0 \\ 0 \\ -r_t \end{bmatrix}, \qquad \dot{\vec{r}}_t^{\,\mathcal{O}_t} = \begin{bmatrix} r_t\dot{\nu} \\ 0 \\ -\dot{r}_t \end{bmatrix}, \qquad \ddot{\vec{r}}_t^{\,\mathcal{O}_t} = \begin{bmatrix} 0 \\ 0 \\ r_t\dot{\nu}^2 - \ddot{r}_t \end{bmatrix}. \tag{2.27}$$

2.2.1.4. Expression of $\left(\frac{d^2\vec{r}_c(t)}{dt^2}\right)_{B_{ot}}$

Taking Expression (2.16b) and deriving it with respect to time, it is possible to get the chaser's relative velocity vector expressed in the basis associated to the LVLH reference frame.

$$\begin{aligned} \dot{\vec{r}}_c &= \dot{x}\vec{X}_{ot} + \dot{\nu}x\vec{Z}_{ot} + \dot{y}\vec{Y}_{ot} + (\dot{z} - \dot{r}_t)\vec{Z}_{ot} - \dot{\nu}(z - r_t)\vec{X}_{ot} \\ &= [\dot{x} - \dot{\nu}(z - r_t)]\vec{X}_{ot} + \dot{y}\vec{Y}_{ot} + [\dot{\nu}x + (\dot{z} - \dot{r}_t)]\vec{Z}_{ot}. \end{aligned} \tag{2.28}$$

The chaser's acceleration vector in the basis of the LVLH frame is obtained by derivation of this last expression:

$$\begin{aligned} \ddot{\vec{r}}_c &= [\ddot{x} - \ddot{\nu}(z - r_t) - \dot{\nu}(\dot{z} - \dot{r}_t)\vec{X}_{ot} + \dot{\nu}[\dot{x} - \dot{\nu}(z - r_t)]\vec{Z}_{ot} + \ddot{y}\vec{Y}_{ot} + [(\ddot{z} - \ddot{r}_t) + \ddot{\nu}x + \dot{\nu}\dot{x}]\vec{Z}_{ot} \\ &\quad - \dot{\nu}[\dot{z} - \dot{r}_t + \dot{\nu}x]\vec{X}_{ot}, \\ &= [\ddot{x} - \dot{\nu}^2 x - \ddot{\nu}(z - r_t) - 2\dot{\nu}(\dot{z} - \dot{r}_t)]\vec{X}_{ot} + \ddot{y}\vec{Y}_{ot} + [\ddot{z} - \ddot{r}_t - \dot{\nu}^2(z - r_t) + 2\dot{\nu}\dot{x} + \ddot{\nu}x]\vec{Z}_{ot}. \end{aligned} \tag{2.29}$$

Expressing Equations (2.16b), (2.28) and (2.29) in a vector form, we obtain:

$$\vec{r}_c^{\,\mathcal{O}_t} = \begin{bmatrix} x \\ y \\ z - r_t \end{bmatrix}, \quad \dot{\vec{r}}_c^{\,\mathcal{O}_t} = \begin{bmatrix} \dot{x} - \dot{\nu}(z - r_t) \\ \dot{y} \\ \dot{\nu}x + (\dot{z} - \dot{r}_t) \end{bmatrix}, \quad \ddot{\vec{r}}_c^{\,\mathcal{O}_t} = \begin{bmatrix} \ddot{x} - \dot{\nu}^2 x - \ddot{\nu}(z - r_t) - 2\dot{\nu}(\dot{z} - \dot{r}_t) \\ \ddot{y} \\ \ddot{z} - \ddot{r}_t - \dot{\nu}^2(z - r_t) + 2\dot{\nu}\dot{x} + \ddot{\nu}x \end{bmatrix}. \tag{2.30}$$

2.2.1.5. Expression of $\left(\frac{d^2\vec{\rho}}{dt^2}\right)_{B_{ot}}$

The difference of Expressions (2.30) and (2.27) results in:

$$\left(\frac{d^2\vec{\rho}}{dt^2}\right)_{\mathcal{O}_t} = \ddot{\vec{r}}_c^{\,\mathcal{O}_t} - \ddot{\vec{r}}_t^{\,\mathcal{O}_t} = \begin{bmatrix} \ddot{x} - \dot{\nu}^2 x - 2\dot{\nu}(\dot{z} - \dot{r}_t) - \ddot{\nu}(z - r_t) \\ \ddot{y} \\ \ddot{z} - \dot{\nu}^2 z + 2\dot{\nu}\dot{x} + \ddot{\nu}x \end{bmatrix}. \tag{2.31}$$

2.2.2. Expressions of $\dot{\nu}$, $\ddot{\nu}$, r_t, $\dot{r}_t$, $\ddot{r}_t$

In the framework of Keplerian Assumptions 2, the target satellite's motion is described by the classical equations of the two body problem [100]. Let us first define some of the orbital mechanics' expressions that will be used:

- *semi-latus rectum* or parameter p:

$$p = a\,(1 - e^2), \tag{2.32}$$

- function $\kappa(\nu)$:

$$\kappa(\nu) = 1 + e\,\cos\nu, \tag{2.33}$$

- mean motion of the target satellite orbit n:

$$n = \sqrt{\frac{\mu}{a^3}}, \tag{2.34}$$

- parameter k^2:

$$k^2 = \sqrt{\frac{\mu}{p^3}} = \frac{n}{(1-e^2)^{3/2}}, \tag{2.35}$$

- orbital angular momentum h_t, also defined in (2.24):

$$h_t = r_t^2 \dot{\nu} = \sqrt{p\mu}, \tag{2.36}$$

- radius of the target's orbit r_t:

$$r_t = \frac{p}{\kappa(\nu)}. \tag{2.37}$$

We deduce therefore the following expressions:

- **Expression of $\dot{\nu}$:** starting from Equation (2.36) and combining it with Expressions (2.33), (2.32) and (2.34), we get:

$$\begin{aligned}\dot{\nu} &= \frac{h_t}{r_t^2} = h_t \frac{\kappa(\nu)^2}{p^2} = \sqrt{p\mu} \frac{(1+e\ \cos\nu)^2}{(a\ (1-e^2))^2}, \\ &= \sqrt{a(1-e^2)\ \mu \cdot \frac{(1+e\cos\nu)^4}{a^4(1-e^2)^4}} = \sqrt{\frac{\mu(1+e\cos\nu)^4}{a^3(1-e^2)^3}} = \sqrt{\frac{\mu}{a^3}} \frac{(1+e\ \cos\nu)^2}{(1-e^2)^{3/2}} = n\frac{(1+e\ \cos\nu)^2}{(1-e^2)^{3/2}}.\end{aligned} \tag{2.38}$$

  Considering now Equations (2.34), (2.35) and again (2.33) into Equation (2.38), we also obtain:

$$\dot{\nu} = n\frac{(1+e\ \cos\nu)^2}{(1-e^2)^{3/2}} = k^2(1+e\ \cos\nu)^2 = k^2\kappa(\nu)^2. \tag{2.39}$$

- **Expression of $\ddot{\nu}$:** we perform the time derivative of $\dot{\nu}$ as:

$$\ddot{\nu} = \frac{d\dot{\nu}}{dt} = \frac{d\dot{\nu}}{d\nu}\frac{d\nu}{dt} = -n^2 \frac{2e\sin\nu\ (1+e\cos\nu)^3}{(1-e^2)^3}. \tag{2.40}$$

  Similarly, if we derive Expression (2.39), we also find that:

$$\ddot{\nu} = \frac{d\dot{\nu}}{dt} = 2k^2\kappa(\nu)\dot{\rho}(\nu) = 2k^2\kappa(\nu)\kappa(\nu)'\dot{\nu} = 2k^4\kappa(\nu)^3\kappa(\nu)'. \tag{2.41}$$

- **Expression of r_t:** as it was already shown in Expression (2.11), the radial distance of the target satellite is:

$$r_t = \frac{p}{\kappa(\nu)} = \frac{a(1-e^2)}{1+e\cos(\nu)}. \tag{2.42}$$

- **Expression of $\dot{r}_t$:** the radial velocity is given by:

$$\dot{r}_t = \frac{h_t e\sin(\nu)}{p} = \sqrt{\frac{\mu}{a(1-e^2)}} e\sin(\nu). \tag{2.43}$$

- **Expression of $\ddot{r}_t$:** the radial acceleration is given by:

$$\ddot{r}_t(t) = r_t\dot{\nu}^2 - \frac{\mu}{r_t^2} = \frac{e\mu\cos(\nu)(1+e\cos(\nu))^2}{a(1-e\cos(\nu))^2}. \tag{2.44}$$

2.2.3. Nonlinear equations of Keplerian relative translational motion

Returning to the original Equation (2.12) of relative motion and using the above expressions derived for the different terms that compose it, we obtain therefore the nonlinear equations:

$$\begin{cases} \ddot{x} - \dot{\nu}^2 x - 2\dot{\nu}(\dot{z} - \dot{r}_t) - \ddot{\nu}(z - r_t) = -\dfrac{\mu}{r_c^3}x + \dfrac{F^x_{prop_c}}{m_c}, \\ \ddot{y} = -\dfrac{\mu}{r_c^3}y + \dfrac{F^y_{prop_c}}{m_c}, \\ \ddot{z} - \dot{\nu}^2 z + 2\dot{\nu}\dot{x} + \ddot{\nu}x = -\dfrac{\mu}{r_c^3}(z - r_t) - \dfrac{\mu}{r_t^2}z + \dfrac{F^z_{prop_c}}{m_c}. \end{cases} \tag{2.45}$$

It should be noted that the terms $2\dot{\nu}\dot{r}_t$ and $\ddot{\nu}r_t$ are cancelled due to the relationships:

$$\dot{\nu} = \frac{h_t}{r_t^2}, \qquad \ddot{\nu} = -2\frac{h_t\dot{r}_t}{r_t^3}, \tag{2.46}$$

obtaining therefore:

$$\begin{cases} \ddot{x} - \dot{\nu}^2 x - 2\dot{\nu}\dot{z} - \ddot{\nu}z = -\dfrac{\mu}{r_c^3}x + \dfrac{F^x_{prop_c}}{m_c}, \\ \ddot{y} = -\dfrac{\mu}{r_c^3}y + \dfrac{F^y_{prop_c}}{m_c}, \\ \ddot{z} - \dot{\nu}^2 z + 2\dot{\nu}\dot{x} + \ddot{\nu}x = -\dfrac{\mu}{r_c^3}(z - r_t) - \dfrac{\mu}{r_t^2}z + \dfrac{F^z_{prop_c}}{m_c}. \end{cases} \tag{2.47}$$

Considering the obtained expressions in (2.39), (2.40), (2.42), (2.43) and (2.44), these equations can be written as a function of the target's orbital parameters.

$$\begin{cases} \ddot{x} - n^2\dfrac{(1+e\cos\nu)^4}{(1-e^2)^3}x - 2n\dfrac{(1+e\cos\nu)^2}{(1-e^2)^{3/2}}\dot{z} + n^2\dfrac{2e\sin\nu\,(1+e\cos\nu)^3}{(1-e^2)^3}z = \\ \qquad -\dfrac{\mu}{\left(x^2+y^2+\left(z-\frac{a(1-e^2)}{1+e\cos(\nu)}\right)^2\right)^{3/2}}x + \dfrac{F^x_{prop_c}}{m_c}, \\ \ddot{y} = -\dfrac{\mu}{\left(x^2+y^2+\left(z-\frac{a(1-e^2)}{1+e\cos(\nu)}\right)^2\right)^{3/2}}y + \dfrac{F^y_{prop_c}}{m_c}, \\ \ddot{z} - n^2\dfrac{(1+e\cos\nu)^4}{(1-e^2)^3}z + 2n\dfrac{(1+e\cos\nu)^2}{(1-e^2)^{3/2}}\dot{x} - n^2\dfrac{2e\sin\nu\,(1+e\cos\nu)^3}{(1-e^2)^3}x = \\ \qquad -\dfrac{\mu}{\left(x^2+y^2+\left(z-\frac{a(1-e^2)}{1+e\cos(\nu)}\right)^2\right)^{3/2}}\left(z-\dfrac{a(1-e^2)}{1+e\cos(\nu)}\right) - \dfrac{\mu(1+e\cos(\nu))^2}{a^2(1-e^2)^2}z + \dfrac{F^z_{prop_c}}{m_c}. \end{cases} \tag{2.48}$$

2.3. Linearized equations of the relative translational motion

2.3.1. Linearization of differential gravity in the local basis $\mathcal{O}_t$

From Equations (2.12), (2.19) and (2.21), we have:

$$\Delta\vec{g}^{\;\mathcal{O}_t} = \vec{g}(C)^{\;\mathcal{O}_t} - \vec{g}(T)^{\;\mathcal{O}_t} = \begin{bmatrix} -\frac{\mu}{r_c^3}x & -\frac{\mu}{r_c^3}y & -\frac{\mu}{r_c^3}(z-r_t)+\frac{\mu}{r_t^2}z \end{bmatrix}^T. \tag{2.49}$$

The linearization of the differential gravity term is done using a first order Taylor expansion. The point of application (op) for linearization is $\vec{r}_{c_0} = \vec{r}_t = [0 \quad 0 \quad -r_t]^T$. So,

$$\vec{g}(C) = \vec{g}(C)_0 + \left.\frac{\partial\vec{g}(C)}{\partial\vec{r}_c}\right|_{op}(\vec{r}_c - \vec{r}_{c_0}). \tag{2.50}$$

The first term corresponds to $\vec{g}(C)_0 = \vec{g}(T)$. The development of the Jacobian matrix is made in accordance with the expression (C.11), which result is reminded below:

$$\left.\frac{\partial\vec{g}(C)}{\partial\vec{r}_c}\right|_{op} = -\frac{\mu}{r_t^3}\begin{bmatrix} 1 & 0 & 0 \\ 0 & 1 & 0 \\ 0 & 0 & -2 \end{bmatrix} = -\frac{\mu}{r_t^3}M. \tag{2.51}$$

The term $\vec{r}_c - \vec{r}_{c_0}$ corresponds to $\vec{r}_c - \vec{r}_t = \vec{\rho}$. It is therefore obtained as:

$$\vec{g}(C) - \vec{g}(T) = \Delta\vec{g} \cong -\frac{\mu}{r_t^3}M\vec{\rho}. \tag{2.52}$$

Thus, developing again the Kepler relative motion from Expression (2.52), it comes:

$$\Delta\vec{g}^{\;\mathcal{O}_t} = -\frac{\mu}{r_t^3}\begin{bmatrix} x \\ y \\ -2z \end{bmatrix}. \tag{2.53}$$

Therefore, Expression (2.47) leads to the following equations, presented in [119]:

$$\begin{cases} \ddot{x} = \left[\dot{\nu}^2 - \frac{\mu}{r_t^3}\right]x + \ddot{\nu}z + 2\dot{\nu}\dot{z} + \frac{F^x_{prop_c}}{m_c}, \\ \ddot{y} = -\frac{\mu}{r_t^3}y + \frac{F^y_{prop_c}}{m_c}, \\ \ddot{z} = -\ddot{\nu}x + \left[\dot{\nu}^2 + 2\frac{\mu}{r_t^3}\right]z - 2\dot{\nu}\dot{x} + \frac{F^z_{prop_c}}{m_c}. \end{cases} \tag{2.54}$$

2.3.2. Linear translational model and simplifications

Considering the state $X(t)$ composed by the positions and velocities in the LVLH reference frame:

$$X(t) = [x \quad y \quad z \quad \dot{x} \quad \dot{y} \quad \dot{z}]^T, \tag{2.55}$$

the linear translational model represented in Equation (2.54) can be written in a state space representation as:

$$\dot{X}(t) = A(t)X(t) + B\,U(t), \tag{2.56}$$

where the Linear Time-Variant (LTV) dynamic matrix $A(t)$ is defined as:

$$A(t) = \begin{bmatrix} 0 & 0 & 0 & 1 & 0 & 0 \\ 0 & 0 & 0 & 0 & 1 & 0 \\ 0 & 0 & 0 & 0 & 0 & 1 \\ \dot{\nu}^2 - \dfrac{\mu}{r_t^3} & 0 & \ddot{\nu} & 0 & 0 & 2\dot{\nu} \\ 0 & -\dfrac{\mu}{r_t^3} & 0 & 0 & 0 & 0 \\ -\ddot{\nu} & 0 & \dot{\nu}^2 + 2\dfrac{\mu}{r_t^3} & -2\dot{\nu} & 0 & 0 \end{bmatrix}, \tag{2.57}$$

the input matrix B is defined as:

$$B = \begin{bmatrix} 0_{3\times 3} \\ I_3 \end{bmatrix}, \tag{2.58}$$

and the input vector $U(t)$ is given by:

$$U(t) = \begin{bmatrix} \dfrac{F^{\,x}_{prop_c}}{m_c} & \dfrac{F^{\,y}_{prop_c}}{m_c} & \dfrac{F^{\,z}_{prop_c}}{m_c} \end{bmatrix}^T. \tag{2.59}$$

In this dissertation, we apply several transformations that allow us to obtain a series of simplified linear models, according to their final use.

The two first transformations are well-known in the literature concerning the relative motion of two spacecraft. The first one, denoted by $H(\nu)$, applies a simplification leading to the well-known *Tschauner-Hempel equations*, firstly proposed by [119]. This is a common operation that changes the time t as independent variable in benefit of the true anomaly ν. The second transformation, denoted by $T(\nu)$, allows us to obtain the *simplified Tschauner-Hempel equations*, whose advantage is that they can be easily solved analytically.

However, we include here two other transformations: the third one, denoted by $C(\nu)$, will lead to a model under which the satellite's free motion may be easily characterized by periodic trajectories; while the fourth one, denoted by $S(\nu)$, allows us to express the satellite's free motion by means of a Linear Time-Invariant (LTI) dynamic matrix.

These four transformations $H(\nu)$, $T(\nu)$, $C(\nu)$ and $S(\nu)$, together with another three auxiliary ones $T_{TH}(\nu)$, $R(\nu)$ and $L(\nu)$, are represented in Figure 2.3 and will be explained in the following sections.

$$\begin{tikzcd} X(t) \arrow[r, "H(\nu)"] \arrow[rr, bend left, "T_{TH}(\nu)"] & X(\nu) \arrow[r, "T(\nu)"] \arrow[rrr, bend right, "R(\nu)"'] & \tilde{X}(\nu) \arrow[r, "C(\nu)"] & \bar{\xi}(\nu) \arrow[r, "S(\nu)"] & \widehat{\xi}(\nu) \end{tikzcd}$$

Figure 2.3: Coordinate transformations.

For the development of these simplified models, we are considering only the part of the equations that describe the satellite's free motion, so that no input is taken into account. The action of the control inputs will be considered individually for each single control scheme in the next chapters of this manuscript. We start the coordinate changes considering the first term of the right-hand Equation in (2.56):

$$\dot{X}(t) = A(t)X(t). \tag{2.60}$$

2.3.2.1. Transformation $H(\nu)$

Let us now define the first simplification. Note that the linear differential equations of Expression (2.54) evolve with respect to the true anomaly ν, which depends itself on the time t for any eccentricity $0 \leq e < 1$. The first change of variable replaces the independent variable, from time t to true anomaly ν, by applying the identities:

$$\begin{aligned} \frac{d(\cdot)}{dt} &= \dot{(\cdot)} = \frac{d(\cdot)}{d\nu}\frac{d\nu}{dt} = (\cdot)'\dot{\nu}, \\ \frac{d^2(\cdot)}{dt^2} &= \ddot{(\cdot)} = (\cdot)''\dot{\nu}^2 + (\cdot)'\ddot{\nu}, \end{aligned} \tag{2.61}$$

where $(\cdot)$ represents any variable, and the prime symbol $'$ represents the derivative with respect to the true anomaly ν.

DEFINITION 2.3.1: ***Coordinate transformation matrix $H(\nu)$:***
$H(\nu)$ is the matrix implementing the change of variable shown in (2.61) *from the state $X(t)$ to the state $X(\nu)$:*

$$X(\nu) = H(\nu)X(t), \tag{2.62}$$

defined as:

$$H(\nu) = \begin{bmatrix} I_3 & 0_{3\times 3} \\ 0_{3\times 3} & \dfrac{1}{\dot{\nu}} I_3 \end{bmatrix}. \tag{2.63}$$

The advantage of such a change of variable is the fact that it provides a simplified system of equations such that their expressions depend on the true anomaly ν. After performing the variable change in Expression (2.61), the free motion terms of the linear model written in Equation (2.54) are therefore:

$$\begin{cases} x''\dot{\nu}^2 + x'\ddot{\nu} = \left[\dot{\nu}^2 - \dfrac{\mu}{r_t^3}\right] x + \ddot{\nu}z + 2\dot{\nu}^2 z', \\ y''\dot{\nu}^2 + y'\ddot{\nu} = -\dfrac{\mu}{r_t^3} y, \\ z''\dot{\nu}^2 + z'\ddot{\nu} = -\ddot{\nu}x + \left[\dot{\nu}^2 + 2\dfrac{\mu}{r_t^3}\right] z - 2\dot{\nu}^2 x'. \end{cases} \tag{2.64}$$

The term $\dfrac{\mu}{r_t^3}$ can be simplified using Equation (2.36), such that we have:

$$\frac{\mu}{r_t^3} = \frac{\mu\,\dot{\nu}^{3/2}}{h_t^{3/2}} = \sqrt{\frac{\mu^2}{{h_t}^3}} \cdot \dot{\nu}^{3/2} = \sqrt{\frac{\mu^2}{\sqrt{p\mu}^3}} \cdot \dot{\nu}^{3/2}. \tag{2.65}$$

Including now Expressions (2.32), (2.34) and (2.35), we obtain:

$$\sqrt{\frac{\mu^2}{\sqrt{p\mu}^3}} \cdot \dot{\nu}^{3/2} = \sqrt{\sqrt{\frac{\mu}{a^3(1-e^2)^3}}} \cdot \dot{\nu}^{3/2} = \sqrt{\frac{n}{(1-e^2)^{3/2}}} \cdot \dot{\nu}^{3/2} = \sqrt{k^2}\,\dot{\nu}^{3/2} = k\,\dot{\nu}^{3/2}. \tag{2.66}$$

Combining this last expression together with the value of $\dot{\nu}$ found in Equation (2.39), we get:

$$\frac{\mu}{r_t^3} = k\,(k^2\kappa(\nu)^2)^{3/2} = k^4\kappa(\nu)^3. \tag{2.67}$$

Including Expressions (2.35) and (2.33) into Equation (2.67), we get:

$$\frac{\mu}{r_t^3} = n^2 \left(\frac{1 + e \cos \nu}{1 - e^2} \right)^3 . \tag{2.68}$$

Replacing the values of $\dot{\nu}$, $\ddot{\nu}$ and $\frac{\mu}{r_t^3}$ given by Equations (2.39), (2.41) and (2.67) respectively into the model given by Equation (2.64), we obtain the following Equation (the full development of Expression (2.69) is given in Appendix C, Section C.3):

$$\begin{cases} (\kappa(\nu)x)'' = 2\left(\kappa(\nu)z\right)', \\ (\kappa(\nu)y)'' = -\kappa(\nu)y, \\ (\kappa(\nu)z)'' = 3z - 2\left(\kappa(\nu)x\right)'. \end{cases} \tag{2.69}$$

2.3.2.2. Transformation $T(\nu)$

If we take a look at the linear translational model given by Equation (2.69), a relation of the form:

$$\left(\kappa(\nu)(\cdot)\right)'' = f(\cdot)\left(\kappa(\nu)(\cdot)\right), \tag{2.70}$$

may be remarked, which allows us to define the second coordinate transformation.

➻ **DEFINITION 2.3.2:** ***Coordinate transformation matrix*** $T(\nu)$***:***
$T(\nu)$ is the matrix implementing the change of variable from the state $X(\nu)$ to the state $\tilde{X}(\nu)$:

$$\tilde{X}(\nu) = T(\nu)X(\nu), \tag{2.71}$$

defined as:

$$T(\nu) = \begin{bmatrix} \kappa(\nu)I_3 & 0_{3\times3} \\ \kappa(\nu)'I_3 & \kappa(\nu)I_3 \end{bmatrix}. \tag{2.72}$$

Applying the variable change defined by the matrix $T(\nu)$ in Expression (2.72) to the linear model given by Equation (2.69), we obtain the so-called *simplified Tschauner-Hempel equations*:

$$\begin{cases} \tilde{x}'' = 2\tilde{z}', \\ \tilde{y}'' = -\tilde{y}, \\ \tilde{z}'' = \dfrac{3}{\kappa(\nu)}\tilde{z} - 2\tilde{x}'. \end{cases} \tag{2.73}$$

The associated model in *tilde* coordinates is given by:

$$\tilde{X}(\nu)' = \tilde{A}(\nu)\tilde{X}(\nu), \tag{2.74}$$

where the dynamic matrix $\tilde{A}(\nu) \in \mathbb{R}^6$ characterising the free motion of the satellite is:

$$\tilde{A}(\nu) = \begin{bmatrix} 0 & 0 & 0 & 1 & 0 & 0 \\ 0 & 0 & 0 & 0 & 1 & 0 \\ 0 & 0 & 0 & 0 & 0 & 1 \\ 0 & 0 & 0 & 0 & 0 & 2 \\ 0 & -1 & 0 & 0 & 0 & 0 \\ 0 & 0 & \dfrac{3}{\kappa(\nu)} & -2 & 0 & 0 \end{bmatrix}. \tag{2.75}$$

For simplification purposes in later chapters, we also define the auxiliary *Tschauner-Hempel* transformation $T_{TH}(\nu)$, who gathers in one single matrix the change of variable $H(\nu)$ in Equation (2.63) and the transformation $T(\nu)$ in (2.72).

DEFINITION 2.3.3: ***Coordinate transformation matrix $T_{TH}(\nu)$:***
$T_{TH}(\nu)$ is the matrix implementing the change of variable from the state $X(t)$ to the state $\tilde{X}(\nu)$:

$$\tilde{X}(\nu) = T_{TH}(\nu) X(t), \tag{2.76}$$

defined as:

$$T_{TH}(\nu) = T(\nu)H(\nu) = \begin{bmatrix} \kappa(\nu) I_3 & 0_{3\times3} \\ \kappa(\nu)' I_3 & \dfrac{k^2}{\kappa(\nu)} I_3 \end{bmatrix}. \tag{2.77}$$

NOTE:
In the literature, we often find the transformation $T_{TH}(\nu)$ simply denoted as $T(\nu)$. However, for clarity purposes in this manuscript, we differentiate the three matrices $H(\nu)$, $T(\nu)$ and $T_{TH}(\nu)$, verifying $T_{TH}(\nu) = T(\nu)H(\nu)$, and we maintain these notations all along this dissertation.

The differential equations of Expression (2.74) can be solved analytically. Due to simplicity reasons regarding the on-board control system implementation, it is not desirable to integrate numerically the dynamic model, specially in the context of rendezvous missions [139], [8].

Equation (2.74) falls into the class of linear homogeneous ordinary differential equations. It is well known that the space of solutions to (2.74) forms a 6-dimensional vector space. Any set of 6 linearly independent solutions $\{\phi^{c_1}, \phi^{c_2}, \phi^{c_3}, \phi^{c_4}, \phi^{c_5}, \phi^{c_6}\}$ to Equation (2.74), called a *fundamental set of solutions* [6], may then be used to build the general solution of (2.74).

A *fundamental matrix* is formed by arranging the 6 fundamental solutions in columns, which form a 6×6 square matrix as follows:

$$\tilde{\phi} = [\phi^{c_1} \quad \phi^{c_2} \quad \phi^{c_3} \quad \phi^{c_4} \quad \phi^{c_5} \quad \phi^{c_6}]. \tag{2.78}$$

Any fundamental matrix $\tilde{\phi}$ verifies Expression (2.74), thus:

$$\tilde{\phi}\,' = \tilde{A}(\nu)\,\tilde{\phi}. \tag{2.79}$$

Any matrix that solves (2.79) is a fundamental matrix if and only if $\tilde{\phi}$ is nonsingular:

$$\det(\tilde{\phi}) \neq 0, \quad \forall \nu \in L. \tag{2.80}$$

The solutions $\phi^{c_i}, i = 1, \cdots, 6$ depend continuously on the initial conditions, meaning that for every initial state there exists a unique solution. Since the initial states can be chosen arbitrarily, as long as they are linearly independent, the fundamental matrix is not unique. There exists infinite different fundamental sets of solutions to matrix differential Equation (2.74), and therefore, an infinite number of fundamental matrices $\tilde{\phi}$ satisfying (2.74).

In order to determine the general solution to Equation (2.74), we are using the *state transition matrix* $\tilde{\Phi}(\nu, \nu_0)$. This state transition matrix is uniquely determined by the dynamic matrix $\tilde{A}(\nu)$ and is independent of the particular choice of the fundamental matrix $\tilde{\phi}$.

DEFINITION 2.3.4: ***State transition matrix:***
Let $\tilde{\Phi}(\nu, \nu_0)$ be the state transition matrix between any initial state $\tilde{X}(\nu_0)$ and any final state $\tilde{X}(\nu)$. This matrix provides a direct mapping – propagation – from $\tilde{X}(\nu_0)$ to $\tilde{X}(\nu)$ at any particular time [99]. In other words, it describes dynamic changes of the state $\tilde{X}$ from step ν_0 to step ν:

$$\tilde{X}(\nu) = \tilde{\Phi}(\nu, \nu_0)\, \tilde{X}(\nu_0). \tag{2.81}$$

If $\tilde{\phi}$ is any fundamental matrix of (2.74)*, then the state transition matrix $\tilde{\Phi}(\nu, \nu_0)$ is determined by:*

$$\tilde{\Phi}(\nu, \nu_0) = \tilde{\phi}_\nu\, \tilde{\phi}_{\nu_0}^{-1} \qquad \forall \nu, \nu_0 \in L, \tag{2.82}$$

where $\tilde{\phi}_\nu$ and $\tilde{\phi}_{\nu_0}^{-1}$ is the fundamental matrix evaluated at any given time ν and at time ν_0 respectively.

Any state transition matrix verifies the following properties:

- *Identity:*
$$\tilde{\Phi}(\nu, \nu) = I. \tag{2.83}$$
- *Inverse:*
$$\tilde{\Phi}(\nu, \nu_0)^{-1} = \tilde{\Phi}(\nu_0, \nu). \tag{2.84}$$
- *Power:*
$$\tilde{\Phi}(\nu, \nu_0)^k = \tilde{\Phi}(k\nu, k\nu_0). \tag{2.85}$$
- *Evaluation over different intervals (semi-group property):*
$$\tilde{\Phi}(\nu, \nu_1)\, \tilde{\Phi}(\nu_1, \nu_0) = \tilde{\Phi}(\nu, \nu_0). \tag{2.86}$$
- *Derivative – the state transition matrix is the unique solution of the matrix equation:*
$$\tilde{\Phi}(\nu, \nu_0)' = \tilde{A}(\nu)\, \tilde{\Phi}(\nu, \nu_0). \tag{2.87}$$
- *LTI systems, where $\tilde{A}(\nu) = \tilde{A}$ [86]:*
$$\tilde{\Phi}(\nu, \nu_0) = e^{(\nu - \nu_0)\tilde{A}} = \sum_{k=0}^{\infty} \frac{1}{k!}(\nu - \nu_0)^k \tilde{A}^k. \tag{2.88}$$

The general solution to System (2.74) can therefore be expressed analytically through the state transition matrix, and it will propagate any given initial state to a desired final state.

The computation of the state transition matrix has been deeply studied in the past. The different state transition matrices treated in the existing references answer to diverse needs, such as taking into account the orbit's eccentricity or orbital perturbations – atmospheric drag, J_2, etc.

A common methodology to references [18], [84], [16], [139], [47] exploits the decoupling that we can clearly observe in Expression (2.73) between the *out-of-plane* (y axis) relative motion and the *in-plane* ($x - z$ axis) relative motion [8]. We can therefore determine the set of solutions – and therefore the fundamental matrix $\tilde{\phi}$ – in two different steps: the first one concerning the *out-of-plane* dynamics axis and the second one for the coupled *in-plane* dynamics.

- **Out-of-plane dynamics:** concerning the y-axis dynamics, all the references [18], [84], [16], [139], [47] converge to the same methodology consisting in the integration of a second order differential equation with constant coefficients.

  The *out-of-plane* dynamics is ruled by the decoupled equation for the y axis in Expression (2.73), given by:

  $$\tilde{y}'' = -\tilde{y}, \tag{2.89}$$

  which corresponds to an harmonic oscillator, whose solution can be analytically integrated as:

  $$\tilde{y} = K_1 \cos(\nu) + K_2 \sin(\nu), \tag{2.90}$$

  where K_1 and K_2 are constants of integration.

  If this expression is derived, we obtain the velocity solutions, given by:

  $$\tilde{y}' = -K_1 \sin(\nu) + K_2 \cos(\nu). \tag{2.91}$$

  We can express the solutions to Expression (2.89) as:

  $$\begin{bmatrix} \tilde{y} \\ \tilde{y}' \end{bmatrix} = \begin{bmatrix} \cos(\nu) & \sin(\nu) \\ -\sin(\nu) & \cos(\nu) \end{bmatrix} \begin{bmatrix} K_1 \\ K_2 \end{bmatrix}, \tag{2.92}$$

  and define the fundamental matrix $\tilde{\phi}_y$ corresponding to the *out-of-plane* dynamics as:

  $$\tilde{\phi}_y = \begin{bmatrix} \cos(\nu) & \sin(\nu) \\ -\sin(\nu) & \cos(\nu) \end{bmatrix}. \tag{2.93}$$

- **In-plane dynamics:**

  However, the approach to solving the coupled equation in $x - z$ axis differs from one reference to another. In this dissertation, the chosen methodology for retrieving the fundamental matrix for the *in-plane* dynamics $\tilde{\phi}_{xz}$ is the one proposed by Yamanaka and Ankersen in [139], leading afterwards to the well-known Yamanaka-Ankersen state transition matrix.

  The *in-plane* dynamics of Expression (2.73) are given by:

  $$\tilde{x}'' = 2\tilde{z}', \tag{2.94a}$$

  $$\tilde{z}'' = \frac{3}{\kappa(\nu)}\tilde{z} - 2\tilde{x}'. \tag{2.94b}$$

  Integrating Equation (2.94a) we get:

  $$\tilde{x}' = 2\tilde{z} + K_{x_1}, \tag{2.95}$$

  and inserting its result in Equation (2.94b), we obtain:

  $$\tilde{z}'' + \left(4 - \frac{3}{\kappa(\nu)}\right)\tilde{z} = -2K_{x_1}. \tag{2.96}$$

  The general solution of Expression (2.96) has the following form:

  $$\tilde{z} = K_{z_1}\varphi_1 + K_{z_2}\varphi_2 + \varphi_3, \tag{2.97}$$

  where K_{x_1}, K_{z_1} and K_{z_2} are constants of integration. The two linearly independent solutions $\varphi_1(\nu)$, $\varphi_2(\nu)$ of the homogeneous second-order differential equation of Expression (2.96) and its particular solution $\varphi_3(\nu)$ are fully detailled in [139]. The results of the solutions are given by:

$$\begin{aligned}\varphi_1(\nu) &= \kappa(\nu)\sin(\nu),\\ \varphi_2(\nu) &= 3e^2\kappa(\nu)\sin(\nu)J(\nu,\nu_0) + \kappa(\nu)\cos(\nu) - 2e,\\ \varphi_3(\nu) &= -\frac{K_{x_1}}{e}\kappa(\nu)\cos(\nu).\end{aligned} \tag{2.98}$$

Within the Yamanaka-Ankersen resolution methodology, the particular solution related to the integral term $J(\nu,\nu_0)$ is used motivated by the fact that the target's angular momentum is constant. This integral term is given by:

$$J(\nu,\nu_0) = k^2(t-t_0) = \int_{\nu_0}^{\nu}\frac{1}{\kappa(\tau)^2}d\tau, \tag{2.99}$$

which can be calculated directly from the transition time without the need of evaluating the integral but necessitating the solution of the Kepler equation.
Considering Solutions (2.98) into Equation (2.97), we get:

$$\tilde{z} = K_{z_1}\kappa(\nu)\sin(\nu) + \left(K_{z_2} - \frac{K_{x_1}}{e}\right)\kappa(\nu)\cos(\nu) - K_{z_2}e\left(2 - 3e\kappa(\nu)\sin(\nu)J(\nu,\nu_0)\right). \tag{2.100}$$

Replacing this last expression into Equation (2.95) and after integration, we obtain:

$$\tilde{x} = K_{x_2} - K_{z_1}\cos(\nu)\left(\kappa(\nu)+1\right) + \left(K_{z_2} - \frac{K_{x_1}}{e}\right)\sin(\nu)\left(\kappa(\nu)+1\right) - 3K_{z_2}e\kappa(\nu)^2J(\nu,\nu_0). \tag{2.101}$$

For simplification purposes, we adopt the following notation:

$$\begin{aligned}s &=: \kappa(\nu)\sin(\nu),\\ c &=: \kappa(\nu)\cos(\nu),\end{aligned} \tag{2.102}$$

and the following constants are redefined:

$$\begin{aligned}K_3 &=: K_{x_2},\\ K_4 &=: K_{z_1},\\ K_5 &=: K_{z_2} - \frac{K_{x_1}}{e},\\ K_6 &=: -K_{z_2}e,\end{aligned} \tag{2.103}$$

after which Equations (2.100) and (2.101) become:

$$\begin{cases}\tilde{x} = K_3 - K_4c\left(1+\dfrac{1}{\kappa(\nu)}\right) + K_5s\left(1+\dfrac{1}{\kappa(\nu)}\right) + 3K_6\kappa(\nu)^2J(\nu,\nu_0),\\ \tilde{z} = K_4s + K_5c + K_6(2 - 3esJ(\nu,\nu_0)).\end{cases} \tag{2.104}$$

If this system of equations is derived, we obtain the velocity solutions, given by:

$$\begin{cases}\tilde{x}' = 2K_4s + K_5(2c-e) + 3K_6(1 - 2esJ(\nu,\nu_0)),\\ \tilde{z}' = K_4s' + K_5c' - 3K_6e\left(s'J(\nu,\nu_0) + \dfrac{s}{\kappa(\nu)^2}\right),\end{cases} \tag{2.105}$$

with $s' = \cos(\nu) + e\cos(2\nu)$ and $c' = -(\sin(\nu) + e\sin(2\nu))$.

We can now express the solutions to Equation (2.94) for the $x-z$ axis as:

$$\begin{bmatrix}\tilde{x}\\ \tilde{z}\\ \tilde{x}'\\ \tilde{z}'\end{bmatrix} = \begin{bmatrix}1 & -c\left(1+\dfrac{1}{\kappa(\nu)}\right) & s\left(1+\dfrac{1}{\kappa(\nu)}\right) & 3\kappa(\nu)^2J(\nu,\nu_0)\\ 0 & s & c & 2-3esJ(\nu,\nu_0)\\ 0 & 2s & 2c-e & 3(1-2esJ(\nu,\nu_0))\\ 0 & s' & c' & -3e\left(s'J(\nu,\nu_0)+\dfrac{s}{\kappa(\nu)^2}\right)\end{bmatrix}\begin{bmatrix}K_3\\ K_4\\ K_5\\ K_6\end{bmatrix}, \tag{2.106}$$

and define the fundamental matrix $\tilde{\phi}_{xz}$ corresponding to the *in-plane* dynamics as:

$$\tilde{\phi}_{xz} = \begin{bmatrix} 1 & -c\left(1+\dfrac{1}{\kappa(\nu)}\right) & s\left(1+\dfrac{1}{\kappa(\nu)}\right) & 3\kappa(\nu)^2 J(\nu,\nu_0) \\ 0 & s & c & 2-3esJ(\nu,\nu_0) \\ 0 & 2s & 2c-e & 3(1-2esJ(\nu,\nu_0)) \\ 0 & s' & c' & -3e\left(s'J(\nu,\nu_0)+\dfrac{s}{\kappa(\nu)^2}\right) \end{bmatrix}. \tag{2.107}$$

Since the *out-of-plane* dynamics are decoupled from the *in-plane* dynamics, it becomes interesting to isolate them in the first position, such that the current state is re-defined as $\tilde{X}(\nu) = [\tilde{y}\ \ \tilde{y}'\ \ \tilde{x}\ \ \tilde{z}\ \ \tilde{x}'\ \ \tilde{z}']^T$.

It is now possible to build the complete fundamental matrix of solutions $\tilde{\phi}^c$ [1] from the previously obtained matrices $\tilde{\phi}_y$ and $\tilde{\phi}_{xz}$ in Expressions (2.93) and (2.107) respectively as:

$$\tilde{\phi}^c = \left[\begin{array}{c|c} \tilde{\phi}_y & 0_{2\times 4} \\ \hline 0_{4\times 2} & \tilde{\phi}_{xz} \end{array}\right]. \tag{2.108}$$

Applying notation of Expression (2.102) to matrix $\tilde{\phi}_y$, and for a particular anomaly ν, we obtain:

$$\tilde{\phi}_\nu = \left[\begin{array}{cc|cccc} \dfrac{c}{\kappa(\nu)} & \dfrac{s}{\kappa(\nu)} & 0 & 0 & 0 & 0 \\ -\dfrac{s}{\kappa(\nu)} & \dfrac{c}{\kappa(\nu)} & 0 & 0 & 0 & 0 \\ \hline 0 & 0 & 1 & -c\left(1+\dfrac{1}{\kappa(\nu)}\right) & s\left(1+\dfrac{1}{\kappa(\nu)}\right) & 3\kappa(\nu)^2 J(\nu,\nu_0) \\ 0 & 0 & 0 & s & c & 2-3esJ(\nu,\nu_0) \\ 0 & 0 & 0 & 2s & 2c-e & 3(1-2esJ(\nu,\nu_0)) \\ 0 & 0 & 0 & s' & c' & -3e\left(s'J(\nu,\nu_0)+\dfrac{s}{\kappa(\nu)^2}\right) \end{array}\right], \tag{2.109}$$

such that the next expression is verified:

$$\tilde{X}(\nu) = \tilde{\phi}^c_\nu\, K, \tag{2.110}$$

where K is composed by the terms K_i, $i = 1, \cdots, 6$, the constants of integration from Expressions (2.90), (2.100) and (2.101).

$$K = [K_1\ \ K_2\ \ K_3\ \ K_4\ \ K_5\ \ K_6]^T\,. \tag{2.111}$$

As explained in the definition of fundamental matrix in (2.78), the columns of $\tilde{\phi}^c_\nu$ are sets of independent solutions to the dynamics, meaning that any linear combination of the columns of $\tilde{\phi}^c_\nu$ will also be a set of independent solutions. In [14], it was observed that the following transformation was useful to simplify furthermore the relative dynamics [2]

$$\tilde{\phi}_\nu = \left[\begin{array}{cc|cccc} \phi^{c_1} & \phi^{c_2} & \phi^{c_3} - e\phi^{c_4} & \phi^{c_4} & \phi^{c_5} & \dfrac{\phi^{c_6}}{3} \end{array}\right]. \tag{2.112}$$

---

[1] We introduce the index c to denote a first arrangement of the columns for the fundamental matrix of solutions.

[2] Note that after the linear transformation in (2.112) ($c_3 \rightarrow c_3 - ec_4$, $c_6 \rightarrow c_6/3$), the fundamental matrix of solutions is written without the superscript c.

The equivalent fundamental matrix of solutions becomes:

$$\tilde{\phi}_\nu = \left[\begin{array}{cc|cccc}
\dfrac{c}{\kappa(\nu)} & \dfrac{s}{\kappa(\nu)} & 0 & 0 & 0 & 0 \\
-\dfrac{s}{\kappa(\nu)} & \dfrac{c}{\kappa(\nu)} & 0 & 0 & 0 & 0 \\
\hline
0 & 0 & 1 + ec\left(1 + \dfrac{1}{\kappa(\nu)}\right) & -c\left(1 + \dfrac{1}{\kappa(\nu)}\right) & s\left(1 + \dfrac{1}{\kappa(\nu)}\right) & \kappa(\nu)^2 J(\nu, \nu_0) \\
0 & 0 & -es & s & c & \dfrac{2}{3} - esJ(\nu, \nu_0) \\
0 & 0 & -2es & 2s & 2c - e & 1 - 2esJ(\nu, \nu_0) \\
0 & 0 & -es' & s' & c' & -e\left(s' J(\nu, \nu_0) + \dfrac{s}{\kappa(\nu)^2}\right)
\end{array}\right]. \tag{2.113}$$

We define now $\tilde{\phi}_{\nu_0}$, the fundamental matrix of solutions at a given location $\nu = \nu_0$. To do so, we define the following quantities at this location ν_0:

$$\begin{aligned}
s_0 &=: \kappa(\nu_0)\sin(\nu_0), \\
c_0 &=: \kappa(\nu_0)\cos(\nu_0),
\end{aligned} \tag{2.114}$$

and the term $J(\nu, \nu_0)$ in Equation (2.99) becomes:

$$J(\nu_0, \nu_0) = k^2(t_0 - t_0) = 0. \tag{2.115}$$

The equivalent fundamental matrix of solutions defined in (2.113) at location ν_0 is denoted by $\tilde{\phi}_{\nu_0}$ and is defined by:

$$\tilde{\phi}_{\nu_0} = \left[\begin{array}{cc|cccc}
\dfrac{c_0}{\kappa(\nu_0)} & \dfrac{s_0}{\kappa(\nu_0)} & 0 & 0 & 0 & 0 \\
-\dfrac{s_0}{\kappa(\nu_0)} & \dfrac{c_0}{\kappa(\nu_0)} & 0 & 0 & 0 & 0 \\
\hline
0 & 0 & 1 + ec_0\left(1 + \dfrac{1}{\kappa(\nu_0)}\right) & -c_0\left(1 + \dfrac{1}{\kappa(\nu_0)}\right) & s_0\left(1 + \dfrac{1}{\kappa(\nu_0)}\right) & 0 \\
0 & 0 & -es_0 & s_0 & c_0 & \dfrac{2}{3} - es_0 J(\nu_0, \nu_0) \\
0 & 0 & -2es_0 & 2s_0 & 2c_0 - e & 1 - 2es_0 J(\nu_0, \nu_0) \\
0 & 0 & -es_0' & s_0' & c_0' & -e\dfrac{s_0}{\kappa(\nu_0)^2}
\end{array}\right]. \tag{2.116}$$

We can now compute the determinant of $\tilde{\phi}_{\nu_0}$, since the fundamental matrix must be nonsingular, as shown in (2.80):

$$\det(\tilde{\phi}_{\nu_0}) = e^2 - 1 \neq 0 \quad \forall e \in [0, 1)\,, \tag{2.117}$$

meaning that $\tilde{\phi}_{\nu_0}$ is invertible for every closed orbit and every initial condition ν_0. The inverse of the fundamental matrix evaluated at time ν_0 is given by:

$$\tilde{\phi}_{\nu_0}^{-1} = \frac{1}{e^2-1}\left[\begin{array}{cc|cccc} \cos(\nu_0)(e^2-1) & -\sin(\nu_0)(e^2-1) & 0 & 0 & 0 & 0 \\ \sin(\nu_0)(e^2-1) & \cos(\nu_0)(e^2-1) & 0 & 0 & 0 & 0 \\ \hline 0 & 0 & e^2-1 & -3es_0\left(\frac{1}{\kappa(\nu_0)}+\frac{1}{\kappa(\nu_0)^2}\right) & es_0\left(1+\frac{1}{\kappa(\nu_0)}\right) & ec_0-2 \\ 0 & 0 & 0 & 3s_0\left(\frac{1}{\kappa(\nu_0)}+\frac{e^2}{\kappa(\nu_0)^2}\right) & -s_0\left(1+\frac{1}{\kappa(\nu_0)}\right) & 2e-c_0 \\ 0 & 0 & 0 & 3\left(\frac{c_0}{\kappa(\nu_0)}+e\right) & -c_0\left(1+\frac{1}{\kappa(\nu_0)}\right)-e & s_0 \\ 0 & 0 & 0 & 1-3\kappa(\nu_0)-e^2 & \kappa(\nu_0)^2 & -es_0 \end{array}\right]. \tag{2.118}$$

Finally, we can express the state transition matrix as shown in (2.82):

$$\tilde{\Phi}(\nu,\nu_0) = \tilde{\phi}_\nu \, \tilde{\phi}_{\nu_0}^{-1}. \tag{2.119}$$

However, the explicit expression of $\tilde{\Phi}(\nu,\nu_0)$ is omitted here, since it has a convoluted analytical form and it's not useful for further developments of the results of this chapter.

The *shape* of the closed-form solutions to Equation (2.73) shown in Expression (2.113) suggests an interesting property that can be exploited, i.e. the periodicity of these solutions. The usefulness of constraining the satellite to move within periodic trajectories, in particular in the context of formation flying applications, lies on the fact that a satellite's trajectory will remain bounded if no control is applied and no perturbation is considered.

The properties of relative trajectories as well as the periodicity conditions have already been investigated in [105], [31]. However, for completeness purposes, we take back the main steps of this development.

Periodicity is ensured by imposing the initial and the final state of the satellite's motion to match. In other words, searching for a periodic trajectory in Equation (2.73) is equivalent to imposing the passage through the same state after one period of free motion [33]:

$$\tilde{X}(\nu+2\pi) = \tilde{\Phi}(\nu,\nu+2\pi)\,\tilde{X}(\nu) = \tilde{X}(\nu). \tag{2.120}$$

$\tilde{\Phi}(\nu,\nu+2\pi)$ is the Yamanaka-Ankersen state transition matrix defined in (2.119) for the considered interval $(\nu,\nu+2\pi)$. It becomes now possible to propagate the relative state of the satellite—considering only free motion— from any given initial state $\tilde{X}(\nu_0)$, verifying Equation (2.81) [32].

2.3.2.3. Transformation $C(\nu)$

From the fundamental matrix ϕ_ν in Equation (2.113), we can observe a particular characteristic of the relative dynamics in *tilde* variables: the drift term $J(\nu,\nu_0)$ is only contained in the sixth column. This unique feature is exploited in the sequel to provide a periodicity condition.

Taking a look at Equation (2.104), we observe that the contribution of $J(\nu,\nu_0)$ to the state vector $\tilde{X}(\nu)$ disappears whenever the last element of the integration constants vector K is zero, i.e. $K_6 = 0$. The objective is therefore to seek in Equation (2.106) for an initial condition $\tilde{X}(\nu_0)$ such that $K_6 = 0$. From Expression (2.118), we get:

$$K_6 = 0 = (1-3\,\kappa(\nu_0)-e^2)\,\tilde{z}(\nu_0) + \kappa(\nu_0)^2\,\tilde{x}'(\nu_0) - e\,s_0\,\tilde{z}'(\nu_0). \tag{2.121}$$

This gives us the periodicity condition:

$$\left(1 - 3\,\kappa(\nu_0) - e^2\right)\ \tilde{z}(\nu_0) + \kappa(\nu_0)^2\ \tilde{x}(\nu_0)' - e\ s_0\ \tilde{z}(\nu_0)' = 0, \tag{2.122}$$

or:

$$\tilde{x}'(\nu_0) = \frac{3\,\kappa(\nu_0) + e^2 - 1}{\kappa(\nu_0)^2}\,\tilde{z}(\nu_0) + \frac{e\sin\nu_0}{\kappa(\nu_0)}\tilde{z}(\nu_0)', \tag{2.123}$$

meaning that for any initial condition $\tilde{X}(\nu_0)$ satisfying Equation (2.123), the chaser's free motion will evolve in a pure periodic orbit.

As shown in [31], it becomes now interesting to parametrize these periodic solutions by means of constant solutions, by exploiting the structure of the fundamental matrix ϕ_ν in (2.113), as shown in [14]. In order to obtain constant solutions, it is enough to select the state transformation matrix as the inverse of the periodic part of the solutions, i.e. by selecting $\nu = \nu_0$ such that the divergent term $J(\nu, \nu_0)$ is zero.

➻ **DEFINITION 2.3.5:** ***Coordinate transformation matrix*** $C(\nu)$***:***

$C(\nu)$ is the matrix implementing the change of variable from the state $\tilde{X}(\nu)$ to the state $\bar{\xi}(\nu)$:

$$\bar{\xi}(\nu) = C(\nu)\tilde{X}(\nu), \tag{2.124}$$

defined as:

$$C(\nu) = \tilde{\phi}_\nu^{-1}, \tag{2.125}$$

where $\tilde{\phi}_\nu$ is the fundamental matrix of solutions in (2.113). *Expression* (2.125) *leads to:*

$$C(\nu) = \left[\begin{array}{cc|cccc} \cos(\nu) & -\sin(\nu) & 0 & 0 & 0 & 0 \\ \sin(\nu) & \cos(\nu) & 0 & 0 & 0 & 0 \\ \hline 0 & 0 & 1 & -\dfrac{3e(s+\sin(\nu))}{\kappa(\nu)(e^2-1)} & \dfrac{e(s+\sin(\nu))}{e^2-1} & \dfrac{\kappa(\nu)^2 - e\cos(\nu) - 3}{e^2-1} \\ 0 & 0 & e & -3\sin(\nu) & s+\sin(\nu) & c \\ 0 & 0 & 0 & \dfrac{3(\cos(\nu)+e)}{e^2-1} & -\dfrac{c+\cos(\nu)+e}{e^2-1} & \dfrac{s}{e^2-1} \\ 0 & 0 & 0 & -\dfrac{3(3e\cos(\nu)+e^2+2)}{e^2-1} & \dfrac{3\kappa(\nu)^2}{e^2-1} & -\dfrac{3es}{e^2-1} \end{array}\right]. \tag{2.126}$$

Matrix $C(\nu)$ is always invertible, as demonstrated in Equation (2.117)*, for every closed trajectory.*

✍ **NOTE:**

It must be noted that after the coordinate transformation $C(\nu)$, the current state is defined by $\bar{\xi}(\nu) = \begin{bmatrix}\bar{\xi}_1 & \bar{\xi}_2 & \bar{\xi}_3 & \bar{\xi}_4 & \bar{\xi}_5 & \bar{\xi}_6\end{bmatrix}^T$ and not by $\tilde{X}(\nu)$, to account for the fact that the state is not defined by the chaser's cartesian positions and velocities anymore, but by a set of parameters $\bar{\xi}_i$, $i = 1, \cdots, 6$.

In order to obtain in the new *bar* coordinates the model equivalent to the one defined in Expression (2.74), we propagate the current state $\bar{\xi}(\nu)$ such that the new dynamic matrix $\bar{A}(\nu)$ can be obtained as:

$$\bar{\xi}(\nu)' = \bar{A}(\nu)\bar{\xi}(\nu), \tag{2.127}$$

where the current state $\bar{\xi}(\nu)$ is found using Expression (2.124), and its derivative is as follows:

$$\begin{aligned} \bar{\xi}(\nu)' &= \left(C(\nu)\tilde{X}(\nu)\right)', \\ &= C(\nu)'\tilde{X}(\nu) + C(\nu)\tilde{X}(\nu)', \\ &= C(\nu)'C(\nu)^{-1}\bar{\xi}(\nu) + C(\nu)\tilde{A}(\nu)C(\nu)^{-1}\bar{\xi}(\nu), \\ &= \left(C(\nu)'C(\nu)^{-1} + C(\nu)\tilde{A}(\nu)C(\nu)^{-1}\right)\bar{\xi}(\nu), \\ &= \bar{A}(\nu)\bar{\xi}(\nu). \end{aligned} \tag{2.128}$$

The analytical expression of matrix $\bar{A}(\nu)$ is therefore:

$$\bar{A}(\nu) = \left[\begin{array}{cc|cccc} 0 & 0 & 0 & 0 & 0 & 0 \\ 0 & 0 & 0 & 0 & 0 & 0 \\ \hline 0 & 0 & 0 & 0 & 0 & \dfrac{1}{\kappa(\nu)^2} \\ 0 & 0 & 0 & 0 & 0 & 0 \\ 0 & 0 & 0 & 0 & 0 & 0 \\ 0 & 0 & 0 & 0 & 0 & 0 \end{array}\right], \tag{2.129}$$

then the model in *bar* coordinates is expressed as:

$$\bar{\xi}_3' = -\frac{1}{\kappa(\nu)^2}\,\bar{\xi}_6\,, \qquad \bar{\xi}_i' = 0\,,\ \ \forall i \neq 3. \tag{2.130}$$

From Expression (2.130), we can see that constant solutions can be obtained when the sixth element of the state in *bar* coordinates is zero, i.e. $\bar{\xi}_6 = 0$.

For future developments, it is useful to determine the state transition matrix in *bar* coordinates, given by the solution to Equation (2.127):

$$\bar{\xi}(\nu) = \bar{\Phi}(\nu, \nu_0)\bar{\xi}(\nu_0). \tag{2.131}$$

The analytical expression of $\bar{\Phi}(\nu_0, \nu)$ can be found from Expression (2.124) as it follows:

$$\begin{aligned} \bar{\xi}(\nu) &= C(\nu)\tilde{X}(\nu) \\ &= C(\nu)\,\tilde{\Phi}(\nu,\nu_0)\,\tilde{X}(\nu_0) \\ &= C(\nu)\,\tilde{\phi}_\nu\,\tilde{\phi}_{\nu_0}^{-1}\,\tilde{X}(\nu_0) \\ &= C(\nu)\,\tilde{\phi}_\nu\,\tilde{\phi}_{\nu_0}^{-1}\,C(\nu_0)^{-1}\,\bar{\xi}(\nu_0) \\ &= C(\nu)\,\tilde{\phi}_\nu\,\tilde{\phi}_{\nu_0}^{-1}\,\tilde{\phi}_{\nu_0}\,\bar{\xi}(\nu_0) \\ &= C(\nu)\,\tilde{\phi}_\nu\,\bar{\xi}(\nu_0). \end{aligned} \tag{2.132}$$

Therefore:

$$\bar{\Phi}(\nu,\nu_0) = C(\nu)\,\tilde{\phi}_\nu, \tag{2.133}$$

or:

$$\bar{\Phi}(\nu,\nu_0) = \left[\begin{array}{cc|cccc} 1 & 0 & 0 & 0 & 0 & 0 \\ 0 & 1 & 0 & 0 & 0 & 0 \\ \hline 0 & 0 & 1 & 0 & 0 & J(\nu,\nu_0) \\ 0 & 0 & 0 & 1 & 0 & 0 \\ 0 & 0 & 0 & 0 & 1 & 0 \\ 0 & 0 & 0 & 0 & 0 & 1 \end{array}\right]. \tag{2.134}$$

2.3.2.4. Transformation $S(\nu)$

By observing matrix $\bar{A}(\nu)$ in (2.129), and being aware of the fact that $\kappa(\nu)$, defined in (2.33), is a periodic function of period 2π, we can apply another coordinate transformation, based on the following observation. Since the system in Expression (2.130) is LTV and periodic, we can take advantage of the *Floquet-Lyapunov transformation*, detailled below, as defined in [13]. Its objective is to find a state-coordinate transformation leading to a LTI periodic system with a constant dynamic matrix.

> ★ **PROPERTY 1:**
> ***Floquet-Lyapunov transformation:***
> *Any autonomous (no external input is considered) LTV system with periodic dynamics can be converted by means of a periodic LTV transformation into an LTI periodic system.*

We consider now the periodic system given by Expression (2.130), whose evolution is given by Equation (2.127). The solution to this equation, considering an initial condition $\bar{\xi}(\nu_0)$ at time ν_0 is given by:

$$\bar{\xi}(\nu) = \bar{\Phi}(\nu, \nu_0)\, \bar{\xi}(\nu_0), \tag{2.135}$$

where $\bar{\Phi}(\nu, \nu_0)$ is the state transition matrix between states $\bar{\xi}(\nu_0)$ and $\bar{\xi}(\nu)$.

Considering that Model (2.130) is periodic of period $T = 2\pi$, we can impose the periodicity condition over the state transition matrix, as it follows:

$$\bar{\Phi}(\nu + 2\pi, \nu_0 + 2\pi) = \bar{\Phi}(\nu, \nu_0). \tag{2.136}$$

If we consider the state transition matrix exactly one period T after the initial time (i.e. true anomaly) ν_0, we obtain the *monodromy matrix*, defined as:

$$\bar{\Psi}(\nu_0) = \bar{\Phi}(\nu_0 + 2\pi, \nu_0). \tag{2.137}$$

Considering T_t the orbital period in time and $nT_t = T = 2\pi$, the orbital period in true anomaly, we can obtain the analytical expression of (2.137) from Expression (2.134), where the term $J(\nu, \nu_0)$ is computed as shown in Equations (2.35) and (2.99), for the considered interval, as it follows:

$$J(\nu_0, \nu_0 + 2\pi) = k^2(t_0 + T_t - t_0) = \frac{nT_t}{(1-e^2)^{3/2}} = \frac{2\pi}{(1-e^2)^{3/2}}, \tag{2.138}$$

The expression for the monodromy matrix is given by:

$$\bar{\Psi}(\nu_0) = \left[\begin{array}{cc|cccc} 1 & 0 & 0 & 0 & 0 & 0 \\ 0 & 1 & 0 & 0 & 0 & 0 \\ \hline 0 & 0 & 1 & 0 & 0 & \frac{2\pi}{(1-e^2)^{3/2}} \\ 0 & 0 & 0 & 1 & 0 & 0 \\ 0 & 0 & 0 & 0 & 1 & 0 \\ 0 & 0 & 0 & 0 & 0 & 1 \end{array}\right]. \tag{2.139}$$

If $S(\nu)$ is a T-periodic invertible state-space transformation $\widehat{\xi}(\nu) = S(\nu)\bar{\xi}(\nu)$, then, according to Floquet-Lyapunov's theory, in the new coordinates the dynamic matrix is given by:

$$\widehat{A}(\nu) = S(\nu)\bar{A}(\nu)S(\nu)^{-1} + S(\nu)'S(\nu)^{-1}. \tag{2.140}$$

Floquet's theory then aims at finding a constant dynamic matrix $\widehat{A}(\nu) = \widehat{A}$, that must satisfy the matrix differential equation:

$$S(\nu)' = \widehat{A}S(\nu) - S(\nu)\bar{A}(\nu), \tag{2.141}$$

whose solution, given the initial condition at ν_0, is:

$$S(\nu) = e^{\widehat{A}(\nu-\nu_0)}S(\nu_0)\bar{\Phi}(\nu,\nu_0). \tag{2.142}$$

By taking now the instant $\nu = \nu_0 + T$, where $T = 2\pi$, and by imposing the periodicity condition $S(\nu_0 + 2\pi) = S(\nu_0)$ to the solution given by Equation (2.142), this last becomes:

$$S(\nu_0 + 2\pi) = S(\nu_0) = e^{2\pi\widehat{A}}S(\nu_0)\ \bar{\Phi}(\nu_0 + 2\pi, \nu_0), \tag{2.143}$$

where:

$$\bar{\Phi}(\nu_0 + 2\pi, \nu_0) = \bar{\Psi}(\nu_0)^{-1}, \tag{2.144}$$

is the inverse of the monodromy matrix shown in Expression (2.137).

The Floquet's problem aims therefore at finding the pair of matrices $(\widehat{A}, \bar{S})$ that solves the algebraic equation:

$$\bar{S} = e^{2\pi\widehat{A}}\bar{S}\bar{\Psi}(\nu_0)^{-1}. \tag{2.145}$$

This equation has many solutions $(\widehat{A}, \bar{S})$. However, it is possible to simplify the choice by taking the solution that verifies $\bar{S} = I$, such that $\widehat{A}$ can be easily obtained as:

$$e^{2\pi\widehat{A}} = \bar{\Psi}(\nu_0). \tag{2.146}$$

The transformation $S(\nu)$ is therefore given by Equation (2.142) considering Expression (2.146):

$$S(\nu) = e^{\widehat{A}(\nu-\nu_0)}\bar{\Phi}(\nu,\nu_0), \tag{2.147}$$

which takes the identity value at $\nu = \nu_0 + 2k\pi$, $k \in \mathbb{Z}$, such that $\widehat{\xi}(\nu_0 + 2k\pi) = \widehat{\xi}(\nu_0)$.

We choose matrix $\widehat{A}$ to be a second degree nilpotent matrix, such that it preserves the structure of $\bar{A}(\nu)$:

$$\widehat{A}^k = 0\,, \quad \forall \quad k \geq 2. \tag{2.148}$$

The matrix exponential can therefore be computed as:

$$e^{\widehat{A}\nu} = \sum_{k=1}^{\infty} \frac{\nu^k}{k!}\widehat{A}^k = I + \nu\widehat{A}. \tag{2.149}$$

Equation (2.146) can be hence written as:

$$e^{2\pi\widehat{A}} = I + 2\pi\widehat{A} = \bar{\Psi}(\nu_0), \tag{2.150}$$

and matrix $\widehat{A}$ can be obtained analytically from Expression (2.139), given by:

$$\widehat{A} = \frac{1}{2\pi}\left(\bar{\Psi}(\nu_0) - I\right), \tag{2.151}$$

or:

$$\widehat{A} = \left[\begin{array}{cc|cccc} 0 & 0 & 0 & 0 & 0 & 0 \\ 0 & 0 & 0 & 0 & 0 & 0 \\ \hline 0 & 0 & 0 & 0 & 0 & \dfrac{1}{(1-e^2)^{3/2}} \\ 0 & 0 & 0 & 0 & 0 & 0 \\ 0 & 0 & 0 & 0 & 0 & 0 \\ 0 & 0 & 0 & 0 & 0 & 0 \end{array}\right]. \tag{2.152}$$

It is now possible to obtain analytically the expression of $S(\nu)$ as shown in Equation (2.147), where the matrix exponential is obtained as in Expression (2.150).

$$S(\nu) = \left(I + (\nu - \nu_0)\widehat{A}\right)\bar{\Phi}(\nu, \nu_0). \tag{2.153}$$

DEFINITION 2.3.6: ***Coordinate transformation matrix $S(\nu)$:***
$S(\nu)$ is the invertible and 2π-periodic matrix implementing the change of variable from the state $\bar{\xi}(\nu)$ to the state $\widehat{\xi}(\nu)$:

$$\widehat{\xi}(\nu) = S(\nu)\bar{\xi}(\nu), \tag{2.154}$$

defined as:

$$S(\nu) = \left[\begin{array}{cc|cccc} 1 & 0 & 0 & 0 & 0 & 0 \\ 0 & 1 & 0 & 0 & 0 & 0 \\ \hline 0 & 0 & 1 & 0 & 0 & \dfrac{\sigma(\nu)}{(1-e^2)^{3/2}} \\ 0 & 0 & 0 & 1 & 0 & 0 \\ 0 & 0 & 0 & 0 & 1 & 0 \\ 0 & 0 & 0 & 0 & 0 & 1 \end{array}\right], \tag{2.155}$$

where the function $\sigma(\nu)$ is defined as:

$$\begin{aligned} \sigma(\nu) :=& (\nu - \nu_0) - (M - M_0) \\ =& \Delta\nu - \Delta M, \end{aligned} \tag{2.156}$$

and where M represents the mean anomaly, as shown in Appendix A, Section A.4.

By means of this coordinate change, the dynamic matrix in the new *hat* coordinates, i.e. $\widehat{A}$ is LTI, leading to the useful feature:

$$\widehat{\xi}(\nu)' = \widehat{A}\,\widehat{\xi}(\nu). \tag{2.157}$$

DEFINITION 2.3.7: ***Coordinate transformation matrix $R(\nu)$:***
$R(\nu)$ is the LTV coordinates change matrix that implements the change of variable from the state $X(\nu)$ to the state $\widehat{\xi}(\nu)$:

$$\widehat{\xi}(\nu) = R(\nu)X(\nu), \tag{2.158}$$

defined as:

$$R(\nu) = S(\nu)\,C(\nu)\,T(\nu), \tag{2.159}$$

which can be seen in Figure 2.3.

However, for future developments in Chapter 3, we also define matrix $R^{-1}(\nu)$ as the matrix that performs the inverse transformation, from the state $\widehat{\xi}(\nu)$ to the state $X(\nu)$:

$$X(\nu) = R^{-1}(\nu)\,\widehat{\xi}(\nu), \tag{2.160}$$

where $R^{-1}(\nu)$ is composed by the following submatrices:

$$R^{-1}(\nu) = \begin{bmatrix} R_1^{-1}(\nu) & R_2^{-1}(\nu) \\ R_3^{-1}(\nu) & R_4^{-1}(\nu) \end{bmatrix}. \tag{2.161}$$

Let $R_i^{-1}(\nu) \in \mathbb{R}^{3\times 3}$, $i = 1, \dots, 4$ *be the submatrices that compose* $R^{-1}(\nu)$*, defined as:*

$$R_1^{-1}(\nu) = \begin{bmatrix} \kappa(\nu) & 0 & -\cos(\nu)\left(\dfrac{1}{\kappa(\nu)} + 1\right) \\ 0 & \dfrac{\cos(\nu)}{\kappa(\nu)} & 0 \\ -e\sin(\nu) & 0 & \sin(\nu) \end{bmatrix}, \tag{2.162}$$

$$R_2^{-1}(\nu) = \begin{bmatrix} \sin(\nu)\left(\dfrac{1}{\kappa(\nu)} + 1\right) & 0 & -\dfrac{\sigma(\nu)\kappa(\nu)}{(1-e^2)^{-3/2}} \\ 0 & \dfrac{\sin(\nu)}{\kappa(\nu)} & 0 \\ \cos(\nu) & 0 & \dfrac{\sigma(\nu)e\sin(\nu)}{(1-e^2)^{-3/2}} + \dfrac{2}{3\kappa(\nu)} \end{bmatrix}, \tag{2.163}$$

$$R_3^{-1}(\nu) = \begin{bmatrix} -e\sin(\nu) & 0 & \sin(\nu)\left(\dfrac{1}{\kappa(\nu)} + 1\right) + \dfrac{\cos(\nu)\kappa'(\nu)}{\kappa^2(\nu)} \\ 0 & -\dfrac{\sin(\nu)}{\kappa^2(\nu)} & 0 \\ -e\cos(\nu) & 0 & \cos(\nu) \end{bmatrix}, \tag{2.164}$$

$$R_4^{-1}(\nu) = \begin{bmatrix} \cos(\nu)\left(\dfrac{1}{\kappa(\nu)} + 1\right) - \dfrac{\sin(\nu)\kappa'(\nu)}{\kappa^2(\nu)} & 0 & -\dfrac{3\sigma(\nu)e\sin(\nu)}{(1-e^2)^{-3/2}} + \dfrac{1}{\kappa(\nu)} \\ 0 & \dfrac{e+\cos(\nu)}{\kappa^2(\nu)} & 0 \\ -\sin(\nu) & 0 & \dfrac{\sigma(\nu)e\cos(\nu)}{(1-e^2)^{-3/2}} - \dfrac{e\sin(\nu)}{3\kappa^2(\nu)} \end{bmatrix}. \tag{2.165}$$

In Equation (2.160)*, we define state* $X(t)$ *composed by the positions and velocities as* $X(\nu) = [x \;\; y \;\; z \;\; x' \;\; y' \;\; z']^T$*, while state* $\widehat{\xi}(\nu)$ *is composed as* $\widehat{\xi}(\nu) = [\widehat{\xi}_3 \;\; \widehat{\xi}_1 \;\; \widehat{\xi}_4 \;\; \widehat{\xi}_5 \;\; \widehat{\xi}_2 \;\; \widehat{\xi}_6]^T$*. The order of the elements in* $\widehat{\xi}(\nu)$ *is altered once taken into account the rows and columns permutations that appear in Expressions* (2.92) *and* (2.106) *due to the decoupling between axes* y *and* $x - z$*.*

The representation in (2.160) *with state* $X(\nu)$ *as defined above allows us to write the expression of the relative trajectory* $\vec{r}(\nu) = [x \;\; y \;\; z]^T$ *as a parametrization in* $\widehat{\xi}(\nu)$ *coordinates, leading to:*

$$\vec{r}(\nu)^{\;\mathcal{O}_t} = \underbrace{\begin{bmatrix} R_1^{-1}(\nu) & R_2^{-1}(\nu) \end{bmatrix}}_{R_r^{-1}(\nu)} \widehat{\xi}(\nu). \tag{2.166}$$

So far, we have performed the simplifications over the free evolution of the satellite dynamics. Let's now give the equivalent form of the constant input matrix B defined in Expression (2.58) in the transformed *hat* coordinates. For this purpose, we need first to give its expression once the true anomaly becomes the independent variable; and then, apply the coordinate change $R(\nu)$ to pass to the transformed coordinates.

We apply now Expression (2.61) to Equation (2.58) to obtain matrix $B(\nu)$, where the independent variable becomes the true anomaly, ν:

$$(\cdot)' = \frac{1}{\dot{\nu}}\dot{(\cdot)}, \tag{2.167}$$

such that the input matrix becomes:

$$B(\nu) = \frac{1}{k^2\kappa(\nu)^2}\begin{bmatrix} 0 & 0 & 0 \\ 0 & 0 & 0 \\ 0 & 0 & 0 \\ \dfrac{1}{m_c} & 0 & 0 \\ 0 & \dfrac{1}{m_c} & 0 \\ 0 & 0 & \dfrac{1}{m_c} \end{bmatrix}, \tag{2.168}$$

while $U(\nu) = U(t)$.

It is now possible to apply the coordinate transformation $R(\nu)$ of Expression (2.158) and obtain its equivalence in *hat* coordinates:

$$\widehat{B}(\nu) = R(\nu)B(\nu), \tag{2.169}$$

and whose analytical expression is:

$$\widehat{B}(\nu) = \frac{1}{k^2\kappa(\nu)^2(1-e^2)} \cdot \begin{bmatrix} 0 & -\left(1-e^2\right)\kappa(\nu)\sin(\nu) & 0 \\ 0 & \left(1-e^2\right)\kappa(\nu)\cos(\nu) & 0 \\ -e(1+\kappa(\nu))\kappa(\nu)\sin(\nu) - \dfrac{3\sigma(\nu)\kappa(\nu)^3}{(1-e^2)^{3/2}} & 0 & \dfrac{3\sigma(\nu)e\kappa(\nu)^2\sin(\nu)}{(1-e^2)^{3/2}} - \kappa(\nu)^3 + \kappa(\nu)^2 + 2\kappa(\nu) \\ (1-e^2)(1+\kappa(\nu))\kappa(\nu)\sin(\nu) & 0 & (1-e^2)\kappa(\nu)^2\cos(\nu) \\ (1+\kappa(\nu))\kappa(\nu)\cos(\nu) + e\kappa(\nu) & 0 & -\kappa(\nu)^2\sin(\nu) \\ -3\kappa(\nu)^3 & 0 & 3e\kappa(\nu)^2\sin(\nu) \end{bmatrix}, \tag{2.170}$$

while matrix $\widehat{U}(\nu) = U(\nu)$.

Matrices $\widehat{A}$ and $\widehat{B}(\nu)$ give us the necessary elements to form the state-space model in *hat* coordinates:

$$\widehat{\xi}(\nu)' = \widehat{A}\,\widehat{\xi}(\nu) + \widehat{B}(\nu)\,\widehat{U}(\nu). \tag{2.171}$$

Note that the different coordinate changes $T(\nu)$, $C(\nu)$ and $S(\nu)$ defined in (2.159) lead to a simpler expression of the dynamic matrix $\widehat{A}$, initially an LTV matrix (c.f. Expression (2.75)), which becomes LTI after the transformations (c.f. Expression (2.152)).

On the other hand, we find the opposite phenomenon concerning the input matrix $\widehat{B}(\nu)$. Initially, matrix $B(\nu)$ is LTI and has a simple expression (c.f. Expression (2.168)), but after the several transformations its expression is more complex, turning out into an LTV matrix (c.f. Expression (2.170)).

2.4. Nonlinear relative attitude dynamic models

The objective of this section is to derive the rotational relative motion model of the chaser satellite C relative to the target satellite T.

The parametrization of the relative rotational motion of a body relative to another has been the subject of various studies in the literature [113], [92], [115], [114], [133], [132], [134], [2], [68], [2], [135], [82], [5], [77], [76]. The reference [5] developed the equations of relative motion using Euler angles, while models in references [61], [77] are parametrized by a rotation matrix of the special orthogonal group vector rotations in space $SO(3)$. In the latter cases parametrization is complete and avoids singularities [21]. We chose to take a more common parametrization in orbital mechanics, based on the use of the Euler-Rodrigues parameters that form a quaternion [113], [92], [115], [114], [133], [132], [134], [2], [68], [2], [135], [82], [76]. This parametrization was originally developed in the reference [92] and taken back in [2], [68], [82] and [76]. Appendix D gives some elements and references on the parametrization of rotations of a rigid body while Appendix 1 recalls the attitude dynamics equations of a rigid body.

2.4.1. Parametrization of the relative attitude

The parametrization of the relative attitude motion between two rigid bodies (a passive target satellite T and an actuated chaser satellite C) is based on the same tools as the parametrization of the usual attitude motion of a satellite. We chose a redundant parametrization using quaternions and rotation velocities. In all cases, the aim is to parametrize the rotation of a reference frame basis with respect to another basis that belongs to another frame. It is therefore important to distinguish the reference frames and their associated basis as well as the associated hypotheses. Within the many overviewed references, this is done in a more or less complete and clear way. A bibliographical note is inserted at the end of the current subsection in order to clarify the various hypotheses appearing in the literature. For the continuation of this section, we recall the various reference frames used and their associated basis (see Figure 2.4).

Reference frame nomenclature	Basis
$\mathcal{I} = \left(O_i, \vec{X}_i, \vec{Y}_i, \vec{Z}_i\right)$: geocentric pseudo-inertial	$B_i = [\vec{X}_i, \vec{Y}_i, \vec{Z}_i]$
$\mathcal{O}_t = \left(O_t, \vec{X}_{ot}, \vec{Y}_{ot}, \vec{Z}_{ot}\right)$: target local orbital LVLH	$B_{ot} = [\vec{X}_{ot}, \vec{Y}_{ot}, \vec{Z}_{ot}]$
$\mathcal{O}_c = \left(O_c, \vec{X}_{oc}, \vec{Y}_{oc}, \vec{Z}_{oc}\right)$: chaser local orbital LVLH	$B_{oc} = [\vec{X}_{oc}, \vec{Y}_{oc}, \vec{Z}_{oc}]$
$\mathcal{B}_t = \left(O_t, \vec{X}_{bt}, \vec{Y}_{bt}, \vec{Z}_{bt}\right)$: target body	$B_{bt} = [\vec{X}_{bt}, \vec{Y}_{bt}, \vec{Z}_{bt}]$
$\mathcal{B}_c = \left(O_c, \vec{X}_{bc}, \vec{Y}_{bc}, \vec{Z}_{bc}\right)$: chaser body	$B_{bc} = [\vec{X}_{bc}, \vec{Y}_{bc}, \vec{Z}_{bc}]$

Table 2.1: Nomenclature for reference frames and basis.

In order to model the relative attitude, it is necessary to express the chaser's relative rotation velocity with respect to the target, defined by:

$$\vec{\omega}_{ct} \triangleq \vec{\omega}_{ci} - \vec{\omega}_{ti} \ , \tag{2.172}$$

where $\vec{\omega}_{ci}$ and $\vec{\omega}_{ti}$ are the angular velocities vectors for the chaser and the target respectively, expressed in the inertial reference frame. In the latter cases, these vectors will be expressed either in the target or the chaser body frame $\mathcal{B}$. To complete the parametrization of the chaser's relative rotations with

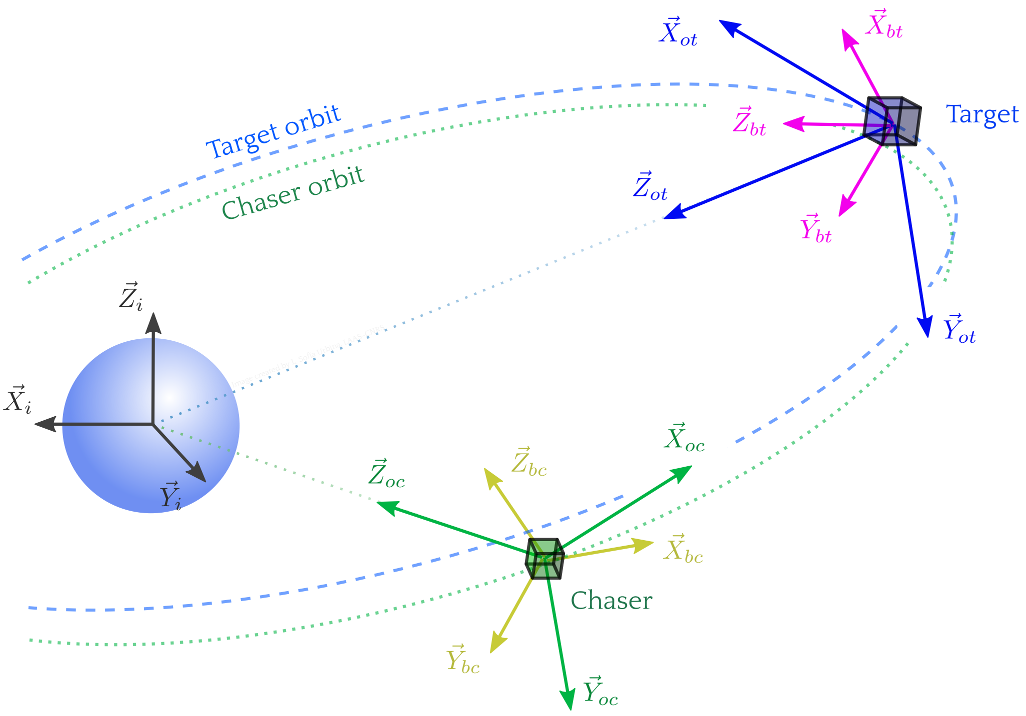

Figure 2.4: Translational relative motion.

respect to the target, we define the quaternion $q^{c/t}$ associated with its rotation matrix $R^{c/t}$ [92], [66], [69].

$$q^{c/t} = q^{c/i} \odot (q^{t/i})^{-1}, \tag{2.173}$$

where $q^{t/i}$ and $q^{c/i}$ are the unit quaternions that describe the target and chaser's orientation with respect to an inertial reference frame. The rotation matrix $R^{c/t}$ is computed as the composition of the rotation matrices:

$$R^{c/t} = R^{c/i}(R^{t/i})^T. \tag{2.174}$$

✍ *REMARK.* The definition of the quaternion describing the relative rotation between the chaser and the target satellite has many variations in the literature [92], [66], [69], [76], [2], [82], both from the point of view of notations and due to the nature of the relative quaternion. A more precise analysis of these references shows that they are unfortunately not free of errors or inconsistencies with respect to the development of the kinematic and dynamic equations of the relative attitude model. Thus, we take here the definition proposed in references [92], [66], [69], [41]. It is important to note that the reference [69] appears to have a sign error in the definition of the relative quaternion equation. [76] chose a different convention focusing on the definition of the relative quaternion associated with the rotation characterized by the rotation matrix $R^{t/c}$. Equation (9.6) of the reference [2] suggests the same choice ($D(\beta) = R^{t/c}$ to identify the respective notations of this book and of this dissertation) but Equations (9.5) and (9.7) show an internal inconsistency. Finally, the definition given in [82] neither matches any convention nor the rotations composition rules recalled in the Appendix D.

2.4.2. Kinematic equations of the relative attitude

Having chosen a particular parametrization to characterize the relative rotations between the chaser and the target, the kinematic equation expressing the relationship between the relative quaternion and the relative angular velocity is obtained identically to the conventional kinematic equation presented in Appendix (D) [92], [66], [69], [41]:

$$\dot{q}^{c/t} = \frac{1}{2} Q(q^{c/t})\, \vec{\omega}_{ct}^{\,\mathcal{B}_c}. \tag{2.175}$$

Note that the rotation velocity vector can be expressed in different reference frames using the following relationships:

$$\begin{aligned} \vec{\omega}_{ct}^{\,\mathcal{B}_c} &= \vec{\omega}_{ci}^{\mathcal{B}_c} - R^{c/t}\, \vec{\omega}_{ti}^{\,\mathcal{B}_t}, \\ \vec{\omega}_{ct}^{\,\mathcal{B}_t} &= R^{t/c} \vec{\omega}_{ci}^{\,\mathcal{B}_c} - \vec{\omega}_{ti}^{\mathcal{B}_t}. \end{aligned} \tag{2.176}$$

In order to write a full relative dynamic model, it is necessary to add to these kinematic equations, the dynamic equations that are applied to each satellite and to deduce the dynamic equations governing the relative motion.

2.4.3. Dynamic equations of the relative attitude

The attitude equation of motion for each satellite is obtained by applying the Euler equation expressing the variation of the angular momentum according to the sum of external torques applied to the body:

$$\left(\frac{d\vec{H}}{dt}\right)_{B_i} = \sum_i \vec{T}_{ext}. \tag{2.177}$$

We can apply the law of composition of velocities to the target satellite as:

$$\left(\frac{d\vec{H}_t}{dt}\right)_{B_i} = \left(\frac{d\vec{H}_t}{dt}\right)_{B_{ot}} + \vec{\omega}_{ti} \wedge \vec{H}_t = \vec{T}_t, \tag{2.178}$$

where the target's angular momentum $\vec{H}_t$ is given by:

$$\vec{H}_t = I_t\, \vec{\omega}_{ti}, \tag{2.179}$$

I_t being the target's moment of inertia and $\vec{\omega}_{ti}$ being the angular velocity.

The inertia matrix of either the chaser or the target becomes diagonal if the basis vectors of the reference frame attached to the satellite's body $\mathcal{B}_t$ coincide with the principal inertia axes of that body.

$$I^{\mathcal{B}_t} = \begin{bmatrix} I_{xx} & I_{xy} & I_{xz} \\ I_{yx} & I_{yy} & I_{yz} \\ I_{zx} & I_{zy} & I_{zz} \end{bmatrix} = \begin{bmatrix} I_{xx} & 0 & 0 \\ 0 & I_{yy} & 0 \\ 0 & 0 & I_{zz} \end{bmatrix}. \tag{2.180}$$

Let us consider the case where the chaser satellite is equipped with reaction wheels aligned with the principal axes of the chaser satellite. Its angular momentum is given by:

$$\vec{H}_c = I_c\, \vec{\omega}_{ci} + \vec{h}_{rw}. \tag{2.181}$$

I_c denotes the chaser's inertia matrix and $\vec{h}_{rw}$ the total angular momentum of the chaser's reaction wheels.

In the case where the reaction wheels are not aligned with the principal axes, Expression (2.181) becomes:

$$\vec{H}_c = I_c\, \vec{\omega}_{ci} + A_{rw}\, \vec{h}_{rw}, \tag{2.182}$$

where $A_{rw} \in \mathbb{R}^{3\times n}$ is a matrix containing the information of the actuators: it is composed by three rows and n columns, as many as the number of reaction wheels, representing the direction of the axis of rotation for each wheel.

The wheels' angular momentum $\vec{h}_{rw}$ is expressed in terms of the wheel velocity vector in the form:

$$\vec{h}_{rw} = I_{rw}\, \vec{\omega}_{rw}, \tag{2.183}$$

while its variation is directly the opposite of the one of the provided torque:

$$\dot{\vec{h}}_{rw} = -\vec{T}_{rw}. \tag{2.184}$$

Applying equation (2.177) to the chaser C and to the target T, we obtain:

$$\begin{aligned} I_t\, \dot{\vec{\omega}}_{ti}^{\,\mathcal{B}_t} &= -\omega_{ti}^{\times}\, I_t\, \vec{\omega}_{ti}^{\,\mathcal{B}_t} + \vec{T}_t^{\,\mathcal{B}_t}, \\ I_c\, \dot{\vec{\omega}}_{ci}^{\,\mathcal{B}_c} &= -\omega_{ci}^{\times}\, I_c\, \vec{\omega}_{ci}^{\,\mathcal{B}_c} - I_{rw}\, \dot{\vec{\omega}}_{rw}^{\mathcal{B}_c} - \omega_{ci}^{\times}\, I_{rw}\, \vec{\omega}_{rw}^{\mathcal{B}_c} + \vec{T}_c^{\,\mathcal{B}_c}, \end{aligned} \tag{2.185}$$

where $\vec{T}_t^{\,\mathcal{B}_t}$ and $\vec{T}_c^{\,\mathcal{B}_c}$ are the external torques applied on the target and chaser, expressed in the reference frame of the target and the chaser respectively.

By using the definition of the relative angular velocity, given by the Expression (2.172), we obtain, by means of the velocity composition law:

$$\begin{aligned} \left(\frac{d\vec{\omega}_{ct}}{dt}\right)_{B_{oc}} &= \left(\frac{d\vec{\omega}_{ci}}{dt}\right)_{B_{oc}} - \vec{\omega}_{ti} \wedge \vec{\omega}_{ct} - \left(\frac{d\vec{\omega}_{ti}}{dt}\right)_{B_{ot}}, \\ \left(\frac{d\vec{\omega}_{ct}}{dt}\right)_{B_{ot}} &= \left(\frac{d\vec{\omega}_{ci}}{dt}\right)_{B_{oc}} - \vec{\omega}_{ci} \wedge \vec{\omega}_{ct} - \left(\frac{d\vec{\omega}_{ti}}{dt}\right)_{B_{ot}}. \end{aligned} \tag{2.186}$$

Equations (2.186) are obtained by the following process:

$$\left(\frac{d\vec{\omega}_{ct}}{dt}\right)_{B_{oc}} = \left(\frac{d\vec{\omega}_{ci}}{dt}\right)_{B_{oc}} - \left(\frac{d\vec{\omega}_{ti}}{dt}\right)_{B_{oc}}. \tag{2.187}$$

$$\begin{aligned} \left(\frac{d\vec{\omega}_{ti}}{dt}\right)_{B_{oc}} &= \left(\frac{d\vec{\omega}_{ti}}{dt}\right)_{B_{ot}} + \vec{\omega}_{tc} \wedge \vec{\omega}_{ti} = \left(\frac{d\vec{\omega}_{ti}}{dt}\right)_{B_{ot}} - \vec{\omega}_{ct} \wedge \vec{\omega}_{ti}, \\ &= \left(\frac{d\vec{\omega}_{ti}}{dt}\right)_{B_{ot}} + \vec{\omega}_{ti} \wedge \vec{\omega}_{ct}, \end{aligned} \tag{2.188}$$

and replacing $-\left(\frac{d\vec{\omega}_{ti}}{dt}\right)_{B_{oc}}$ in Equation (2.187), we get the first Equation of (2.186). Similarly, starting from:

$$\left(\frac{d\vec{\omega}_{ct}}{dt}\right)_{B_{ot}} = \left(\frac{d\vec{\omega}_{ci}}{dt}\right)_{B_{ot}} - \left(\frac{d\vec{\omega}_{ti}}{dt}\right)_{B_{ot}}, \tag{2.189}$$

we obtain:

$$\left(\frac{d\vec{\omega}_{ci}}{dt}\right)_{B_t} = \left(\frac{d\vec{\omega}_{ci}}{dt}\right)_{B_c} + \vec{\omega}_{ct} \wedge \vec{\omega}_{ci} = \left(\frac{d\vec{\omega}_{ci}}{dt}\right)_{B_c} - \vec{\omega}_{ci} \wedge \vec{\omega}_{ct}\ . \tag{2.190}$$

Replacing $\left(\frac{d\vec{\omega}_{ci}}{dt}\right)_{B_t}$ in Equation (2.186), we obtain the second Equation of (2.186).
By combining Equations (2.185) with Equation (2.186), we obtain the relative dynamic equation written in the chaser's reference frame [92]:

$$\begin{aligned} I_c\, \dot{\vec{\omega}}_{ct}^{\,\mathcal{B}_c} = &- (\vec{\omega}_{ct}^{\,\mathcal{B}_c} + R^{c/t}\, \vec{\omega}_{ti}^{\,\mathcal{B}_t})^{\times}\, I_c\, (\vec{\omega}_{ct}^{\,\mathcal{B}_c} + R^{c/t}\, \vec{\omega}_{ti}^{\,\mathcal{B}_t}) \\ &- I_c \left(R^{c/t}\, \vec{\omega}_{ti}^{\,\mathcal{B}_t}\right)^{\times} \vec{\omega}_{ct}^{\,\mathcal{B}_c} - I_c\, R^{c/t}\, I_t^{-1}(\vec{T}_t^{\mathcal{B}_t} - \omega_{ti}^{\times}\, I_t\, \vec{\omega}_{ti}^{\,\mathcal{B}_t}) + \vec{T}_c^{\mathcal{B}_c} + (\vec{\omega}_{ct}^{\,\mathcal{B}_c} + R^{c/t}\, \vec{\omega}_{ti}^{\,\mathcal{B}_t})^{\times} I_{rw}\, \vec{\omega}_{rw}^{\,\mathcal{B}_c} \\ &+ \vec{T}_{rw}^{\,\mathcal{B}_c}, \end{aligned} \tag{2.191}$$

or in the target's reference frame [2]:

$$\begin{aligned} I_t\,\dot{\vec{\omega}}_{ct}^{\,\mathcal{B}_t} =& - I_t\,\omega_{ti}^{\times}\,\vec{\omega}_{ct}^{\,\mathcal{B}_t} + I_t\,R^{t/c}\,I_c^{-1}\left\{\vec{T}_c^{\mathcal{B}_c} - \left[R^{c/t}(\vec{\omega}_{ct}^{\,\mathcal{B}_t} + \vec{\omega}_{ti}^{\,\mathcal{B}_t})\right]^{\times} I_c R^{c/t}(\vec{\omega}_{ct}^{\,\mathcal{B}_t} + \vec{\omega}_{ti}^{\,\mathcal{B}_t})\right\} \\ & - (\vec{T}_t^{\,\mathcal{B}_t} - \omega_{ti}^{\times}\,I_t\,\vec{\omega}_{ti}^{\,\mathcal{B}_t}) + R^{c/t}\,\vec{T}_{rw}^{\,\mathcal{B}_t} + \left[R^{c/t}(\vec{\omega}_{ct}^{\,\mathcal{B}_t} + \vec{\omega}_{ti}^{\,\mathcal{B}_t})\right]^{\times} I_{rw}\,R^{c/t}\,\vec{\omega}_{rw}^{\,\mathcal{B}_t}. \end{aligned} \tag{2.192}$$

2.4.4. State space models for the relative attitude motion

By defining a state vector for the relative rotational motion of size 7 and composed as the vector $[\vec{\omega}_{ct}^{T} \quad (q^{c/t})^T]^T$, the dynamic equations of nonlinear dynamic state of the relative rotation is given by the equations:

$$\begin{aligned} \dot{q}^{c/t} &= \frac{1}{2}\,Q(q^{c/t})\,\vec{\omega}_{ct}^{\,\mathcal{B}_c}, \\ I_c\,\dot{\vec{\omega}}_{ct}^{\,\mathcal{B}_c} &= -(\vec{\omega}_{ct}^{\,\mathcal{B}_c} + R^{c/t}\,\vec{\omega}_{ti}^{\,\mathcal{B}_t})^{\times}\,I_c(\vec{\omega}_{ct}^{\,\mathcal{B}_c} + R^{c/t}\,\vec{\omega}_{ti}^{\,\mathcal{B}_t}) - I_c\left(R^{c/t}\,\vec{\omega}_{ti}^{\,\mathcal{B}_t}\right)^{\times}\,\vec{\omega}_{ct}^{\,\mathcal{B}_c} - \\ & -I_c\,R^{c/t}\,I_t^{-1}(\vec{T}_t^{\mathcal{B}_t} - \omega_{ti}^{\times}\,I_t\,\vec{\omega}_{ti}^{\,\mathcal{B}_t}) + \vec{T}_c^{\mathcal{B}_c} + (\vec{\omega}_{ct}^{\,\mathcal{B}_c} + R^{c/t}\,\vec{\omega}_{ti}^{\,\mathcal{B}_t})^{\times} I_{rw}\,\vec{\omega}_{rw}^{\,\mathcal{B}_c} + \vec{T}_{rw}^{\,\mathcal{B}_c}, \end{aligned} \tag{2.193}$$

considering the dynamic equation written in the chaser's reference frame; or

$$\begin{aligned} \dot{q}^{c/t} =& \frac{1}{2}\,Q(q^{c/t})\,R^{c/t}\,\vec{\omega}_{ct}^{\,\mathcal{B}_t}, \\ I_t\,\dot{\vec{\omega}}_{ct}^{\,\mathcal{B}_t} =& - I_t\,\omega_{ti}^{\times}\,\vec{\omega}_{ct}^{\,\mathcal{B}_t} + I_t R^{t/c} I_c^{-1}\left\{\vec{T}_c^{\mathcal{B}_c} - \left[R^{c/t}(\vec{\omega}_{ct}^{\,\mathcal{B}_t} + \vec{\omega}_{ti}^{\,\mathcal{B}_t})\right]^{\times} I_c\,R^{c/t}(\vec{\omega}_{ct}^{\,\mathcal{B}_t} + \vec{\omega}_{ti}^{\,\mathcal{B}_t})\right\} - (\vec{T}_t^{\,\mathcal{B}_t} \\ & - \omega_{ti}^{\times}\,I_t\,\vec{\omega}_{ti}^{\,\mathcal{B}_t}) + R^{c/t}\,\vec{T}_{rw}^{\,\mathcal{B}_t} + \left[R^{c/t}(\vec{\omega}_{ct}^{\,\mathcal{B}_t} + \vec{\omega}_{ti}^{\,\mathcal{B}_t})\right]^{\times} I_{rw}\,R^{c/t}\,\vec{\omega}_{rw}^{\,\mathcal{B}_t}, \end{aligned} \tag{2.194}$$

if we consider the dynamic equation written in the target's reference frame.

✍ *REMARK.* As it was mentioned in the introduction to this section, there are many works dedicated to the modeling of the relative rotational motion, which are characterized by a variable formalism and relatively different assumptions. In particular, the hypotheses related to the reference frames vary widely. Most of these works assume that the satellite reference frames have their axes aligned with the principal axes of inertia of each satellite [69], [72], [129], [128], [125], [1], [141], [121]. Others go further and assume that the reference frame related to the chaser's body coincides with the local orbital reference frame [66], [137], [98], [125], [61], [30]. The same hypothesis applied to the chaser can be found in [103], [101]. These last two hypotheses are met simultaneously in [76], [108]. Finally, it should be noted a curious hypothesis in [135] which implies that the target's local orbital frame coincides with an inertial reference frame and the two frames $\mathcal{B}_c$ and $\mathcal{B}_t$ also coincide.

2.5. Coupled models

The literature dedicated to the relative coupled models in translation and rotation [137], [82] agrees to distinguish between *dynamic* and *kinematic couplings*. The origin of the first coupling might be the chaser's actuators pointing constraints, considered fixed in the body reference frame; or the consideration of the gravity gradient, for example. Regarding the *kinematic coupling*, its justification is essentially based on the fact of not considering the spacecraft as point masses anymore but considering them as rigid bodies, focusing on the relative motion of a point outside the body's center of mass (chaser's docking port pointing direction towards the target's docking port along the final approach). In this section, we take the essential of the developments encountered in the literature trying as much as possible to give them a uniform treatment.

Throughout the consulted literature, with the exception of the reference [5], the relative rotation equations are not linearized by the fact that the approach and inspection phases of a non-cooperative target, are likely to lead the chaser to perform maneuvers with large angles that would not be correctly approximated by the linearized models. We have therefore chosen to retain the nonlinear coupled models of the relative motion.

2.5.1. Kinematic coupling

In order to model the kinematic coupling between the two spacecraft, we essentially take back the elements given in the reference [103]. Figure 2.5 illustrates the definition of the different geometric elements that are needed for this modeling. Points O_t and O_c are the respective centers of mass of the target and chaser satellites.

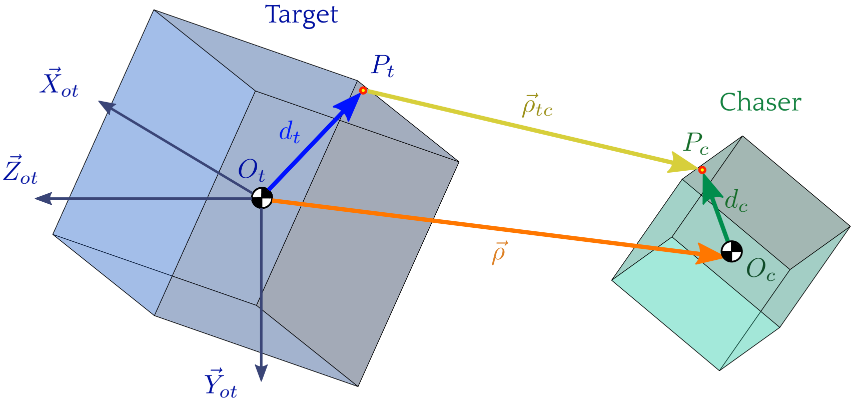

Figure 2.5: Target and chaser: kinematic coupling.

We also define two particular points P_t and P_c on the target and chaser satellites respectively, which are not coincident with their center of mass. The vectors $\vec{d_t} = \overrightarrow{O_tP_t}$ and $\vec{d_c} = \overrightarrow{O_cP_c}$ are characterized by their coordinates in the local orbital frame associated to the target (see Figure 2.5).

$$\begin{aligned} \vec{d_t}^{\mathcal{O}_t} &= [x_{bt} \quad y_{bt} \quad z_{bt}]^T, \\ \vec{d_c}^{\mathcal{O}_t} &= [x_{bc} \quad y_{bc} \quad z_{bc}]^T. \end{aligned} \tag{2.195}$$

The relative vector between points P_t and P_c, $\vec{\rho}_{tc} = \overrightarrow{P_tP_c}$ and P_c is also defined by its coordinates in the target's LVLH frame $\vec{\rho}_{tc}^{\,\mathcal{O}_t} = [x_{tc} \quad y_{tc} \quad z_{tc}]^T$. It can also be written as:

$$\vec{\rho}_{tc}^{\,\mathcal{O}_t} = \vec{\rho}^{\,\mathcal{O}_t} + \vec{d_c}^{\mathcal{O}_t} - \vec{d_t}^{\mathcal{O}_t} . \tag{2.196}$$

where $\vec{\rho} = \overrightarrow{O_tO_c}$ and $\vec{\rho}^{\,\mathcal{O}_t} = [x \quad y \quad z]^T$. Expression (2.196) is written, coordinate by coordinate as:

$$\begin{aligned} x_{tc} &= x + x_{bc} - x_{bt}, \\ y_{tc} &= y + y_{bc} - y_{bt}, \\ z_{tc} &= z + z_{bc} - z_{bt}. \end{aligned} \tag{2.197}$$

Assuming that the two satellites are non-deformable rigid bodies:

$$\left(\frac{d\vec{d_t}}{dt}\right)_{\mathcal{B}_t} = 0, \quad \left(\frac{d\vec{d_c}}{dt}\right)_{\mathcal{B}_c} = 0, \tag{2.198}$$

and applying the composition of velocities rule:

$$\left(\frac{d\vec{d}_c}{dt}\right)_{B_{ot}} = \left(\frac{d\vec{d}_c}{dt}\right)_{B_{oc}} + \vec{\omega}_{ct} \wedge \vec{d}_c, \tag{2.199}$$

the relative velocity is obtained in the target's orbital local frame as:

$$\dot{\vec{\rho}}_{tc}^{\,\mathcal{O}_t} = \dot{\vec{\rho}}^{\,\mathcal{O}_t} + \vec{\omega}_{ct}^{\,\mathcal{O}_t} \wedge \vec{d}_c^{\,\mathcal{O}_t}, \tag{2.200}$$

where $\vec{\omega}_{ct}^{\,\mathcal{O}_t} = [\omega_x \quad \omega_y \quad \omega_z]^T$. Thus, the coordinates of the relative velocity in the target's local orbital frame satisfy:

$$\begin{aligned}
\dot{x}_{tc} &= \dot{x} + \omega_y z_{bc} - \omega_z y_{bc}, \\
\dot{y}_{tc} &= \dot{y} + \omega_z x_{bc} - \omega_x z_{bc}, \\
\dot{z}_{tc} &= \dot{z} + \omega_x y_{bc} - \omega_y x_{bc}.
\end{aligned} \tag{2.201}$$

Similarly, the acceleration vector is given by:

$$\ddot{\vec{\rho}}_{tc}^{\,\mathcal{O}_t} = \ddot{\vec{\rho}}^{\,\mathcal{O}_t} + \dot{\vec{\omega}}_{ct}^{\,\mathcal{O}_t} \wedge \vec{d}_c^{\,\mathcal{O}_t} + \vec{\omega}_{ct}^{\,\mathcal{O}_t} \wedge (\vec{\omega}_{ct}^{\,\mathcal{O}_t} \wedge \vec{d}_c^{\,\mathcal{O}_t}), \tag{2.202}$$

while its coordinates in the target's local orbital frame satisfy:

$$\begin{aligned}
\ddot{x}_{tc} &= \ddot{x} + \dot{\omega}_y z_{bc} - \dot{\omega}_z y_{bc} + \omega_y(\omega_x y_{bc} - \omega_y x_{bc}) - \omega_z(\omega_z x_{bc} - \omega_x z_{bc}), \\
\ddot{y}_{tc} &= \ddot{y} + \dot{\omega}_z x_{bc} - \dot{\omega}_x z_{bc} + \omega_z(\omega_y z_{bc} - \omega_z y_{bc}) - \omega_x(\omega_x y_{bc} - \omega_y x_{bc}), \\
\ddot{z}_{tc} &= \ddot{z} + \dot{\omega}_x y_{bc} - \dot{\omega}_y x_{bc} + \omega_x(\omega_z x_{bc} - \omega_x z_{bc}) - \omega_y(\omega_y z_{bc} - \omega_z y_{bc}).
\end{aligned} \tag{2.203}$$

In summary, Equations (2.196), (2.200) and (2.202) become:

$$\begin{aligned}
\vec{\rho}_{tc}^{\,\mathcal{O}_t} &= \begin{bmatrix} x + x_{bc} - x_{bt} \\ y + y_{bc} - y_{bt} \\ z + z_{bc} - z_{bt} \end{bmatrix}, \qquad \dot{\vec{\rho}}_{tc}^{\,\mathcal{O}_t} = \begin{bmatrix} \dot{x} + \omega_y z_{bc} - \omega_z y_{bc} \\ \dot{y} + \omega_z x_{bc} - \omega_x z_{bc} \\ \dot{z} + \omega_x y_{bc} - \omega_y x_{bc} \end{bmatrix}, \\
\ddot{\vec{\rho}}_{tc}^{\,\mathcal{O}_t} &= \begin{bmatrix} \ddot{x} + \dot{\omega}_y z_{bc} - \dot{\omega}_z y_{bc} + \omega_y(\omega_x y_{bc} - \omega_y x_{bc}) - \omega_z(\omega_z x_{bc} - \omega_x z_{bc}) \\ \ddot{y} + \dot{\omega}_z x_{bc} - \dot{\omega}_x z_{bc} + \omega_z(\omega_y z_{bc} - \omega_z y_{bc}) - \omega_x(\omega_x y_{bc} - \omega_y x_{bc}) \\ \ddot{z} + \dot{\omega}_x y_{bc} - \dot{\omega}_y x_{bc} + \omega_x(\omega_z x_{bc} - \omega_x z_{bc}) - \omega_y(\omega_y z_{bc} - \omega_z y_{bc}) \end{bmatrix}.
\end{aligned} \tag{2.204}$$

By substituting the coordinates of $\vec{\rho}^{\,\mathcal{O}_t}$, $\dot{\vec{\rho}}^{\,\mathcal{O}_t}$ and $\ddot{\vec{\rho}}^{\,\mathcal{O}_t}$ given by Equations (2.197), (2.201) et (2.203) in Equation (2.47), it is possible to obtain a general description of the equations of translational motion of an arbitrary point on the chaser's body with respect to the target satellite.

$$\begin{cases} \ddot{x}_{tc} - [\dot{\omega}_y z_{bc} - \dot{\omega}_z y_{bc} + \omega_y(\omega_x y_{bc} - \omega_y x_{bc}) - \omega_z(\omega_z x_{bc} - \omega_x z_{bc})] \\ -\dot{\nu}^2\,(x_{tc} - x_{bc} + x_{bt}) - 2\dot{\nu}\,[\dot{z}_{tc} - \omega_x y_{bc} + \omega_y x_{bc}] - \ddot{\nu}\,(z_{tc} - z_{bc} + z_{bt}) = \\ = -\dfrac{\mu(x_{tc} - x_{bc} + x_{bt})}{[(x_{tc} - x_{bc} + x_{bt})^2 + (y_{tc} - y_{bc} + y_{bt})^2 + (z_{tc} - z_{bc} + z_{bt} - r_t)^2]^{\frac{3}{2}}} + \dfrac{F^x_{prop_c}}{m_c}, \\ \\ \ddot{y}_{tc} - [\dot{\omega}_z x_{bc} - \dot{\omega}_x z_{bc} + \omega_z(\omega_y z_{bc} - \omega_z y_{bc}) - \omega_x(\omega_x y_{bc} - \omega_y x_{bc})] = \\ = -\dfrac{\mu(y_{tc} - y_{bc} + y_{bt})}{[(x_{tc} - x_{bc} + x_{bt})^2 + (y_{tc} - y_{bc} + y_{bt})^2 + (z_{tc} - z_{bc} + z_{bt} - r_t)^2]^{\frac{3}{2}}} + \dfrac{F^y_{prop_c}}{m_c}, \\ \\ \ddot{z}_{tc} - [\dot{\omega}_x y_{bc} - \dot{\omega}_y x_{bc} + \omega_x(\omega_z x_{bc} - \omega_x z_{bc}) - \omega_y(\omega_y z_{bc} - \omega_z y_{bc})] - \\ -\dot{\nu}^2(z_{tc} - z_{bc} + z_{bt} - r_t) + 2\dot{\nu}(\dot{x}_{tc} - \omega_y z_{bc} + \omega_z y_{bc}) + \ddot{\nu}(x_{tc} - x_{bc} + x_{bt}) = \\ -\dfrac{\mu(z_{tc} - z_{bc} + z_{bt} - r_t)}{[(x_{tc} - x_{bc} + x_{bt})^2 + (y_{tc} - y_{bc} + y_{bt})^2 + (z_{tc} - z_{bc} + z_{bt} - r_t)^2]^{\frac{3}{2}}} - \dfrac{\mu}{r_t^2} + \dfrac{F^z_{prop_c}}{m_c}. \end{cases} \tag{2.205}$$

We recall the expressions for $\dot{\nu}$, $\ddot{\nu}$ and r_t as a function of the targer's orbital elements, which were derived in the first part of this manuscript (c.f. Expressions (2.38), (2.40) and (2.42)) for Keplerian hypotheses:

$$\dot{\nu} = n\frac{(1+e\cos\nu)^2}{(1-e^2)^{3/2}}, \quad \ddot{\nu} = -n^2\frac{2e\sin\nu\ (1+e\cos\nu)^3}{(1-e^2)^3}, \quad r_t = \frac{a(1-e^2)}{1+e\cos(\nu)}. \tag{2.206}$$

The kinematic coupling of the translational Equations (2.205) together with the nonlinear dynamic and kinematic rotational Equations (2.192) and (2.175) therefore originates from the presence of coordinates of the relative rotational velocity $\vec{\omega}_{ct}^{\,\mathcal{O}_t}$.

2.5.2. Dynamic coupling

The dynamic coupling between orbital relative motion and relative rotational motion is clearly expressed through the presence of external torques $\vec{T}_t^{\,\mathcal{B}_t}$ and $\vec{T}_c^{\,\mathcal{B}_c}$ affecting Equations (2.191) and (2.192) that are recalled hereafter:

$$\begin{aligned} I_c\,\dot{\vec{\omega}}_{ct}^{\,\mathcal{B}_c} = &-(\vec{\omega}_{ct}^{\,\mathcal{B}_c} + R^{c/t}\,\vec{\omega}_{ti}^{\,\mathcal{B}_t})^\times I_c(\vec{\omega}_{ct}^{\,\mathcal{B}_c} + R^{c/t}\,\vec{\omega}_{ti}^{\,\mathcal{B}_t}) - I_c\left(R^{c/t}\,\vec{\omega}_{ti}^{\,\mathcal{B}_t}\right)^\times \vec{\omega}_{ct}^{\,\mathcal{B}_c} - I_c\,R^{c/t}\,I_t^{-1}(\vec{T}_t^{\mathcal{B}_t} \\ &- \omega_{ti}^\times\,I_t\,\vec{\omega}_{ti}^{\,\mathcal{B}_t}) + \vec{T}_c^{\mathcal{B}_c} + (\vec{\omega}_{ct}^{\,\mathcal{B}_c} + R^{c/t}\,\vec{\omega}_{ti}^{\,\mathcal{B}_t})^\times I_{rw}\,\vec{\omega}_{rw}^{\,\mathcal{B}_c} + \vec{T}_{rw}^{\,\mathcal{B}_c}, \end{aligned} \tag{2.207}$$

and

$$\begin{aligned} I_t\,\dot{\vec{\omega}}_{ct}^{\,\mathcal{B}_{ti}} = &-I_t\,\omega_{ti}^\times\,\vec{\omega}_{ct}^{\,\mathcal{B}_t} + I_t\,R^{t/c}\,I_c^{-1}\left\{\vec{T}_c^{\mathcal{B}_c} - \left[R^{c/t}(\vec{\omega}_{ct}^{\,\mathcal{B}_t} + \vec{\omega}_{ti}^{\,\mathcal{B}_t})\right]^\times I_c\,R^{c/t}(\vec{\omega}_{ct}^{\,\mathcal{B}_t} + \vec{\omega}_{ti}^{\,\mathcal{B}_t})\right\} \\ &-(\vec{T}_t^{\,\mathcal{B}_t} - \omega_{ti}^\times\,I_t\,\vec{\omega}_{ti}^{\,\mathcal{B}_t}) + R^{c/t}\,\vec{T}_{rw}^{\,\mathcal{B}_t} + \left[R^{c/t}(\vec{\omega}_{ct}^{\,\mathcal{B}_t} + \vec{\omega}_{ti}^{\,\mathcal{B}_t})\right]^\times I_{rw}\,R^{c/t}\,\vec{\omega}_{rw}^{\,\mathcal{B}_t}. \end{aligned} \tag{2.208}$$

These torques may well represent different types of orbital perturbations according to the reviewed references. In particular, the influence of the gravity gradient [92], [48], [76], the solar radiation pressure torque [48] (and [53] in a different context from that of the relative motion) are particularly well documented. References [69], [72], [70] give a clear and structured overview of the formulations for these perturbation torques for atmospheric drag, solar radiation pressure, the harmonics of the Earth potential and the influence of the third body. It is important to keep in mind that this dynamic coupling disappears if the chosen model does not account for orbital perturbations or if the alignment of the orbital thrusts is not considered as constrained [69]. The contribution of each of these perturbing torques on a generic satellite characterized by the index "$*$" ("$* = t$" or "$* = c$") is given by:

$$\vec{T}_* = \vec{r}_*^{\,com} \wedge \vec{f}_*^{\,j}, \tag{2.209}$$

where $\vec{r}_*^{\,com}$ is the distance from the center of mass of satellite "$*$" to the application point of the perturbing force $\vec{f}_*^{\,j}$. The expressions of the different perturbing forces are given in reference [69] and are themselves taken back from conventional formulations of orbital mechanics textbooks. We recall the particular examples of disturbances such as solar radiation pressure and gravity gradient.

2.5.2.1. Solar radiation pressure

The orbital perturbing force due to solar radiation is generally dependent on the reflection characteristics of the satellite's surface. Each photon is then intercepted by the satellite's surface, consisting of absorption, specular reflection (elastic rebound) and diffuse reflection. The reference [69] assumes that the surface of the satellite subjected to solar radiation pressure does not allow the diffusion, and reflection is therefore a specular and absorption combination (see Figure 2.6).

For a flat surface A whose orientation with respect to the sun is characterized by its orthogonal vector $\vec{n}$ and vector $\vec{e}_{sun}$ pointing in the direction of the sun angle i_{sun} with respect to $\vec{n}$, the resultant forces for both reflection modes ($\vec{F}_{reflection}$ and $\vec{F}_{absorption}$) are shown in Figure 2.6. The overall force due to solar radiation pressure is therefore given by:

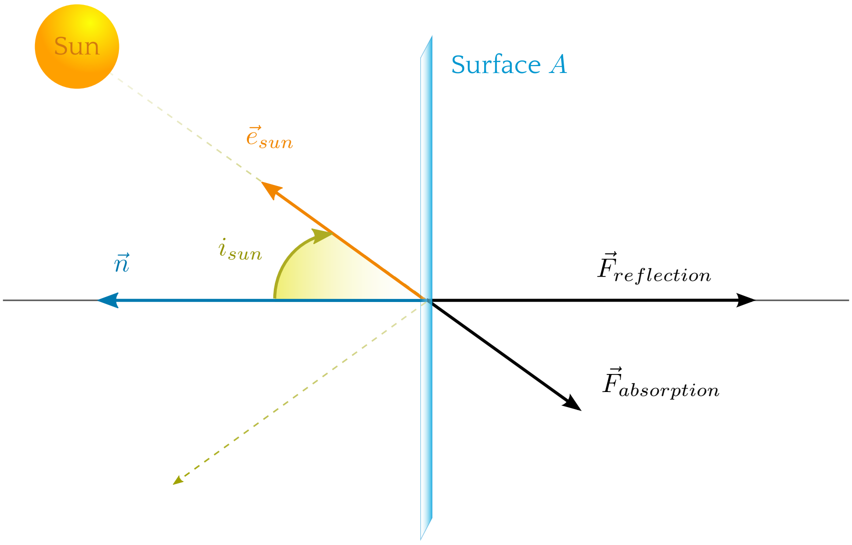

Figure 2.6: Disturbing forces due to solar radiation pressure.

$$\vec{f}_*^{\,\mathcal{B}_*} = \frac{F_{sun}}{c}\cos(i_{sun})\,A\left[(\gamma-1)\,\vec{e}_{sun}^{\,\mathcal{B}_*} - 2\gamma\cos(i_{sun})\,\vec{n}^{\mathcal{B}_*}\right], \tag{2.210}$$

where $F_{sun} = 1367\;W/m^2$ is the solar constant, c is the speed of light and γ is the reflection coefficient.

2.5.2.2. Gravity gradient

Since the satellite is considered as a rigid body, it follows that the gravitational force acting on it is not the same on all parts of the body that are considered masses located at different distances from the center of the Earth. This gravitational difference results in a torque called *gravity gradient torque*. This torque, calculated at the satellite's CoM, is given by [92], [76]:

$$
\begin{aligned}
\vec{T}_* &= \frac{3\mu}{r_*^3}\vec{Z}_{ot} \wedge I_* \, \vec{Z}_{ot}, \\
\vec{T}_*^{\mathcal{B}_*} &= \frac{3\mu}{r_*^3} R^{\mathcal{B}_*/\mathcal{O}_*} \begin{bmatrix} 0 \\ 0 \\ 1 \end{bmatrix} \wedge I_* \, R^{\mathcal{B}_*/\mathcal{O}_*} \begin{bmatrix} 0 \\ 0 \\ 1 \end{bmatrix} = \frac{3\mu}{r_*^3} R_{c3}^{\mathcal{B}_*/\mathcal{O}_* \times} I_* \, R_{c3}^{\mathcal{B}_*/\mathcal{O}_*},
\end{aligned}
\tag{2.211}
$$

where r_* is the orbital radius of the body $*$ ("$* = t$" or "$* = c$"), $R_{c3}^{\mathcal{B}_*/\mathcal{O}_*}$ is the third column of the rotation matrix $R^{\mathcal{B}_*/\mathcal{O}_*}$ and I_* is the body $*$'s inertia matrix. A more accurate derivation of these formulas can be found in the reference [100].

2.6. Joint modeling of the relative position and attitude by means of dual quaternions

We present in this section a unified modeling based on the dual quaternion formalism and the relative dynamic and kinematic coupled equations in translation and rotation. The material presented here is essentially based on the references [125], [41], [42], [43]. The basics of the dual quaternion theory is referenced in Section D.2 in Appendix D.

Dual quaternions have been found to provide the most compact and efficient way to represent the attitude and position of a body in order to take into account the natural coupling between the rotational and translational motion [40], [59], [60].

2.6.1. Relative translational and rotational kinematic equations

Consider an inertial reference frame $\mathcal{I}$ whose origin is O_i and its basis is $B_i = [\vec{X}_i, \vec{Y}_i, \vec{Z}_i]$. Two reference frames $\mathcal{B}_c = (O_c, \vec{X}_{bc}, \vec{Y}_{bc}, \vec{Z}_{bc})$ and $\mathcal{B}_t = (O_t, \vec{X}_{bt}, \vec{Y}_{bt}, \vec{Z}_{bt})$ are respectively attached to the chaser and to the target as shown in Table 2.1 and in Figure 2.7. Two quaternions can be defined to represent the position and orientation of the two reference frames with respect to the inertial one as:

$$
\begin{aligned}
\hat{q}^{t/i} &= q^{t/i} + \epsilon\frac{1}{2}\begin{bmatrix} \vec{r}_{ti}^{\,\mathcal{I}} \\ 0 \end{bmatrix} \odot q^{t/i} = q^{t/i} + \epsilon\frac{1}{2} q^{t/i} \odot \begin{bmatrix} \vec{r}_{ti}^{\,\mathcal{B}_t} \\ 0 \end{bmatrix}, \\
\hat{q}^{c/i} &= q^{c/i} + \epsilon\frac{1}{2}\begin{bmatrix} \vec{r}_{ci}^{\,\mathcal{I}} \\ 0 \end{bmatrix} \odot q^{c/i} = q^{c/i} + \epsilon\frac{1}{2} q^{c/i} \odot \begin{bmatrix} \vec{r}_{ci}^{\,\mathcal{B}_c} \\ 0 \end{bmatrix}.
\end{aligned}
\tag{2.212}
$$

Each dual quaternion verifies the kinematic differential equation:

$$
\begin{aligned}
\dot{\hat{q}}^{t/i} &= \frac{1}{2}\hat{\omega}_{ti}^{\mathcal{I}} \odot \hat{q}^{t/i} = \frac{1}{2}\hat{q}^{t/i} \odot \hat{\omega}_{ti}^{\mathcal{B}_t}, \\
\dot{\hat{q}}^{c/i} &= \frac{1}{2}\hat{\omega}_{ci}^{\mathcal{I}} \odot \hat{q}^{c/i} = \frac{1}{2}\hat{q}^{c/i} \odot \hat{\omega}_{ci}^{\mathcal{B}_c},
\end{aligned}
\tag{2.213}
$$

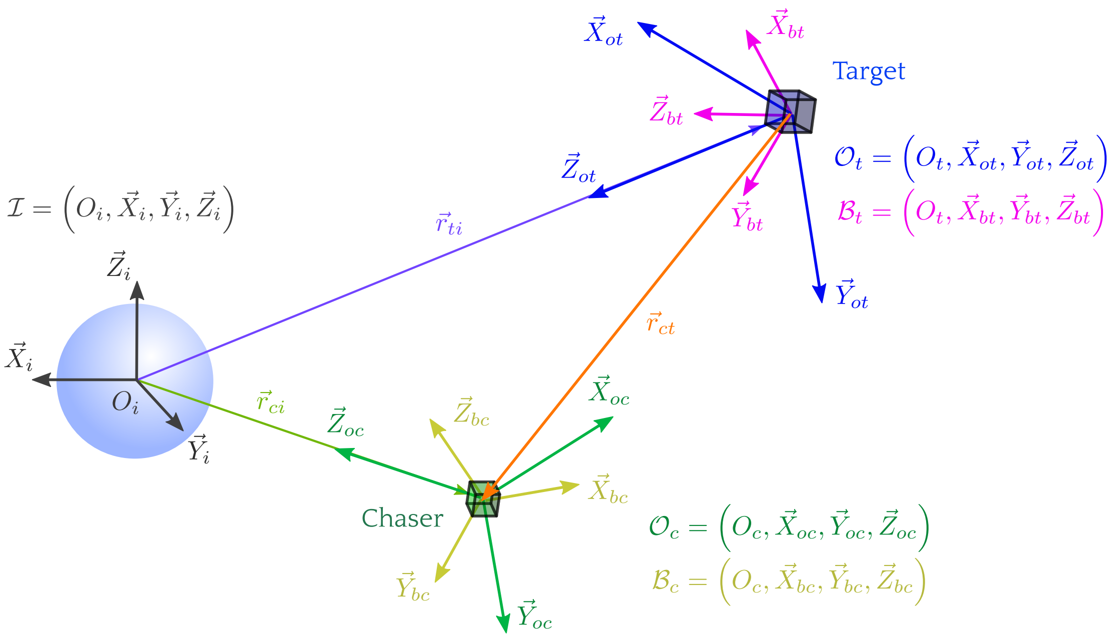

Figure 2.7: Relationships between the different reference frames.

where $\hat{\omega}^{\mathcal{I}}_{*i}$ is the dual quaternion composed from the relative angular velocity between the reference frame $*$ ("$* = t$" or "$* = c$") and the frame $\mathcal{I}$, expressed in the inertial frame $\mathcal{I}$, which is defined by:

$$\begin{aligned}\hat{\omega}^{\mathcal{I}}_{*i} = \begin{bmatrix} \hat{\vec{\omega}}^{\mathcal{I}}_{*i} \\ 0 \end{bmatrix} &= \begin{bmatrix} \vec{\omega}^{\mathcal{I}}_{*i} \\ 0 \end{bmatrix} + \epsilon \begin{bmatrix} \vec{v}^{\mathcal{I}}_{*i} + \vec{r}^{\mathcal{I}}_{*i} \wedge \vec{\omega}^{\mathcal{I}}_{*i} \\ 0 \end{bmatrix}, \\ &= \begin{bmatrix} \vec{\omega}^{\mathcal{I}}_{*i} \\ 0 \end{bmatrix} + \epsilon \left[\begin{bmatrix} \vec{v}^{\mathcal{I}}_{*i} \\ 0 \end{bmatrix} + \begin{bmatrix} \vec{r}^{\mathcal{I}}_{*i} \\ 0 \end{bmatrix} \times \begin{bmatrix} \vec{\omega}^{\mathcal{I}}_{*i} \\ 0 \end{bmatrix} \right].\end{aligned} \tag{2.214}$$

$\hat{q}^{*/i}$ is the dual quaternion defining the rigid transformation between the reference frame $\mathcal{B}_*$ and the reference frame $\mathcal{I}$, defined by:

$$\hat{q}^{*/i} = q^{*/i} + \frac{1}{2}\epsilon \begin{bmatrix} \vec{r}^{\mathcal{I}}_{*i} \\ 0 \end{bmatrix} \odot q^{*/i}. \tag{2.215}$$

Similarly, for the second member of Equation (2.213), we define the dual quaternion of the angular velocity expressed in the reference frame $\mathcal{B}_*$ by:

$$\begin{aligned}\hat{\omega}^{\mathcal{B}_*}_{*i} = \begin{bmatrix} \hat{\vec{\omega}}^{\mathcal{B}_*}_{*i} \\ 0 \end{bmatrix} &= \begin{bmatrix} \vec{\omega}^{\mathcal{B}_*}_{*i} \\ 0 \end{bmatrix} + \epsilon \begin{bmatrix} \vec{v}^{\mathcal{B}_*}_{*i} + \vec{\omega}^{\mathcal{B}_*}_{*i} \wedge \vec{r}^{\mathcal{B}_*}_{*i} \\ 0 \end{bmatrix}, \\ &= \begin{bmatrix} \vec{\omega}^{\mathcal{B}_*}_{*i} \\ 0 \end{bmatrix} + \epsilon \left[\begin{bmatrix} \vec{v}^{\mathcal{B}_*}_{*i} \\ 0 \end{bmatrix} + \begin{bmatrix} \vec{\omega}^{\mathcal{B}_*}_{*i} \\ 0 \end{bmatrix} \times \begin{bmatrix} \vec{r}^{\mathcal{B}_*}_{*i} \\ 0 \end{bmatrix} \right].\end{aligned} \tag{2.216}$$

The Equations (2.213), (2.214) and (2.215) are obtained by deriving Expressions (2.212). We give below, the complete demonstration for the first equation.

Differentiating the first equation in Expression (2.212) yields:

$$2\dot{\hat{q}}^{t/i} \quad = \quad 2\dot{q}^{t/i} + \epsilon \begin{bmatrix} \dot{\vec{r}}_{ti}^{\,\mathcal{I}} \\ 0 \end{bmatrix} \odot q^{t/i} + \epsilon \begin{bmatrix} \vec{r}_{ti}^{\,\mathcal{I}} \\ 0 \end{bmatrix} \odot \dot{q}^{t/i}. \tag{2.217}$$

However, as:

$$\dot{q}^{t/i} = \frac{1}{2} q^{t/i} \odot \begin{bmatrix} \vec{\omega}_{ti}^{\,\mathcal{B}_t} \\ 0 \end{bmatrix},$$

Equation (2.217) can be written as:

$$\begin{aligned} 2\dot{\hat{q}}^{t/i} &= q^{t/i} \odot \begin{bmatrix} \vec{\omega}_{ti}^{\,\mathcal{B}_t} \\ 0 \end{bmatrix} + \epsilon \begin{bmatrix} \dot{\vec{r}}_{ti}^{\,\mathcal{I}} \\ 0 \end{bmatrix} \odot q^{t/i} + \frac{1}{2}\epsilon \begin{bmatrix} \vec{r}_{ti}^{\,\mathcal{I}} \\ 0 \end{bmatrix} \odot \begin{bmatrix} \vec{\omega}_{ti}^{\,\mathcal{I}} \\ 0 \end{bmatrix} \odot q^{t/i}, \\ &= q^{t/i} \odot \begin{bmatrix} \vec{\omega}_{ti}^{\,\mathcal{B}_t} \\ 0 \end{bmatrix} + \epsilon \begin{bmatrix} \dot{\vec{r}}_{ti}^{\,\mathcal{I}} \\ 0 \end{bmatrix} \odot q^{t/i} + \epsilon \left(\frac{1}{2} \begin{bmatrix} \vec{r}_{ti}^{\,\mathcal{I}} \\ 0 \end{bmatrix} \odot \begin{bmatrix} \vec{\omega}_{ti}^{\,\mathcal{I}} \\ 0 \end{bmatrix} \right) \odot q^{t/i}, \end{aligned} \tag{2.218}$$

by product properties of quaternions, it is possible to write:

$$\left(\frac{1}{2} \begin{bmatrix} \vec{r}_{ti}^{\,\mathcal{I}} \\ 0 \end{bmatrix} \odot \begin{bmatrix} \vec{\omega}_{ti}^{\,\mathcal{I}} \\ 0 \end{bmatrix} \right) = \begin{bmatrix} \vec{r}_{ti}^{\,\mathcal{I}} \\ 0 \end{bmatrix} \times \begin{bmatrix} \vec{\omega}_{ti}^{\,\mathcal{I}} \\ 0 \end{bmatrix} + \frac{1}{2} \begin{bmatrix} \vec{\omega}_{ti}^{\,\mathcal{I}} \\ 0 \end{bmatrix} \odot \begin{bmatrix} \vec{r}_{ti}^{\,\mathcal{I}} \\ 0 \end{bmatrix}. \tag{2.219}$$

Equation (2.218) becomes:

$$\begin{aligned} 2\dot{\hat{q}}^{t/i} &= \begin{bmatrix} \vec{\omega}_{ti}^{\,\mathcal{I}} \\ 0 \end{bmatrix} \odot q^{t/i} + \epsilon \begin{bmatrix} \dot{\vec{r}}_{ti}^{\,\mathcal{I}} \\ 0 \end{bmatrix} \odot q^{t/i} + \epsilon \begin{bmatrix} \vec{r}_{ti}^{\,\mathcal{I}} \\ 0 \end{bmatrix} \times \begin{bmatrix} \vec{\omega}_{ti}^{\,\mathcal{I}} \\ 0 \end{bmatrix} \odot q^{t/i} + \frac{1}{2}\epsilon \begin{bmatrix} \vec{\omega}_{ti}^{\,\mathcal{I}} \\ 0 \end{bmatrix} \odot \begin{bmatrix} \vec{r}_{ti}^{\,\mathcal{I}} \\ 0 \end{bmatrix} \odot q^{t/i}, \\ &= \left(\begin{bmatrix} \vec{\omega}_{ti}^{\,\mathcal{I}} \\ 0 \end{bmatrix} + \epsilon \left(\begin{bmatrix} \dot{\vec{r}}_{ti}^{\,\mathcal{I}} \\ 0 \end{bmatrix} + \begin{bmatrix} \vec{r}_{ti}^{\,\mathcal{I}} \\ 0 \end{bmatrix} \times \begin{bmatrix} \vec{\omega}_{ti}^{\,\mathcal{I}} \\ 0 \end{bmatrix} \right) \right) \odot \left(q^{t/i} + \epsilon \frac{1}{2} \begin{bmatrix} \vec{r}_{ti}^{\,\mathcal{I}} \\ 0 \end{bmatrix} \odot q^{t/i} \right), \\ &= \hat{\omega}_{ti}^{\,\mathcal{I}} \odot \hat{q}^{t/i}. \end{aligned} \tag{2.220}$$

The second equality from the first Equation (2.213) is achieved by defining a new dual quaternion $\hat{\omega}_{ti}^{\,\mathcal{B}_t}$:

$$\hat{\omega}_{ti}^{\,\mathcal{B}_t} = \left(\hat{q}^{t/i} \right)^{*} \odot \hat{\omega}_{ti}^{\,\mathcal{I}} \odot \hat{q}^{t/i}. \tag{2.221}$$

Using the Definitions (2.214) and (2.215), it is possible to rewrite (2.221) as:

$$\begin{aligned}\hat{\omega}_{ti}^{\mathcal{B}_t} = & \left(\left(q^{t/i}\right)^* + \epsilon \frac{1}{2} \left[\begin{bmatrix} \vec{r}_{ti}^{\mathcal{I}} \\ 0 \end{bmatrix} \odot q^{t/i} \right]^* \right) \odot \left(\begin{bmatrix} \vec{\omega}_{*i}^{\mathcal{I}} \\ 0 \end{bmatrix} + \epsilon \begin{bmatrix} \vec{v}_{ti}^{\mathcal{I}} + \vec{r}_{ti}^{\mathcal{I}} \wedge \vec{\omega}_{ti}^{\mathcal{I}} \\ 0 \end{bmatrix} \right) \\ & \odot \left(q^{t/i} + \epsilon \frac{1}{2} \begin{bmatrix} \vec{r}_{ti}^{\mathcal{I}} \\ 0 \end{bmatrix} \odot q^{t/i} \right). \end{aligned} \tag{2.222}$$

By developing this last expression and using the algebra of dual quaternions, it is obtained:

$$\begin{aligned}\hat{\omega}_{ti}^{\mathcal{B}_t} &= \left(q^{t/i}\right)^* \odot \begin{bmatrix} \vec{\omega}_{ti}^{\mathcal{I}} \\ 0 \end{bmatrix} \odot q^{t/i} + \epsilon \left(q^{t/i}\right)^* \odot \begin{bmatrix} \vec{v}_{ti}^{\mathcal{I}} + \vec{r}_{ti}^{\mathcal{I}} \wedge \vec{\omega}_{ti}^{\mathcal{I}} \\ 0 \end{bmatrix} \odot q^{t/i} + \\ & \quad \epsilon \frac{1}{2} \left(q^{t/i}\right)^* \odot \begin{bmatrix} \vec{\omega}_{ti}^{\mathcal{I}} \\ 0 \end{bmatrix} \odot \begin{bmatrix} \vec{r}_{ti}^{\mathcal{I}} \\ 0 \end{bmatrix} \odot q^{t/i} + \epsilon \frac{1}{2} \left(q^{t/i}\right)^* \odot \begin{bmatrix} \vec{r}_{ti}^{\mathcal{I}} \\ 0 \end{bmatrix}^* \odot \begin{bmatrix} \vec{\omega}_{ti}^{\mathcal{I}} \\ 0 \end{bmatrix} \odot q^{t/i}, \\ &= \begin{bmatrix} \vec{\omega}_{ti}^{\mathcal{B}_t} \\ 0 \end{bmatrix} + \epsilon \left(q^{t/i}\right)^* \odot \begin{bmatrix} \vec{v}_{ti}^{\mathcal{I}} + \vec{r}_{ti}^{\mathcal{I}} \wedge \vec{\omega}_{ti}^{\mathcal{I}} \\ 0 \end{bmatrix} \odot q^{t/i} + \epsilon \begin{bmatrix} \vec{\omega}_{ti}^{\mathcal{B}_t} \\ 0 \end{bmatrix} \times \begin{bmatrix} \vec{r}_{ti}^{\mathcal{B}_t} \\ 0 \end{bmatrix}. \end{aligned} \tag{2.223}$$

The term $\left(q^{t/i}\right)^* \odot \begin{bmatrix} \vec{v}_{ti}^{\mathcal{I}} + \vec{r}_{ti}^{\mathcal{I}} \wedge \vec{\omega}_{ti}^{\mathcal{I}} \\ 0 \end{bmatrix} \odot q^{t/i}$ of this last expression is actually equal to $\begin{bmatrix} \vec{v}_{ti}^{\mathcal{B}_t} \\ 0 \end{bmatrix}$. Indeed,

$$\begin{aligned}\frac{d}{dt}\left(\left(q^{t/i}\right)^*\right) &= \left(\dot{q}^{t/i}\right)^* = -\frac{1}{2}\left(q^{t/i}\right)^* \odot \begin{bmatrix} \vec{\omega}_{ti}^{\mathcal{I}} \\ 0 \end{bmatrix} = -\frac{1}{2}\left(q^{t/i}\right)^* \odot \begin{bmatrix} \vec{\omega}_{ti}^{\mathcal{I}} \\ 0 \end{bmatrix} \odot q^{t/i} \odot \left(q^{t/i}\right)^*, \\ &= -\left(q^{t/i}\right)^* \odot \dot{q}^{t/i} \odot \left(q^{t/i}\right)^*, \end{aligned}$$

and so:

$$\begin{aligned}\begin{bmatrix} \vec{v}_{ti}^{\mathcal{B}_t} \\ 0 \end{bmatrix} &= \frac{d}{dt}\left(\left(q^{t/i}\right)^*\right) \odot \begin{bmatrix} \vec{r}_{ti}^{\mathcal{I}} \\ 0 \end{bmatrix} \odot q^{t/i} + \left(q^{t/i}\right)^* \odot \begin{bmatrix} \vec{v}_{ti}^{\mathcal{I}} \\ 0 \end{bmatrix} \odot q^{t/i} + \left(q^{t/i}\right)^* \odot \begin{bmatrix} \vec{r}_{ti}^{\mathcal{I}} \\ 0 \end{bmatrix} \odot \dot{q}^{t/i}, \\ &= \left(q^{t/i}\right)^* \odot \left(\begin{bmatrix} \vec{v}_{ti}^{\mathcal{I}} \\ 0 \end{bmatrix} + \begin{bmatrix} \vec{r}_{ti}^{\mathcal{I}} \\ 0 \end{bmatrix} \times \begin{bmatrix} \vec{\omega}_{ti}^{\mathcal{I}} \\ 0 \end{bmatrix} \right) \odot q^{t/i}. \end{aligned} \tag{2.224}$$

Finally, it is found that:

$$\hat{\omega}_{ti}^{\mathcal{B}_t} = \begin{bmatrix} \vec{\omega}_{ti}^{\mathcal{B}_t} \\ 0 \end{bmatrix} + \epsilon \left(\begin{bmatrix} \vec{v}_{ti}^{\mathcal{B}_t} \\ 0 \end{bmatrix} + \begin{bmatrix} \vec{\omega}_{ti}^{\mathcal{B}_t} \\ 0 \end{bmatrix} \times \begin{bmatrix} \vec{r}_{ti}^{\mathcal{B}_t} \\ 0 \end{bmatrix} \right). \tag{2.225}$$

From this last formulation and definition of the dual quaternion $\hat{q}^{t/i}$, the second equality from the first Equation (2.213) is thus found. ■

By analogy with what has just been calculated and by defining naturally *the relative dual quaternion* $\hat{q}^{c/t}$ as:

$$\hat{q}^{c/t} = \left(\hat{q}^{t/i}\right)^{*} \odot \hat{q}^{c/i} = q^{c/t} + \epsilon \frac{1}{2} q^{c/t} \odot \begin{bmatrix} \vec{r}_{ct}^{\,\mathcal{O}_c} \\ 0 \end{bmatrix}, \tag{2.226}$$

the kinematic equation of the relative motion is then given by:

$$\dot{\hat{q}}^{c/t} = \frac{1}{2} \hat{\omega}_{ct}^{\mathcal{O}_t} \odot \hat{q}^{c/t} = \frac{1}{2} \hat{q}^{c/t} \odot \hat{\omega}_{ct}^{\mathcal{O}_c}, \tag{2.227}$$

where $\hat{\omega}_{ct}^{\mathcal{B}_c} = \hat{\omega}_{ci}^{\mathcal{B}_c} - \hat{\omega}_{ti}^{\mathcal{B}_c} = \hat{\omega}_{ci}^{\mathcal{B}_c} - \left(\hat{q}^{c/t}\right)^{*} \odot \hat{\omega}_{ti}^{\mathcal{B}_t} \odot \hat{q}^{c/t}$ is the dual angular velocity vector between the frame $\mathcal{B}_c$ and the frame $\mathcal{B}_t$ expressed in frame $\mathcal{B}_c$.

2.6.2. Relative dynamic equations

The computation of the relative dynamic model presented below borrows some stages of the development in the given reference [125] and the notations finally used in reference [41]. First, it is necessary to write the chaser's dynamic equation expressed in the reference frame $\mathcal{B}_c$: for this purpose, we define the chaser's dual angular momentum from its center of mass as:

$$\hat{h}_c^{\mathcal{B}_c} = M_c^{\mathcal{B}_c} \star \left(\hat{\omega}_{ci}^{\mathcal{B}_c}\right)^{s}, \tag{2.228}$$

where $M_c^{\mathcal{B}_c}$ is *the dual inertia matrix* expressed in $\mathcal{B}_c$ and defined by:

$$M_c^{\mathcal{B}_c} = \begin{bmatrix} m_c I_3 & 0_{3\times1} & 0_{3\times3} & 0_{3\times1} \\ 0_{1\times3} & 1 & 0_{1\times3} & 0 \\ 0_{3\times3} & 0_{3\times1} & I^{\mathcal{B}_c} & 0_{3\times1} \\ 0_{1\times3} & 0 & 0_{1\times3} & 1 \end{bmatrix}. \tag{2.229}$$

$I^{\mathcal{B}_c}$ is the chaser's inertia tensor expressed in $\mathcal{B}_c$. By deriving Expression (2.228) in frame $\mathcal{B}_c$ and generalizing the derivation rule with respect to a non Galilean reference frame, we obtain the chaser's dynamic equation expressed in its frame $\mathcal{B}_c$.

$$\begin{aligned} \frac{d}{dt}\left(\hat{h}_c\right)_{\mathcal{B}_i} &= \frac{d}{dt}\left(\hat{h}_c\right)_{\mathcal{B}_c} + \hat{\omega}_{ci} \times \hat{h}_c = \hat{f}_c, \\ &= \frac{d}{dt}\left(\hat{h}_c\right)_{\mathcal{B}_c} + \hat{\omega}_{ci} \times M_c \star \left(\hat{\omega}_{ci}\right)^{s} = \hat{f}_c, \end{aligned} \tag{2.230}$$

where $\hat{f}_c = \begin{bmatrix} \vec{f}_c \\ 0 \end{bmatrix} + \epsilon \begin{bmatrix} \vec{T}_c \\ 0 \end{bmatrix}$ is the total external dual force acting on the chaser with respect to its center of mass. $\vec{f}_c$ is the total external force applied to the chaser's body and $\vec{T}_c$ is the total external torque applied to the chaser's body with respect to its center of mass. Expressing Equation (2.230) in the frame $\mathcal{B}_c$, we obtain the chaser's dynamic equation:

$$\dot{\hat{h}}_c^{\mathcal{B}_c} = \hat{f}_c^{\mathcal{B}_c} - \hat{\omega}_{ci}^{\mathcal{B}_c} \times M_c^{\mathcal{B}_c} \star \left(\hat{\omega}_{ci}^{\mathcal{B}_c}\right)^{s} = M_c \star \left(\dot{\hat{\omega}}_{ci}^{\mathcal{B}_c}\right)^{s}. \tag{2.231}$$

Remind that the dual quaternion of the relative angular velocity can be expressed as:

$$\hat{\omega}_{ct}^{\mathcal{B}_c} = \hat{\omega}_{ci}^{\mathcal{B}_c} - \hat{\omega}_{ti}^{\mathcal{B}_c} = \hat{\omega}_{ci}^{\mathcal{B}_c} - \left(\hat{q}^{c/t}\right)^* \odot \hat{\omega}_{ti}^{\mathcal{B}_t} \odot \hat{q}^{c/t}. \tag{2.232}$$

By differenciating (2.232), it is possible to state:

$$\begin{aligned} \dot{\hat{\omega}}_{ct}^{\mathcal{B}_c} &= \dot{\hat{\omega}}_{ci}^{\mathcal{B}_c} - \left(\dot{\hat{q}}^{c/t}\right)^* \odot \hat{\omega}_{ti}^{\mathcal{B}_t} \odot \hat{q}^{c/t} - \left(\hat{q}^{c/t}\right)^* \odot \dot{\hat{\omega}}_{ti}^{\mathcal{B}_t} \odot \hat{q}^{c/t} - \left(\hat{q}^{c/t}\right)^* \odot \hat{\omega}_{ti}^{\mathcal{B}_t} \odot \dot{\hat{q}}^{c/t}, \\ &= \dot{\hat{\omega}}_{ci}^{\mathcal{B}_c} - \left(\hat{q}^{c/t}\right)^* \odot \dot{\hat{\omega}}_{ti}^{\mathcal{B}_t} \odot \hat{q}^{c/t} + \frac{1}{2}\hat{\omega}_{ct}^{\mathcal{B}_c} \odot \left(\hat{q}^{c/t}\right)^* \odot \hat{\omega}_{ti}^{\mathcal{B}_t} \odot \hat{q}^{c/t} - \frac{1}{2}\left(\hat{q}^{c/t}\right)^* \odot \hat{\omega}_{ti}^{\mathcal{B}_t} \odot \hat{q}^{c/t} \odot \hat{\omega}_{ct}^{\mathcal{B}_c}, \\ &= \dot{\hat{\omega}}_{ci}^{\mathcal{B}_c} - \left(\hat{q}^{c/t}\right)^* \odot \dot{\hat{\omega}}_{ti}^{\mathcal{B}_t} \odot \hat{q}^{c/t} + \hat{\omega}_{ct}^{\mathcal{B}_c} \times \left(\hat{q}^{c/t}\right)^* \odot \hat{\omega}_{ti}^{\mathcal{B}_t} \odot \hat{q}^{c/t}. \end{aligned} \tag{2.233}$$

Expressing $\dot{\hat{\omega}}_{ci}^{\mathcal{B}_c}$ together with the second part of Equation (2.231), we obtain the complete relative dynamic equation (rotation and translation):

$$\begin{aligned} \left(\dot{\hat{\omega}}_{ct}^{\mathcal{B}_c}\right)^s = \left(M_c^{\mathcal{B}_c}\right)^{-1} \star \left(\hat{f}_c^{\mathcal{B}_c} - \hat{\omega}_{ci}^{\mathcal{B}_c} \times M_c^{\mathcal{B}_c} \star \left(\hat{\omega}_{ci}^{\mathcal{B}_c}\right)^s\right) - \left(\left(\hat{q}^{c/t}\right)^* \odot \dot{\hat{\omega}}_{ti}^{\mathcal{B}_t} \odot \hat{q}^{c/t}\right)^s \\ + \left(\hat{\omega}_{ct}^{\mathcal{B}_c} \times \left(\hat{q}^{c/t}\right)^* \odot \hat{\omega}_{ti}^{\mathcal{B}_t} \odot \hat{q}^{c/t}\right)^s. \end{aligned} \tag{2.234}$$

Expression (2.234) is formally identical to Equation (2.191) of the relative rotation dynamic equation if one expresses the term $\dot{\hat{\omega}}_{ti}^{\mathcal{B}_t}$ using the target's dynamic equation and adding the terms corresponding to the reaction wheels.

2.7. Conclusion

In this chapter we have addressed the modeling of the relative motion for the rendezvous phase in an elliptic orbit in the context of satellite formation flying, considering a non-cooperative target.

Due to the need of highly accurate models in the terminal phases of the rendezvous towards a passive target, the relative motion must take into account not only the translational and attitude models independently, but the effects that the translational motion originates over the attitude motion and viceversa. This fact is known as coupling, where the relative model takes into account the 6 DoF instead of the 3 DoF of the translation plus the 3 DoF of the rotation.

The coupled model is developed progressively. First, the nonlinear relative translational motion is described within the LVLH reference frame. A linearization process is then performed with respect to the target's elliptical orbit, leading to the translational linear equations used for the kinematic coupling modeling.

However, the translational linear model undergoes four coordinate transformations that allows us to obtain a final representation under which we are able to characterize periodic trajectories of the chaser defined by a linear time-invariant matrix. This transformed model will not be used within the coupling representation, but will be of key importance in Chapter 3.

Afterwards, the attitude motion modeling is presented by means of the Euler-Rodrigues parameters that form a quaternion, and establish the kinematic and dynamic equations of the relative attitude motion.

The coupled model is then addressed by the joint modeling of the relative translational and attitude motions based on the dual quaternion formalism. The dual quaternions have shown to be a compact and efficient way to represent the translation and attitude characteristics of the relative motion, as well as the natural coupling affecting it.

CHAPTER 3

APPROACH AND OBSERVATION PHASES WITHIN A HYBRID FRAMEWORK

Contents

Résumé

Différents processus qui se produisent dans la nature peuvent être étudiés à travers de la théorie des systèmes dynamiques [57]. Du point de vue de l'ingénierie, ces systèmes dynamiques impliquent un mélange de dynamiques continues et discrètes qui intéragisent entre elles et présentent des flux discontinus.

La complexité croissante des systèmes d'ingénierie implique la nécessité d'architectures de contrôle capables de gérer ces technologies de pointe, qui impliquent généralement de multiples modes de fonctionnement. Ces technologies sont de plus en plus regroupées dans des architectures hiérarchiques, caractérisées par des unités à temps continu àux niveaux inférieurs — interagissant directement avec le système dynamique — et des unités de prise de décision logique à temps discret aux niveaux supérieurs [57].

Historiquement, la plupart des systèmes dynamiques ont normalement été classés en systèmes à temps continu ou temps discret. Cependant, de nombreux systèmes dynamiques ne présentent pas un comportement qui peut facilement être classé dans l'un de ces deux groupes. En outre, certains de ces systèmes montrent des propriétés des deux groupes, et aussi définit un autre groupe, appelé systèmes dynamiques hybrides ou simplement systèmes hybrides [52]. Les systèmes dynamiques hybrides ont attiré d'importants efforts de recherche au cours des dernières années en tant que discipline émergente dans la théorie et le contrôle des systèmes dynamiques pour élaborer un cadre systématique pour l'analyse et la conception de systèmes d'ingénierie complexes, comme l'on peut le constater dans les systèmes aérospatiaux [78].

Un système hybride est donc un système qui présente — ou est modélisé avec — une combinaison de variables — ou outils — à temps continu et temps discret [52].

Selon les auteurs de [57], un système hybride est un ensemble interactif dénombrable de systèmes dynamiques impliquant un mélange de dynamiques continues et d'événements discrets pouvant comprendre des systèmes dynamiques impulsionnels, des systèmes hiérarchiques et des systèmes de commutation.

Les systèmes dynamiques impulsionnels sont une sous-classe de systèmes hybrides composés de trois éléments:

1. *des équations différentielles en temps continu décrivant le mouvement libre des systèmes dynamiques entre deux événements de saut;*
2. *des équations en différences décrivant la façon dont les états sont instantanément modifiés lors de l'événement de réinitialisation par les commandes impulsionnelles; et*
3. *un critère pour réinitialiser les états du système.*

Dans ce second chapitre, nous abordons le problème de stabilisation du mouvement relatif, en posant le problème de synthèse de lois de commande impulsionnelles.

Dans le cadre de manoeuvres de proximité, il est intéressant de maintenir le véhicule chasseur dans une zone de l'espace afin d'assurer un mission d'observation de la cible ou d'assurer la sécurité de la mission. Pour ce faire, nous allons contrôler l'état relatif du chasseur autour d'une orbite relative d'intérêt.

Le problème de commande associé à toute phase de rendez-vous ou d'approche d'un satellite chasseur vers une cible dépend fortement de la nature du système de propulsion, comme indiqué au Chapitre 1. La commande est ici considérée comme impulsionnelle à cause de la nature chimique de la propulsion. À cause des débits importants de gaz en sortie de tuyère et des poussées fortes associées, la vitesse du véhicule évolue très vite devant les constantes de temps du mouvement relatifs. Dans [10], on remarque que les systèmes présentant des dynamiques à des échelles de temps très différentes comme c'est le cas pour le rendez-vous à propulsion chimique peuvent être vu dans le cadre des systèmes impulsionnels. En effet, du point de vue de la dynamique relative, lors d'une poussée, la vitesse subit une discontinuité. Les signaux de commande seront donc considérés comme des manœuvres impulsionnelles — changements instantanés de la vitesse du satellite — et modélisés au moyen d'équations à temps discret, comme indiqué au point 2. *En outre, quand aucune entrée de contrôle n'est appliquée, la dynamique des satellites peut être modélisée comme un système à temps continu au moyen d'équations différentielles, comme décrit dans l'item* 1.

Notre approche pour ce chapitre est d'étudier la phase de rendez-vous comme un système dynamique hybride impulsionnel, en considérant un satellite chasseur équipé de propulseurs chimiques, de telle sorte que le problème de contrôle associé rentre dans la classe des systèmes dynamiques hybrides impulsionnels, comme décrit dans les trois points précédents. Sous le formalisme des systèmes hybrides impulsionnels, la phase d'approche du satellite peut être modélisée en tant que système à temps continu alors qu'aucune entrée de commande n'est appliquée sur le satellite et en tant que système à temps discret lorsque les entrées de commande sont appliquées.

Nous allons créer des lois de commande impulsionnelles dans le cadre du formalisme hybride: en définissant à la fois les instants des commandes impulsionnelles et la fonction de calcul de l'impulsion. Plusieurs propositions sont faites. Nous utiliserons les outils de la théorie de systèmes hybrides pour analyser chacune des lois de commande proposées. Enfin, nous proposons une étude numérique qui aura pour objet de mettre en évidence les forces et les limites de chaque loi de commande.

3.1. Introduction

Many of the dynamical processes that occur in nature, can be studied through the dynamical systems theory [57]. From an engineering point of view, these dynamical systems involve an interacting mixture of continuous and discrete dynamics exhibiting discontinuous flows.

The increasing complex nature of engineering systems involves the necessity of control architectures able to manage these cutting-edge technologies, which usually involve multiple modes of operation. These technologies are more and more recasted under hierarchical architectures, characterized by continuous-time units at lower levels — directly interacting with the dynamical system — and discrete-time logical decision-making units at higher levels [57].

Historically, most of the dynamic systems have been firstly classified into continuous-time or discrete-time systems. However, many dynamic systems do not present a behavior that can easily be classified into one of these two groups. Furthermore, some of these systems show properties of both groups, leading to a new class of systems, called *hybrid dynamic systems* or just *hybrid systems* [52]. Hybrid dynamical systems have attracted important research efforts over the recent years as an emerging discipline within the dynamical systems theory and control [57] to develop a systematic framework for the analysis and design of complex engineering systems, as can be found in aerospace systems [78].

A hybrid system is therefore a system that exhibits — or is modeled with — a combination of continuous-time and discrete-time variables — or tools [52].

According to the authors in [57], a hybrid system is an interacting countable collection of dynamical systems involving a mixture of continuous-time dynamics and discrete events that includes impulsive dynamical systems, hierarchical systems and switching systems.

Impulsive dynamical systems are a subclass of hybrid systems consisting of three elements:

1. continuous-time differential equations describing the motion of the dynamical systems between two control impulses or reset events;
2. discrete-time difference equations describing the way states are instantaneously changed at the reset event; and
3. a criterion to reset the system's states.

In this second chapter, we address the problem of stabilization of the spacecraft relative motion, setting the problem of synthesizing different impulsive control laws.

In the context of proximity maneuvers, it is beneficial to keep the chaser satellite in an area of the space in order to eventually allow an observation phase or ensure the safety of the target. To do this, we will control the chaser's relative state over a relative orbit of interest.

Any rendezvous or approach phase of a chaser satellite towards a target will depend on the nature of the propulsion system, as stated in Chapter 1, here considered as impulsive due to the chemical thrusters assumptions. Due to the high flows of gas at the outlet of the nozzle and the strong associated thrusts, the speed of the spacecraft evolves very quickly with respect to the time constants of the relative motion. In [10], it can be seen that systems showing dynamics at very different time scales, as is the case for the chemical propulsion rendezvous, can be seen in the context of impulsive systems. Indeed, from the point of view of the relative dynamics, during a thrust, the acceleration thus the velocity undergoes a discontinuity. The control signals will therefore be considered as impulsive maneuvers — instantaneous changes of the satellite's velocity — and modeled by means of discrete-time equations, as stated in item 2. Furthermore, while no control input is applied, the satellite dynamics can be modeled as a continuous-time system by means of differential equations, as in item 1.

Our approach for this current chapter is to study the rendezvous phase as an impulsive hybrid dynamical system, considering a chaser satellite equipped with chemical thrusters, such that the associated control problem falls into the class of impulsive hybrid control problems, as described in the previous three items. Under the impulsive hybrid systems formalism, the satellite's approach phase can be modeled as a continuous-time system while no control input is applied on the satellite, and as a discrete-time system when the control inputs are applied at a given time — to be determined within the controller.

We will create impulsive control laws within the hybrid systems framework, by defining both the instants of the impulsive controls and the function allowing calculating the impulse. We will use the tools of the hybrid systems theory to analyse each of the proposed control laws, and show their strengths and limitations by means of numerical simulations.

✍ *REMARK.* In the sequel of this chapter, all arrows corresponding to vectors are removed for clarity purposes.

3.2. Hybrid systems modeling

3.2.1. Hybrid formalism

According to the formalism developed in [52], any hybrid dynamical system can be represented by a quadruple $\mathcal{H} = (\mathcal{C}, F, \mathcal{D}, G)$. It is composed by both continuous-time and discrete-time behaviors, and is directly translated into equations as:

$$\begin{cases} x \in \mathcal{C} & \dot{x} \in F(x), \\ x \in \mathcal{D} & x^{+} \in G(x), \end{cases} \tag{3.1}$$

or

$$\begin{cases} x \in \mathcal{C} & \dot{x} = f(x), \\ x \in \mathcal{D} & x^{+} = g(x). \end{cases} \tag{3.2}$$

Equations (3.1) and (3.2) show the combination of continuous and discrete behaviors of the hybrid system, whose state, represented by x, changes as detailed in the sequel:

- $\mathcal{C} \subset \mathbb{R}^n$ is the *flow set*, or set in which the system presents a free evolution, representing the continuous behavior. The state is represented by a differential inclusion in (3.1) or by a differential equation in (3.2), where $\dot{x}$ is the velocity of x;
- F — with $\mathcal{C} \subset \operatorname{dom} F$ — or f represents the *flow map*, where F has a nonempty value — or f be defined — on $\mathcal{C}$;
- $\mathcal{D} \subset \mathbb{R}^n$ is the *jump set*, or set in which instantaneous changes take place, representing the discrete behavior. The state is represented by a difference inclusion in (3.1) or by a difference equation in (3.2), where x^{+} is the state of x after the instantaneous change;
- G — with $\mathcal{D} \subset \operatorname{dom} G$ — or g represents the *jump map*, where G has a nonempty value — or g be defined — on $\mathcal{D}$.

3.3. Satellite relative dynamics within a hybrid context

In Chapter 2, Section 2.3, we developed the linearized equations of the relative translational motion between an actuated chaser satellite and a non-cooperative target spacecraft under Keplerian assumptions. After several coordinate transformations, a simplified linear model was obtained, whose state-space representation was given in Expression (2.171):

$$\widehat{\xi}\,'(\nu) = \widehat{A}\,\widehat{\xi}(\nu) + \widehat{B}(\nu)\,\widehat{U}(\nu). \tag{3.3}$$

We take advantage of the hybrid formalism in (3.2) to describe the satellite relative dynamics in (3.3). Consider the differential equation:

$$\widehat{\xi}(\nu)\,' = f(\widehat{\xi}(\nu)), \tag{3.4}$$

for some $f : \mathbb{R}^6 \to \mathbb{R}^6$, with impulses leading to instantaneous changes at predetermined locations $\nu_1, \nu_2, \ldots, \nu_k$ according to:

$$\widehat{\xi}(\nu_i)^+ = g(\widehat{\xi}(\nu), \nu_i), \tag{3.5}$$

for some $g : \mathbb{R}^6 \times \mathcal{V}$ and $\mathcal{V} = \{\nu_1, \nu_2, \ldots \nu_k\}$.

The current state represented by $\widehat{\xi}(\nu)$ will be noted $\widehat{\xi}$ from here on for lightness purposes.

Equation (3.3) can be therefore decomposed in two parts: the continuous-time and discrete-time behaviors respectively. To do so, we decouple the term that represents the free evolution of the chaser satellite from the term that represents its behavior when the control inputs are applied. This leads to the following hybrid system representation for the satellite dynamics:

$$\begin{cases} \widehat{\xi}\,' = \widehat{A}\,\widehat{\xi}, & \widehat{\xi} \in \mathcal{C}, \qquad (3.6a) \\ \widehat{\xi}^{+} = \widehat{\xi} + \widehat{B}(\nu)\,\widehat{U}(\nu), & \widehat{\xi} \in \mathcal{D}, \qquad (3.6b) \end{cases}$$

where the flow set $\mathcal{C}$ and the jump set $\mathcal{D}$ will be defined in the latter.

The dynamic matrix $\widehat{A}$ has a quasi-Jordan form, whose analytical expression was given in Equation (2.152), recalled hereafter:

$$\widehat{A} = \left[\begin{array}{cc|ccc|c} 0 & 0 & 0 & 0 & 0 & 0 \\ 0 & 0 & 0 & 0 & 0 & 0 \\ \hline 0 & 0 & 0 & 0 & 0 & \dfrac{1}{(1-e^2)^{3/2}} \\ 0 & 0 & 0 & 0 & 0 & 0 \\ 0 & 0 & 0 & 0 & 0 & 0 \\ 0 & 0 & 0 & 0 & 0 & 0 \end{array}\right]. \tag{3.7}$$

The different coordinate changes that led to Expression (3.7) exploit the useful feature of the periodic trajectories representation (c.f. Subsection 2.3.2.3).

The input matrix $\widehat{B}(\nu)$ from Expression (2.170) is also recalled here for simplicity reasons, where the dependencies on ν of the different elements have been omitted for brevity's sake:

$$\widehat{B}(\nu) = \frac{1}{k^2\kappa^2(1-e^2)} \left[\begin{array}{c|c|c} 0 & -\left(1-e^2\right)\kappa\sin\nu & 0 \\ 0 & \left(1-e^2\right)\kappa\cos\nu & 0 \\ \hline -e(1+\kappa)\kappa\sin\nu - \dfrac{3\sigma\kappa^3}{(1-e^2)^{3/2}} & 0 & \dfrac{3\sigma e\kappa^2\sin\nu}{(1-e^2)^{3/2}} - \kappa^3 + \kappa^2 + 2\kappa \\ (1-e^2)(1+\kappa)\kappa\sin\nu & 0 & (1-e^2)\kappa^2\cos\nu \\ (1+\kappa)\kappa\cos\nu + e\kappa & 0 & -\kappa^2\sin\nu \\ -3\kappa^3 & 0 & 3e\kappa^2\sin\nu \end{array} \right]. \tag{3.8}$$

3.3.1. Timers

Timers are extra states that keep track of a specific event — reset criterion—, denoted by T, at which modes change, in response to zero-crossing or timer events. These particular states evolve following its continuous-time dynamics (flow) under the effect of constant (or zero) control input. After every T units of time, the closed-loop system undergoes a jump, at which the control input is updated and applied to the system [97].

From Expression (3.5), we observe that the ν variable represents the locations at which the impulses are applied. In other words, the satellite dynamics will flow whenever $\nu_i \notin \mathcal{V}$. However reference [52] prefers the approach in which an extra variable $\tau \in \mathcal{T}$ is introduced ensuring that flow does not occur when $\nu_i \in \mathcal{V}$. These ν and τ variables are the timers we will use for our hybrid modeling of the satellite relative dynamics.

3.3.1.1. Timer ν

The satellite dynamics during the rendezvous phase are periodic of period 2π, as shown in Chapter 2. We can take advantage of this feature to set a timer ν that tracks the periodic time-varying nature of the satellite dynamics. This timer is reset to zero each time it reaches the value 2π, as shown in Figure 3.1, thereby being confined to the compact set $[0; 2\pi]$.

3.3.1.2. Timer τ

According to each controller, the impulsive control actions — thrusters firings — will take place at different instants T_τ. We set another timer τ in order to capture the information about how long we need to wait until the next impulsive control action. Whenever the timer τ crosses zero, the thrusters are fired, as shown in Figure 3.1.

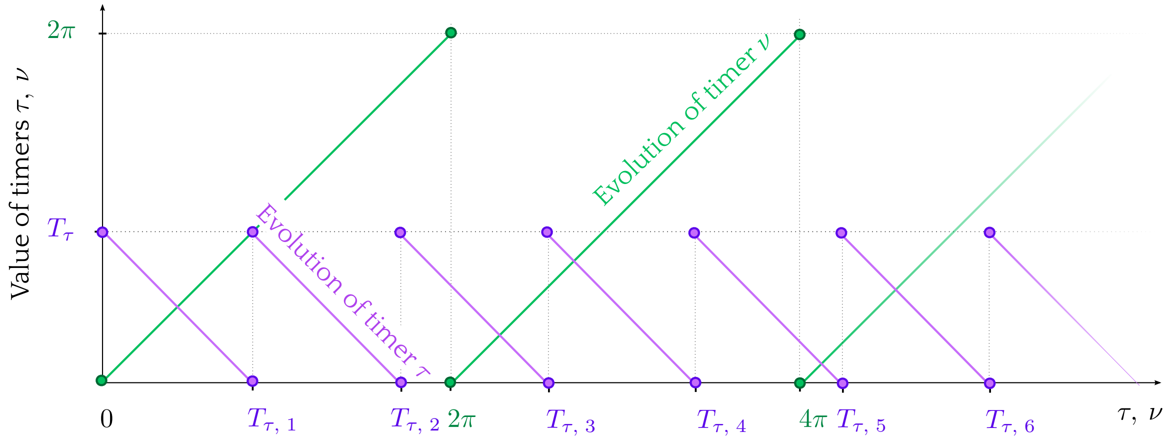

Figure 3.1: Evolution of timers ν and τ.

3.4. Impulsive control scheme design for the relative dynamics

Before entering into the details of each single hybrid controller, we give the common features to all of them.

First, we give a description of the reference periodic trajectory $\widehat{\xi}^{\,ref}$. Once the chaser tracks $\widehat{\xi}^{\,ref}$, its trajectory will remain bounded if a Keplerian model is considered (environmental disturbances are disregarded).

Then, we describe the closed-loop dynamics by means of the mismatch between the current state of the satellite and the chosen reference periodic trajectory in order to define the jumps and flow equations of the hybrid problem.

Finally, we define all the common specifications to all the designed controllers.

3.4.1. Reference periodic trajectories

We can observe that the kernel of matrix $\widehat{A}$ in (3.7) is:

$$\ker(\widehat{A}) = \begin{bmatrix} I_5 \\ 0 \end{bmatrix} \widehat{\xi}, \tag{3.9}$$

with $\widehat{\xi} \in \mathbb{R}^5$. Then, any state $\widehat{\xi}$ satisfying $\widehat{\xi}_6 = 0$ is an equilibrium point for the homogeneous equation $\widehat{\xi}\,' = \widehat{A}\,\widehat{\xi}$.

The major characteristic of LTI matrix $\widehat{A}$ comes out from the fact that any periodic free motion of the original dynamics in Equation (2.54) can be suitably parametrized by specific selections of the state $\widehat{\xi}$ with the last component being zero:

$$\widehat{\xi}_6 = 0, \tag{3.10}$$

as it will be fully explained in the sequel. Any equilibrium point $\widehat{\xi}$ corresponds to a periodic relative trajectory.

In [35], a method to characterise constrained periodic trajectories is developed. In that work, solutions are parametrized by means of a vector of states referred to $D(\nu)$ –, as it was shown by the vector K in Equation (2.111) in Subsection 2.3.2.

By analysing the structure of the relative trajectories' parametric expressions in [31], some geometric properties on the vector of parameters K are imposed to characterise a given periodic trajectory. These properties are synthetised as follows:

- constant K_3: position offset on the original x axis; the periodic trajectory is always centered on y and z axes;
- constants K_4 and K_5: dimensions of the periodic trajectory in the $x-z$ plane;
- constant K_6 must be zero to ensure that the trajectory is periodic (see Subsection 2.3.2.3 for justification);
- constants K_1 and K_2: amplitude of the relative motion on the y axis (the trajectory is planar — $x-z$ plane — whenever these two constants are zero).

Following similar transformations from Figure 2.3, the periodicity property $K_6 = 0$ is equivalent to $\widehat{\xi}_6 = 0$.

According to the satellite's mission goals, the periodic relative trajectories may vary, whose common characteristic is:

$$\widehat{\xi}_6^{ref} = 0, \tag{3.11}$$

hence their general expression being:

$$\widehat{\xi}^{\,ref} = \begin{bmatrix}\widehat{\xi}_1^{ref} & \widehat{\xi}_2^{ref} & \widehat{\xi}_3^{ref} & \widehat{\xi}_4^{ref} & \widehat{\xi}_5^{ref} & 0\end{bmatrix}^T. \tag{3.12}$$

Within the objectives of this dissertation, the periodic relative trajectory should be designed to orbit in the neighborhood of the target satellite to perform inspection tasks. [34] characterises any relative periodic trajectory motion included in a polytope and proposes a method to compute values for vector K in Equation (2.111) that satisfies position constraints. Our periodic relative trajectory $\widehat{\xi}^{\,ref}$ is computed following such method, where the last state in the transformed coordinates is always zero. The sixth state of the dynamics mismatch in (3.18) is therefore zero due to (3.10) and (3.11):

$$\widehat{\varepsilon}_6 = 0. \tag{3.13}$$

However, we can give the parametrization of any reference periodic trajectory $\widehat{\xi}^{\,ref}$ in the LVLH coordinates, denoted by:

$$X^{ref}(\nu) = [x(\nu) \quad y(\nu) \quad z(\nu) \quad x'(\nu) \quad y'(\nu) \quad z'(\nu)]^T. \tag{3.14}$$

For this purpose, we apply the inverse coordinate transformation — denoted by $R^{-1}(\nu) \in \mathbb{R}^{6\times 6}$ and previously defined in Expression (2.161) — that performs the change from state $\widehat{\xi}(\nu)$ to state $X(\nu)$. The reference periodic trajectory in the LVLH coordinates is thus given by:

$$X^{ref}(\nu) = R^{-1}(\nu)\,\widehat{\xi}^{\,ref}. \tag{3.15}$$

The parametric equations of the reference periodic trajectory are therefore:

$$\begin{cases} x^{ref}(\nu) = \kappa(\nu)\,\widehat{\xi}_3^{ref} - \cos(\nu)\left(\dfrac{1}{\kappa(\nu)}+1\right)\,\widehat{\xi}_4^{ref} + \sin(\nu)\left(\dfrac{1}{\kappa(\nu)}+1\right)\,\widehat{\xi}_5^{ref}, \\ y^{ref}(\nu) = \dfrac{\cos(\nu)}{\kappa(\nu)}\,\widehat{\xi}_1^{ref} + \dfrac{\sin(\nu)}{\kappa(\nu)}\,\widehat{\xi}_2^{ref}, \\ z^{ref}(\nu) = -e\sin(\nu)\,\widehat{\xi}_3^{ref} + \sin(\nu)\,\widehat{\xi}_4^{ref} + \cos(\nu)\,\widehat{\xi}_5^{ref}. \end{cases} \tag{3.16}$$

The periodic reference trajectories in LVLH are bounded and they are periodic of period 2π. The shape of these trajectories will vary according to the eccentricity e of the orbit.

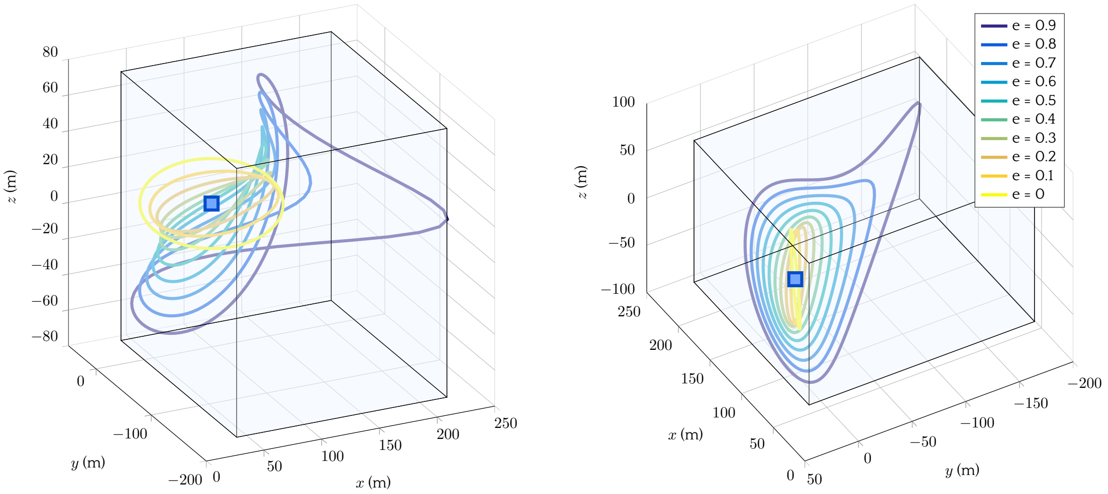

Figure 3.2: 3D views of $\widehat{\xi}^{\,ref,1}$ for $0 \leq e < 0.9$.

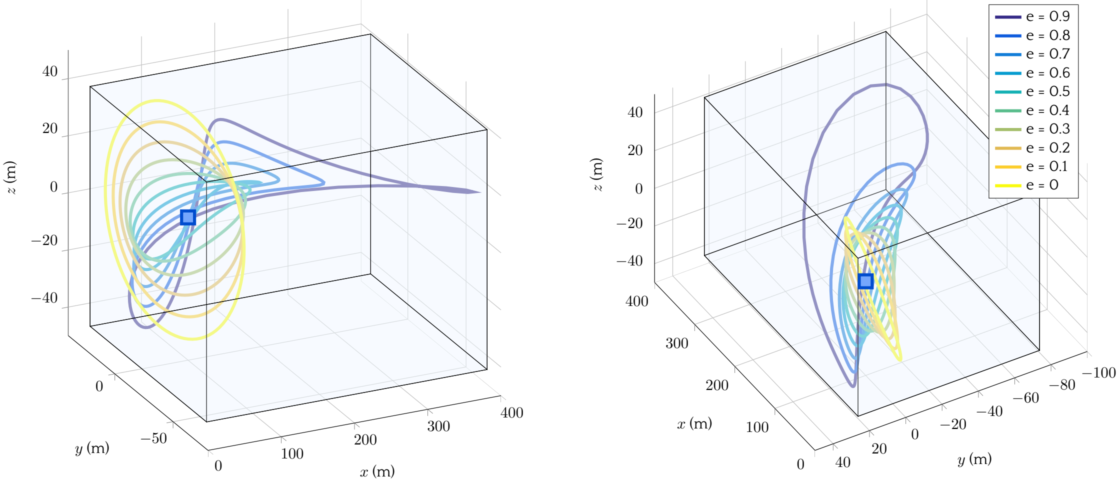

Figure 3.3: 3D views of $\widehat{\xi}^{\,ref,2}$ for $0 \leq e < 0.9$.

As a numerical example, in Figures 3.2 and 3.3, we have represented two different periodic trajectories $\widehat{\xi}^{\,ref,1}$ and $\widehat{\xi}^{\,ref,2}$ for different values of the eccentricity varying between 0 and 0.9. The numerical values of the reference periodic trajectories are set to:

$$\begin{aligned}\widehat{\xi}^{\,ref,1} &= [17.6 \quad 17.7 \quad 99.9 \quad 17.8 \quad -17.7 \quad 0]^T,\\ \widehat{\xi}^{\,ref,2} &= [5.2 \quad 17.7 \quad 81.7 \quad 34.3 \quad -13.6 \quad 0]^T.\end{aligned} \tag{3.17}$$

These values have been obtained based on the definition of admissible trajectories within a tolerance box in a given region of the space. The corresponding continuous constraints for the tolerance box are compactly written as a polytopic set and are discretized later on and solved using non-negative polynomials techniques given by Nesterov in [89]. The followed methodology to retrieve the numerical values in Expression (3.17) is explained in [35].

3.4.2. Description of the closed-loop dynamics

After defining the reference periodic trajectory $\widehat{\xi}^{\,ref}$, it becomes interesting to analyse the dynamics of the error between the current state $\widehat{\xi}$ and the given $\widehat{\xi}^{\,ref}$:

$$\widehat{\varepsilon} = \widehat{\xi} - \widehat{\xi}^{\,ref}. \tag{3.18}$$

The hybrid description of the problem is obtained thanks to the presence of the two timers, ν and τ — defined in Subsection 3.3.1. These two timers are extra states to be included into the system's original state $\widehat{\varepsilon}$, leading to the augmented state $\widehat{\eta}$, defined as:

$$\widehat{\eta} = (\widehat{\varepsilon}, \nu, \tau)^T. \tag{3.19}$$

From the material of Section 3.3, we can now propose the hybrid system equations for the augmented state $\widehat{\eta}$.

The independent variable ν is taken to be a state variable for the closed-loop dynamics in order to track the satellite dynamics along the orbit. Flow occurs when the timer variable τ belongs to the interval $[0, T)$. During flow, the variable ν evolves in the interval $[0, 2\pi]$ while τ keeps track of the elapsed time, and the state $\widehat{\varepsilon}$ evolves according to the dynamics in (3.6a). On the other hand, jumps occur when the timer τ reaches T_τ (c.f. Figure 3.1). At jumps, the timer τ is reset to zero, and the state $\widehat{\varepsilon}$ does not change. This description of the flow and the jumps will set the flow set $\mathcal{C}$ and jumps sets $\mathcal{D}_\tau$ and $\mathcal{D}_\nu$.

3.4.2.1. Jumps equation

The jump equation is given by two different subsystems, corresponding to the dynamics of each of the timers τ and ν.

The first subsystem is given by the second equation of System (3.6), which becomes active when the timer τ reaches a determined value given by the trigger law denoted by $\gamma_\tau\left(\widehat{\varepsilon}, \nu\right)$, i.e. it describes the reset of timer τ. At that point, the control input law, denoted by $\gamma_u\left(\widehat{\varepsilon}, \nu\right) = \Delta\widehat{V} = \widehat{U}(\nu)$, also becomes active and is applied to the system. These dynamics are synthetised as:

$$\begin{cases} \widehat{\varepsilon}^{\,+} = \widehat{\varepsilon} + \widehat{B}(\nu)\, \gamma_u\left(\widehat{\varepsilon}, \nu\right) \\ \nu^+ = \nu, \\ \tau^+ = \gamma_\tau\left(\widehat{\varepsilon}, \nu\right), \end{cases} \qquad (\widehat{\varepsilon}, \nu, \tau) \in \mathcal{D}_\tau, \tag{3.20}$$

where the jump set $\mathcal{D}_\tau$ is defined as:

$$\mathcal{D}_\tau := \mathbb{R}^6 \times [0, 2\pi] \times \{0\}. \tag{3.21}$$

The second subsystem for the jump equation describes the reset of timer ν. This becomes zero whenever it crosses the value 2π, without changing the rest of the states, preventing ν from growing unbounded. The dynamics for this second part are synthetised as:

$$\begin{cases} \widehat{\varepsilon}^{\,+} = \widehat{\varepsilon}, \\ \nu^+ = 0, \\ \tau^+ = \tau, \end{cases} \qquad (\widehat{\varepsilon}^{\,+}, \nu, \tau) \in \mathcal{D}_\nu, \tag{3.22}$$

where the jump set $\mathcal{D}_\nu$ is defined as:

$$\mathcal{D}_\nu := \mathbb{R}^6 \times \{2\pi\} \times [0, 2\pi]. \tag{3.23}$$

We can therefore define the full jump set $\mathcal{D}$ as the union between sets $\mathcal{D}_\nu$ and $\mathcal{D}_\tau$:

$$\mathcal{D} := \mathcal{D}_\nu \cup \mathcal{D}_\tau. \tag{3.24}$$

3.4.2.2. Flow equation

The flow equation is given by the free evolution of the dynamics. From Expression (3.18), it is possible to see the underlying interest of analysing the error between the current satellite's state $\widehat{\xi}$ and the constant state representing the reference periodic trajectory $\widehat{\xi}^{\,ref}$. The first equation of (3.6) becomes then:

$$\widehat{\varepsilon}\,' = \widehat{A}\,(\widehat{\xi} - \widehat{\xi}^{\,ref}) = \widehat{A}\,\widehat{\xi}, \tag{3.25}$$

since $\widehat{A}\,\widehat{\xi}^{\,ref} = 0$ due to (3.10).

The flow equation can therefore be written as:

$$\begin{cases} \widehat{\varepsilon}\,' = \widehat{A}\,\widehat{\xi}, \\ \nu' = 1, \\ \tau' = -1, \end{cases} \qquad (\widehat{\varepsilon}, \nu, \tau) \in \mathcal{C}, \tag{3.26}$$

where the flow set $\mathcal{C}$ is defined as the complement of all the elements of $\widehat{\varepsilon}$, ν and τ which are not members of $\mathcal{D}$:

$$\mathcal{C} := \overline{(\mathbb{R}^6 \times [0, 2\pi] \times [0, 2\pi]) \setminus \mathcal{D}}. \tag{3.27}$$

3.4.3. Control specifications

In this dissertation, four different controllers have been developed, with different trade-offs between cost, complexity and performance, whose objective is to perform an approach maneuver to a stable orbit close to the target satellite.

The procedure for designing the controllers is done as follows: first, we set some of the specifications that should be met by each control law; then, we select the trigger law or timer function $\gamma_\tau\,(\widehat{\varepsilon}, \nu)$ and the control input law $\gamma_u\,(\widehat{\varepsilon}, \nu)$, according to the desired requirements.

The proposed control laws answer to different requirements, translated into the following specifications.

Specification A. Concerning the approach phase, it is desirable that the actuated chaser satellite departs from an initial point and arrives at any point that belongs to the given reference periodic trajectory.

Specification B. Once that the chaser arrives at the periodic reference trajectory, during the observation phase, it should track it to maintain the station.

Specification C. Due to the importance of the fuel expense, the chaser should minimize the cost along the maneuvers. The fuel consumption metrics are fully developed in Appendix F. For the study case, we consider a chaser equipped with 6 identical thrusters rigidly mounted on the satellite. Its associated cost function is given by Expression (F.5), recalled hereafter:

$$J = \sum_{k=1}^{N} ||\Delta V_k||_1 = \sum_{k=1}^{N} \left(|\Delta v_{x\ k}| + |\Delta v_{y\ k}| + |\Delta v_{z\ k}|\right). \tag{3.28}$$

The complexity of the control algorithms should be taken into account and evaluated with respect to the on-board software capabilities. The different specifications are translated to a greater or lesser extent into the different proposed controllers.

3.5. Guidance law #1: periodic norm-minimizing

For the first controller, we propose the simplest possible selection for the thrusters firing function, and a conservative selection of the control function.

> *REQUIREMENT* 1. (Specifications A + B)
>
> The chaser satellite should arrive from any initial departure point to a point of the given periodic reference trajectory by means of periodic — then bounded — trajectories themselves.
>
> Once the approach phase completed, the continuous evolution of the chaser should lie within the reference trajectory $\widehat{\xi}^{\,ref}$ (whose main characteristic is recalled in Equation (3.13)), meaning that for any selection of the reference (3.12), the point $\left\{\widehat{\xi} = \widehat{\xi}^{\,ref}\right\}$ is globally asymptotically stable for the closed loop dynamics. Mathematically, this means that the sixth element of the state vector, shall be driven to zero after each thrust: $\widehat{\varepsilon}_6 = 0$.

> *REQUIREMENT* 2. (Specification C)
>
> The applied control input $\Delta\widehat{V}$ shall minimize the euclidean norm of the rest of the state vector elements $\widehat{\varepsilon}^{\,+}_{1\ldots5}$ after each impulse to make the mismatch in (3.18) be as close to 0 as possible (tracking of the reference trajectory). Therefore the consumption J should be minimized.

The simplest selection for the timer function $\gamma_\tau\left(\widehat{\varepsilon}, \nu\right)$ sets a constant value, namely $\bar{\nu}$. This means that two consecutive control impulses are separated by $\bar{\nu}$ degrees within an orbit, considering that the trigger law $\gamma_\tau\left(\widehat{\varepsilon}, \nu\right)$ evolves in the compact set $[0, 2\pi]$:

$$\gamma_\tau\left(\widehat{\varepsilon}, \nu\right) = \bar{\nu}. \tag{3.29}$$

The control law function $\gamma_u\left(\widehat{\varepsilon}, \nu\right)$ is designed such that it satisfies Requirement 1 while minimizing the euclidean norm of the state $\widehat{\varepsilon}$. The control law function $\gamma_u\left(\widehat{\varepsilon}, \nu\right)$ can therefore be written as:

$$\gamma_u\left(\widehat{\varepsilon}, \nu\right) = \Delta\widehat{V}, \tag{3.30}$$

where the control input $\Delta\widehat{V}$ satisfies the specifications of Requirements 1 and 2. This can be synthetised through the following optimization problem:

$$\begin{aligned} \Delta\widehat{V}^\star &= \arg\min_{\Delta\widehat{V}} |\widehat{\varepsilon}^{\,+}|^2, \\ \text{s.t.} & \\ &\widehat{\varepsilon}^{\,+} = \widehat{\varepsilon} + \widehat{B}(\nu)\,\Delta\widehat{V} \\ &\widehat{\varepsilon}^{+}_6 = 0, \end{aligned} \tag{3.31}$$

where the input matrix $\widehat{B}(\nu) \in \mathbb{R}^{6\times3}$ was firstly defined in (2.170). For simplicity in the sequel, $\widehat{B}(\nu)$ is represented as follows:

$$\widehat{B}(\nu) = \begin{bmatrix} \widehat{b}_1(\nu)^T & \widehat{b}_2(\nu)^T & \widehat{b}_3(\nu)^T & \widehat{b}_4(\nu)^T & \widehat{b}_5(\nu)^T & \widehat{b}_6(\nu)^T \end{bmatrix}^T, \tag{3.32}$$

$\widehat{b}_i(\nu)$ being the row vectors of matrix $\widehat{B}(\nu)$.

Developing the hybrid dynamics jump equation appearing in (3.31) into single terms, we have:

$$\begin{bmatrix} \widehat{\varepsilon}_1^+ \\ \widehat{\varepsilon}_2^+ \\ \widehat{\varepsilon}_3^+ \\ \widehat{\varepsilon}_4^+ \\ \widehat{\varepsilon}_5^+ \\ \hline 0 \end{bmatrix} = \begin{bmatrix} \widehat{\varepsilon}_1 \\ \widehat{\varepsilon}_2 \\ \widehat{\varepsilon}_3 \\ \widehat{\varepsilon}_4 \\ \widehat{\varepsilon}_5 \\ \hline \widehat{\varepsilon}_6 \end{bmatrix} + \begin{bmatrix} \widehat{b}_1(\nu) \\ \widehat{b}_2(\nu) \\ \widehat{b}_3(\nu) \\ \widehat{b}_4(\nu) \\ \widehat{b}_5(\nu) \\ \hline \widehat{b}_6(\nu) \end{bmatrix} \Delta\widehat{V}, \tag{3.33}$$

which, expressed in a compact form, leads to:

$$\begin{bmatrix} \widehat{\varepsilon}_{1\cdots5}^+ \\ \hline 0 \end{bmatrix} = \begin{bmatrix} \widehat{\varepsilon}_{1\cdots5} \\ \hline \widehat{\varepsilon}_6 \end{bmatrix} + \begin{bmatrix} \widehat{b}_{1\cdots5}(\nu) \\ \hline \widehat{b}_6(\nu) \end{bmatrix} \Delta\widehat{V}. \tag{3.34}$$

The design of the control input $\Delta\widehat{V}$ can be achieved by splitting it in two terms, each one targeting one of the two Requirements 1 and 2 and acting over different parts of the control input $\Delta\widehat{V}$:

$$\Delta\widehat{V} = \Delta\widehat{V}^{\parallel_6} + \Delta\widehat{V}^{\perp_6}. \tag{3.35}$$

The input term $\Delta\widehat{V}^{\parallel_6}$ is used to fix $\widehat{\varepsilon}_6^+ = 0$ in Requirement 1. The input term $\Delta\widehat{V}^{\perp_6}$ is used to minimize the norm of the remaining state $\widehat{\varepsilon}_{1\cdots5}^+$ in Requirement 1 while avoiding interferences over the action of $\Delta\widehat{V}^{\parallel_6}$. This means that by design, the term $\Delta\widehat{V}^{\perp_6}$ must not have any influence on $\widehat{\varepsilon}_6$:

$$\widehat{b}_6(\nu)\, \Delta\widehat{V}^{\perp_6} = 0. \tag{3.36}$$

The compact jump equation (3.34) with (3.36) can then be written as:

$$\begin{bmatrix} \widehat{\varepsilon}_{1\cdots5}^+ \\ \hline 0 \end{bmatrix} = \begin{bmatrix} \widehat{\varepsilon}_{1\cdots5} \\ \hline \widehat{\varepsilon}_6 \end{bmatrix} + \begin{bmatrix} \widehat{b}_{1\cdots5}(\nu)\, (\Delta\widehat{V}^{\parallel_6} + \Delta\widehat{V}^{\perp_6}) \\ \hline \widehat{b}_6(\nu)\, \Delta\widehat{V}^{\parallel_6} \end{bmatrix}. \tag{3.37}$$

The design of the input components $\Delta\widehat{V}^{\parallel_6}$ and $\Delta\widehat{V}^{\perp_6}$ is done in the sequel.

3.5.1. Design of the input component $\Delta\widehat{V}^{\parallel_6}$.

In order to fulfill Requirement 1, i.e. $\widehat{\varepsilon}_6^+ = 0$, $\Delta\widehat{V}^{\parallel_6}$ must satisfy the last row of Equation (3.37):

$$0 = \widehat{\varepsilon}_6 + \widehat{b}_6(\nu)\Delta\widehat{V}^{\parallel_6}. \tag{3.38}$$

Thus, an admissible $\Delta\widehat{V}^{\parallel_6}$ is given by:

$$\Delta\widehat{V}^{\parallel_6} = -\frac{\widehat{b}_6(\nu)^T}{|\widehat{b}_6(\nu)|^2}\, \widehat{\varepsilon}_6. \tag{3.39}$$

The control $\Delta\widehat{V}^{\parallel_6}$ is applied in the direction of the vector given by $\widehat{b}_6(\nu)$ – hence the notation $\parallel_6$. Note that by applying $\Delta\widehat{V}^{\parallel_6}$ at any instant, the trajectory becomes periodic and bounded, since the sixth state becomes zero after the impulse, as proven hereafter, where the last row of Equation (3.37) remains:

$$\begin{aligned} 0 &= \widehat{\varepsilon}_6 + \widehat{b}_6(\nu)\, \Delta\widehat{V}^{\parallel_6} \\ &= \widehat{\varepsilon}_6 - \widehat{b}_6(\nu)\frac{\widehat{b}_6(\nu)^T}{|\widehat{b}_6(\nu)|^2}\, \widehat{\varepsilon}_6 = \\ &= \widehat{\varepsilon}_6 - \widehat{\varepsilon}_6. \end{aligned} \tag{3.40}$$

3.5.2. Design of the input component $\Delta\widehat{V}^{\perp_6}$.

$\Delta\widehat{V}^{\perp_6}$ minimizes the euclidean norm of the rest of the states $\widehat{\varepsilon}^{+}_{1\ldots5}$ without interfering over $\Delta\widehat{V}^{\parallel_6}$, as shown in Equation (3.36). For this purpose, $\Delta\widehat{V}^{\perp_6}$ will be contained in the plane that is orthogonal to $\Delta\widehat{V}^{\parallel_6}$ and therefore, to the direction given by $\widehat{b}_6(\nu)^T$ – hence the notation $\perp_6$. Whatever the value of $\Delta\widehat{V}^{\perp_6}$, it will have no effect on $\Delta\widehat{V}^{\parallel_6}$.

Let us express $\Delta\widehat{V}^{\perp_6}$ as:

$$\Delta\widehat{V}^{\perp_6} = \widehat{B}_6^{\perp}(\nu)\,\widehat{v}, \tag{3.41}$$

where $\widehat{B}_6^{\perp}(\nu)$ is the orthogonal complement of $\widehat{b}_6(\nu)^T$.

$\Delta\widehat{V}^{\perp_6}$ can be computed in two steps. In the first, we define matrix $\widehat{B}_6^{\perp}(\nu)$. Both matrices $\widehat{b}_6(\nu)^T$ and $\widehat{B}_6^{\perp}(\nu)$ are orthogonal to each other if their inner product is zero [109]:

$$\widehat{b}_6(\nu)^T \cdot \widehat{B}_6^{\perp}(\nu) = 0. \tag{3.42}$$

In Expression 3.42, matrix $\widehat{b}_6(\nu)^T$ is left-orthogonal to $\widehat{B}_6^{\perp}(\nu)$ and $\widehat{B}_6^{\perp}(\nu)$ is right-orthogonal to $\widehat{b}_6(\nu)^T$.

Remark that $\Delta\widehat{V}^{\parallel_6}$ as defined in (3.39) belongs to the left null space of $\widehat{B}_6^{\perp}(\nu)$. Since $\Delta\widehat{V}^{\parallel_6}$ has the direction of $\widehat{b}_6(\nu)^T$, whatever the vector contained in the orthogonal plane to $\widehat{b}_6(\nu)^T$, it will have no influence on $\Delta\widehat{V}^{\parallel_6}$. From Equation (2.170) it comes that:

$$\widehat{b}_6(\nu)^T = \frac{1}{k^2}\begin{bmatrix} \dfrac{3\kappa(\nu)}{e^2-1} \\ 0 \\ \dfrac{3e\sin\nu}{1-e^2} \end{bmatrix}. \tag{3.43}$$

The orthogonal complement basis is given by:

$$\widehat{B}_6^{\perp}(\nu) = \begin{bmatrix} e\sin\nu & 0 \\ 0 & 1 \\ \kappa(\nu) & 0 \end{bmatrix}. \tag{3.44}$$

A second step, in which the optimal input, denoted $\widehat{V}^{\star}$ is found as:

$$\widehat{V}^{\star} = \arg\min_{\widehat{v}} |\widehat{\varepsilon}^{+}_{1\ldots5}|^2, \tag{3.45}$$

where $\widehat{\varepsilon}_{1\ldots5}$ comes out from the five first rows of Equation (3.37):

$$\widehat{\varepsilon}^{+}_{1\ldots5} = \widehat{\varepsilon}_{1\ldots5} + \widehat{b}_{1\ldots5}(\nu)\,\Delta\widehat{V}^{\parallel_6} + \widehat{b}_{1\ldots5}(\nu)\,\Delta\widehat{V}^{\perp_6}. \tag{3.46}$$

Developing expression (3.46), using Equation (3.41), we get:

$$\widehat{\varepsilon}^{+}_{1\ldots5} = \widehat{\varepsilon}_{1\ldots5} + \widehat{b}_{1\ldots5}(\nu)\,\Delta\widehat{V}^{\parallel_6} + \widehat{b}_{1\ldots5}(\nu)\,\widehat{B}_6^{\perp}(\nu)\,\widehat{v}, \tag{3.47}$$

so, in (3.45):

$$|\widehat{\varepsilon}^{+}_{1\ldots5}|^2 = |\widehat{\varepsilon}_{1\ldots5} + \widehat{b}_{1\ldots5}(\nu)\,\Delta\widehat{V}^{\parallel_6} + \widehat{b}_{1\ldots5}(\nu)\,\widehat{B}_6^{\perp}(\nu)\,\hat{v}|^2. \tag{3.48}$$

The solution of (3.45) boils down to the least-squares linear system:

$$\widehat{b}_{1\ldots5}(\nu)\,\widehat{B}_6^{\perp}(\nu)\,\widehat{v} = -\left(\widehat{\varepsilon}_{1\ldots5} + \widehat{b}_{1\ldots5}(\nu)\,\Delta\widehat{V}^{\parallel_6}\right). \tag{3.49}$$

In order to find the optimal value $\widehat{V}^\star$, we use the left-pseudoinverse $A^{-L} = (A^TA)^{-1}A^T$. Let:

$$M := \widehat{b}_{1\cdots5}(\nu)\,\widehat{B}_6^\perp(\nu), \text{ with } M \in \mathbb{R}^{m\times n}, \tag{3.50}$$

then an admissible $\widehat{V}^\star$ satisfies:

$$\begin{aligned}
M\,\widehat{V}^\star &= -\left(\widehat{\varepsilon}_{1\cdots5} + \widehat{b}_{1\cdots5}(\nu)\,\Delta\widehat{V}^{\parallel_6}\right), \\
M^TM\,\widehat{V}^\star &= -M^T\left(\widehat{\varepsilon}_{1\cdots5} + \widehat{b}_{1\cdots5}(\nu)\,\Delta\widehat{V}^{\parallel_6}\right), \\
\left[M^TM\right]^{-1}\left[M^TM\right]\,\widehat{V}^\star &= -\left[M^TM\right]^{-1}M^T\left(\widehat{\varepsilon}_{1\cdots5} + \widehat{b}_{1\cdots5}(\nu)\,\Delta\widehat{V}^{\parallel_6}\right), \\
\widehat{V}^\star &= -\left[M^TM\right]^{-1}M^T\left(\widehat{\varepsilon}_{1\cdots5} + \widehat{b}_{1\cdots5}(\nu)\,\Delta\widehat{V}^{\parallel_6}\right) \\
\widehat{V}^\star &= -M^{-L}\left(\widehat{\varepsilon}_{1\cdots5} + \widehat{b}_{1\cdots5}(\nu)\,\Delta\widehat{V}^{\parallel_6}\right),
\end{aligned} \tag{3.51}$$

or explicitely:

$$\widehat{V}^\star = -\left[\left(\widehat{b}_{1\cdots5}(\nu)\,\widehat{B}_6^\perp(\nu)\right)^T\,\left(\widehat{b}_{1\cdots5}(\nu)\,\widehat{B}_6^\perp(\nu)\right)\right]^{-1}\left(\widehat{b}_{1\cdots5}(\nu)\,\widehat{B}_6^\perp(\nu)\right)^T\left(\widehat{\varepsilon}_{1\cdots5} + \widehat{b}_{1\cdots5}(\nu)\,\Delta\widehat{V}^{\parallel_6}\right). \tag{3.52}$$

➠ **PROPOSITION 1:**
For any value of ν, the inverse in (3.52) *always exists and selection* (3.52) *coincides with the minimizer in* (3.45), *namely $\widehat{V}^\star$.*

The control law function is therefore expressed as:

$$\begin{aligned}
\gamma_u\left(\widehat{\varepsilon},\nu\right) &= \Delta\widehat{V} \\
&= -\frac{\widehat{b}_6(\nu)^T}{|\widehat{b}_6(\nu)|^2}\,\widehat{\varepsilon}_6 \\
&\quad - \widehat{B}_6^\perp(\nu)\,\left[\left(\widehat{b}_{1\cdots5}(\nu)\,\widehat{B}_6^\perp(\nu)\right)^T\,\left(\widehat{b}_{1\cdots5}(\nu)\,\widehat{B}_6^\perp(\nu)\right)\right]^{-1}\left(\widehat{b}_{1\cdots5}(\nu)\,\widehat{B}_6^\perp(\nu)\right)^T\left(\widehat{\varepsilon}_{1\cdots5} - \widehat{b}_{1\cdots5}(\nu)\,\frac{\widehat{b}_6(\nu)^T}{|\widehat{b}_6(\nu)|^2}\,\widehat{\varepsilon}_6\right).
\end{aligned} \tag{3.53}$$

3.5.3. Stability proof.

Based on Proposition 1, a desirable property of control law (3.29), (3.53) is that it instantaneously minimizes the norm of $\widehat{\varepsilon}$ constrained to the fact that the subsequent motion is periodic. Since the norm of $\widehat{b}_6(\nu)$ in (3.43) is never zero, then clearly, Equation (3.53) is always well-posed and ensures that $\widehat{\varepsilon}_6^+ = 0$. In addition to this, instantaneously minimizing the norm of $\widehat{\varepsilon}$ also ensures the best possible decrease at the specific fixed instant of time enforced by the rigid periodic selection. With this logic in place, we can guarantee stability of the closed-loop but not convergence. Indeed, we can guarantee non-increase of $|\widehat{\varepsilon}|$ across jumps but there is no guarantee of obtaining a strict decrease. As a result, we anticipate a slow convergence (if any) in our simulation section when using this controller. Despite this fact, the choice (3.29), (3.53) is still an interesting one because it ensures that approaching between the two satellites is performed through periodic (bounded) motions, leading to some degree of fault tolerance (in case of malfunctioning, the satellite is on a stable orbit).

Within the proposed hybrid context, the stability goal formulated in Requirement 2 is well characterized in terms of the stability properties of the bounded attractor:

$$\mathcal{A} := \{0\} \times [0, 2\pi] \times [0, 2\pi], \tag{3.54}$$

which may be analyzed using the tools of [52, Chapter 7], because selections (3.21), (3.23), (3.24) and (3.27) satisfy the hybrid basic conditions of reference [52, Assumption 6.5].

The stability definitions for hybrid systems that we use in the sequel are not recalled in this manuscript, since their description is far from being trivial. However, we adopt the same formalism as in reference [52], where the reader will find all the needed elements.

The following theorem certifies that the proposed controller solves part of Requirement 1. The definition for *uniform global asymptotic stability* can be found in [52, Definition 3.6].

✪ **THEOREM 1.** *Given control law* (3.29), (3.53), *the attractor* $\mathcal{A}$ *in* (3.54) *is uniformly globally asymptotically stable along the arising closed-loop dynamics with* (3.20), (3.22), (3.26).

Proof. First notice that $|(\widehat{\varepsilon}, \nu, \tau)|_{\mathcal{A}} = |\widehat{\varepsilon}|$. Recall that solutions $(\nu, j) \mapsto \widehat{\varepsilon}(\nu, j)$ to hybrid systems have a domain *dom* $\widehat{\varepsilon}$ parametrized by a flowing direction (here represented by the amount ν of true anomaly elapsed since the initial condition, as opposed to continuous time t for a classical hybrid systems representation) and by a jumping direction j (see [52, Chap. 2] for details). We first realize that before the first impulse, all solutions evolve in free motion along the LTI flow dynamics in (3.20), (3.22), (3.26), leading to:

$$|\widehat{\varepsilon}(\nu, 0)| \leq |e^{2\pi \widehat{A}}||\widehat{\varepsilon}(0, 0)|. \tag{3.55}$$

Notice now that Proposition 1 ensures that $\gamma_u(\widehat{\varepsilon}, \nu) = \widehat{V}^{\star}$. In particular, after the first jump the state $\widehat{\varepsilon}_6$ remains at zero for all (hybrid) times. Then during all subsequent flows, the state $\widehat{\varepsilon}$ remains constant due to the structure of $\widehat{A}$. Moreover, across jumps, the control law is the minimizer of (3.45), clearly satisfying $|\widehat{\varepsilon}^{+}| \leq |\widehat{\varepsilon}|$. As a consequence, we get:

$$|\widehat{\varepsilon}(\nu, j)| \leq |e^{2\pi \widehat{A}}||\widehat{\varepsilon}(0, 0)|, \tag{3.56}$$

for all $(\nu, j) \in$ *dom* $\widehat{\varepsilon}$, which establishes uniform global stability. □

3.6. Guidance law #2: periodic bi-impulsive

A second selection that we propose for the next controller is once again periodic, similar to Guidance law #1. However, it corresponds to a wiser selection of function $\gamma_u\left(\widehat{\varepsilon}, \nu\right)$ in terms on envisioned fuel consumption, performed in similar ways to what is proposed in [33].

✪ *REQUIREMENT* 3. (Specifications A + B)

Based on the proposal in [33], the chaser satellite should arrive from any initial departure point to a point that belongs to the given periodic reference trajectory $\widehat{\xi}^{\,ref}$, such that for any selection of the reference (3.12), the point $\left\{\widehat{\xi} = \widehat{\xi}^{\,ref}\right\}$ is globally asymptotically stable for the closed loop dynamics.

This maneuver is executed in two consecutive control actions $\Delta\widehat{V}_1$ and $\Delta\widehat{V}_2$ separated by an angle $\bar{\nu}$. Let ν_1 and ν_2 be the locations at which a couple of consecutive thrusts $\Delta\widehat{V}_1$ and $\Delta\widehat{V}_2$ are applied, with $\bar{\nu} = \nu_2 - \nu_1$.

After these two control actions, the error's state shall be zero, meaning that the continuous evolution of the chaser lies within the periodic reference trajectory $\widehat{\xi}^{\,ref}$ whose main characteristic is recalled in Equation (3.13).

The timer function $\gamma_\tau\left(\widehat{\varepsilon}, \nu\right)$ remains constant, as for the Guidance law #1 in Section 3.5. Two consecutive control inputs are therefore separated by $\bar{\nu}$ degrees from one another within an orbit:

$$\gamma_\tau\left(\widehat{\varepsilon}, \nu\right) = \bar{\nu}. \tag{3.57}$$

The control law function is therefore based on two consecutive control actions $\Delta\widehat{V}_1$ and $\Delta\widehat{V}_2$:

$$\gamma_u\left(\widehat{\varepsilon},\nu\right)=\Delta\widehat{V}=\begin{bmatrix}I_3 & 0_{3\times3}\end{bmatrix}\begin{bmatrix}\Delta\widehat{V}_1\\ \Delta\widehat{V}_2\end{bmatrix}. \tag{3.58}$$

In order to identify the expression of the two impulses $\Delta\widehat{V}_1$ and $\Delta\widehat{V}_2$, we study and propagate the hybrid dynamics using Figure (3.4).

Consider an initial state $\widehat{\varepsilon}(\nu_1,j)$, at which the jump set is activated. The first control input $\Delta\widehat{V}_1$ is applied, leading to state $\widehat{\varepsilon}(\nu_1,j+1)$. The satellite then evolves in the flow set, according to the free dynamics until time ν_2 given by the choice $\bar{\nu}=\nu_2-\nu_1$. At state $\widehat{\varepsilon}(\nu_2,j+1)$, the dynamics triggers again to the jump set and the second control input $\Delta\widehat{V}_2$ is applied, leading to final state $\widehat{\varepsilon}(\nu_2,j+2)$ that must be zero to track the reference periodic trajectory in (3.18).

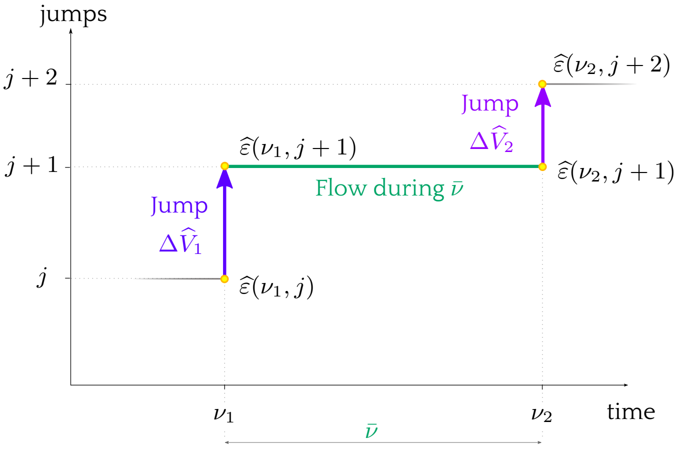

Figure 3.4: Hybrid dynamics for Guidance law #2.

It becomes now straightforward to set the propagation equations by taking into account the previous explanation; the flow and jump equations in Expressions (3.26) and (3.20) respectively and the input matrix $\widehat{B}(\nu)$ recalled hereafter for simplicity reasons:

$$\widehat{B}(\nu)=\frac{1}{k^2\kappa^2(1-e^2)}\left[\begin{array}{c|c|c}0 & -\left(1-e^2\right)\kappa\sin\nu & 0\\ 0 & \left(1-e^2\right)\kappa\cos\nu & 0\\ \hline -e(1+\kappa)\kappa\sin\nu-\dfrac{3\sigma\kappa^3}{(1-e^2)^{3/2}} & 0 & \dfrac{3\sigma e\kappa^2\sin\nu}{(1-e^2)^{3/2}}-\kappa^3+\kappa^2+2\kappa\\ (1-e^2)(1+\kappa)\kappa\sin\nu & 0 & (1-e^2)\kappa^2\cos\nu\\ (1+\kappa)\kappa\cos\nu+e\kappa & 0 & -\kappa^2\sin\nu\\ -3\kappa^3 & 0 & 3e\kappa^2\sin\nu\end{array}\right]. \tag{3.59}$$

From initial state $\widehat{\varepsilon}(\nu_1,j)$ at time ν_1, we apply the first impulse $\Delta\widehat{V}_1$, such that state $\widehat{\varepsilon}(\nu_1,j+1)$ is expressed as:

$$\widehat{\varepsilon}(\nu_1,j+1)=\widehat{\varepsilon}(\nu_1,j)+\widehat{B}(\nu_1)\,\Delta\widehat{V}_1. \tag{3.60}$$

After impulse $\Delta\widehat{V}_1$ at time ν_1, the state flows according to the linear dynamics in Expression (3.26), of the type $\widehat{\varepsilon}\,'=\widehat{A}\,\widehat{\varepsilon}$, whose explicit solution depends both on $\widehat{A}$ and the elapsed time $\bar{\nu}$. This solution is given by the state transition matrix for this elapsed time $\bar{\nu} = \nu_2 - \nu_1$, hence the exponential:

$$\widehat{\Phi}(\nu_2, \nu_1) = e^{\widehat{A}(\nu_2 - \nu_1)} = \begin{bmatrix} 1 & 0 & 0 & 0 & 0 & 0 \\ 0 & 1 & 0 & 0 & 0 & 0 \\ 0 & 0 & 1 & 0 & 0 & \bar{\nu}\,(1-e^2)^{-3/2} \\ 0 & 0 & 0 & 1 & 0 & 0 \\ 0 & 0 & 0 & 0 & 1 & 0 \\ 0 & 0 & 0 & 0 & 0 & 1 \end{bmatrix}. \tag{3.61}$$

Using Equation (3.60) we have therefore:

$$\begin{aligned} \widehat{\varepsilon}(\nu_2, j+1) &= \widehat{\Phi}(\nu_2, \nu_1)\, \widehat{\varepsilon}(\nu_1, j+1) \\ &= \widehat{\Phi}(\nu_2, \nu_1)\, [\widehat{\varepsilon}(\nu_1, j) + \widehat{B}(\nu_1)\, \Delta \widehat{V}_1]. \end{aligned} \tag{3.62}$$

At time $\nu_2 = \nu_1 + \bar{\nu}$, the second impulse $\Delta \widehat{V}_2$ is applied. Using Expression (3.62), the state $\widehat{\varepsilon}(\nu_2, j+2)$ is expressed as:

$$\begin{aligned} \widehat{\varepsilon}(\nu_2, j+2) &= \widehat{\varepsilon}(\nu_2, j+1) + \widehat{B}(\nu_1 + \bar{\nu})\, \Delta \widehat{V}_2 \\ &= \widehat{\Phi}(\nu_2, \nu_1)\, [\widehat{\varepsilon}(\nu_1, j) + \widehat{B}(\nu_1)\, \Delta \widehat{V}_1] + \widehat{B}(\nu_1 + \bar{\nu})\, \Delta \widehat{V}_2 \\ &= \widehat{\Phi}(\nu_2, \nu_1)\, \widehat{\varepsilon}(\nu_1, j) + \begin{bmatrix} \widehat{\Phi}(\nu_2, \nu_1)\, \widehat{B}(\nu_1) & \widehat{B}(\nu_1 + \bar{\nu}) \end{bmatrix} \begin{bmatrix} \Delta \widehat{V}_1 \\ \Delta \widehat{V}_2 \end{bmatrix}. \end{aligned} \tag{3.63}$$

Denoting:

$$M(\nu_1, \bar{\nu}) = \begin{bmatrix} \widehat{\Phi}(\nu_2, \nu_1)\, \widehat{B}(\nu_1) & \widehat{B}(\nu_1 + \bar{\nu}) \end{bmatrix}, \tag{3.64}$$

and using Expression (3.58), we obtain:

$$\widehat{\varepsilon}(\nu_2, j+2) = \widehat{\Phi}(\nu_2, \nu_1)\, \widehat{\varepsilon}(\nu_1, j) + M(\nu_1, \bar{\nu})\, \Delta \widehat{V}. \tag{3.65}$$

In order to find the necessary controls $\Delta \widehat{V}_1$ and $\Delta \widehat{V}_2$, it becomes necessary to study the invertibility properties of matrix $M(\nu_1, \bar{\nu})$ in (3.63). By design, the desirable property for this second controller is that after two impulses, the satellite tracks the reference periodic trajectory:

$$\widehat{\varepsilon}(\nu_2, j+2) = 0, \tag{3.66}$$

such that:

$$\Delta \widehat{V} = -M(\nu_1, \bar{\nu})^{-1}\, \widehat{\Phi}(\nu_2, \nu_1)\, \widehat{\varepsilon}(\nu_1, j). \tag{3.67}$$

There exists a unique solution to Equation (3.67) whenever matrix $M(\nu_1, \bar{\nu})$ is invertible. It becomes therefore important to analyse the determinant of matrix $M(\nu_1, \bar{\nu})$, which is done in the following conjecture. The result of the conjecture restricts the set of possible selections of $\bar{\nu}$ in (3.57).

✻ **CONJECTURE 3.6.1:**
For any value of $\nu_1 \in [0, 2\pi]$, *matrix* $M(\nu_1, \bar{\nu})$ *in* (3.64) *is invertible if and only if* $\bar{\nu} \neq k\pi$, $k \in \mathbb{Z}$ *for any value of the eccentricity* $e \in [0, 1)$.

Conjecture 3.6.1 is motivated by numerical experience, as shown in Figure 3.5, where we can see the determinant of matrix $M(\nu_1, \bar{\nu})$ for an eccentricity $e = 0.4$ for every value of $\nu_1 \in [0, 2\pi]$ and $\bar{\nu} \in [0, 2\pi]$.

Figure 3.6 shows the zero set level[1] of $M(\nu_1, \bar{\nu})$, where we can see the points in which the determinant equals zero (right plot).

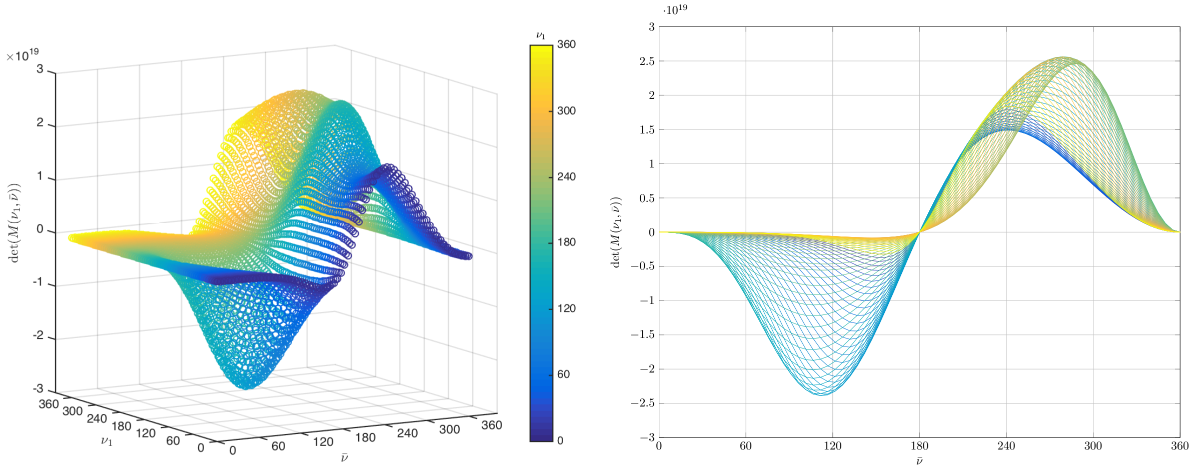

Figure 3.5: Value of $\det(M(\nu_1, \bar{\nu}))$ with $e = 0.4$.

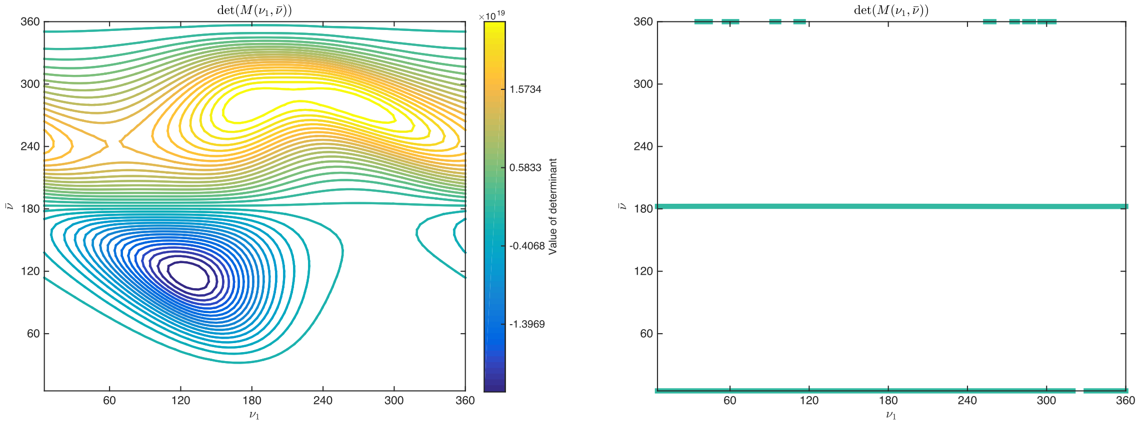

Figure 3.6: View of the determinant $\det(M(\nu_1, \bar{\nu}))$ at zero level for $e = 0.4$.

The solution is unique since it is based on the inverse of a matrix. If Conjecture 3.6.1 holds, for any selection $\bar{\nu} \in (0, 2\pi) \setminus \{\pi\}$, Equation (3.63) can be inverted to compute the unique pair of inputs $\Delta\widehat{V}_1$, $\Delta\widehat{V}_2$ ensuring $\widehat{\varepsilon}(\nu_2, j+2) = 0$.

According to Equation (3.67), we can set the control function $\gamma_u\left(\widehat{\varepsilon}, \nu\right)$ evaluated at instant ν_1 to the first computed impulse as:

$$\gamma_u\left(\widehat{\varepsilon}, \nu\right) = \Delta\widehat{V} = -[I_3 \quad 0_{3\times 3}]\, M(\nu_1, \bar{\nu})^{-1}\, \widehat{\Phi}(\nu_2, \nu_1)\, \widehat{\varepsilon}. \tag{3.68}$$

3.6.1. Stability proof.

The overall control strategy (3.57), (3.68) guarantees convergence to zero of the error $\widehat{\varepsilon}$ after two impulses, as established next.

---

[1] Zero set level: set where the matrix $M(\nu_1, \bar{\nu})$ takes zero value.

LEMMA 1:
If $M(\nu_1, \bar{\nu})$ is invertible for all $\nu \in [0, 2\pi]$, then selection (3.57), (3.68) *guarantees that all solutions to* (3.20), (3.22), (3.26) *have the state $\widehat{\varepsilon}$ equal to zero after at most two jumps.*

Proof. Consider two subsequent impulses $\Delta\widehat{V} = \begin{bmatrix}\Delta\widehat{V}_1\\ \Delta\widehat{V}_2\end{bmatrix}$ in (3.67). Then, due to the property that $\Delta\widehat{V}$ brings the state to zero after two impulses, it follows that selection $\begin{bmatrix}\Delta\widehat{V}_2\\ 0_{3\times 1}\end{bmatrix}$ is a feasible one for the second impulse. As a consequence of uniqueness, arising from relation (3.63), this is the only possible solution and we must have $\widehat{\varepsilon}^+ = 0$ after the second impulse. ☐

Based on Lemma 2 we can now prove that Guidance law #2 solves Requirement 3 as established in the next theorem.

THEOREM 2. *Given $\bar{\nu} \in (0, 2\pi) \setminus \{\pi\}$, assume that matrix $M(\nu_1, \bar{\nu})$ is invertible for any value of $\nu \in [0, \pi]$.*

Then, the control law (3.57), (3.68) *ensures that attractor $\mathcal{A}$ in (3.54) is uniformly globally asymptotically stable along the arising closed-loop dynamics with* (3.20), (3.22), (3.26).

Proof. The proof is carried out by exploiting the following global version of [52, Prop. 7.5] (its proof is straightforward, taking $\nu \to \infty$ in the semiglobal version of [52, Prop. 7.5], and is actually therein implicitly used for establishing the result in [52, Ex. 7.6]). ☐

The next Proposition regarding stability from invariance and uniform convergence is extracted from reference [52, Proposition 7.5].

PROPOSITION 2:
Given a nominally well-posed hybrid system $\mathcal{H}$, suppose that the compact set $\mathcal{A}$ in (3.54) *is strongly forward invariant and globally uniformly attractive for $\mathcal{H}$. Then, it is uniformly globally asymptotically stable for $\mathcal{H}$.*

To apply Proposition 2 in our case, we first notice that the data of hybrid system (3.20), (3.22), (3.26), (3.57), (3.68) satisfies the hybrid basic conditions in [52, As. 6.5], therefore, from [52, Thm 6.8], it is nominally well-posed. Concerning forward invariance of $\mathcal{A}$ (namely, all solutions starting in $\mathcal{A}$ remain in $\mathcal{A}$ for all times), it follows from the fact that the flow dynamics of $\widehat{\varepsilon}$ is linear (so the origin is an equilibrium) and the jumps guarantee non-increase of $\widehat{\varepsilon}$ (see the proof of Theorem 1). Finally, global uniform convergence is a straightforward consequence of the stronger property of uniform finite-time convergence established in Lemma 1.

REMARK. A desirable feature of the established uniform global asymptotic stability of set $\mathcal{A}$ can be obtained by the robustness characterization given in [52, Ch. 7], which holds under the mild assumption that the hybrid dynamics satisfy the hybrid basic conditions (these are easily checked for dynamics (3.20), (3.22), (3.26), (3.57), (3.68)) and that the attractor is compact (this is easy to verify as well for set $\mathcal{A}$ in (3.54)). Robustness of asymptotic stability (established in [52, Thm 7.21]) allows to conclude that there exists a sufficiently small, but nonzero perturbation of the dynamics, for which the established nominal asymptotic stability is not destroyed. As a consequence, we expect our control law to perform well also under the presence of uncertainties, such as unmodeled dynamics, or external perturbations, as long as they are sufficiently small, and they are zero when the state belongs to the attractor (see, [52, Ch. 7] for details). For more general settings, another useful feature arising from these robustness properties is that for stronger perturbations we have a semiglobal practical robust stability result, established in [52, Thm 7.20]. This result ensures that perturbations not vanishing in $\mathcal{A}$ lead to a gradual deterioration of the convergence properties, which is what one should expect when persistent disturbances, such as atmospheric drag or high solar activities affect the closed-loop dynamics. All these desirable properties are confirmed by our simulation results of Section 3.9.

3.7. Guidance law #3: non-periodic bi-impulsive

After the choices made in controllers #1 and #2, we can add an extra requirement regarding the consumption. Actually, the fuel cost is not optimized neither in controllers #1 nor #2. This fact leads us to set the following requirements for this controller #3.

> *REQUIREMENT* 4. (Specifications A + B)
>
> Based on the proposal in [33], the chaser satellite should arrive from any initial departure point to a point that belongs to the given periodic reference trajectory $\widehat{\xi}^{\,ref}$, such that for any selection of the reference (3.12), the point $\left\{\widehat{\xi} = \widehat{\xi}^{\,ref}\right\}$ is globally asymptotically stable for the closed loop dynamics.
>
> This maneuver is executed in two consecutive control actions $\Delta\widehat{V}_1$ and $\Delta\widehat{V}_2$ separated by an angle $\bar{\nu}$. Let ν_1 and ν_2 be the locations at which a couple of consecutive thrusts $\Delta\widehat{V}_1$ and $\Delta\widehat{V}_2$ are applied, with $\bar{\nu} = \nu_2 - \nu_1$.
>
> After these two control actions, the chaser's state shall be zero, meaning that the continuous evolution of the chaser lies within the periodic reference trajectory $\widehat{\xi}^{\,ref}$ whose main characteristic is recalled in Equation (3.13).

> *REQUIREMENT* 5. (SpecificationC)
>
> The fuel consumption shall be minimized along the different maneuvers. From the cost expression in Equation (F.5), this can be achieved by selecting at each thrust instant k an appropriate value of the thrust execution angle value ν_k.

After setting the timer functions $\gamma_\tau\left(\widehat{\varepsilon},\nu\right)$ to a constant angular distance value in controllers #1 and #2 in Sections 3.5 and 3.6 respectively, a more interesting choice comes out when optimizing this angular distance $\bar{\nu}$, while maintaining the control function $\gamma_u\left(\widehat{\varepsilon},\nu\right)$ identical to the one explained in Section 3.6 — hence compliant with Requirement 4 .

The timer function will now be based on an optimized selection of the waiting time τ^+ in (3.22) before the next impulse, such that the fuel consumption index in Expression (F.5) for the transformed coordinates is minimized:

$$J = \sum_{\nu_k \in \mathcal{V}} |\Delta\widehat{V}(\nu_k)|_1, \tag{3.69}$$

where $|\Delta\widehat{V}(\nu_k)|_1 = |\Delta\widehat{v}_a(\nu_k)| + |\Delta\widehat{v}_b(\nu_k)| + |\Delta\widehat{v}_c(\nu_k)|$ denotes the 1-norm of the cost function when firing is achieved by 6 identical thrusters rigidly mounted to the satellite[2].

Using Expression (3.68), the timer function $\gamma_\tau\left(\widehat{\varepsilon},\nu\right)$ is set to:

$$\gamma_\tau(\widehat{\varepsilon},\nu) = \arg \min_{\bar{\nu}\in[0,2\pi]} J = \arg \min_{\bar{\nu}\in[0,2\pi]} \left|M(\nu_1,\bar{\nu})^{-1}\,\widehat{\varepsilon}\,\right|_1 . \tag{3.70}$$

---

[2] Note that the subindices of the three components of $\Delta\widehat{V}$ are not noted x, y and z as in Expression (F.5), but a, b and c. This is done to account for the fact that the components of $\Delta\widehat{V}$ do not coincide with the ones in LVLH coordinates (ΔV) due to transformations $C(\nu)$ and $S(\nu)$ in Subsection 2.3.2.

It must be noted that the minimization is done over the inverse of matrix $M(\nu_1, \bar{\nu})$, which is invertible if and only if $\bar{\nu} \neq k\pi$, $k \in \mathbb{Z}$, as conjectured in 3.6.1. The optimization process is then performed in the two intervals where the matrix is invertible, $(0, \pi)$ and $(\pi, 2\pi)$, such that the global minimum will be selected as the minimum in the two intervals, as shown in an example in Figure (3.7) by the symbol $\otimes$. Hence, by selecting the appropriate value of $\bar{\nu} \in (0, 2\pi) \setminus \{\pi\}$, we ensure the optimality of the solution.

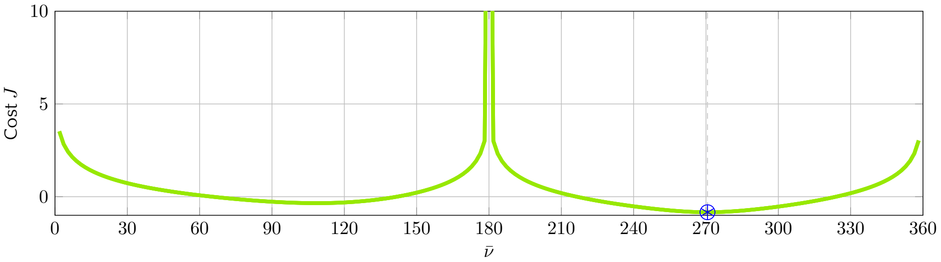

Figure 3.7: Example for a given state $\widehat{\varepsilon}$ of the value of the function at the right hand side of (3.70).

Since the control function $\gamma_u(\widehat{\varepsilon}, \nu)$ is similar to the one for controller #2 in Section 3.6, the difference here is therefore the choice of the new separation between impulses given by the timer function $\gamma_\tau(\widehat{\varepsilon}, \nu)$ which will minimize the cost J in (3.69):

$$\gamma_u(\widehat{\varepsilon}, \nu) = \Delta\widehat{V} = -[I_3 \quad 0_{3\times 3}]\, M(\nu_1, \gamma_\tau(\widehat{\varepsilon}, \nu))^{-1}\, \widehat{\varepsilon}. \tag{3.71}$$

As compared to the previous controllers, control law (3.70), (3.71) is associated with an increased computational complexity. Indeed, at each impulse time, a numerical optimization providing the solution to (3.70) needs to be performed. Nonetheless, the advantages in terms of fuel consumption are clearly illustrated by the simulation results of the next section. It should be emphasized that the minimization is carried out over a compact set $[0, 2\pi]$, so it may be easily performed following some heuristics. Numerical evidence reveals that the function in Figure 3.7 is strictly convex in the intervals $(0, \pi)$ and $(\pi, 2\pi)$.

3.7.1. Stability proof.

The following result can be established by similar derivations to those in the proof of Theorem 2, relying on the uniqueness of the solution to the inverse of Equation (3.67). This, together with the optimal selection of γ_τ in (3.70) provides a solution to both Requirements 4 and 5. Its proof is omitted due to this similarity to that of Theorem 2.

> ✪ **THEOREM 3.** *Control law* (3.70), (3.71) *ensures that attractor $\mathcal{A}$ in (3.54) is uniformly globally asymptotically stable along the arising closed-loop dynamics with* (3.20), (3.22), (3.26).

The three controllers designed so far have the following features:

- controller 3.5 is desirable because it forces the chaser to evolve along periodic (therefore bounded) motions, but does not guarantee to reach exactly the target trajectory;
- controllers 3.6 and 3.7 are desirable because they guarantee finite time convergence, but these maneuvers are fragile since the chaser evolves on unbounded trajectories until it reaches its goal. This can be unsafe in case of actuators failure.

In the next section, we combine the desirable features of the three above laws in a single enhanced control law following again a receding horizon paradigm.

3.8. Guidance law #4: periodic tri-impulsive

This fourth controller is a generalization of the bi-impulsive method developed in Section 3.6, with an extra requirement regarding the periodicity of the trajectories themselves.

> ✪ *REQUIREMENT* 6. (Specification A)
>
> The chaser satellite should arrive from any initial departure point to a point of the given periodic reference trajectory by means of periodic — then bounded — trajectories themselves. Mathematically, this means that the sixth element of the state vector, shall be driven to zero after each thrust: $\widehat{\varepsilon}_6 = 0$.

> ✪ *REQUIREMENT* 7. (Specification B)
>
> Generalizing the proposed bi-impulsive methodology in Section 3.6, the maneuvers will be executed in three consecutive control actions $\Delta\widehat{V}_1$, $\Delta\widehat{V}_2$ and $\Delta\widehat{V}_3$ separated by a certain angle $\bar{\nu}$ from one another. After these three control actions, the chaser's state shall be zero, meaning that the continuous evolution of the chaser lies within the periodic reference trajectory $\widehat{\xi}^{\,ref}$ whose main characteristic is recalled in Equation (3.13).

As for controller #2, the timer function $\gamma_\tau\left(\widehat{\varepsilon}, \nu\right)$ is fixed to a constant value $\bar{\nu}$ for the angle separation between thrusts[3] — hence the controller is periodic. Since we have three thrusts, they will be applied at three different locations, ν_1, ν_2 and ν_3, verifying:

$$\begin{aligned} \nu_2 - \nu_1 &= \bar{\nu}_1, \\ \nu_3 - \nu_2 &= \bar{\nu}_2, \end{aligned} \tag{3.72}$$

therefore $\bar{\nu}_1 = \bar{\nu}_2 = \bar{\nu}$. The timer function is set to:

$$\gamma_\tau\left(\widehat{\varepsilon}, \nu\right) = \bar{\nu}. \tag{3.73}$$

Regarding the development of the control law function $\gamma_u\left(\widehat{\varepsilon}, \nu\right)$ for this fourth controller, the *shape* of $\widehat{B}(\nu)$ in Expression (2.170), recalled hereafter, is analyzed.

$$\begin{aligned} \widehat{B}(\nu) &= \underbrace{\frac{1}{k^2\kappa^2(1-e^2)}}_{K} \left[\begin{array}{c|c|c} 0 & -\left(1-e^2\right)\kappa\sin\nu & 0 \\ 0 & \left(1-e^2\right)\kappa\cos\nu & 0 \\ \hline -e(1+\kappa)\kappa\sin\nu - \dfrac{3\sigma\kappa^3}{(1-e^2)^{3/2}} & 0 & \dfrac{3\sigma e\kappa^2\sin\nu}{(1-e^2)^{3/2}} - \kappa^3 + \kappa^2 + 2\kappa \\ (1-e^2)(1+\kappa)\kappa\sin\nu & 0 & (1-e^2)\kappa^2\cos\nu \\ (1+\kappa)\kappa\cos\nu + e\kappa & 0 & -\kappa^2\sin\nu \\ -3\kappa^3 & 0 & 3e\kappa^2\sin\nu \end{array}\right] \\ &= K\left[\begin{array}{c|c|c} 0_{2\times1} & \widehat{B}_\alpha(\nu) & 0_{2\times1} \\ \hline \widehat{B}_\beta(\nu) & 0_{4\times1} & \widehat{B}_\theta(\nu) \end{array}\right], \end{aligned} \tag{3.74}$$

---

[3] Its justification will be fully explained in the later.

where we have considered the following partitions of matrix $\widehat{B}(\nu)$:

$$\widehat{B}_\alpha(\nu) = \begin{bmatrix} -(1-e^2)\,\kappa\sin\nu \\ (1-e^2)\,\kappa\cos\nu \end{bmatrix}, \tag{3.75}$$

$$\widehat{B}_\beta(\nu) = \begin{bmatrix} -e(1+\kappa)\kappa\sin\nu - \dfrac{3\sigma\kappa^3}{(1-e^2)^{3/2}} \\ (1-e^2)(1+\kappa)\kappa\sin\nu \\ (1+\kappa)\kappa\cos\nu + e\kappa \\ -3\kappa^3 \end{bmatrix}, \tag{3.76}$$

$$\widehat{B}_\theta(\nu) = \begin{bmatrix} \dfrac{3\sigma e\kappa^2\sin\nu}{(1-e^2)^{3/2}} - \kappa^3 + \kappa^2 + 2\kappa \\ (1-e^2)\kappa^2\cos\nu \\ -\kappa^2\sin\nu \\ 3e\kappa^2\sin\nu \end{bmatrix}. \tag{3.77}$$

We notice the existing decoupling, highlighted by the vertical and horizontal lines in (3.74). This decoupling also appears over the dynamic matrix $\widehat{A}$ in (3.7), also re-written below:

$$\widehat{A} = \left[\begin{array}{cc|cccc} 0 & 0 & 0 & 0 & 0 & 0 \\ 0 & 0 & 0 & 0 & 0 & 0 \\ \hline 0 & 0 & 0 & 0 & 0 & \dfrac{1}{(1-e^2)^{3/2}} \\ 0 & 0 & 0 & 0 & 0 & 0 \\ 0 & 0 & 0 & 0 & 0 & 0 \\ 0 & 0 & 0 & 0 & 0 & 0 \end{array}\right] = \left[\begin{array}{c|c} 0_{2\times 2} & 0_{2\times 4} \\ \hline 0_{4\times 2} & \widehat{A}_\psi \end{array}\right], \tag{3.78}$$

with:

$$\widehat{A}_\psi = \begin{bmatrix} 0 & 0 & 0 & (1-e^2)^{-3/2} \\ 0 & 0 & 0 & 0 \\ 0 & 0 & 0 & 0 \\ 0 & 0 & 0 & 0 \end{bmatrix}. \tag{3.79}$$

✍ *REMARK.* Note that this decoupling is strongly reminiscent of the usual decoupling between out-of-plane and in-plane dynamics in linearized Keplerian relative motion equations.

We have therefore taken advantage of these decoupled dynamics to propose the new controller #4.

The hybrid dynamics of Equations (3.26) and (3.20) are written as:

$$\begin{cases} \widehat{\varepsilon}\,' = \widehat{A}\,\widehat{\varepsilon}, & \text{if } \widehat{\eta} \in \mathcal{C}, \\ \widehat{\varepsilon}^{\,+} = \widehat{\varepsilon} + \widehat{B}(\nu)\,\gamma_u\left(\widehat{\varepsilon},\nu\right), & \text{if } \widehat{\eta} \in \mathcal{D}, \end{cases} \tag{3.80}$$

where $\gamma_u\left(\widehat{\varepsilon},\nu\right) = \Delta\widehat{V}$ is the control input that will be designed.

Consider also the related partitions of the state vector $\widehat{\varepsilon}$:

$$\widehat{\varepsilon} = \left[\begin{array}{c} \widehat{\varepsilon}_1 \\ \widehat{\varepsilon}_2 \\ \hline \widehat{\varepsilon}_3 \\ \widehat{\varepsilon}_4 \\ \widehat{\varepsilon}_5 \\ \widehat{\varepsilon}_6 \end{array}\right] = \left[\begin{array}{c} \widehat{\varepsilon}_{1,2} \\ \hline \widehat{\varepsilon}_{3\cdots 6} \end{array}\right], \tag{3.81}$$

with $\widehat{\varepsilon}_{1,2} \in \mathbb{R}^{2\times 1}$; $\widehat{\varepsilon}_{3\cdots 6} \in \mathbb{R}^{4\times 1}$, and the partitions of the control input vector $\Delta\widehat{V}$:

$$\Delta\widehat{V} = \left[\begin{array}{c} \Delta\widehat{v}_a \\ \hline \Delta\widehat{v}_b \\ \hline \Delta\widehat{v}_c \end{array}\right], \tag{3.82}$$

with $\Delta\widehat{v}_a,\ \Delta\widehat{v}_b,\ \Delta\widehat{v}_c \in \mathbb{R}$. Note that the subindices are a, b and c and not x, y and z, as explained in Footnote 2.

According to the decoupling observed in (3.74) and (3.78), and the partitions above, we can compactly write the System (3.80) as:

$$\left[\begin{array}{c} \widehat{\varepsilon}'_{1,2} \\ \hline \widehat{\varepsilon}'_{3\cdots 6} \end{array}\right] = \left[\begin{array}{c|c} 0_{2\times 2} & 0_{2\times 4} \\ \hline 0_{4\times 2} & \widehat{A}_{\psi} \end{array}\right] \left[\begin{array}{c} \widehat{\varepsilon}_{1,2} \\ \hline \widehat{\varepsilon}_{3\cdots 6} \end{array}\right], \tag{3.83}$$

$$\left[\begin{array}{c} \widehat{\varepsilon}^{+}_{1,2} \\ \hline \widehat{\varepsilon}^{+}_{3\cdots 6} \end{array}\right] = \left[\begin{array}{c} \widehat{\varepsilon}_{1,2} \\ \hline \widehat{\varepsilon}_{3\cdots 6} \end{array}\right] + K \left[\begin{array}{c|c|c} 0_{2\times 1} & \widehat{B}_{\alpha}(\nu) & 0_{2\times 1} \\ \hline \widehat{B}_{\beta}(\nu) & 0_{4\times 1} & \widehat{B}_{\theta}(\nu) \end{array}\right] \left[\begin{array}{c} \Delta\widehat{v}_a \\ \hline \Delta\widehat{v}_b \\ \hline \Delta\widehat{v}_c \end{array}\right]. \tag{3.84}$$

From Expressions (3.83) and (3.84), we see that the terms with subindices 1 and 2 are decoupled from the terms with subindices 3 to 6, recasted in the subindex $3\cdots 6$. We can once more re-write the jump equation (3.84) as:

$$\left[\begin{array}{c} \widehat{\varepsilon}^{+}_{1,2} \\ \hline \widehat{\varepsilon}^{+}_{3\cdots 6} \end{array}\right] = \left[\begin{array}{c} \widehat{\varepsilon}_{1,2} \\ \hline \widehat{\varepsilon}_{3\cdots 6} \end{array}\right] + \left[\begin{array}{c|c} \widehat{B}_{1,2}(\nu) & 0_{2\times 2} \\ \hline 0_{4\times 1} & \widehat{B}_{3\cdots 6}(\nu) \end{array}\right] \left[\begin{array}{c} \Delta\widehat{v}_b \\ \hline \Delta\widehat{V}_{ac} \end{array}\right], \tag{3.85}$$

where $\widehat{B}_{1,2}(\nu) = K\widehat{B}_{\alpha}(\nu), \in \mathbb{R}^{2\times 1}$, $\widehat{B}_{3\cdots 6}(\nu) = K\left[\widehat{B}_{\beta}(\nu) \quad \widehat{B}_{\theta}(\nu)\right], \in \mathbb{R}^{4\times 2}$ and $\Delta\widehat{V}_{ac} = \left[\Delta\widehat{v}_a \quad \Delta\widehat{v}_c\right]^T, \in \mathbb{R}^{2\times 1}$. We can express the control input of Expression (3.82) as:

$$\Delta\widehat{V} = \left[\begin{array}{c} \Delta\widehat{v}_b \\ \hline \Delta\widehat{V}_{ac} \end{array}\right]. \tag{3.86}$$

In order to design the control input law $\gamma_u(\widehat{\varepsilon}, \nu) = \Delta\widehat{V}$, we need to define on one hand the term $\Delta\widehat{v}_b$ and on the other hand, the term $\Delta\widehat{V}_{ac}$. Equation (3.85) can be decomposed as:

$$\widehat{\varepsilon}^{+}_{1,2} = \widehat{\varepsilon}_{1,2} + \widehat{B}_{1,2}(\nu)\,\Delta\widehat{v}_b, \tag{3.87a}$$

$$\widehat{\varepsilon}^{+}_{3\cdots 6} = \widehat{\varepsilon}_{3\cdots 6} + \widehat{B}_{3\cdots 6}(\nu)\,\Delta\widehat{V}_{ac}. \tag{3.87b}$$

The design of $\Delta\widehat{V}$ must comply with Requirement 1, meaning that the sixth state after each impulse is zero as defined in Equation (3.13).

Note that the state $\widehat{\varepsilon}_6$ is the last element of the new state $\widehat{\varepsilon}_{3\cdots 6}$, as shown in (3.81). By observing Equations (3.87a) and (3.87b), we see that the control input affecting $\widehat{\varepsilon}_6$ is $\Delta\widehat{V}_{ac}$ and not $\Delta\widehat{v}_b$. Consequently, $\Delta\widehat{v}_b$ can be designed independently from $\Delta\widehat{V}_{ac}$ – hence, from Requirement 1.

Regarding $\Delta\widehat{V}_{ac}$, and proceeding in a similar way to Section 3.5, we decompose the control input affecting the sixth state, $\Delta\widehat{V}_{ac}$, into two terms:

$$\Delta\widehat{V}_{ac} = \Delta\widehat{V}^{\parallel_6}_{ac} + \Delta\widehat{V}^{\perp_6}_{ac}, \tag{3.88}$$

where the term $\Delta\widehat{V}^{\parallel_6}_{ac}$ is in charge of validating Equation (3.13), while the term $\Delta\widehat{V}^{\perp_6}_{ac}$ is designed such that it does not interfere over the action of $\Delta\widehat{V}^{\parallel_6}_{ac}$. In order to avoid interferences, matrices $\Delta\widehat{V}^{\parallel_6}_{ac}$ and $\Delta\widehat{V}^{\perp_6}_{ac}$ must be orthogonal to each other, verifying that their inner product is zero:

$$\Delta\widehat{V}^{\parallel_6}_{ac} \cdot \Delta\widehat{V}^{\perp_6}_{ac} = 0. \tag{3.89}$$

Note also that the control actions $\Delta\widehat{v}_b$ and $\Delta\widehat{V}_{ac}$ are both applied at once, by just taking a look at Expression (3.85). This is the reason why controller #4 has its timer function $\gamma_\tau(\widehat{\varepsilon}, \nu)$ in (3.73) set to a constant value $\bar{\nu}$, as for controller #2 (see Equation (3.57)) and it is not chosen to optimize the cost J contrary to controller #3 (see Equation (3.70)). Since the design of $\Delta\widehat{v}_b$ and $\Delta\widehat{V}_{ac}$ is done separately, it is not likely that their control instant application coincides if their $\bar{\nu}$ values are chosen to minimize the cost. This independency in the design of $\Delta\widehat{v}_b$ and $\Delta\widehat{V}_{ac}$ justifies therefore the choice of a periodic application of the impulses in (3.73), as firstly noticed in Footnote 3.

3.8.1. Design of control input $\Delta\widehat{v}_b$

As stated above, the control input $\Delta\widehat{v}_b$ does not have any influence over state $\widehat{\varepsilon}_6$, meaning that it does not affect the periodicity of the trajectory. This control input is then designed independently by means of the bi-impulsive methodology described in Section 3.6. As a reminder, the bi-impulsive method ensures that the state $\widehat{\varepsilon}_{1,2}$ converges to zero after two impulses noted $\Delta\widehat{v}_{b,\,1}$ and $\Delta\widehat{v}_{b,\,2}$, meaning that the satellite tracks the two corresponding states of the reference periodic trajectory in (3.12).

We will then follow the same steps as for controller #2, starting from an initial state $\widehat{\varepsilon}_{1,2}(\nu_1, j)$ and propagating the hybrid dynamics using Figure 3.8.

Consider an initial state $\widehat{\varepsilon}_{1,2}(\nu_1, j)$, at which the jump set is activated. The first control input $\Delta\widehat{v}_{b,\,1}$ is applied, leading to state $\widehat{\varepsilon}_{1,2}(\nu_1, j+1)$. The satellite then evolves in the flow set, according to the free dynamics until time ν_2 given by the choice $\bar{\nu} = \nu_2 - \nu_1$. At state $\widehat{\varepsilon}_{1,2}(\nu_2, j+1)$, the dynamics trigger again to the jump set and the second control input $\Delta\widehat{v}_{b,\,2}$ is applied, leading to final state $\widehat{\varepsilon}_{1,2}(\nu_2, j+2)$ that must be zero by design to track the reference periodic trajectory in (3.18).

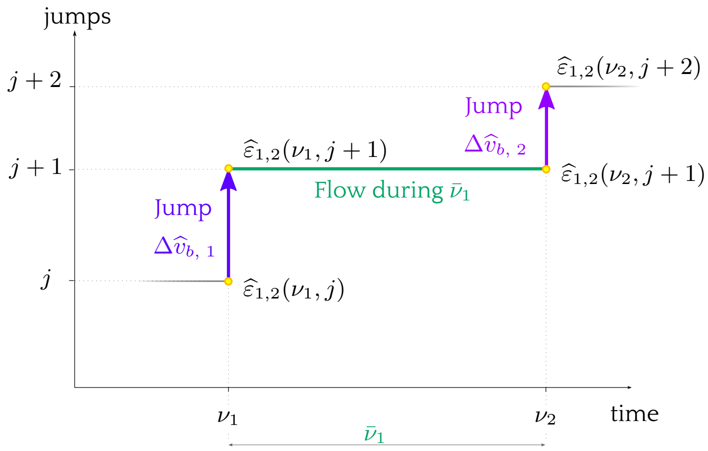

Figure 3.8: Hybrid dynamics for state $\widehat{\varepsilon}_{1,2}$.

It becomes now possible to set the propagation equations by taking into account the previous explanation and the flow and jump equations in Expressions (3.26) and (3.20).

From initial state $\widehat{\varepsilon}_{1,2}(\nu_1, j)$ at time ν_1, we apply the first impulse $\Delta\widehat{v}_{b,\,1}$, such that state $\widehat{\varepsilon}_{1,2}(\nu_1, j+1)$ is expressed as:

$$\widehat{\varepsilon}_{1,2}(\nu_1, j+1) = \widehat{\varepsilon}_{1,2}(\nu_1, j) + \widehat{B}_{1,2}(\nu_1)\, \Delta\widehat{v}_{b,\,1}. \tag{3.90}$$

After impulse $\Delta\widehat{v}_{b,\,1}$ at time ν_1, the solution flows along time $\bar{\nu}$, specified in (3.73). Using Equation (3.90) we have therefore:

$$\begin{aligned} \widehat{\varepsilon}_{1,2}(\nu_2, j+1) &= \widehat{\Phi}_{1,2}(\bar{\nu})\, \widehat{\varepsilon}_{1,2}(\nu_1, j+1) \\ &= \widehat{\Phi}_{1,2}(\bar{\nu})\, [\widehat{\varepsilon}_{1,2}(\nu_1, j) + \widehat{B}_{1,2}(\nu_1)\, \Delta\widehat{v}_{b,\,1}], \end{aligned} \tag{3.91}$$

where:

$$\widehat{\Phi}_{1,2}(\bar{\nu}) = \begin{bmatrix} 1 & 0 \\ 0 & 1 \end{bmatrix} = I_2. \tag{3.92}$$

At time $\nu_2 = \nu_1 + \bar{\nu}$, the second impulse $\Delta\widehat{v}_{b,\,2}$ is applied. Using Expression (3.91), the state $\widehat{\varepsilon}_{1,2}(\nu_2, j+2)$ is expressed as:

$$\begin{aligned} \widehat{\varepsilon}_{1,2}(\nu_2, j+2) &= \widehat{\varepsilon}_{1,2}(\nu_2, j+1) + \widehat{B}_{1,2}(\nu_1 + \bar{\nu})\, \Delta\widehat{v}_{b,\,2} \\ &= \widehat{\varepsilon}_{1,2}(\nu_1, j) + \widehat{B}_{1,2}(\nu_1)\, \Delta\widehat{v}_{b,\,1} + \widehat{B}_{1,2}(\nu_1 + \bar{\nu})\, \Delta\widehat{v}_{b,\,2} \\ &= \widehat{\varepsilon}_{1,2}(\nu_1, j) + \begin{bmatrix} \widehat{B}_{1,2}(\nu_1) & \widehat{B}_{1,2}(\nu_1 + \bar{\nu}) \end{bmatrix} \begin{bmatrix} \Delta\widehat{v}_{b,\,1} \\ \Delta\widehat{v}_{b,\,2} \end{bmatrix}. \end{aligned} \tag{3.93}$$

Denoting:

$$M_{1,2}(\nu_1, \bar{\nu}) =: \begin{bmatrix} \widehat{B}_{1,2}(\nu_1) & \widehat{B}_{1,2}(\nu_1 + \bar{\nu}) \end{bmatrix}, \tag{3.94}$$

and:

$$\widehat{V}^B = \begin{bmatrix} \Delta\widehat{v}_{b,\,1} \\ \Delta\widehat{v}_{b,\,2} \end{bmatrix}, \tag{3.95}$$

we obtain:

$$\widehat{\varepsilon}_{1,2}(\nu_2, j+2) = \widehat{\varepsilon}_{1,2}(\nu_1, j) + M_{1,2}(\nu_1, \bar{\nu})\, \widehat{V}^B. \tag{3.96}$$

Expression (3.96) is simpler than Expression (3.63) in Section 3.6 because $\widehat{\varepsilon}_{1,2}$ remains constant along flowing solutions due to (3.92). The following result then parallels Conjecture 3.6.1 and Lemma 1.

✻ **LEMMA 2:**
Given any value of $\bar{\nu} \neq k\pi,\ k \in \mathbb{Z}$, *matrix* $M_{1,2}(\nu,\bar{\nu})$ *is nonsingular for all* $\nu \in [0, 2\pi]$. *Moreover, for any such value of* $\bar{\nu}$, *selection* (3.73), (3.103) *guarantees that all solutions to* (3.20), (3.22), (3.26), (3.83), (3.85) *have the* $\widehat{\varepsilon}_{1,2}$ *component equal to zero after at most two jumps.*

By design, the desirable property for this second controller is that after the two impulses $\Delta\widehat{v}_{b,\,1}$ and $\Delta\widehat{v}_{b,\,2}$, the satellite tracks the reference periodic trajectory:

$$\widehat{\varepsilon}_{1,2}(\nu_2, j+2) = 0, \tag{3.97}$$

such that:

$$\widehat{V}^B = -M_{1,2}(\nu_1,\bar{\nu})^{-1}\,\widehat{\varepsilon}_{1,2}(\nu_1, j). \tag{3.98}$$

In order to find the necessary controls $\Delta\widehat{v}_{b,\,1}$ and $\Delta\widehat{v}_{b,\,2}$, it becomes necessary to study the invertibility properties of matrix $M_{1,2}(\nu_1,\bar{\nu})$ in (3.94). Its analytical expression is given by:

$$M_{1,2}(\nu_1,\bar{\nu}) = \begin{bmatrix} \dfrac{-\sin\nu_1}{k^2\kappa(\nu_1)} & \dfrac{-\sin(\nu_1+\bar{\nu})}{k^2\kappa(\nu_1+\bar{\nu})} \\ \dfrac{\cos\nu_1}{k^2\kappa(\nu_1)} & \dfrac{\cos(\nu_1+\bar{\nu})}{k^2\kappa(\nu_1+\bar{\nu})} \end{bmatrix}. \tag{3.99}$$

The numerator of the determinant of $M_{1,2}(\nu_1,\bar{\nu})$ will set its invertibility properties, whose expression is:

$$-\sin(\nu_1)\cos(\nu_1+\bar{\nu}) + \sin(\nu_1+\bar{\nu})\cos(\nu_1) = 0, \tag{3.100}$$

or:

$$\sin(\bar{\nu})\cos(2\nu_1) = 0. \tag{3.101}$$

Its graphical representation is given in Figure 3.9. The solutions to equation (3.101) are given below and represented in Figures 3.10 and 3.11.

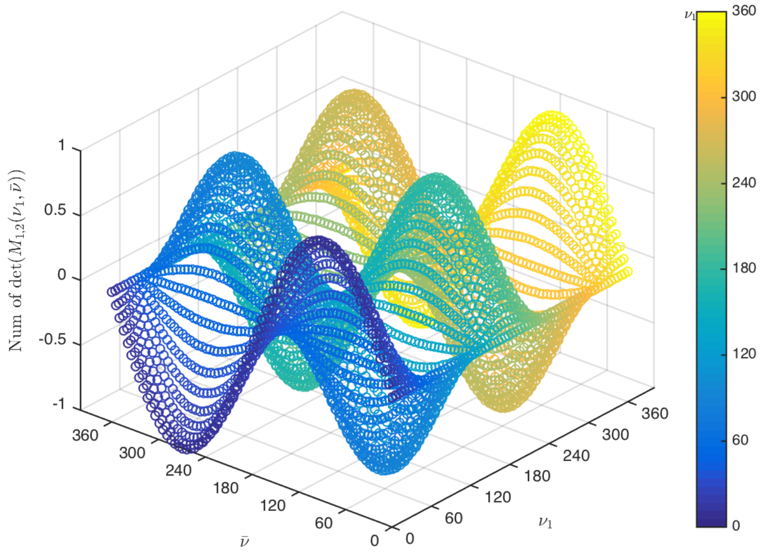

Figure 3.9: Value of Equation (3.101).

$$\begin{aligned} &I. \quad \forall\nu_1,\ \sin(\bar{\nu}) = 0, \quad , \qquad \bar{\nu} = k\pi,\ k \in \mathbb{Z}, \\ &II. \quad \forall\bar{\nu},\ \cos(2\nu_1) = 0 \quad , \quad \nu_1 = \frac{k\pi}{2} - \frac{\pi}{4},\ k \in \mathbb{Z}. \end{aligned} \tag{3.102}$$

These are then the forbidden values that must not be chosen in order to have a solution. From these values above we can determine the values of ν_1 and $\bar{\nu}$ (and therefore setting also ν_2 and ν_3) that makes the determinant zero.

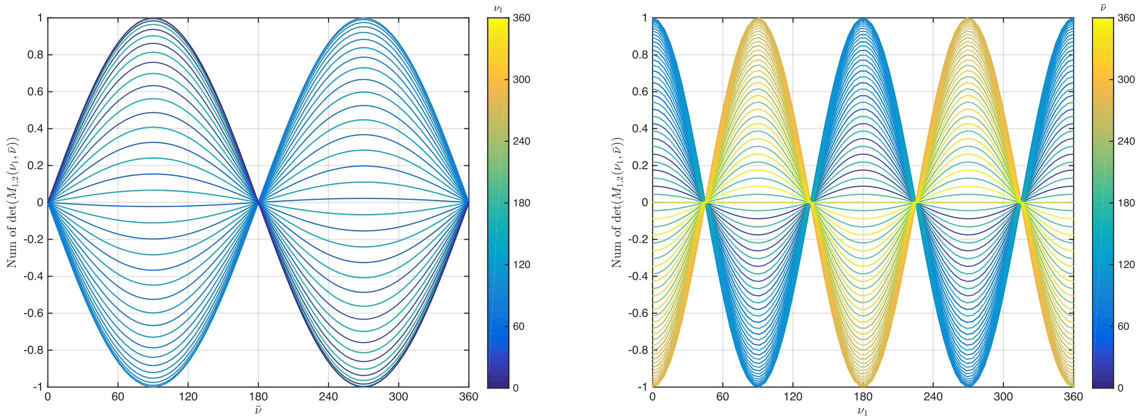

Figure 3.10: Values of Equation (3.101) in 2D.

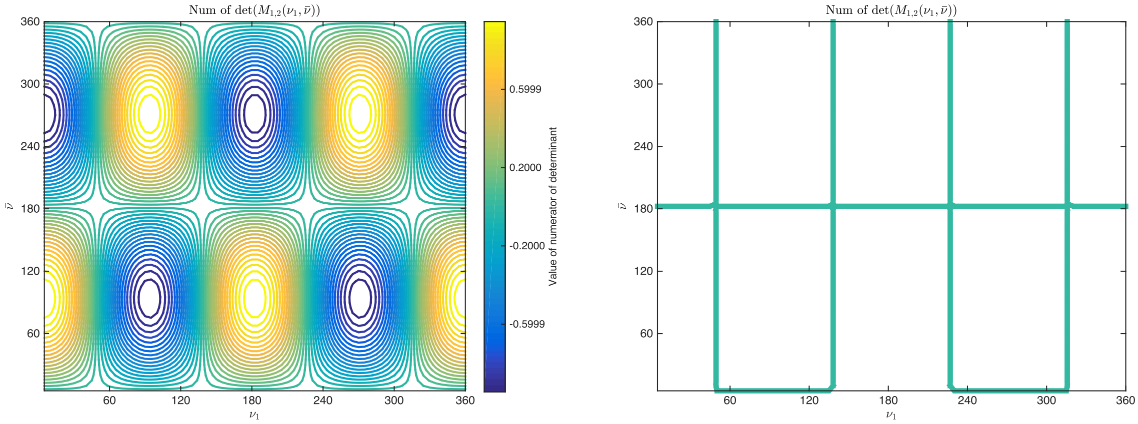

Figure 3.11: Top view of Equation (3.101) and its solutions at zero set level.

There exists a unique solution to Equation (3.98) whenever matrix $M_{1,2}(\nu_1, \bar{\nu})$ is invertible. At each instant j, both controls $\Delta\widehat{v}_{b,\,1}$ and $\Delta\widehat{v}_{b,\,2}$ are computed, but only the first one is actually executed, i.e. $\Delta\widehat{v}_{b,\,1}$. The control function can therefore be set to:

$$\gamma_{u,\,(1,2)}(\widehat{\varepsilon}, \nu) = \Delta\widehat{v}_{b,\,1} = [1 \quad 0]\, \widehat{V}^B = -\,[1 \quad 0]\;\, M_{1,2}(\nu_1, \bar{\nu})^{-1}\, \widehat{\varepsilon}_{1,2}(\nu_1, j). \tag{3.103}$$

3.8.2. Design of control input $\Delta\widehat{V}_{ac}$

The second control input $\Delta\widehat{V}_{ac} \in \mathbb{R}^{2\times 1}$ is designed to comply with Requirement 6, meaning that the sixth state $\widehat{\varepsilon}_6$ equals zero after each impulse. The control input $\Delta\widehat{V}_{ac}$, composed by two terms as shown in Expression (3.88), must therefore be designed such that the sixth state $\widehat{\varepsilon}_6$ verifies Equation (3.13) after each impulse. We can partition state $\widehat{\varepsilon}_{3\dots 6} \in \mathbb{R}^{4\times 1}$ and matrix $\widehat{B}_{3\dots 6}(\nu) \in \mathbb{R}^{4\times 2}$ in Equation (3.87b) to isolate the sixth row where $\widehat{\varepsilon}_6$ is contained:

$$\left[\begin{array}{c}\widehat{\varepsilon}_{3\cdots5}^{+}\\\hline\widehat{\varepsilon}_6^{+}\end{array}\right]=\left[\begin{array}{c}\widehat{\varepsilon}_{3\cdots5}\\\hline\widehat{\varepsilon}_6\end{array}\right]+\left[\begin{array}{c}\widehat{B}_{3\cdots5}(\nu)\\\hline\widehat{B}_6(\nu)\end{array}\right](\Delta\widehat{V}_{ac}^{\parallel_6}+\Delta\widehat{V}_{ac}^{\perp_6}), \tag{3.104}$$

where $\widehat{\varepsilon}_{3\cdots5}\in\mathbb{R}^{3\times1}$, $\widehat{\varepsilon}_6\in\mathbb{R}$, $\widehat{B}_{3\cdots5}(\nu)\in\mathbb{R}^{3\times2}$ and $\widehat{B}_6(\nu)\in\mathbb{R}^{1\times2}$. Equation (3.104) leads to the following system:

$$\widehat{\varepsilon}_{3\cdots5}{}^{+}=\widehat{\varepsilon}_{3\cdots5}+\widehat{B}_{3\cdots5}(\nu)\,\Delta\widehat{V}_{ac}^{\parallel_6}+\widehat{B}_{3\cdots5}(\nu)\,\Delta\widehat{V}_{ac}^{\perp_6}, \tag{3.105a}$$

$$\widehat{\varepsilon}_6{}^{+}=\widehat{\varepsilon}_6+\widehat{B}_6(\nu)\,\Delta\widehat{V}_{ac}^{\parallel_6}+\widehat{B}_6(\nu)\,\Delta\widehat{V}_{ac}^{\perp_6}. \tag{3.105b}$$

Note that by design, the control input $\Delta\widehat{V}_{ac}^{\perp_6}$ is computed such that it has no influence over $\Delta\widehat{V}_{ac}^{\parallel_6}$, hence over $\widehat{\varepsilon}_6$. We set therefore:

$$\widehat{B}_6(\nu)\,\Delta\widehat{V}_{ac}^{\perp_6}=0, \tag{3.106}$$

leading to system:

$$\widehat{\varepsilon}_{3\cdots5}{}^{+}=\widehat{\varepsilon}_{3\cdots5}+\widehat{B}_{3\cdots5}\,\Delta\widehat{V}_{ac}^{\parallel_6}+\widehat{B}_{3\cdots5}\,\Delta\widehat{V}_{ac}^{\perp_6}, \tag{3.107a}$$

$$\widehat{\varepsilon}_6{}^{+}=\widehat{\varepsilon}_6+\widehat{B}_6(\nu)\,\Delta\widehat{V}_{ac}^{\parallel_6}. \tag{3.107b}$$

The design of the input components $\Delta\widehat{V}_{ac}^{\parallel_6}$ and $\Delta\widehat{V}_{ac}^{\perp_6}$ is done in the sequel.

3.8.2.1. Design of the input component $\Delta\widehat{V}_{ac}^{\parallel_6}$

In order to make zero the last state after the impulse, $\widehat{\varepsilon}_6^{+}=0$, the following expression is found directly from Equation (3.107b):

$$0=\widehat{\varepsilon}_6+\widehat{B}_6(\nu)\,\Delta\widehat{V}_{ac}^{\parallel_6}. \tag{3.108}$$

Since matrix $\widehat{B}_6(\nu)\in\mathbb{R}^{1\times2}$ is not square, we use its left pseudo-inverse, denoted $\widehat{B}_6{}^{L}(\nu)\in\mathbb{R}^{2\times1}$, to isolate the control input $\Delta\widehat{V}_{ac}^{\parallel_6}$. The expression for the left pseudo-inverse is:

$$\widehat{B}_6{}^{L}(\nu)=\left(\widehat{B}_6{}^{T}(\nu)\,\widehat{B}_6(\nu)\right)^{-1}\widehat{B}_6{}^{T}(\nu). \tag{3.109}$$

We can now express the analytical expression for the control input $\Delta\widehat{V}_{ac}^{\parallel_6}$ as:

$$\Delta\widehat{V}_{ac}^{\parallel_6}=-\widehat{B}_6{}^{L}(\nu)\,\widehat{\varepsilon}_6. \tag{3.110}$$

3.8.2.2. Design of the input component $\Delta\widehat{V}_{ac}^{\perp_6}$

The control input $\Delta\widehat{V}_{ac}^{\perp_6}$ must not interfere with the action of $\Delta\widehat{V}_{ac}^{\parallel_6}$, meaning that $\Delta\widehat{V}_{ac}^{\perp_6}$ must be orthogonal to the input component $\Delta\widehat{V}_{ac}^{\parallel_6}$, as shown in Expression (3.89). Two steps are required to find $\Delta\widehat{V}_{ac}^{\perp_6}$, that can be expressed as:

$$\Delta\widehat{V}_{ac}^{\perp_6}=\widehat{B}_6{}^{\perp}(\nu)\,\Delta\widehat{v}_{ac}, \tag{3.111}$$

where $\widehat{B}_6{}^{\perp}(\nu)\in\mathbb{R}^{2\times1}$ is the orthogonal complement of $\widehat{B}_6{}^{T}(\nu)$ and $\Delta\widehat{v}_{ac}\in\mathbb{R}$ is the control input to be computed.

The first step generates $\widehat{B}_6{}^{\perp}(\nu)$. From Expressions (3.74) and (3.104) we have:

$$\widehat{B}_6(\nu)=\begin{bmatrix}\dfrac{-3\kappa(\nu)}{k^2(1-e^2)} & \dfrac{3e\sin\nu}{k^2(1-e^2)}\end{bmatrix}. \tag{3.112}$$

The orthogonal complement can be chosen as:

$$\widehat{B}_6^{\perp}(\nu) = \begin{bmatrix} \dfrac{e \sin \nu}{\kappa(\nu)} \\ 1 \end{bmatrix}. \tag{3.113}$$

In the second step, we have to find the expression for the input $\Delta \widehat{v}_{ac}$.

From Expressions (3.88), (3.110) and (3.111), we have that, at each control location, the following equality must be verified:

$$\Delta \widehat{V}_{ac} = -\widehat{B}_6^{L}(\nu)\, \widehat{\varepsilon}_6 + \widehat{B}_6^{\perp}(\nu)\, \Delta \widehat{v}_{ac}. \tag{3.114}$$

By using Expressions (3.110) and (3.111), we can express Equation (3.105a) as:

$$\widehat{\varepsilon}_{3\cdots5}{}^{+} = \widehat{\varepsilon}_{3\cdots5} - \widehat{B}_{3\cdots5}(\nu)\, \widehat{B}_6^{L}(\nu)\, \widehat{\varepsilon}_6 + \widehat{B}_{3\cdots5}\, \widehat{B}_6^{\perp}(\nu)\, \Delta \widehat{v}_{ac}. \tag{3.115}$$

From Expression (3.115), we can see that the control input $\Delta \widehat{v}_{ac}$ has dimensions $[1 \times 1]$, whereas state $\widehat{\varepsilon}_{3\cdots5}$ has dimensions $[3 \times 1]$. In order to track the reference periodic trajectory, the three states that compose $\widehat{\varepsilon}_{3\cdots5}$ must be driven to zero. For this purpose, we will need three control inputs $\Delta \widehat{v}_{ac,\,1}$, $\Delta \widehat{v}_{ac,\,2}$ and $\Delta \widehat{v}_{ac,\,3}$ executed at times (ν_1, j), $(\nu_2, j+1)$ and $(\nu_3, j+2)$ respectively, such that each one leads to zero one of the three states — hence the name of *tri-impulsive* controller. The fact of having to execute the impulses three times means that there are two flow times, given by the parameters $\bar{\nu}_1$ and $\bar{\nu}_2$, as shown in Expression (3.72).

In order to give the analytical expression of these three control inputs, we show how to propagate the initial state $\widehat{\varepsilon}_{3\cdots5}(\nu_1, j)$ along the following sequence, using Figure 3.12 — similar to Section 3.6.

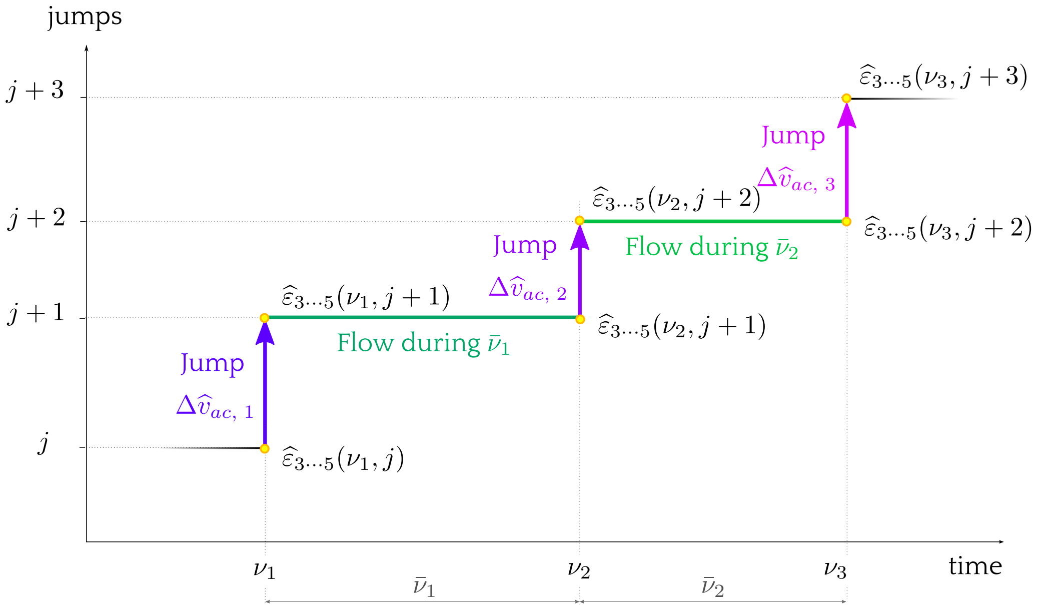

Figure 3.12: Hybrid dynamics for state $\widehat{\varepsilon}_{1,2}$.

Consider an initial state $\widehat{\varepsilon}_{3\cdots5}(\nu_1, j)$, at which the jump set is activated. The first control input $\Delta \widehat{v}_{ac,\,1}$ is applied, leading to state $\widehat{\varepsilon}_{3\cdots5}(\nu_1, j+1)$. The satellite then evolves in the flow set, according to the free dynamics until time ν_2 given by the choice $\bar{\nu}_1 = \nu_2 - \nu_1$. At state $\widehat{\varepsilon}_{3\cdots5}(\nu_2, j+1)$, the dynamics triggers again to the jump set and the second control input $\Delta \widehat{v}_{ac,\,2}$ is applied, leading to state $\widehat{\varepsilon}_{3\cdots5}(\nu_2, j+2)$. The satellite flows once more, and the dynamics trigger to the jump set at ν_3, given by $\bar{\nu}_2 = \nu_3 - \nu_2$, at state $\widehat{\varepsilon}_{3\cdots5}(\nu_3, j+2)$. At this point, the third and last control input $\Delta \widehat{v}_{ac,\,3}$ is applied, leading to final state $\widehat{\varepsilon}_{3\cdots5}(\nu_3, j+3)$, that must be zero to track the reference periodic trajectory in (3.18).

We set now the propagation equations by taking into account the previous explanation and the flow and jump equations in Expressions (3.26) and (3.20).

From initial state $\widehat{\varepsilon}_{3\cdots5}(\nu_1, j)$ at time ν_1, we apply the first impulse $\Delta\widehat{v}_{ac,\,1}$, such that state $\widehat{\varepsilon}_{3\cdots5}(\nu_1, j+1)$ is expressed as:

$$\widehat{\varepsilon}_{3\cdots5}(\nu_1, j+1) = \widehat{\varepsilon}_{3\cdots5}(\nu_1, j) + \widehat{B}_{3\cdots5}(\nu_1)\,[-\widehat{B}_6^{\,L}(\nu_1)\,\widehat{\varepsilon}_6 + \widehat{B}_6^{\,\perp}(\nu_1)\,\Delta\widehat{v}_{ac,\,1}]. \tag{3.116}$$

✍ *REMARK.* In Expression (3.116) the term $-\widehat{B}_6^{\,L}(\nu)\,\widehat{\varepsilon}_6$, which corresponds to the control input $\Delta\widehat{V}_{ac}^{\parallel_6}$, is non-zero only the first time, since it was designed to make $\widehat{\varepsilon}_6 = 0$ in one impulse (c.f. Requirement 1).

✍ *REMARK.* If a satellite moves through a periodic trajectory, then the state transition matrix corresponding to the elapsed time between impulses — flow time — equals the identity matrix of the corresponding dimensions, as shown in Equation (2.83). This means that the states after the flows are the same as the states before the flows: $\widehat{\varepsilon}_{3\cdots5}(\nu_2, j+1) = \widehat{\varepsilon}_{3\cdots5}(\nu_1, j+1)$ and $\widehat{\varepsilon}_{3\cdots5}(\nu_3, j+2) = \widehat{\varepsilon}_{3\cdots5}(\nu_2, j+2)$.

At time $\nu_2 = \nu_1 + \bar{\nu}_1$, the second impulse $\Delta\widehat{v}_{ac,\,2}$ is applied. Using Expression (3.116), the state $\widehat{\varepsilon}_{3\cdots5}(\nu_2, j+2)$ is expressed as:

$$\begin{aligned}\widehat{\varepsilon}_{3\cdots5}(\nu_2, j+2) = \widehat{\varepsilon}_{3\cdots5}(\nu_1, j) - \widehat{B}_{3\cdots5}(\nu_1)\,\widehat{B}_6^{\,L}(\nu_1)\,\widehat{\varepsilon}_6 + \widehat{B}_{3\cdots5}(\nu_1)\,\widehat{B}_6^{\,\perp}(\nu_1)\,\Delta\widehat{v}_{ac,\,1}&\\ +\widehat{B}_6^{\,\perp}(\nu_2)\,\Delta\widehat{v}_{ac,\,2}.&\end{aligned} \tag{3.117}$$

Similarly, at time $\nu_3 = \nu_1 + \bar{\nu}_1 + \bar{\nu}_2$, the third and last impulse $\Delta\widehat{v}_{ac,\,3}$ is applied. Using (3.117), the state $\widehat{\varepsilon}_{3\cdots5}(\nu_3, j+3)$ is:

$$\begin{aligned}\widehat{\varepsilon}_{3\cdots5}(\nu_3, j+3) = \widehat{\varepsilon}_{3\cdots5}(\nu_1, j) - \widehat{B}_{3\cdots5}(\nu_1)\,\widehat{B}_6^{\,L}(\nu_1)\,\widehat{\varepsilon}_6 + \widehat{B}_{3\cdots5}(\nu_1)\,\widehat{B}_6^{\,\perp}(\nu_1)\,\Delta\widehat{v}_{ac,\,1}&\\ +\widehat{B}_{3\cdots5}(\nu_2)\,\widehat{B}_6^{\,\perp}(\nu_2)\,\Delta\widehat{v}_{ac,\,2}&\\ +\widehat{B}_{3\cdots5}(\nu_3)\,\widehat{B}_6^{\,\perp}(\nu_3)\,\Delta\widehat{v}_{ac,\,3}.&\end{aligned} \tag{3.118}$$

The state after the three impulses $\widehat{\varepsilon}_{3\cdots5}(\nu_3, j+3)$ must be zero to satisfy Equation (3.18) and track the reference periodic trajectory, so we get:

$$0 = \widehat{\varepsilon}_{3\cdots5}(\nu_1, j) - \widehat{B}_{3\cdots5}(\nu_1)\,\widehat{B}_6^{\,L}(\nu_1)\,\widehat{\varepsilon}_6 + \begin{bmatrix}\widehat{B}_{3\cdots5}(\nu_1)\,\widehat{B}_6^{\,\perp}(\nu_1) & \widehat{B}_{3\cdots5}(\nu_2)\,\widehat{B}_6^{\,\perp}(\nu_2) & \widehat{B}_{3\cdots5}(\nu_3)\,\widehat{B}_6^{\,\perp}(\nu_3)\end{bmatrix}\begin{bmatrix}\Delta\widehat{v}_{ac,\,1}\\ \Delta\widehat{v}_{ac,\,2}\\ \Delta\widehat{v}_{ac,\,3}\end{bmatrix}. \tag{3.119}$$

Taking:

$$\widehat{\varepsilon}_{3i} =: \widehat{\varepsilon}_{3\cdots5}(\nu_1, j) - \widehat{B}_{3\cdots5}(\nu_1)\,\widehat{B}_6^{\,L}(\nu_1)\,\widehat{\varepsilon}_6, \tag{3.120}$$

and

$$\widehat{B}_i(\nu_i) = \widehat{B}_{3\cdots5}(\nu_i)\,\widehat{B}_6^{\,\perp}(\nu_i), \tag{3.121}$$

with $i = 1, 2, 3$, Expression (3.119) remains:

$$0 = \widehat{\varepsilon}_{3i} + \begin{bmatrix}\widehat{B}_1(\nu_1) & \widehat{B}_2(\nu_2) & \widehat{B}_3(\nu_3)\end{bmatrix}\begin{bmatrix}\Delta\widehat{v}_{ac,\,1}\\ \Delta\widehat{v}_{ac,\,2}\\ \Delta\widehat{v}_{ac,\,3}\end{bmatrix}. \tag{3.122}$$

We finally define matrix $M_{3\cdots5}(\nu_1, \bar{\nu}_1, \bar{\nu}_2) \in \mathbb{R}^{3\times3}$ as:

$$M_{3\cdots5}(\nu_1, \bar{\nu}_1, \bar{\nu}_2) =: \begin{bmatrix}\widehat{B}_1(\nu_1) & \widehat{B}_2(\nu_2) & \widehat{B}_3(\nu_3)\end{bmatrix}, \tag{3.123}$$

and matrix $\widehat{V}^{AC} \in \mathbb{R}^{3\times 1}$ as:

$$\widehat{V}^{AC} = \begin{bmatrix} \Delta\widehat{v}_{ac,\,1} \\ \Delta\widehat{v}_{ac,\,2} \\ \Delta\widehat{v}_{ac,\,3} \end{bmatrix}, \tag{3.124}$$

such that from Equation (3.122), we obtain:

$$0 = \widehat{\varepsilon}_{3i} + M_{3\cdots 5}(\nu_1, \bar{\nu}_1, \bar{\nu}_2)\, \widehat{V}^{AC}. \tag{3.125}$$

In order to retrieve the control vector $\widehat{V}^{AC}$ in Expression (3.125), matrix $M_{3\cdots 5}(\nu_1, \bar{\nu}_1, \bar{\nu}_2)$ must be invertible. Its analytical expression is:

$$M_{3\cdots 5}(\nu_1, \bar{\nu}_1, \bar{\nu}_2) = \begin{bmatrix} \dfrac{2+e\ \cos\nu_1}{k^2\ (1+e\ \cos\nu_1)^2} & \dfrac{2+e\ \cos(\nu_1+\bar{\nu}_1)}{k^2\ (1+e\ \cos(\nu_1+\bar{\nu}_1))^2} & \dfrac{2+e\ \cos(\nu_1+\bar{\nu}_1+\bar{\nu}_2)}{k^2\ (1+e\ \cos(\nu_1+\bar{\nu}_1+\bar{\nu}_2))^2} \\ \dfrac{2e+\cos\nu_1(1+e^2)}{k^2\ (1+e\ \cos\nu_1)^2} & \dfrac{2e+\cos(\nu_1+\bar{\nu}_1)(1+e^2)}{k^2\ (1+e\ \cos(\nu_1+\bar{\nu}_1))^2} & \dfrac{2e+\cos(\nu_1+\bar{\nu}_1+\bar{\nu}_2)(1+e^2)}{k^2\ (1+e\ \cos(\nu_1+\bar{\nu}_1+\bar{\nu}_2))^2} \\ \dfrac{-\sin\nu_1}{k^2\ (1+e\ \cos\nu_1)^2} & \dfrac{-\sin(\nu_1+\bar{\nu}_1)}{k^2\ (1+e\ \cos(\nu_1+\bar{\nu}_1))^2} & \dfrac{-\sin(\nu_1+\bar{\nu}_1+\bar{\nu}_2)}{k^2\ (1+e\ \cos(\nu_1+\bar{\nu}_1+\bar{\nu}_2))^2} \end{bmatrix}. \tag{3.126}$$

The numerator of the determinant of $M_{3\cdots 5}(\nu_1, \bar{\nu}_1, \bar{\nu}_2)$ will set its invertibility properties, since the denominator never turns out to be zero (see Expression (2.35) for parameter k^2). After some calculus, we obtain the expression for the numerator, that equals zero to obtain the values for which matrix $M_{3\cdots 5}(\nu_1, \bar{\nu}_1, \bar{\nu}_2)$ is not invertible:

$$2\sin(\bar{\nu}_1+\bar{\nu}_2) + 2\sin(-\bar{\nu}_1) + 2\sin(-\bar{\nu}_2) = 0. \tag{3.127}$$

From Expression (3.127), we notice that the invertibility properties depend exclusively on $\bar{\nu}_1$ and $\bar{\nu}_2$, and not on ν_1. Developing Equation (3.127), we get:

$$\sin(\bar{\nu}_1)\ \cos(\bar{\nu}_2) + \sin(\bar{\nu}_2)\ \cos(\bar{\nu}_1) - \sin(\bar{\nu}_1) - \sin(\bar{\nu}_2) = 0. \tag{3.128}$$

The following variable change is implemented:

$$\lambda_1 = \tan\left(\frac{\bar{\nu}_1}{2}\right), \qquad \lambda_2 = \tan\left(\frac{\bar{\nu}_2}{2}\right), \tag{3.129}$$

such that:

$$\begin{aligned} \sin(\bar{\nu}_1) &= \frac{2\lambda_1}{1+\lambda_1^2}, & \sin(\bar{\nu}_2) &= \frac{2\lambda_2}{1+\lambda_2^2}, \\ \cos(\bar{\nu}_1) &= \frac{1-\lambda_1^2}{1+\lambda_1^2}, & \cos(\bar{\nu}_2) &= \frac{1-\lambda_2^2}{1+\lambda_2^2}. \end{aligned} \tag{3.130}$$

Expression (3.128) remains therefore:

$$\frac{2\lambda_2}{(1+\lambda_2^2)}\frac{(1-\lambda_1^2)}{(1+\lambda_1^2)} + \frac{2\lambda_1}{(1+\lambda_1^2)}\frac{(1-\lambda_2^2)}{(1+\lambda_2^2)} - \frac{2\lambda_1}{(1+\lambda_1^2)} - \frac{2\lambda_2}{(1+\lambda_2^2)} = 0. \tag{3.131}$$

From (3.131), it comes:

$$\lambda_1\lambda_2\,(\lambda_1+\lambda_2) = 0. \tag{3.132}$$

The solutions to equation (3.132) are:

$$\begin{aligned} &I. && \lambda_1 = 0,\ \forall\lambda_2 && \Leftrightarrow && \bar{\nu}_1 = 2k\pi,\ k\in\mathbb{Z},\ \forall\bar{\nu}_2. \\ &II. && \forall\lambda_1,\ \lambda_2 = 0 && \Leftrightarrow && \forall\bar{\nu}_1,\ \bar{\nu}_2 = 2k\pi,\ k\in\mathbb{Z}. \\ &III. && \lambda_1 = -\lambda_2 && \Leftrightarrow && \bar{\nu}_1+\bar{\nu}_2 = 2k\pi,\ k\in\mathbb{Z}. \end{aligned} \tag{3.133}$$

In Figure 3.13, we find the values for the numerator of determinant of matrix $M_{3\cdots5}(\nu_1, \bar{\nu}_1, \bar{\nu}_2)$ with respect to the values $\bar{\nu}_1$ and $\bar{\nu}_2$.

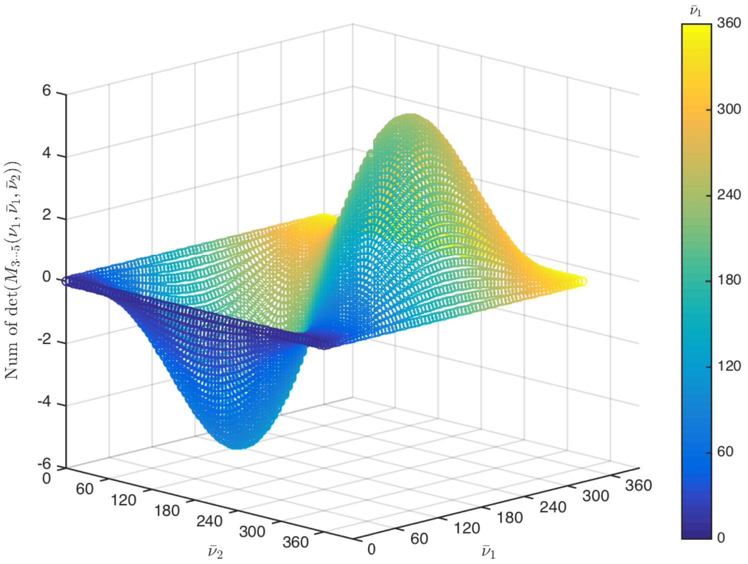

Figure 3.13: Value of Equation (3.132).

In Figures 3.14 and 3.15, we see the solutions to Equation (3.132) and the zero set level, verifying the analytical results in Expression (3.133), items (I), (II) and (III). We can easily observe on the left plot of Figure 3.15 that the determinant $M_{3\cdots5}(\nu_1, \bar{\nu}_1, \bar{\nu}_2)$ is maximized with $\bar{\nu}_1 = \bar{\nu}_2 = 120^o$. Due to this fact and to reduce consumption, we select this value for $\bar{\nu}_1 = \bar{\nu}_2$ in the simulations section.

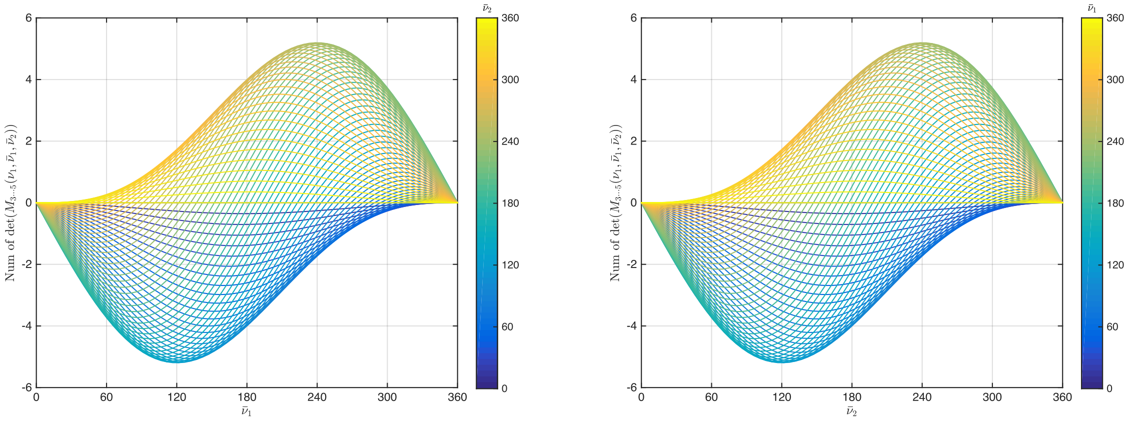

Figure 3.14: Values of Equation (3.132) in 2D.

Recalling that by design two different impulses cannot be applied at the same location, $\bar{\nu}_1 \neq 0$ and $\bar{\nu}_2 \neq 0$, we can uniquely consider solution (III). Therefore, by fixing:

$$\bar{\nu}_1 + \bar{\nu}_2 \neq 2k\pi, \quad k \in \mathbb{Z}, \tag{3.134}$$

we obtain the set of values $(\bar{\nu}_1, \bar{\nu}_2)$ for which matrix $M_{3\cdots5}(\nu_1, \bar{\nu}_1, \bar{\nu}_2)$ is invertible. Whenever this happens, the control vector $\widehat{V}^{AC}$ in (3.125) is found as:

$$\widehat{V}^{AC} = -M_{3\cdots5}(\nu_1, \bar{\nu}_1, \bar{\nu}_2)^{-1}\, \widehat{\varepsilon}_{3i}. \tag{3.135}$$

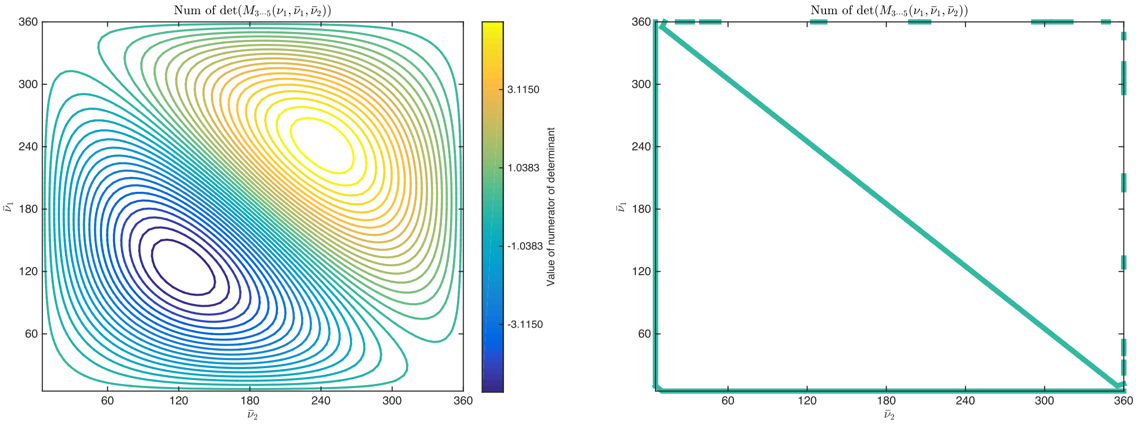

Figure 3.15: Top view of Equation (3.132) and its solutions at zero set level.

Vector $\widehat{V}^{AC}$ contains the three control inputs to apply at three consecutive control instants. At each current instant (ν, j), the three controls are computed, but only the first one is executed. Considering Expression (3.124), the current control $\Delta\widehat{v}_{ac,\,1}$ to be applied can be expressed as:

$$\begin{aligned}\Delta\widehat{v}_{ac,\,1} &= [1\ \ 0\ \ 0]\,\widehat{V}^{AC}\\ &= -[1\ \ 0\ \ 0]\,M_{3\cdots5}(\nu_1,\bar{\nu}_1,\bar{\nu}_2)^{-1}\left[\widehat{\varepsilon}_{3\cdots5}(\nu_1,j)-\widehat{B}_{3\cdots5}(\nu_1)\,\widehat{B}_6^{\,L}(\nu_1)\,\widehat{\varepsilon}_6\right].\end{aligned}\tag{3.136}$$

The previous result then parallels Lemma 2.

✻ **LEMMA 3:**
Given any values of $\bar{\nu}_1$*,* $\bar{\nu}_2$ *such that Expression* (3.133) *holds, matrix* $M_{3\cdots5}(\nu_1,\bar{\nu}_1,\bar{\nu}_2)$ *is nonsingular for all* $\nu\in[0,2\pi]$*. Moreover, selecting any value of* $\bar{\nu}_1=\bar{\nu}_2=\bar{\nu}$*, selection* (3.73), (3.136), (3.83), (3.85) *have the* $\widehat{\varepsilon}_{3\cdots5}$*,* $\widehat{\varepsilon}_6$ *components equal to zero after at most three jumps.*

The fact that with controller (3.73), (3.136) all solutions $\widehat{\varepsilon}_{3\cdots5}$, $\widehat{\varepsilon}_6$ converge to zero in finite time follows similar steps to the proof of Lemma 2 from uniqueness of $\Delta\widehat{v}_{ac,\,1}$ in (3.136).

Coming back to Expression (3.88) and using the results in (3.110), (3.111) — where $\Delta\widehat{v}_{ac}$ is actually $\Delta\widehat{v}_{ac,\,1}$ — and (3.136), we can express the control function $\gamma_{u,\,(3\cdots6)}(\widehat{\varepsilon},\nu)$ as:

$$\gamma_{u,\,(3\cdots6)}(\widehat{\varepsilon},\nu)=\Delta\widehat{V}_{ac}=-\widehat{B}_6^{\,L}(\nu_1)\,\widehat{\varepsilon}_6-\widehat{B}_6^{\,\perp}(\nu_1)\ [1\ \ 0\ \ 0]\ M_{3\cdots5}(\nu_1,\bar{\nu}_1,\bar{\nu}_2)^{-1}\left[\widehat{\varepsilon}_{3\cdots5}-\widehat{B}_{3\cdots5}(\nu_1)\,\widehat{B}_6^{\,L}(\nu_1)\,\widehat{\varepsilon}_6\right].\tag{3.137}$$

After some calculus, $\gamma_{u,\,(3\cdots6)}(\widehat{\varepsilon},\nu)$ can be reformulated such that:

$$\begin{aligned}\gamma_{u,\,(3\cdots6)}(\widehat{\varepsilon},\nu)=&\Delta\widehat{V}_{ac}=\\ &=\Big[\widehat{B}_6^{\,\perp}(\nu_1)\ [1\ \ 0_{1\times2}]\ M_{3\cdots5}(\nu_1,\bar{\nu}_1,\bar{\nu}_2)^{-1}\left[\widehat{B}_{3\cdots5}(\nu_1)\,\widehat{B}_6^{\,L}(\nu_1)\,[0_{1\times3}\ \ 1]\,I_4-[I_3\ \ 0_{3\times1}]\,I_4\right]\\ &\quad-\widehat{B}_6^{\,L}(\nu_1)\,[0_{1\times3}\ \ 1]\,I_4\Big]\ \widehat{\varepsilon}_{3\cdots6}.\end{aligned}\tag{3.138}$$

From Expressions (3.86), (3.103) and (3.138), the control function $\gamma_u\,(\widehat{\varepsilon},\nu)$ can be expressed as a function of $\gamma_{u,\,(1,2)}(\widehat{\varepsilon},\nu)$ and $\gamma_{u,\,(3\cdots 6)}(\widehat{\varepsilon},\nu)$:

$$\begin{aligned}\gamma_u\,(\widehat{\varepsilon},\nu) = \Delta\widehat{V} = \Big(& -[1\ \ 0]\ M_{1,2}(\nu_1,\bar{\nu})^{-1}\ [I_2\ \ 0_{2\times 4}] \\ & + \Big[\widehat{B}_6^{\perp}(\nu_1)\ [1\ \ 0_{1\times 2}]\ M_{3\cdots 5}(\nu_1,\bar{\nu}_1,\bar{\nu}_2)^{-1}\ \Big[\widehat{B}_{3\cdots 5}(\nu_1)\ \widehat{B}_6^{\,L}(\nu_1)\ [0_{1\times 3}\ \ 1]\ I_4 - [I_3\ \ 0_{3\times 1}]\ I_4\Big] \\ & - \widehat{B}_6^{\,L}(\nu_1)\ [0_{1\times 3}\ \ 1]\ I_4\Big]\ \ [0_{4\times 2}\ \ I_4]\Big)\widehat{\varepsilon}. \end{aligned} \tag{3.139}$$

3.8.3. Synthesis of control inputs

In order to clarify the different control inputs in Subsections 3.8.1 and 3.8.2 and their application instant, we have gathered their information in Figure 3.16.

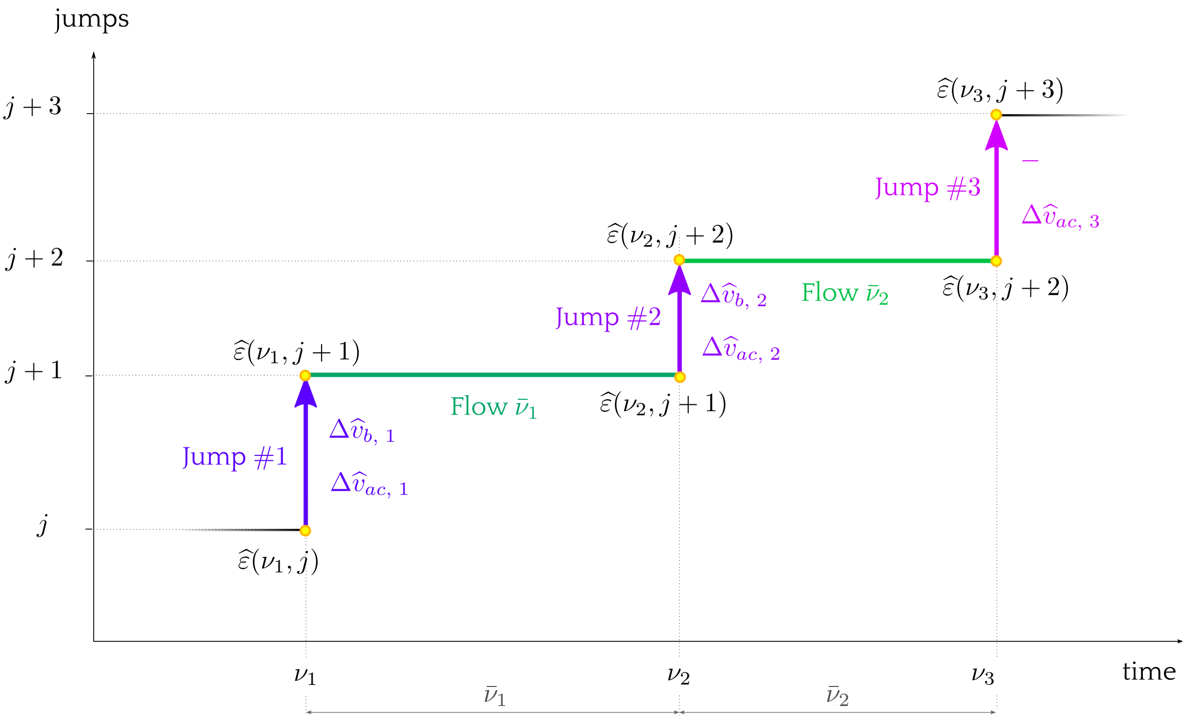

Figure 3.16: Hybrid dynamics for the full state $\widehat{\varepsilon}$.

3.8.4. Stability proof.

The following result can be established by similar derivations to those in the proof of Theorem 2, relying on the uniform finite-time convergence established in Lemmas 2 and 3. Its proof is omitted due to this similarity to that of Theorem 2.

THEOREM 4. *Control law* (3.73), (3.139) *ensures that attractor* $\mathcal{A}$ *in* (3.54) *is uniformly globally asymptotically stable along the arising closed-loop dynamics with* (3.20), (3.22), (3.26).

3.9. Simulations

In this section, we present the simulation results obtained with the four control laws designed in Sections 3.5, 3.6, 3.7 and 3.8.

The simulations are done with a nonlinear simulator and their results are then compared to the ones obtained using a linearized simulator, in the context of the PRISMA mission. The differences between the two simulation set-ups are given in detail below.

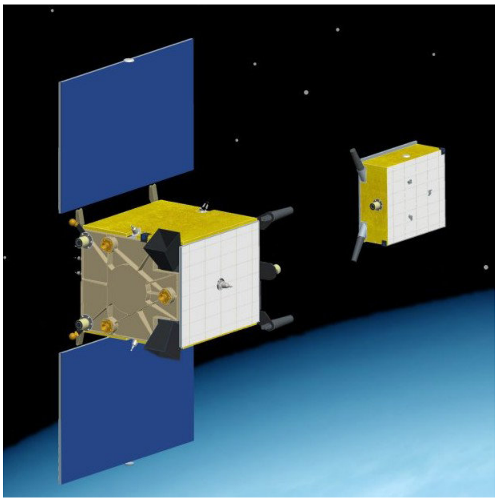

Figure 3.17: *Tango* (left) and *Mango* (right) satellites composing the PRISMA mission. Photo courtesy of ESA [63].

3.9.1. The PRISMA program

PRISMA was a technology demonstration mission for the in-flight validation of sensor technologies and guidance/navigation strategies for SFF and rendezvous. PRISMA was originating from an initiative of the Swedish National Space Board (SNSB) and the Swedish Space Corporation (SSC) and has provided a precursor mission for critical technologies related to advanced formation flying and In-Orbit-Servicing [94].

The two satellites of the PRISMA mission, named Mango and Tango, were launched on 15 June 2010 from Yasny launch base in Russia. The mission had an initial lifetime of 10 months but was finally extended until the end of 2014. More details can be obtained from the CNES website [26].

3.9.1.1. Mission overview and objectives

The mission objectives of PRISMA [117] may be divided into:

- validation of sensor and actuator technologies, which supports and enables the demonstration of autonomous formation flying, homing and rendezvous scenarios, as well as close range proximity operations;
- demonstration of experiments for formation flying and rendezvous, which comprise the testing of new power control systems and the demonstration of autonomous orbit keeping of a single spacecraft.

3.9.1.2. PRISMA data

The PRISMA test bed comprised two satellites as shown in Figure 3.17: the fully maneuverable main satellite nicknamed *Tango*, as well as the smaller satellite, nicknamed *Mango*, both built by SSC. For this simulations section, we will refer to *Mango* satellite as the target, and to *Tango* satellite as the chaser.

The orbital parameters[4] corresponding to the PRISMA mission have been specified in Table 3.1.

Orbit data	**Value**
Semi-major axis	$a = 7011$ km
Eccentricity	$e = 0.004$
Inclination	$i = 98$ deg
RAAN	$\Omega = 190$ deg
Argument of perigee	$\omega = 0$ deg
True anomaly	$\nu = 180$ deg

Table 3.1: Orbit data for the PRISMA mission.

Other PRISMA information corresponding to each satellite and the atmospheric conditions is collected in Table 3.2. Notice that the maximum and minimum thrust are only given for the chaser — Tango — satellite, since we consider a non-actuated target spacecraft as explicited in Assumption 1.

Satellites parameters	**Value for target (*Mango*)**	**Value for chaser (*Tango*)**
Mass	$m_t = 40$ kg	$m_c = 140$ kg
Reference surface for atmospheric drag	$S_t = 0.5$ m^2	$S_c = 0.2$ m^2
Drag coefficient	$C_{D,\,t} = 2.3$	$C_{D,\,c} = 2.3$
Reference surface for solar radiation pressure	$A_t = 0.5$ m^2	$A_c = 0.2$ m^2
Reflection coefficient	$\gamma_t = 1$	$\gamma_c = 1$
Maximum thrust	-	$\Delta v_{max} = 0.5$ m/s
Minimum thrust	-	$\Delta v_{min} = 5\ 10^{-4}$ m/s

Table 3.2: Satellites parameters for the PRISMA mission.

3.9.2. Description of the simulators

In this section, we present the simulation results obtained using a nonlinear simulator and comparing the results with a linearized model using the software *Matlab©-Simulink©* for a given orbital ren-

---

[4] The description of the orbital parameters is fully developed in Appendix A.

dezvous scenario within the PRISMA mission.

3.9.2.1. Block diagram

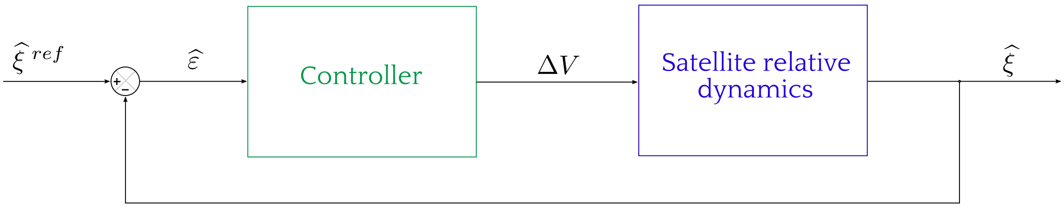

Figure 3.18: Block diagram for the PRISMA mission.

The block diagram of both the linear and nonlinear simulators within *Simulink©* is synthetized in Figure 3.18. In both cases, the simulator is composed by two main blocks: the controller and the dynamics.

- Controller: the controller recovers the current state in the transformed *hat* coordinates and performs the mismatch defined in Expression (3.18). Afterwards, the control input $\Delta\widehat{V}$ is computed according to the different control strategies defined in Sections 3.5, 3.6, 3.7 or 3.8. The control input is then transformed back to the original ΔV values defined in the LVLH reference frame, which might be limited by saturation and dead zone constraints.

- Satellite relative dynamics: the dynamics block is composed by the chaser's and target's relative dynamics, which will be either linear or nonlinear depending on the simulation. This block gets the control input ΔV delivered by the controller, which is applied to the chaser satellite, since the target is a non-actuated spacecraft. This block delivers the current state $\widehat{\xi}$ in order to perform the feedback control.

  All the data coming from the transformed state $\widehat{\xi}$ is then transformed back to their original relative position and velocity coordinates $X(\nu)$ in the LVLH reference frame by means of the transformation $R^{-1}(\nu)$ defined in Expression (2.161) and stored in *Matlab©* for later processing.

3.9.2.2. Running linear and nonlinear simulations

Both the linear and nonlinear simulators have the same process, described in the sequel. The chaser satellite begins the rendezvous maneuver when the target's initial true anomaly equals ν_0. At this instant, the chaser's corresponding initial state in LVLH coordinates is X_0.

This state X_0 is then transformed into its *hat* equivalent via the $R(\nu)$ transformation given in Expression (2.159). The transformed initial state is denoted by $\widehat{\xi}_0$ for state $\widehat{\xi}$ in (3.6), and the simulator is initialized at this initial state.

The objective of the rendezvous is to stabilize the chaser satellite in a periodic trajectory specified by a suitable selection of $\widehat{\xi}^{ref}$ in (3.12). The reference periodic trajectory is free to evolve inside a tolerance box $\mathcal{B}$, centered at point $X_{\mathcal{B}}$ (expressed in the target's LVLH reference frame), and has positive and negative widths $X_{tol} = [x_{tol} \quad y_{tol} \quad z_{tol}]^T$ in the three LVLH directions, as shown in Figure 3.19.

During the simulation, the different control maneuvers are separated by an angular distance given by the timer function $\gamma_\tau\left(\widehat{\varepsilon}, \nu\right) = \bar{\nu}$, characteristic to each controller.

Finally, the simulation stops when the simulation length is met, which happens at the final true anomaly $\nu_f = \nu_0 + 20\pi$, namely ten orbital periods later.

Table 3.3 synthetizes the simulator information concerning the rendezvous length and the reference periodic trajectory data.

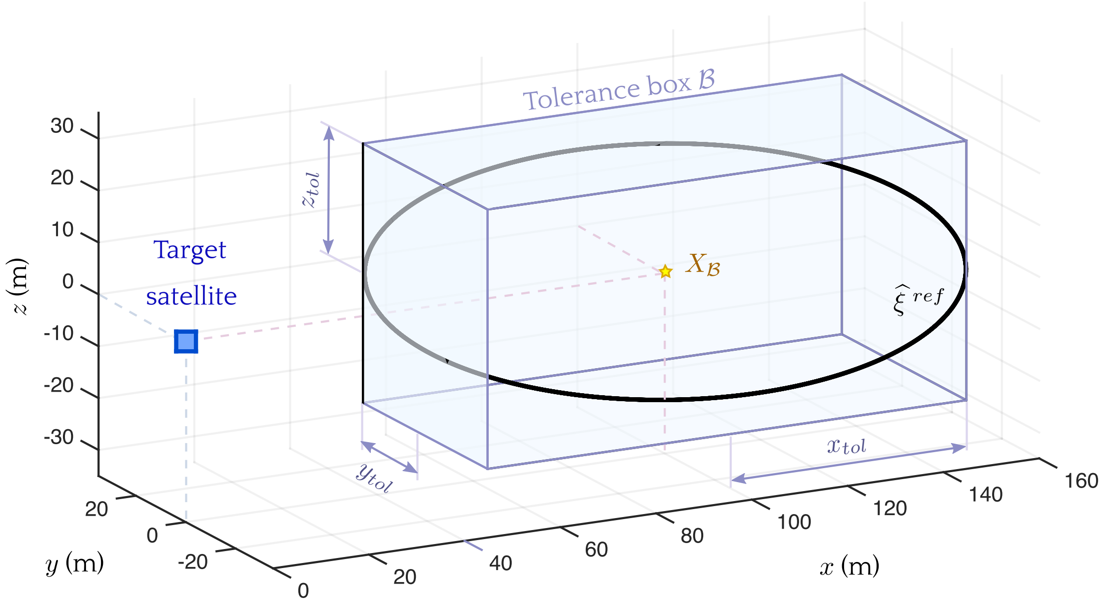

Figure 3.19: Reference periodic trajectory $\widehat{\xi}^{ref}$ contained inside the tolerance box $\mathcal{B}$.

Other data	**Value**
Center of tolerance box $\mathcal{B}$ (m)	$X_{\mathcal{B}} = [100\ 0\ 0]^T$
Widths tolerance box $\mathcal{B}$ (m)	$X_{tol} = [50\ 25\ 25]^T$
Reference trajectory	$\widehat{\xi}^{ref} = [15.18\ \ 17.68\ \ 97.98\ \ 22.49\ \ -17.63\ \ 0]^T$
Simulation length (rad)	$\nu_f = \nu_0 + 10 * 2\pi$

Table 3.3: Data concerning the reference periodic trajectory and simulation length.

For each one of the four controllers defined in Sections 3.5, 3.6, 3.7 and 3.8, three different initial conditions X_{0i}, $i = 1, \cdots, 3$ have been used, which are chosen at three different distances from the target satellite located at the origin of the LVLH frame, and which are summarized in Table 3.4.

Initial state	**Distance to target (m)**	**Position (m)**			**Velocity (m/s)**		
		x	y	z	$\dot{x}$	$\dot{y}$	$\dot{z}$
X_{01}	$\approx$ 500	300	-350	200	0	0	0
X_{02}	$\approx$ 2000	-1500	1300	150	0	0	0
X_{03}	$\approx$ 3500	-1300	3200	50	0	0	0

Table 3.4: Values of the initial states X_{0i}, $i = 1, \cdots, 3$.

The initial relative velocity for every initial state X_{0i} has been selected to be zero to account for the fact that the starting point of the rendezvous may be a holding point arising from a previous station keeping along the space mission.

After several simulations, we found that the furthest initial position for which the nonlinear simulations converge, taking into account the perturbations data given in Table 3.5, is located at around 5 km from the target.

3.9.2.3. Linear and nonlinear simulators

The linear simulator propagates the linearized relative motion equations under the Keplerian assumptions given in 2, meaning that no perturbations are considered (neither environment disturbances nor actuation or sensing uncertainties).

The nonlinear simulator models the relative dynamics by means of non-classical Gauss planetary equations using equinoctial orbital elements to avoid singularities for low eccentricity e and inclination i values. The Gauss equations of motion are integrated and propagated taking into account three types of disturbances: J_2 effect due to the Earth's oblateness, atmospheric drag and high solar activity.

Moreover, uncertainties that originate from GNC devices are also simulated, and are composed of:

- **position and velocity measurement noise:** the measured relative state is affected by a white noise characterised by a standard deviation on the relative position and velocity denoted by d_p and d_v respectively, as shown in Table 3.5;
- **chemical thrusters limitations:** the applied control $\Delta V = [\Delta v_x \quad \Delta v_y \quad \Delta v_z]^T$ is obtained once the computed control undergoes eventual saturations and dead zone filters along each axis independently. For $i = x, y, z$, we have the impulse on each axis:

$$\Delta v_i = \begin{cases} -\Delta v_{max} & \text{if} \quad \Delta v_i \in (-\infty \quad -\Delta v_{max}), \\ -\Delta v_i & \text{if} \quad \Delta v_i \in [-\Delta v_{max} \quad -\Delta v_{min}], \\ 0 & \text{if} \quad \Delta v_i \in (-\Delta v_{min} \quad \Delta v_{min}), \\ \Delta v_i & \text{if} \quad \Delta v_i \in [\Delta v_{min} \quad \Delta v_{max}], \\ \Delta v_{max} & \text{if} \quad \Delta v_i \in (\Delta v_{max} \quad \infty). \end{cases} \tag{3.140}$$

The nonlinear simulator details can be found in reference [49].

Table 3.5 synthetizes the disturbances acting over the nonlinear simulator and their associated values for the PRISMA mission.

3.9.2.4. Performance indices

Along the simulations, two performance indices are considered in order to measure the quality of the controllers:

- **Fuel consumption** J**:** this performance index has been fully developed in Appendix F. The cost function associated to the PRISMA mission is best chosen when the configuration is set to six identical ungimbaled thrusters rigidly mounted on the chaser body axes, therefore J will be chosen as for Expression (F.5), recalled hereafter:

$$J = \sum_{k=1}^{N} ||\Delta \vec{V}_k||_1 = \sum_{k=1}^{N} \left(|\Delta v_{x\ k}| + |\Delta v_{y\ k}| + |\Delta v_{z\ k}| \right), \tag{3.141}$$

  where N represents the number of maneuvers.

Active perturbations	
$J2$	✓
Atmospheric drag	✓
High solar activity	✓
Active constraints	**Value**
Saturation Δv_{max}	0.5 m/s
Dead zone Δv_{min}	$0.5 \cdot 10^{-3}$ m/s
Noise over the nonlinear simulations	**Value**
Position d_p	$1 \cdot 10^{-2}$ m
Velocity d_v	$1 \cdot 10^{-5}$ m/s

Table 3.5: Disturbances over the nonlinear simulations.

- **Convergence time** T_c: we define the convergence time as the elapsed time until the chaser satellite remains in the δ vicinity of the periodic reference trajectory $\widehat{\xi}^{\,ref}$, such as:

$$\frac{\|\widehat{\xi} - \widehat{\xi}^{\,ref}\|}{\|\widehat{\xi}_{0i} - \widehat{\xi}^{\,ref}\|} \leq \delta, \tag{3.142}$$

  where δ is set to 5%.

3.9.3. Algorithm

The corresponding pseudo-algorithm tdescribing the simulator functioning detailed in Subsection 3.9.2.2 can be synthetized as follows:

```
Data: chaser and target information;
Data: scenario information: orbital parameters;
                            rendezvous length;
                            active disturbances;
                            reference periodic trajectory;
Initialization: initial state $X_0$ and target true anomaly $\nu_0$ ;
while rendezvous length do
    if timer function $\gamma_\tau\,(\widehat{\varepsilon}, \nu)$ is activated then
        compute: control input law $\gamma_u\,(\widehat{\varepsilon}, \nu)$;
        apply: jump equation for the obtained thrust $\Delta\widehat{V}$ ;
    else
        apply: flow equation for propagating the free dynamics;
    end
end
```

3.9.4. Results

Different simulations have been performed for each control law defined in Sections 3.5, 3.6, 3.7 and 3.8, and each initial condition specified in Table 3.4. In the following figures, we present the results through different graphs, concerning both the linear and nonlinear simulations:

- **Trajectories:** the chaser trajectories to approach the tolerance box close to the target, in the LVLH reference frame are drawn.
- **Executed thrusts:** at each thrust location, we compute the *1-norm* as specified in the cost function Equation in (F.5).
- **Convergence/error profile and convergence time:** the last graph concerns the error profile, or the convergence of the state towards the reference periodic trajectory, as well as the time T_c set in (3.142) where the chaser has arrived at the δ vicinity (set to 5%) of the reference trajectory.

3.9.4.1. Results for initial condition X_{01}

Figure 3.20 reveals how the four different studied control strategies steer the chaser to the tolerance box along different approaches, for initial condition X_{01}. Guidance laws 3.6 and 3.7 have more "straight" approaches towards the tolerance box. On the other hand, controllers 3.5 and mainly 3.8 do have less direct approaches in terms of travelled distance. However, this fact does not penalize the cost, as it will be shown later.

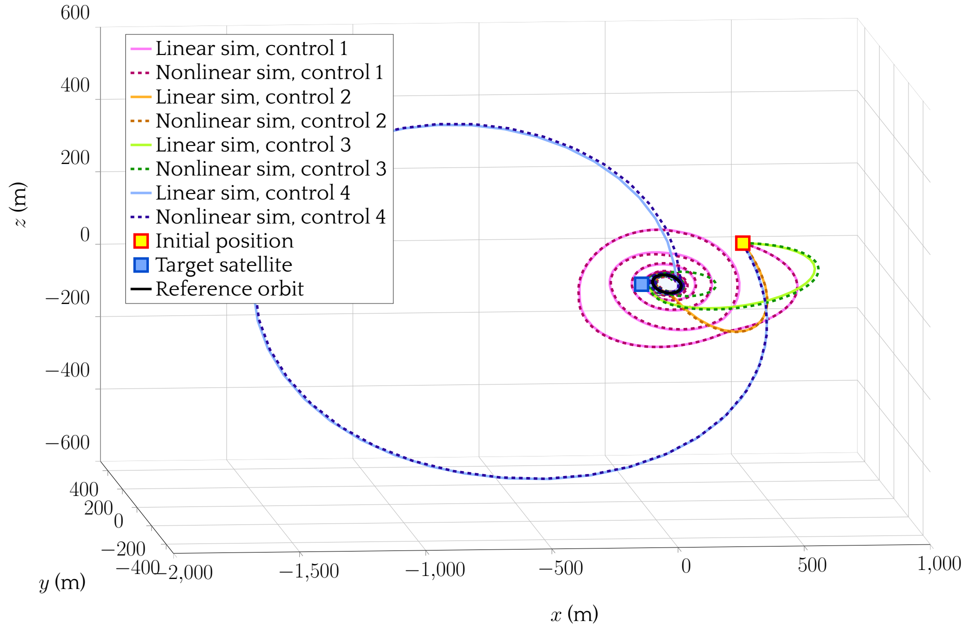

Figure 3.20: Comparison of the trajectories for each controller and initial condition X_{01}.

From Figure 3.20, we can validate the linear simulator, showing good approximations of the real dynamics modeled by the nonlinear simulator for every numerical experience.

From Figures 3.21 to 3.24, we represent the simulations corresponding to initial condition X_{01}, where the trajectory is exactly the same as represented in Figure 3.20 from another view point.

The impulsive control plan appearing in the upper graph of Figure 3.21b — corresponding to controller 3.5 — show that the seven first controls have a relative importance; while the control plans for Figures 3.22b, 3.23b and 3.24b — corresponding to controllers 3.6, 3.7 and 3.8 — concentrate most of their consumption on the very first control thrusts.

The differences between the control strategies can also be observed on the evolution of the errors norm. Guidance law #1 in Section 3.5 shows in the lower graph of Figure 3.21b a slower convergence, therefore a relatively higher convergence time $T_c \approx 2.3$ orbits. On the other hand, in Figures 3.22b, 3.23b and 3.24b we see that the convergence time is smaller, achieved just after the main control impulses.

For these different close-range control maneuvers of Figures 3.21 to 3.24, the differences between the linear and nonlinear simulations are slight: the consumption and the convergence time are similar. However, the trajectories have small differences that can be imputed to the dynamics linearisation process.

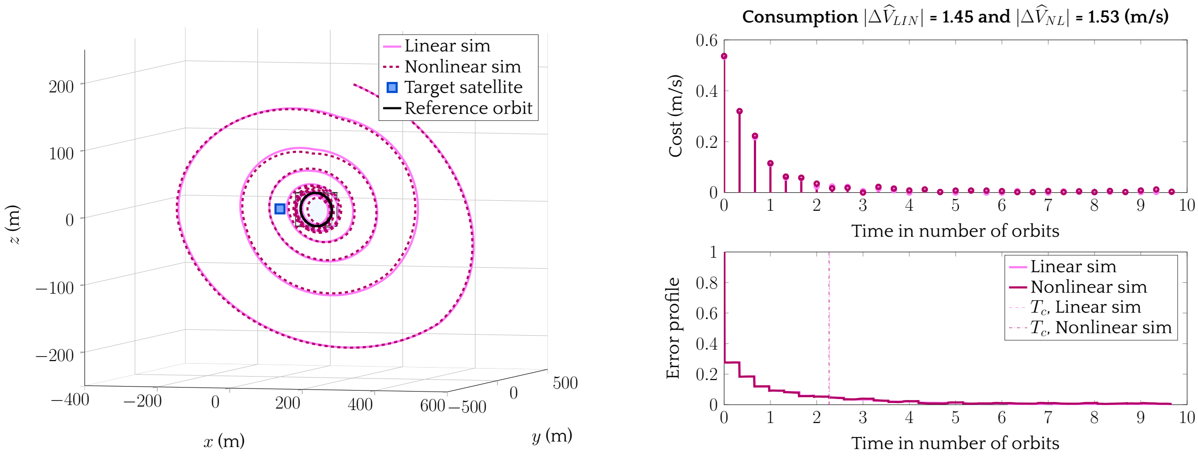

(a) Trajectory.
(b) Impulses and error profile.

Figure 3.21: Periodic norm-minimizing controller of Section 3.5 for X_{01}.

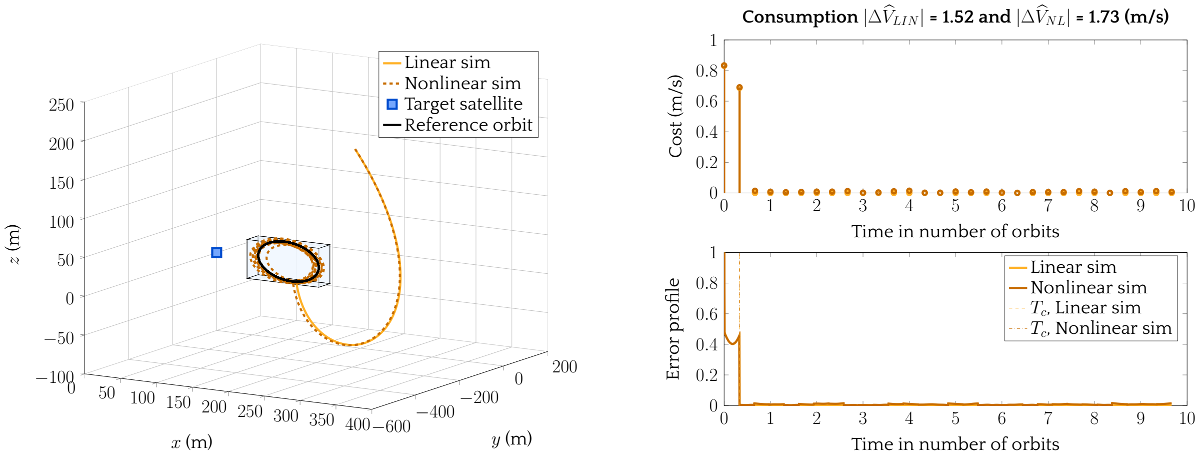

(a) Trajectory.
(b) Impulses and error profile.

Figure 3.22: Bi-impulsive controller of Section 3.6 for X_{01}.

In Figure 3.23b we can notice that the control impulses for the linear and nonlinear simulations are not located at the same point. This is due to the fact that controller 3.7 optimizes the cost, meaning that the thrust is applied at the location where the cost is minimum. Due to the differences between the linear and nonlinear simulators, it is consistent that the computed thrust location does not coincide.

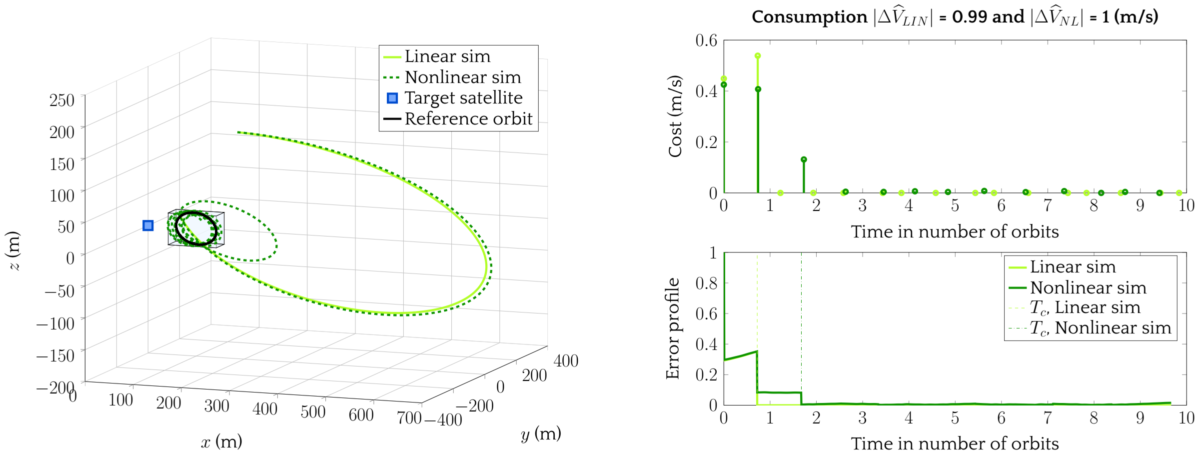

(a) Trajectory.

(b) Impulses and error profile.

Figure 3.23: Non-periodic bi-impulsive controller of Section 3.7 for X_{01}.

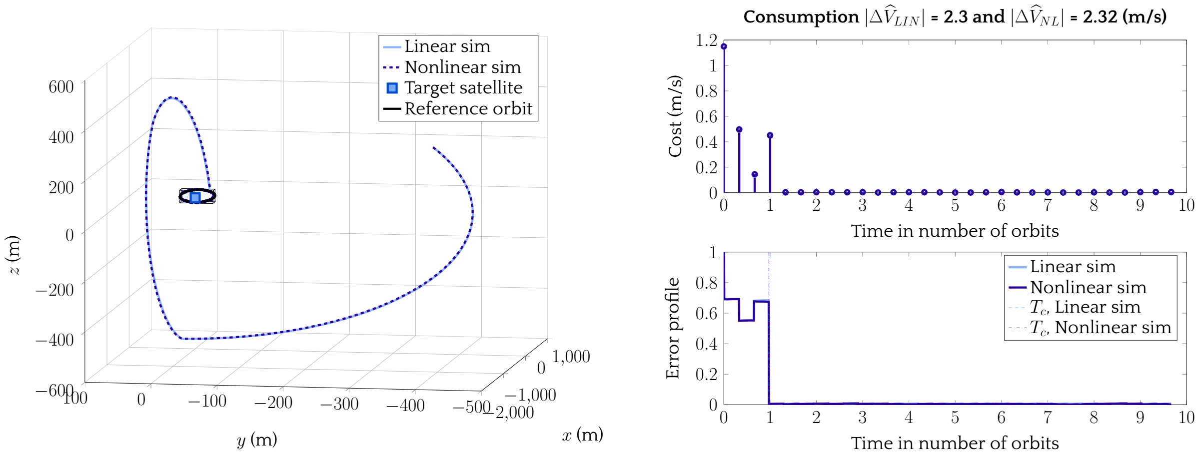

(a) Trajectory.

(b) Impulses and error profile.

Figure 3.24: Tri-impulsive controller of Section 3.8 for X_{01}.

3.9.4.2. Results for initial condition X_{02}

Figures 3.25 to 3.29 represent the simulations corresponding to initial condition X_{02}. The conclusions that can be drawn from these results are similar to their counterparts for X_{01}.

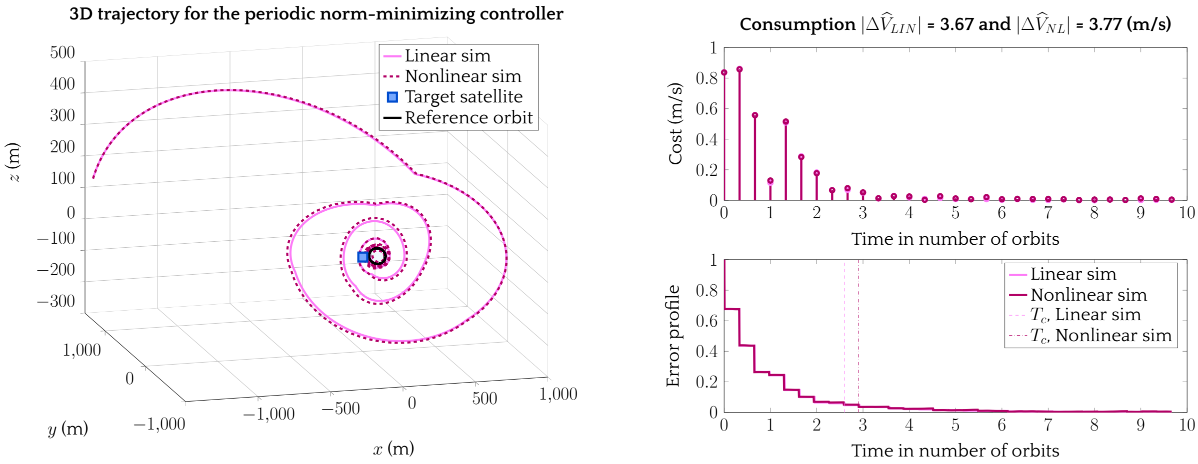

(a) Trajectory.

(b) Impulses and error profile.

Figure 3.25: Periodic norm-minimizing controller of Section 3.5 for X_{02}.

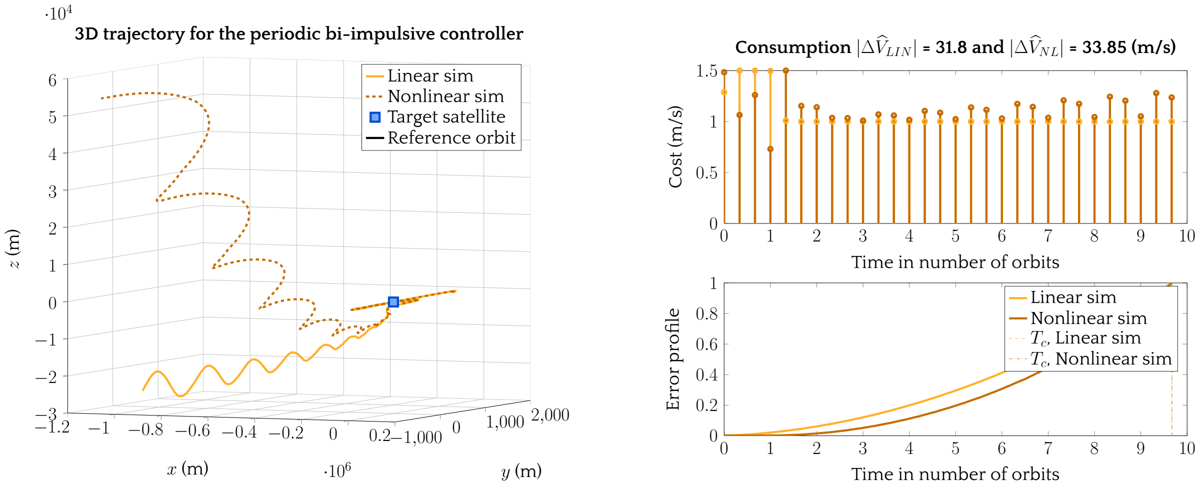

(a) Trajectory.

(b) Impulses and error profile.

Figure 3.26: Bi-impulsive controller of Section 3.6 for X_{02}.

However for this initial condition X_{02}, controller 3.6 diverges, as shown in Figure 3.26. This is due to the thrusters saturation constraints. The same simulations have been performed for a new value of the saturation, set to $\Delta v_{max} = 0.6$ m/s (instead of the previous $\Delta v_{max} = 0.5$ m/s), and whose results are represented in Figure 3.27. The conclusions that can be extracted from Graph 3.27 is that no control plan exists that leads to the reference periodic trajectory in two impulses when the thrust saturation constraints are tight.

We observe an interesting phenomena appearing in Figure 3.27b. If we take a look at the error profile, we can see that between two impulses, the slope of the curve decreases step by step. From numerical simulations, we observed that this is a marker of convergence towards the reference periodic trajectory.

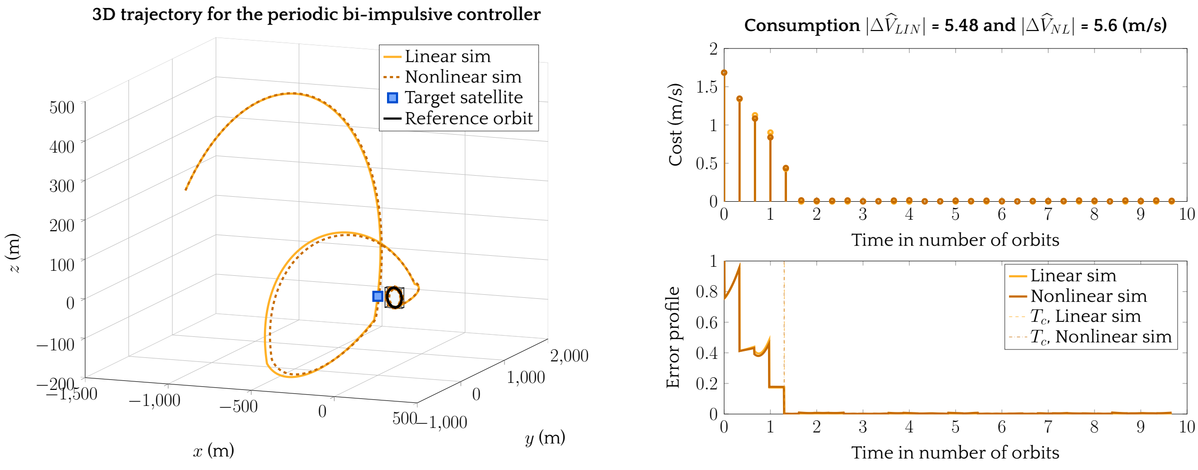

3D trajectory for the periodic bi-impulsive controller

Consumption $|\Delta\widehat{V}_{LIN}|$ = 5.48 and $|\Delta\widehat{V}_{NL}|$ = 5.6 (m/s)

(a) Trajectory.

(b) Impulses and error profile.

Figure 3.27: Bi-impulsive controller of Section 3.6 for X_{02}. Saturation set to $\Delta v_{max} = 0.6$ m/s.

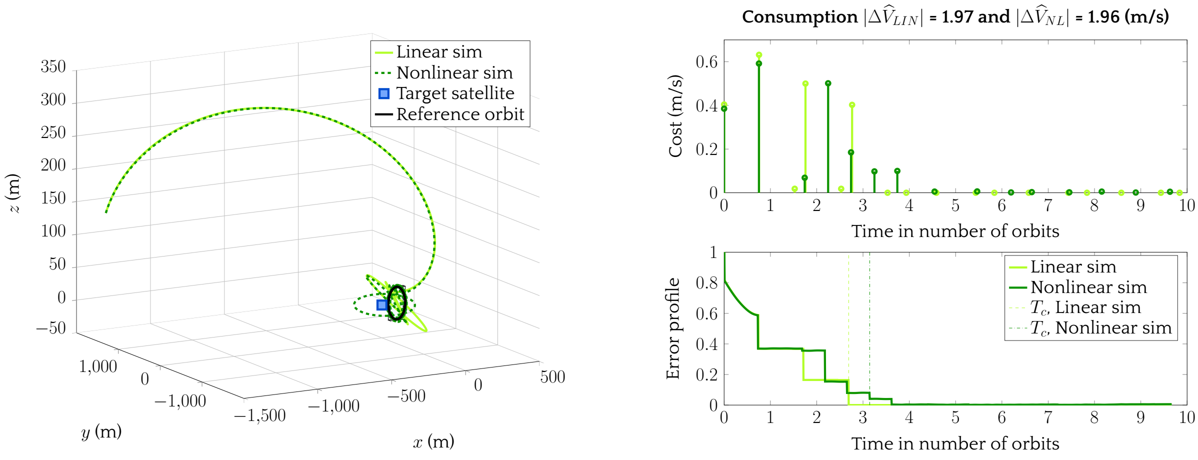

Consumption $|\Delta\widehat{V}_{LIN}|$ = 1.97 and $|\Delta\widehat{V}_{NL}|$ = 1.96 (m/s)

(a) Trajectory.

(b) Impulses and error profile.

Figure 3.28: Non-periodic bi-impulsive controller of Section 3.7 for X_{02}.

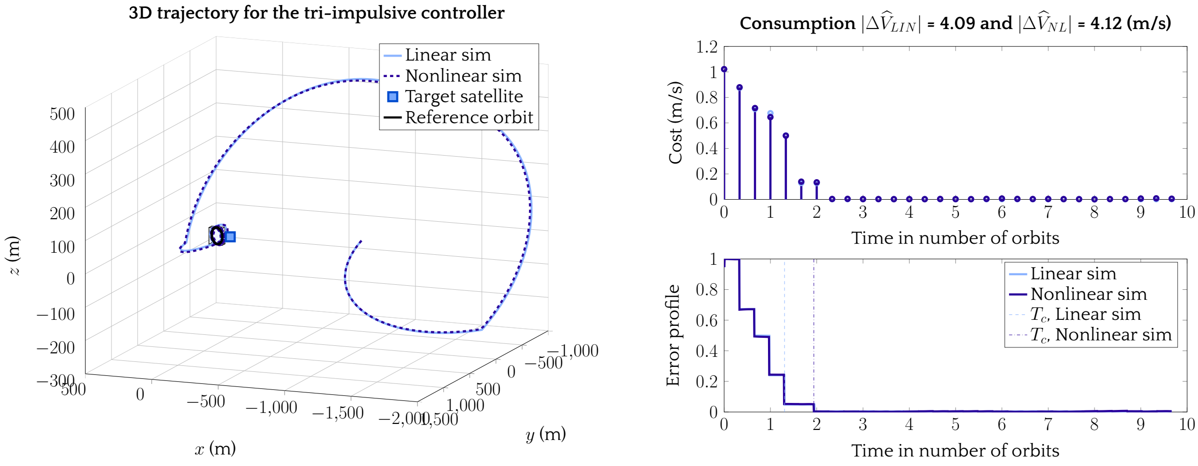

3D trajectory for the tri-impulsive controller

Consumption $|\Delta\widehat{V}_{LIN}|$ = 4.09 and $|\Delta\widehat{V}_{NL}|$ = 4.12 (m/s)

(a) Trajectory.

(b) Impulses and error profile.

Figure 3.29: Tri-impulsive controller of Section 3.8 for X_{02}.

3.9.4.3. Results for initial condition X_{03}

Figures 3.30 to 3.33 represent the simulations corresponding to initial condition X_{03}. The conclusions that can be drawn from these results are similar to their counterparts for X_{02} and X_{03}.

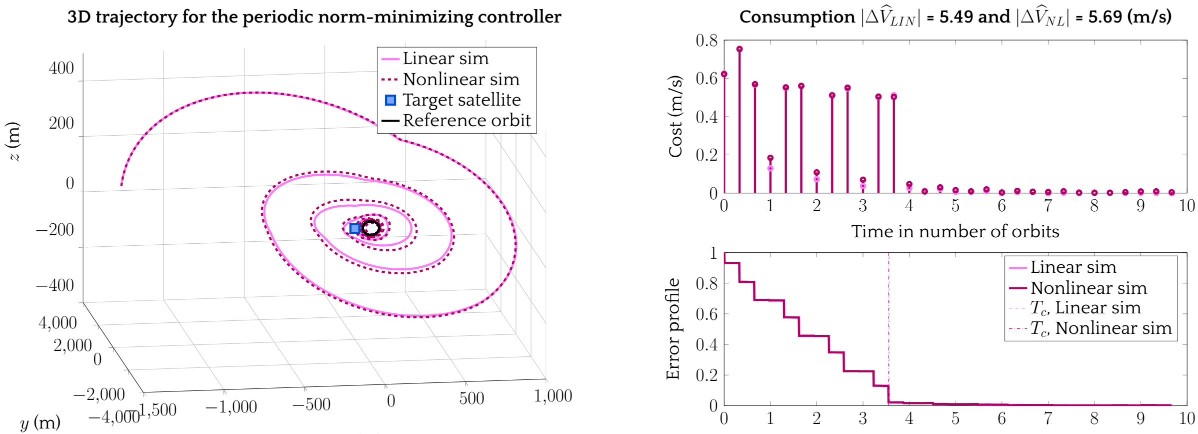

(a) Trajectory.

(b) Impulses and error profile.

Figure 3.30: Periodic norm-minimizing controller of Section 3.5 for X_{03}.

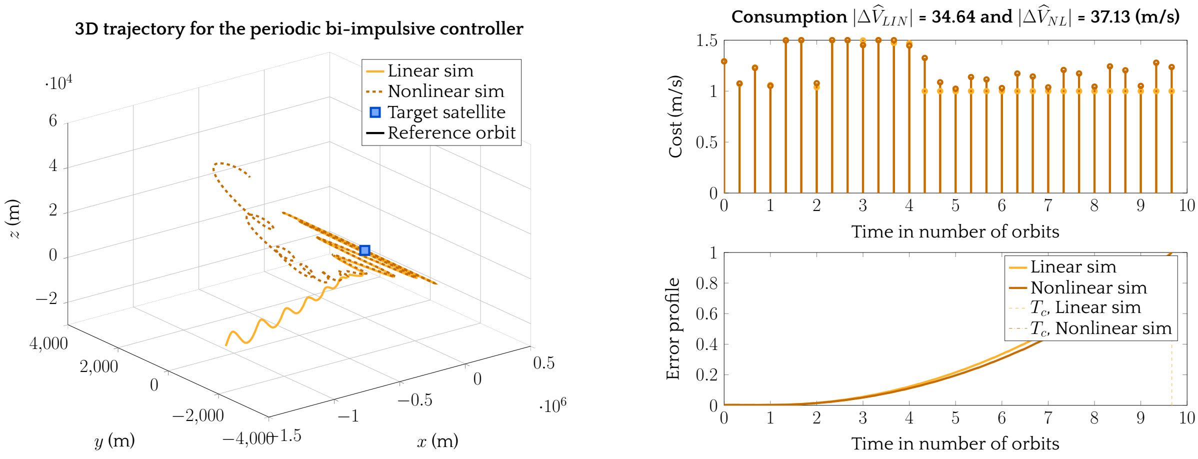

(a) Trajectory.

(b) Impulses and error profile.

Figure 3.31: Bi-impulsive controller of Section 3.6 for X_{03}.

From Figures 3.21 to 3.33 we can observe that the results corresponding to the bi-impulsive controllers of Section 3.6 is the most efficient in terms of convergence time (considering the non-divergent cases). In fact, in an ideal context, only two impulses are needed to bring the chaser to steady states.

From the initial states X_{02} and X_{03} we see that, due to a larger distance to the box, every controller requires first large impulsive controls — the greater the distance of the initial positions, the larger the value and number of the first impulses.

We can observe from Figures 3.26 and 3.31 how the bi-impulsive controller reacts to saturations, whose behavior can be extrapolated to the rest of controllers. Actually, it fails to stabilize the chaser in presence of saturations. In fact, the amount of $\Delta\widehat{V}$ demanded by the controller is way beyond the thrusters capabilities while such an amount is supposed to steer the chaser to the box after two

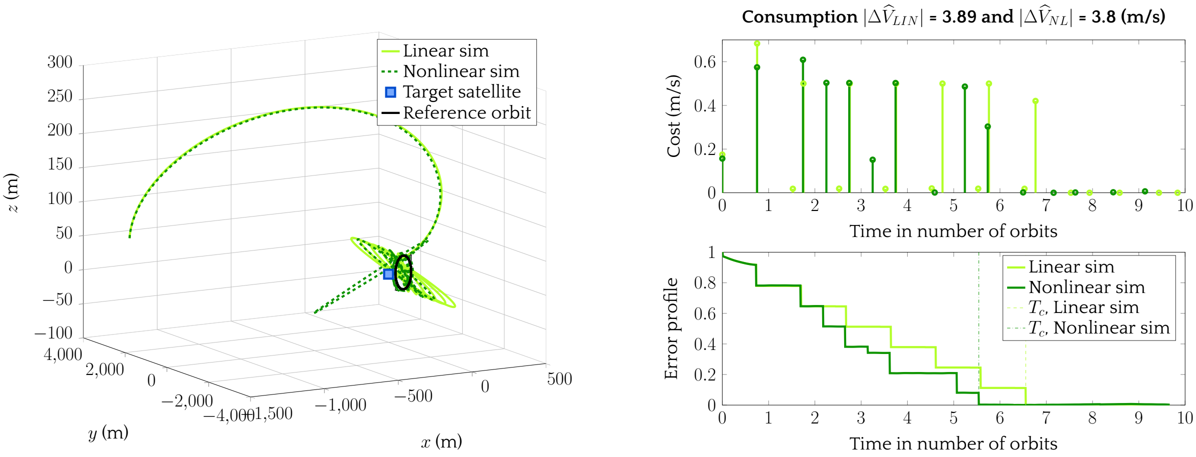

(a) Trajectory.

(b) Impulses and error profile.

Figure 3.32: Non-periodic bi-impulsive controller of Section 3.7 for X_{03}.

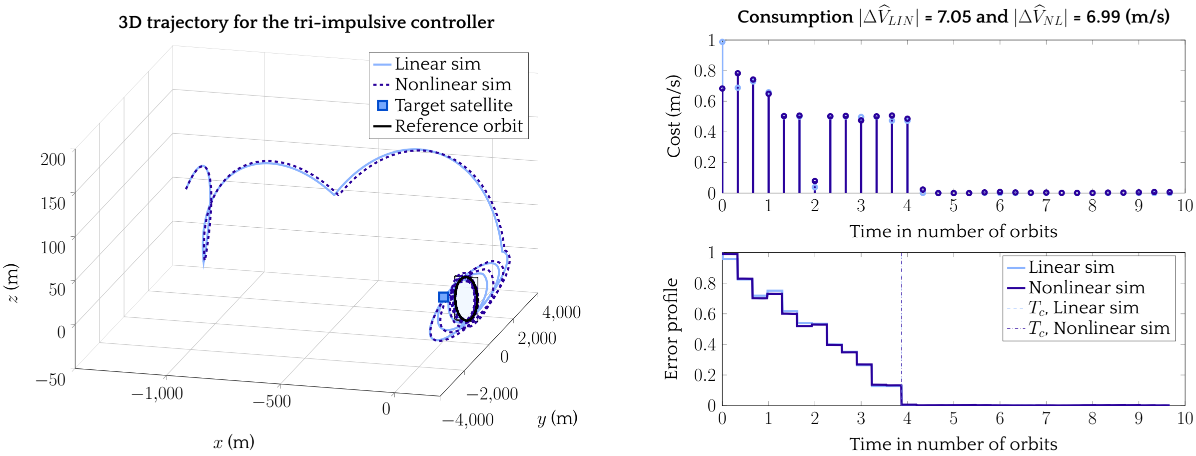

(a) Trajectory.

(b) Impulses and error profile.

Figure 3.33: Tri-impulsive controller of Section 3.8 for X_{03}.

impulses. Instead, since the impulsive controls are truncated, the chaser is brought on a random orbit with no particular interest and it diverges. However, if the saturation constraint is released, as in Figure 3.27, the chaser is steered to the periodic reference orbit — therefore reducing the error — even if the controls are truncated (first control in the figure). We also observe that the slope of the error norm profile decreases after each impulsive control and tends to zero. This fact limits the divergence of the chaser so that the subsequent controls can stabilize it. The consequence is that the convergence time is degraded when saturation occurs. But on the other hand, the presence of saturation constraints limits the consumption for every controller.

Tables 3.6 and 3.7 show the different costs (m/s) and convergence time (number of orbits) for the different controllers and initial conditions. Note that the asterisk * in both tables stands for the divergent simulations in Figures 3.26 and 3.31.

Initial condition	Control 3.5		Control 3.6		Control 3.7		Control 3.8	
	LIN	NL	LIN	NL	LIN	NL	LIN	NL
X_{01}	1.45	1.53	1.52	1.73	0.99	1.00	2.30	2.32
X_{02}	3.67	3.77	*	*	1.97	1.96	4.09	4.12
X_{03}	5.49	5.69	*	*	3.89	3.80	7.05	6.99

Table 3.6: Consumption (m/s) for the different controllers and initial conditions.

Initial condition	Control 3.5		Control 3.6		Control 3.7		Control 3.8	
	LIN	NL	LIN	NL	LIN	NL	LIN	NL
X_{01}	2.28	2.26	0.34	0.33	0.72	1.68	0.98	0.97
X_{02}	2.60	2.91	0.34	*	2.69	3.14	1.30	1.94
X_{03}	3.56	3.55	0.34	*	6.56	5.54	3.88	3.87

Table 3.7: Convergence time (nb. orbits) for the different controllers and initial conditions.

From Tables 3.6 and 3.7 we can extract some general conclusions.

First, we see that both the consumption and the convergence times are increased as the initial condition X_0 recedes from the target.

Both performance indices are almost equivalent for both linear and nonlinear cases in every numerical experience. Concerning the cost, we can observe a general light increase of the nonlinear cost with respect to the linear counterpart. However, some opposite behaviors can be noticed, where some nonlinear simulations show a slightly reduced cost with respect to the linear ones. This behavior may be explained according to the disturbances contribution, which can *help* reduce the cost if the conditions are advantageous.

In every case, we find the best consumption in Guidance law #3 in Section 3.7 — designed to minimize the cost. The fuel saving arrives up to 50% with respect to Guidance laws 3.5 and 3.6, while Guidance law 3.8 largely overpasses this percentage. Even though the cost is reduced in this case, we must recall that the on-board complexity of this controller is much higher than any of its counterparts.

Guidance law 3.5 shows a slow convergence for initial condition X_{01} with respect to the rest of controllers and similar values for further initial conditions. Remind that this controller was designed to instantaneously minimize the norm of the state, ensuring the best possible decrease at each thrust instant. With that logic in place, it was possible to guarantee stability of the closed-loop but not convergence or a strict decrease of the error. We anticipated a slow convergence (if any), which is finally verified by these numerical simulations.

In Figures 3.26a and 3.31a concerning Guidance law 3.6, the trajectories diverged due to too tight saturations constraints. However, for the linear case, in absence of saturation, we retrieve the desired behavior, in which the chaser is stabilized after two control maneuvers, leading to a convergence time of 0.34 orbits (written down in green in Table 3.7 to show up the difference).

In general, Guidance laws 3.6 and 3.7 show a reduced consumption with respect to Guidance laws 3.5 and 3.8. However, in terms of on-board complexity, both controllers require more power, specially

Guidance law 3.7.

On the other hand, Guidance laws 3.5 and 3.8 perform their approach maneuvers through periodic (bounded) trajectories, so the satellite is on a stable orbit in case of malfunctioning, paying a higher price in terms of consumption and convergence time.

3.9.5. Comparison of approach methodologies: hybrid vs MPC

In this subsection we aim at comparing the tri-impulsive hybrid methodology described in Section 3.8 and the MPC approach developed in [50].

In [50], the authors propose an MPC algorithm which aims at minimizing the fuel consumption accounting for convex constraints, such as periodicity, saturation of the thrusters and space restrictions in the same rendezvous context to the one presented in this chapter for the PRISMA mission.

The approach consists in providing a redefinition of the set of periodic space-constrained trajectories by evaluating convex semi-algebraic functions — computed by finding the envelope of the curves defining the boundary of the so called admissible set — that can be used to indicate whether a given relative trajectory respects the restrictions or not. The problem is formulated as an MPC scheme characterized by the resolution of convex but non-differentiable constrained optimization problems.

Since the MPC scheme minimizes the cost, we can already predict a better performance of this controller in terms of fuel consumption with respect to the hybrid controller presented in Section 3.7.

However, this MPC controller does not bring the chaser satellite to a periodic trajectory at each maneuver, but steers the spacecraft from a given initial state to any periodic orbit included in the given subspace of interest, so-called tolerance box $\mathcal{B}$. This means that the objective is not a particular reference orbit $\widehat{\xi}^{ref}$ as for our tri-impulsive controller, but any periodic orbit lying within $\mathcal{B}$, which will change the way the convergence time T_c is defined with respect to Expression (3.142). Within [50], the convergence time T_c is set as the elapsed time from the initial time up to the first instant in which the chaser's periodic trajectory does not leave the tolerance box.

The results of this methodologies comparison are presented in the sequel. The chaser satellite departs from initial condition X_{01} in Figure 3.34a, initial condition X_{02} in Figure 3.36a and initial condition X_{03} in Figure 3.37a respectively, where X_{01}, X_{02} and X_{03} are defined in Table 3.4. In both approach methods, the chaser must arrive at the tolerance box — $\widehat{\xi}^{ref}$ for the hybrid controller and any periodic trajectory for the MPC controller — by means of impulsive maneuvers executed at $\bar{\nu} = 120^o$ from one another. All data remain invariant with respect to Tables 3.1, 3.2, 3.5 and 3.3 (except for $\widehat{\xi}^{ref}$ in the MPC controller).

For the three initial conditions, we observe a more direct trajectory towards the reference trajectory in the case of the MPC controller, while the hybrid controller seems to get away at first to come back later on.

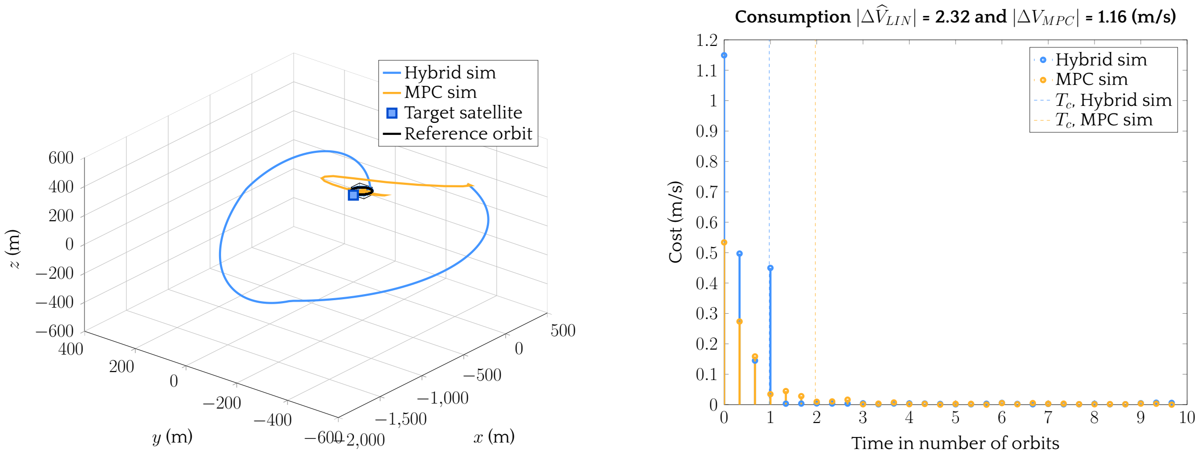

(a) Trajectory.

(b) Impulses and convergence.

Figure 3.34: Comparison of Guidance law 3.7 vs MPC Controller in [50] for initial condition X_{01}.

However, if we zoom at the tolerance box containing the reference, we observe that the hybrid controller injects the chaser in the reference trajectory much faster than the MPC controller, leading to smaller convergence times T_c.

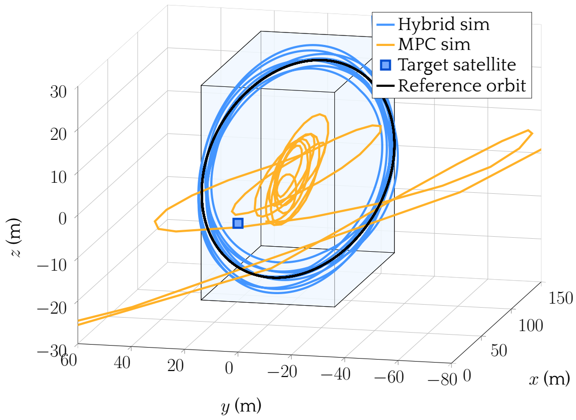

Figure 3.35: Zoom to the trajectories of Figure 3.34a.

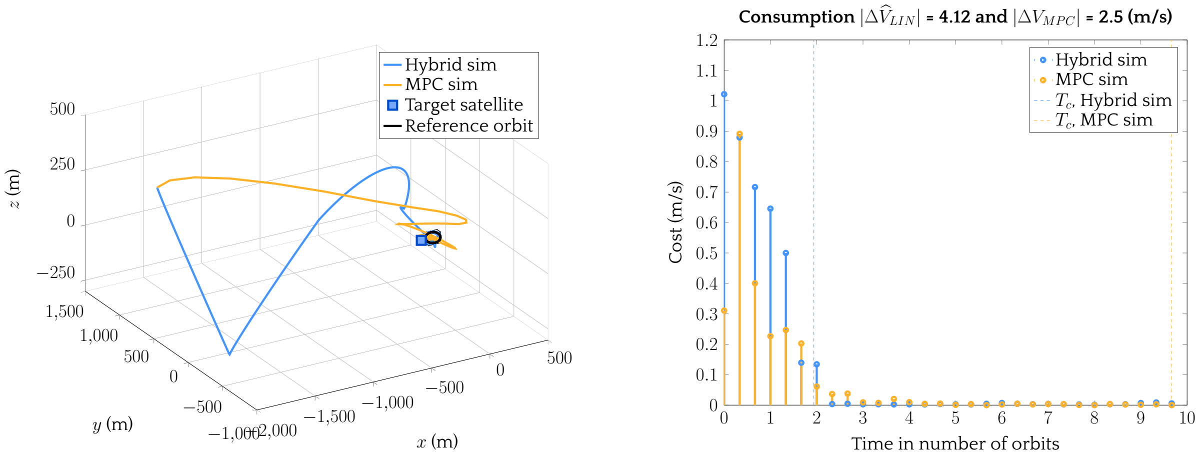

(a) Trajectory.

(b) Impulses and convergence.

Figure 3.36: Comparison of Guidance law 3.7 vs MPC Controller in [50] for initial condition X_{02}.

Concerning the cost, we observe on Figures 3.34b and 3.36b that the hybrid controller has larger

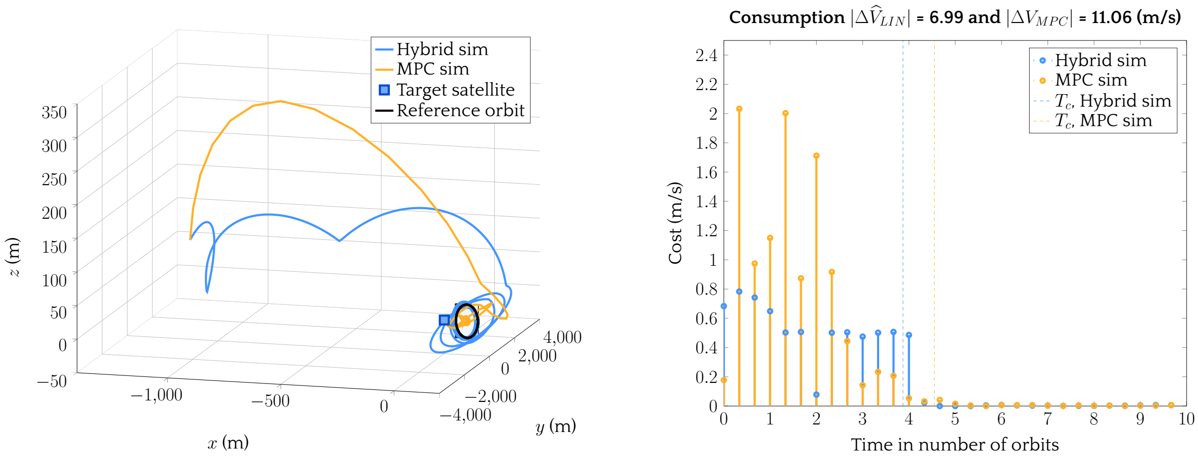
Consumption $|\Delta\widehat{V}_{LIN}|$ = 6.99 and $|\Delta V_{MPC}|$ = 11.06 (m/s)

(a) Trajectory.

(b) Impulses and convergence.

Figure 3.37: Comparison of Guidance law 3.7 vs MPC Controller in [50] for initial condition X_{03}.

values of consumption at the first maneuvers, while the MPC controller shows smaller thrusts, which is normal since this last minimizes the consumption at each maneuver. However, for initial condition X_{03} we observe that the MPC consumption is higher than its hybrid equivalent. This might be caused by the influence of perturbations and measure errors that affect the chaser during longer time. Even though the fact that the consumption is optimal at each computation, it is necessary to apply more thrusts to enter — and stay — within the tolerance box. The comparison of the costs for both controllers is shown in Table 3.8.

Initial condition	Hybrid controller 3.7	MPC controller [50]
X_{01}	2.32	1.16
X_{02}	4.12	2.50
X_{03}	6.99	11.06

Table 3.8: Consumption (m/s) for the Guidance law 3.7 vs MPC Controller in [50].

In a similar way, in Table 3.9 we have represented the convergence time in number of orbits for each controller. As it was predicted, the hybrid controller takes shorter time to get to the reference periodic trajectory contained inside the tolerance box.

Initial condition	Hybrid controller 3.7	MPC controller [50]
X_{01}	0.97	1.97
X_{02}	1.94	9.66
X_{03}	3.87	4.55

Table 3.9: Convergence time (nb. orbits) for the Guidance law 3.7 vs MPC Controller in [50].

We can conclude that both approach methods have their advantages and disadvantages. Concerning the hybrid controller, the chaser is steered towards $\widehat{\xi}^{ref}$ by means of periodic trajectories, but these are not optimized, leading to larger consumption values. However, the tri-impulsive methodology ensures global asymptotical stability along the closed-loop dynamics, according to Theorem 4.

On the other hand, the MPC controller performs the approach by means of optimized maneuvers in terms of consumption, leading to smaller values of cost with respect to the hybrid controller. However, these maneuvers do not inject the chaser into periodic orbits, which can be an issue in case of actuators malfunctioning. In the same way, this controller does not have any guarantee of convergence.

The overall conclusion is that both methods offer a compromise between fuel consumption, security and time of convergence.

3.10. Conclusions

In this chapter, we have addressed the chaser's impulsive rendezvous maneuver towards the target satellite under an impulsive dynamical hybrid systems framework. Within the hybrid context, we are able to model the satellite's approach as a continuous-time system when no control input is applied, and as a discrete-time system when the thrusters firings are executed. The jump set to execute a firing relies on the presence of two different timers.

The objective of the chaser's rendezvous maneuver is to perform an approach towards a periodic reference trajectory located in the neighborhood of the target satellite, and track it once it arrives. In order to perform these maneuvers, we propose a new controller, which is then compared to three other different control schemes — which are re-interpreted in this hybrid context — with different trade-offs between fuel consumption and computation complexity.

The new controllers take the advantage of steering the satellite motion along periodic (therefore bounded) transient relative orbits. The use of the hybrid formalism allows us to prove asymptotic stability of the desired motion, in addition to robustness to perturbations. Such a robustness is confirmed by suitable simulation results showing desirable responses also in the presence of unmodeled nonlinear phenomena and external disturbances affecting the satellite motion.

CHAPTER 4

APPROACH PHASE VIA A GLIDESLOPE METHOD

Contents

Résumé

La phase de rendez-vous proximal (appelée close-range rendezvous en anglais) est une des étapes du processus global de rendez-vous durant laquelle le chasseur prépare son entrée dans le couloir final d'approche (closing) et réalise ensuite les conditions de docking avec la cible [39].

En fonction de diverses contraintes opérationnelles et de sécurité, diverses stratégies de phase d'approche peuvent être envisagées et proposées pour effectuer le rendez-vous proximal: V-bar (direction de l'orbite curviligne en ligne droite) et R-bar (direction du centre d'attraction) sont des approches très classiques alors que la trajectoire de looping ou l'orbite de dérive naturelle à l'approche R-bar sont des variations intéressantes de cette dernière comme décrit par [39]. L'observabilité (contraintes LoS), les contraintes de sécurité et le budget du carburant sont les principales raisons pour faire un choix parmi toutes les approches possibles.

Un système simple et général respectant certaines restrictions de sécurité est connu sous le nom d'approche glideslope. Cette trajectoire impose au satellite chasseur de suivre une ligne droite dans n'importe quelle direction du repère de référence locale reliant l'emplacement actuel du chasseur à sa destination finale.

Ces types d'approches du rendez-vous semblent avoir été définis pour la première fois dans leur plus grande généralité par Pearson [93]. Le concept de glideslope a été développé par la MPAD au Johnson Space Center de la NASA, dans le cadre des activités de définition de la conception des phases de rendez-vous pour la navette spatiale Shuttle en 1983. On pourra se reporter utilement à la référence [93] pour connaitre l'histoire, les motivations et une analyse technique succincte du développement de cette technique dans le contexte du programme de la navette spatiale américaine. Seule une trajectoire relative dans le plan orbital est étudiée. Elle est paramétrée ensuite en coordonnées polaires et il est fait l'hypothèse que les moteurs avant et arrière (de la navette spatiale en l'occurence) font un angle donné avec l'axe de la navette. Dans ce cadre, Pearson propose d'étudier la relation entre l'angle fait par la trajectoire rectiligne avec la direction V-bar dans le plan orbital, l'angle d'inclinaison des poussées, la distance relative à la cible ainsi que la vitesse relative en module.

Les trajectoires de glideslope ont également été utilisées pour les approches terminales lors des missions cargo ATV [46] et HTV [122] vers l'ISS. Dans ces derniers cas, il s'agit essentiellement d'une des approches classiques dans les opérations de proximité, suivant les directions R-bar ou V-bar, et qui sont rappelées en détail dans la réference [39].

Les travaux préliminaires de [93] ont été généralisés dans [56] tout en conservant l'hypothèse de linéarisation autour d'une trajectoire circulaire conduisant à l'utilisation des équations HCW, et pour

l'orbite de référence elliptique dans [91]. Ces résultats constituent la référence sur le sujet et définissent l'algorithme classique glideslope tel que décrit usuellement dans la littérature.

Le concept de trajectoire rectiligne génèralise les approches suivant les directions R-bar et V-bar puisqu'il s'agit d'une approche directe de type LoS avec un angle arbitraire par rapport à l'approche V-bar. Des différences notables existent toutefois suivant le type d'hypothèses faites sur la propulsion: impulsionnelle [93], [56], [124], [91], continue [55], [140] ou à poussée constante [80], [81].

Sous les hypothèses de propulsion impulsionnelle, l'objectif est de revisiter l'algorithme de Hablani dans [56] dans une configuration plus générale et pour une orbite de référence elliptique, afin d'identifier une nouvelle formulation du problème, y compris des degrés de liberté utiles, qui permettent de minimiser la consommation de carburant et qui aident à inclure les segments de trajectoire résultants entre deux manœuvres successives dans un couloir d'approche défini par l'utilisateur.

4.1. Introduction

The close-range rendezvous phase is one of the stages of the global rendezvous process during which the chaser spacecraft prepares its entry into the final approach corridor and performs the docking action with the target satellite [39].

Depending on various operational and safety constraints, various closing phase strategies may be envisioned and proposed to perform the proximal rendezvous: V-bar (curvilinear orbit direction as a straight line) and R-bar (direction of the center of attraction) are very classical approaches while looping trajectory or natural drift orbit to R-bar approach are interesting variations of the latter as described by [39]. Observability (LoS constraints), safety reasons and fuel budget are the main incentives to make a choice among all possible approaches.

One simple and general scheme complying some safety restrictions is known as the glideslope approach. This trajectory imposes the chaser satellite to follow a straight path in any direction of the local reference frame connecting the current location of the chaser to its final destination.

These types of rendezvous approaches seem to have been defined in their broadest generality for the first time by Pearson [93]. He proposes to study the relationship between the angle made by the linear trajectory with respect to the V-bar ($\vec{X}$ axis of the LVLH frame) direction in the orbital plane, the angle of inclination of the thrusts, the relative distance to the target and the module of the relative velocity.

Glideslope trajectories were also used for terminal approaches during ATV cargo missions [46] and HTV [122] to the ISS. In these last cases, glideslope is essentially one of the conventional approaches in proximity operations, following the R-bar ($\vec{Z}$ axis of the LVLH frame) or V-bar directions, which are recalled in detail in [39].

The preliminary works in [93] have been extended and generalized for any direction in space in [56], [124], preserving the linearization hypothesis around a circular orbit, leading to the use of the HCW equations, and for elliptic reference orbit in [91]. Indeed, the results presented in [56] are well-known and constitute the reference on the subject and define the classical glideslope algorithm as usually described in the literature.

The concept of rectilinear trajectory generalizes the R-bar and V-bar types of closing, since it is a direct approach of type LoS with an arbitrary angle with respect to the V-bar approach. However, there exist notable differences depending on the type of propulsion hypotheses: impulsive maneuvers [93], [56], [124], [91]; continuous-thrust maneuvers [55], [140] or constant-thrust maneuvers [80], [81].

Under the assumptions of impulsive propulsion, the objective is to revisit Hablani's algorithm in [56] in a more general setup and for an elliptic reference orbit, in order to identify a new formulation of the problem, including useful degrees of freedom that allows to minimize the fuel consumption and helps to enclose the resulting trajectory segments between two successive maneuvers in a user-defined approach corridor.

4.2. Satellite relative dynamics for glideslope approach

The equations of motion describing the relative dynamics between a chaser and a target satellite in any approach context are fully developed in Chapter 2, which will be useful for the sequel.

Under Keplerian hypothesis (Assumption 2 in Chapter 2) and within an elliptic reference orbit, the equations of motion for the relative dynamics in the target's LVLH reference frame may be linearized for close separation between the chaser and the target satellites [2, Chapter 5, Section 5.6.1], as shown in Equation (2.56), rewritten below for simplicity:

$$\dot{X}(t) = A(t)X(t) + B\,U(t), \tag{4.1}$$

where $X = [x, y, z, \dot{x}, \dot{y}, \dot{z}]^T$ is the state representing relative positions and velocities in the three fundamental axes of the LVLH frame — as defined in Appendix B.3. $A(t)$ is the dynamic periodic matrix of time t in Expression (2.57); B is the input matrix, defined in Equation (2.58) and $U(t)$ is the control input vector, given by (2.59).

However if we are considering linear impulsive problems — as justified in Section 3.1 —, the control function $U(t)$ in (4.1) is replaced by a finite set of generalized velocity jumps $\{\Delta\vec{V}_k \in \mathbb{R}^m, k = 0, \cdots, N\}$, where N is a positive integer [19], as shown in (F.3):

$$\dot{X}(t) = A(t)X(t) + \sum_{k=0}^{N} B\,\Delta\vec{V}_k, \tag{4.2}$$

whose solution is of the form:

$$X(t) = \Phi(t, t_0)X(t_0) + \sum_{k=0}^{N} \Phi(t, t_k)B\,\Delta\vec{V}_k, \tag{4.3}$$

where $\Phi(t, t_0)$ is the state transition matrix of the relative motion.

Classical derivations dating back to the seminal publications of Lawden [74, Chapter 5] and Tschauner-Hempel [118] consist in applying a change of independent variable from time t to true anomaly ν and a simplifying coordinate change leading to state $\tilde{X}(\nu)$. These two transformations are gathered into a single matrix, $T_{TH}(\nu)$, defined in Expression (2.77), such that $\tilde{X}(\nu) = T_{TH}(\nu)X(t)$.

Although the new linear representation after the coordinate change $T_{TH}(\nu)$ is LTV — as shown in (2.75) —, $\tilde{A}(\nu)$ is simple enough to allow for the derivation of the autonomous solution via the computation of a fundamental matrix $\tilde{\phi}_{\nu_0}$ and a transition matrix $\tilde{\Phi}(\nu, \nu_0)$.

The form of the so-called Yamanaka-Ankersen state transition matrix [139] (Expression (2.82)) is particularly appealing for computation purposes. For the current case, the transition matrix in the time-domain, $\Phi(t, t_0)$, may be considered as readily computable by:

$$\Phi(t, t_0) = T_{TH}(\nu)^{-1}\,\tilde{\phi}_{\nu}\tilde{\phi}_{\nu_0}^{-1}\,T_{TH}(\nu_0). \tag{4.4}$$

Thus, the expression of the solution (4.3) can be directly computed taking into account Equation (4.4).

Let us now consider the first term of the right-hand side of Equation (4.3), describing the free dynamics of the chaser's relative motion:

$$X(t) = \Phi(t, t_0) X(t_0). \tag{4.5}$$

The state transition matrix $\Phi(t, t_0)$ in (4.5) can be block-partitioned as:

$$\Phi(t, t_0) = \left[\begin{array}{c|c} \Phi_{rr}(t, t_0) & \Phi_{rv}(t, t_0) \\ \hline \Phi_{vr}(t, t_0) & \Phi_{vv}(t, t_0) \end{array}\right]. \tag{4.6}$$

The analytical expressions of each partition of the state transition matrix $\Phi(t, t_0)$ in the context of an elliptical orbit is not given here, since, as noted after Equation (2.119), it has a convoluted analytical form and it will be just used numerically for the simulations.

However, in the case of a circular orbit, the relative dynamics are governed by the *Hill-Clohessy-Wiltshire* equations [24], leading to a simpler expression of the four partitions of $\Phi(t, t_0) \in \mathbb{R}^{6\times 6}$ in Equation (4.6), each one of dimensions 3×3:

$$\begin{aligned}
\Phi_{rr}(t, t_0) &= \begin{bmatrix} 1 & 0 & 6\,(\omega t - s) \\ 0 & c & 0 \\ 0 & 0 & 4 - 3c \end{bmatrix}, &
\Phi_{rv}(t, t_0) &= \begin{bmatrix} (4/\omega)s - 3t & 0 & (2/\omega)(1-c) \\ 0 & s/\omega & 0 \\ -(2/\omega)(1-c) & 0 & s/\omega \end{bmatrix}, \\
\Phi_{vr}(t, t_0) &= \begin{bmatrix} 0 & 0 & 6\,\omega(1-c) \\ 0 & -\omega s & 0 \\ 0 & 0 & 3\omega s \end{bmatrix}, &
\Phi_{vv}(t, t_0) &= \begin{bmatrix} -3 + 4c & 0 & 2s \\ 0 & c & 0 \\ -2s & 0 & c \end{bmatrix},
\end{aligned} \tag{4.7}$$

with $s = \sin(\omega(t - t_0))$ and $c = \cos(\omega(t - t_0))$.

By denoting the state vector $X(t) = [\vec{\rho}(t) \;\; \vec{v}(t)]^T$, we can express Equation (4.5), in both elliptical and circular orbits, Expression (4.6) gives the position and velocity vectors at a later time t:

$$\begin{cases} \vec{\rho}(t) = \Phi_{rr}(t, t_0)\, \vec{\rho}_0 + \Phi_{rv}(t, t_0)\, \vec{v}_0, \\ \vec{v}(t) = \Phi_{vr}(t, t_0)\, \vec{\rho}_0 + \Phi_{vv}(t, t_0)\, \vec{v}_0. \end{cases} \tag{4.8}$$

4.3. Glideslope trajectories for rendezvous

When considering the design of impulsive maneuvers for a glideslope rendezvous, the most cited reference is the paper by Hablani [56] in which the so-called classical inbound and outbound glideslope approaches for a circular reference orbit are presented in a general setup.

When the chaser must approach the target satellite, an inbound glideslope guidance algorithm is used. On the other hand, an outbound algorithm is used for receding away from the target. In both cases, the chaser's relative velocity must diminish when it is close to the target, in order to comply with safety constraints. Within the objectives of this dissertation, we are only considering the inbound glideslope to approach the target.

This inbound glideslope algorithm consists in a controlled trajectory of N impulses described by Equation (4.3). The real path of the chaser, however, will not actually be a straight line, but a sequence of *humps* between the different thrust locations, as shown in Figure 4.1. These humps appear because of the gravitational forces acting over the chaser, and will vary according to the type of orbit.

The general principle for an inbound glideslope approach is represented in Figure 4.1. The relative position vector between the target and the chaser is given by vector $\vec{\rho}(t)$.

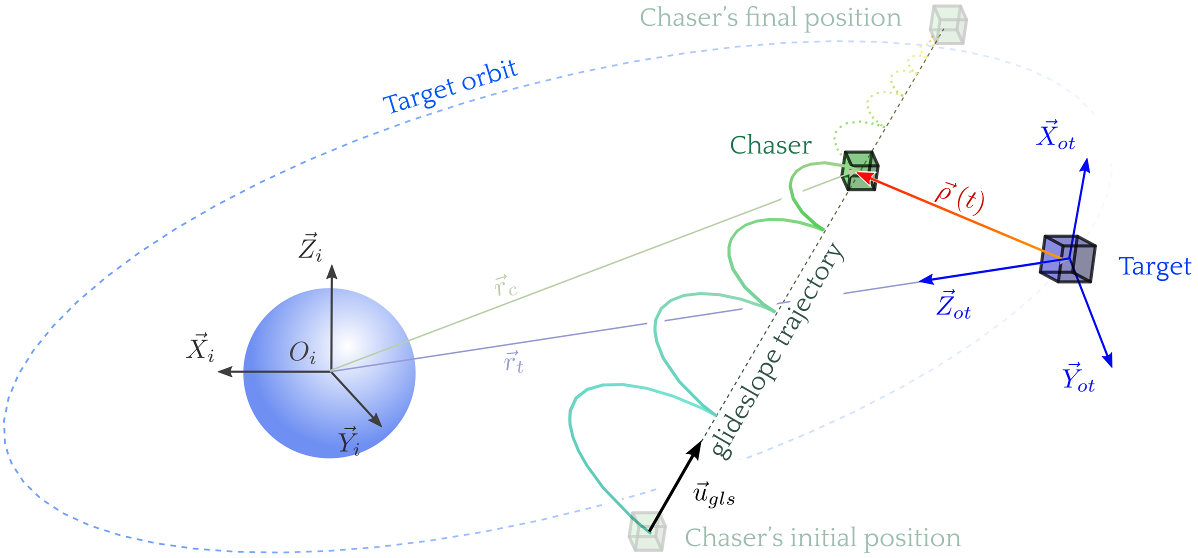

Figure 4.1: Glideslope approach (not to scale).

For the sake of simplicity in the sequel, we are considering the target's LVLH local reference frame $\mathcal{O}_t$ – appearing in Appendix B.3 –, defined by its basis vectors $B_{ot} = [\vec{X}_{ot}, \vec{Y}_{ot}, \vec{Z}_{ot}]$. From here on, all the magnitudes are expressed in the target's local LVLH, therefore the superscript $\mathcal{O}_t$ will be omitted for concision purposes.

Within the target's LVLH frame, the chaser will perform the glideslope approach, departing from an initial position at time t_0 and arriving at a final position at a final time t_f. This final position can be a station keeping position, a point that belongs to a given periodic reference trajectory – as shown in Chapter 3 – or a docking point.

As shown in Figure 4.2a, the chaser starts the glideslope approach at time t_0, located at its initial position, given by the relative position vector:

$$\vec{\rho}(t_0)^{\mathcal{O}_t} = \vec{\rho}_0 = [x_0 \;\; y_0 \;\; z_0]^T, \tag{4.9}$$

and must arrive at its final position:

$$\vec{\rho}(t_f)^{\mathcal{O}_t} = \vec{\rho}_f = [x_f \;\; y_f \;\; z_f]^T, \tag{4.10}$$

at the end of the rectilinear path approach at time t_f, as shown in Figure 4.2c.

In order to parametrize the rectilinear trajectory to be followed by the chaser – also known as commanded path [56] – from $\vec{\rho}_0$ to $\vec{\rho}_f$, we introduce vector $\vec{\lambda}(t)$, whose origin is located at the chaser's final position and pointing the chaser's current position, as in Figure 4.3, thus verifying:

$$\vec{\lambda}(t) = \vec{\rho}_{gls}(t) - \vec{\rho}_f. \tag{4.11}$$

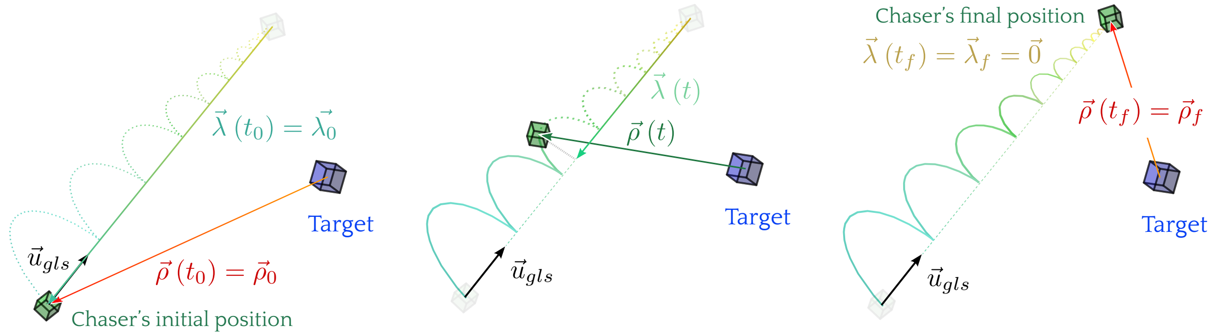

(a) Initial position. (b) General position. (c) Final position.

Figure 4.2: Chaser satellite following a glideslope approach.

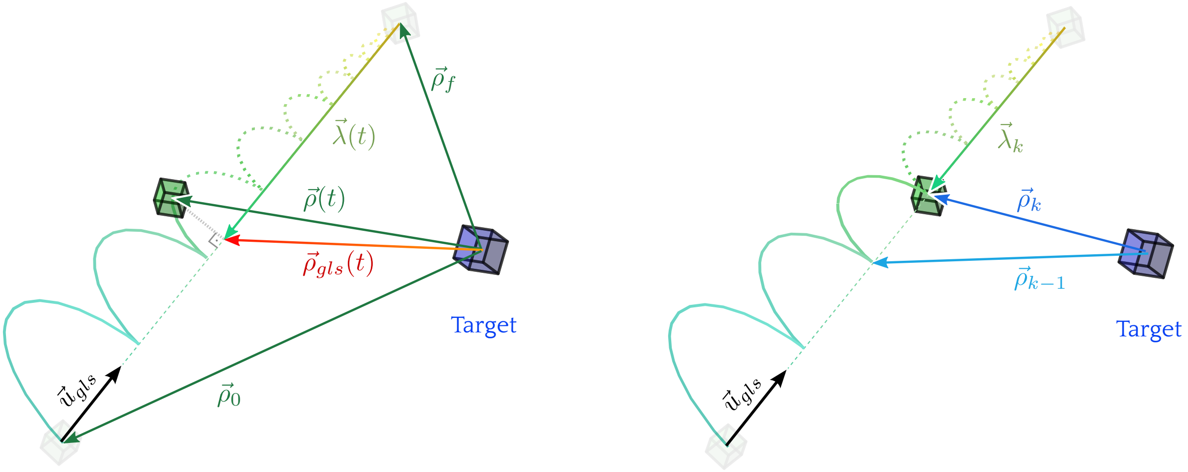

Figure 4.3: General position.

The following notation is used in the sequel:

$$(\cdot)(t_i) = (\cdot)_i, \tag{4.12}$$

where $(\cdot)$ will be either $\vec{\rho}$ or $\vec{\lambda}$.

We define thus the commanded path $\vec{\lambda}_0$ at time t_0 as:

$$\vec{\lambda}_0 = \vec{\rho}_0 - \vec{\rho}_f, \tag{4.13}$$

and the commanded path $\vec{\lambda}_f$ at final time t_f, that is zero by definition:

$$\vec{\lambda}_f = \vec{0}. \tag{4.14}$$

We define also the unit vector of the rectilinear trajectory's direction, whose expression is:

$$\vec{u}_{gls} = \begin{bmatrix} \dfrac{x_f - x_0}{||\vec{\lambda}_0||} & \dfrac{y_f - y_0}{||\vec{\lambda}_0||} & \dfrac{z_f - z_0}{||\vec{\lambda}_0||} \end{bmatrix}. \tag{4.15}$$

At every instant t, the *distance to go* is a function of time, and it is given by $||\vec{\lambda}(t)||$ in the direction of the unit vector $\vec{u}_{gls}$:

$$\vec{\lambda}(t) = -\lambda(t)\,\vec{u}_{gls}. \tag{4.16}$$

The basic principle of the glideslope classical algorithm is then to analytically compute a fixed number N of impulses $\left\{\Delta\vec{V}_0, \Delta\vec{V}_1, \cdots, \Delta\vec{V}_k, \cdots, \Delta\vec{V}_{N-1}\right\}$ – where N is chosen by the user – equally spaced in time over the transfer duration $T = t_f - t_0$, verifying $\vec{\rho}_f = \vec{\rho}_N$ and $\vec{\lambda}_f = \vec{\lambda}_N$.

In order to perform the transfer from $\vec{\rho}_0$ to $\vec{\rho}_f$, the N impulses are to be applied uniformly along the transfer time T, leading to a constant interval between two consecutive thrusts, given by:

$$\Delta t = \frac{T}{N}. \tag{4.17}$$

The thrusters will be then fired at times:

$$t_k = k\ \Delta t\ , \quad k = 0, 1, \cdots, N-1. \tag{4.18}$$

Throughout the transfer, the spacecraft must follow the commanded path. After each maneuver, the chaser must be back on the glideslope line, as shown on the right side of Figure 4.3. Since the initial and final positions $\vec{\rho}_0$ and $\vec{\rho}_N = \vec{\rho}_f$ are fixed by specifications, the intermediate positions are set free and are parametrized as:

$$\vec{\rho}_k = \vec{\rho}_0 - \lambda_k\ \vec{u}_{gls},\ k = 0, 1, \cdots, N-1, \tag{4.19}$$

where the scalars λ_k are free and denote the travelled distance from $\vec{\rho}_0$ to $\vec{\rho}_k$.

We will use Equation (4.8) to obtain a set of N equations to deduce the chaser positions and instantaneous changes of relative velocity at each date t_k. For this purpose, we adopt the following notation: the arrival velocity at $\vec{\rho}_k$ is given by $\vec{v}_k^{\,-}$; while the departure velocity from that position is given by $\vec{v}_k^{\,+}$, where the superscripts $-$ and $+$ denote the velocity right before or just after the thrust maneuver, respectively. The relative velocity at any generic position is then changed instantaneously by applying the impulsive maneuver $\Delta\vec{V}_k$:

$$\Delta\vec{V}_k = \vec{v}_k^{\,+} - \vec{v}_k^{\,-}, \tag{4.20}$$

as shown in Figure 4.4 for the initial maneuver $\Delta\vec{V}_0$ and a generic maneuver $\Delta\vec{V}_k$.

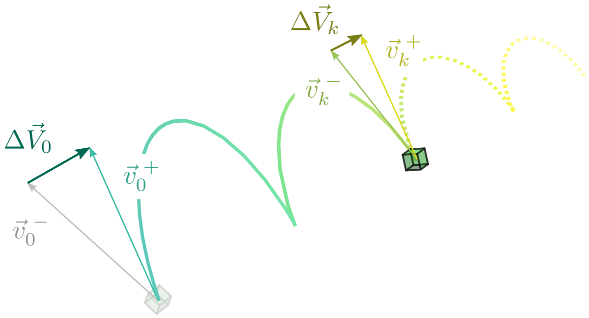

Figure 4.4: Impulsive maneuvers along the glideslope approach.

In order to obtain the maneuver plan composed by the N impulses $\left\{\Delta\vec{V}_0, \Delta\vec{V}_1, \cdots, \Delta\vec{V}_k, \cdots, \Delta\vec{V}_{N-1}\right\}$, we need the relative velocities right before and just after the thrust, as shown in (4.20). The velocity at time t_{k+1} right before the impulse (denoted $\vec{v}_{k+1}^{\,-}$), resulting from the impulse at time k can be obtained from Equation (4.8):

$$\vec{\rho}_{k+1} = \Phi_{rr}(t_{k+1}, t_k)\ \vec{\rho}_k + \Phi_{rv}(t_{k+1}, t_k)\ \vec{v}_k^{\,+}, \tag{4.21a}$$

$$\vec{v}_{k+1}^{\,-} = \Phi_{vr}(t_{k+1}, t_k)\ \vec{\rho}_k + \Phi_{vv}(t_{k+1}, t_k)\ \vec{v}_k^{\,+}. \tag{4.21b}$$

It is straightforward to obtain the needed departure velocity $\vec{v}_k^{\,+}$ from (4.21a) as:

$$\vec{v}_k^{\,+} = \Phi_{rv}(t_{k+1}, t_k)^{-1}\left[\vec{\rho}_{k+1} - \Phi_{rr}(t_{k+1}, t_k)\ \vec{\rho}_k\right], \tag{4.22}$$

that allows the chaser to arrive at the next position $\vec{\rho}_{k+1}$ with relative velocity $\vec{v}_{k+1}^-$ at time $t_k + \Delta t$.

Expressions (4.20), (4.21) and (4.22) allow us to obtain the k-th impulsive maneuver to be applied at t_k to pass from $\vec{\lambda}_k$ to $\vec{\lambda}_{k+1}$:

$$\Delta\vec{V}_k = \Phi_{rv}(t_{k+1}, t_k)^{-1}\left[\vec{\rho}_{k+1} - \Phi_{rr}(t_{k+1}, t_k)\,\vec{\rho}_k\right] - \Phi_{vr}(t_k, t_{k-1})\,\vec{\rho}_{k-1} + \Phi_{vv}(t_k, t_{k-1})\,\vec{v}_{k-1}^{+}. \tag{4.23}$$

By sequencing the computations, we are able to obtain the full maneuver plan $\left\{\Delta\vec{V}_0, \Delta\vec{V}_1, \cdots, \Delta\vec{V}_k, \cdots, \Delta\vec{V}_{N-1}\right\}$.

Sections 4.2 and 4.3 contain the common elements that are used in the different glideslope approaches that are developed in the sequel. In the next sections, we present the classical multipulse glideslope problem by Hablani [56], followed by two new algorithms to tackle some issues such as the optimisation of the fuel consumption or the control of the humps amplitude.

4.4. Guidance law #1: Hablani's classical glideslope approach

In the following, we present the classical inbound glideslope guidance scheme from [56], where the chaser approaches the target in a circular reference orbit.

Within this context, the chaser is commanded to reach the final position $\vec{\rho}_f$ from the initial position $\vec{\rho}_0$ in Figure 4.2 following a specific commanded profile for the distance to go $||\vec{\lambda}(t)|| = \lambda(t)$. The velocity profile imposed to the chaser satellite along the straight trajectory is defined by the following linear relationship:

$$\dot{\lambda} = \alpha\,\lambda + \dot{\lambda}_f, \tag{4.24}$$

where α is the slope of $\dot{\lambda}$ vs λ.

In Hablani's glideslope algorithm, the initial distance to go λ_0, the initial commanded profile velocity $\dot{\lambda}_0 < 0$ and final arrival profile velocity $\dot{\lambda}_f < 0$ are quantities specified by the designer, required to define the slope α:

$$\alpha = \frac{\dot{\lambda}_0 - \dot{\lambda}_f}{\lambda_0} < 0. \tag{4.25}$$

The solution to Equation (4.24) is:

$$\lambda(t) = \lambda_0\, e^{\alpha t} + \frac{\dot{\lambda}_f}{\alpha}(e^{\alpha t} - 1). \tag{4.26}$$

The transfer time T is not fixed *a priori* but deduced from the initial and final commanded velocities $(\dot{\lambda}_0, \dot{\lambda}_f)$ and from the initial distance to go λ_0:

$$T = \frac{1}{\alpha}\ln\left[\frac{\dot{\lambda}_f}{\dot{\lambda}_0}\right] = \frac{\lambda_0}{\dot{\lambda}_0 - \dot{\lambda}_f}\ln\left[\frac{\dot{\lambda}_f}{\dot{\lambda}_0}\right]. \tag{4.27}$$

Once the impulse dates t_k are known from Expression (4.18), it becomes possible to determine every distance to go $\vec{\lambda}_k$, $k = 1, 2, \cdots, N-1$ from Expression (4.26), implying that all the intermediate positions $\vec{\rho}_k$ are instantaneously known by applying Equation (4.11).

It must be recalled that Hablani's algorithm is developed for a target's circular orbit. This means that the intervals between consecutive thrusts (t_{k-1}, t_k) and (t_k, t_{k+1}) are constant; hence the state transition matrices only need to be computed once from Expressions (4.7).

4.4.1. Algorithm

```
Data: chaser's information:
        initial position and velocity in target's LVLH frame $\vec{\rho}_0$, $\vec{v}_0^{\,-}$;
        final position in target's LVLH frame $\vec{\rho}_f$;
        initial and final profile velocity $\dot{\vec{\lambda}}_0$, $\dot{\vec{\lambda}}_f$;
        number of maneuvers $N$;
Initialization: initial distance to go $\vec{\lambda}_0$;
        unit vector $\vec{u}_{gls}$;
        transfer time $T$;
        interval between consecutive impulses $\Delta t$;
        distances to go $\vec{\lambda}_k$;
        relative position vectors $\vec{\rho}_k$;
        state transition matrices $\Phi_{rr}(t_{k+1}, t_k)$, $\Phi_{rv}(t_{k+1}, t_k)$, $\Phi_{vr}(t_{k+1}, t_k)$, $\Phi_{vv}(t_{k+1}, t_k)$;
for $k = 1, \cdots, N$ do
    compute: relative velocity right after the thrust at $k-1$, $\vec{v}_{k-1}^{\,+}$ ;
    compute: relative velocity just before the thrust, $\vec{v}_k^{\,-}$ ;
    compute: impulsive maneuver, $\Delta\vec{V}_k$
end
```

Algorithm 1: Classical Hablani glideslope.

The classical glideslope algorithm is straightforward and easy to implement but suffers from key shortcomings.

First, it is limited to circular reference orbits. In addition, it is important to mention that the actual trajectory of the chaser will not be strictly along the commanded straight line path but will exhibit humps between the N points where an impulsive maneuver is performed and located on the commanded path (cf. Figure 4.1). These humps coming from the natural relative motion of the chaser driven by the Hill-Clohessy-Wiltshire equations are nothing but lateral guidance position errors possibly occurring in and out-of-plane that cannot be directly controlled in the classical glideslope algorithm.

In addition, if the initial and final commanded velocities of the glideslope profile are *a priori* given, there is no degree of freedom left to control the transfer time and the consumption when the initial and final states are fixed. In a similar way, the transfer time T is not fixed *a priori* but deduced from the initial and final commanded velocities and from the initial distance to go, leading to a problem with no degree of freedom.

The consumption itself is computed *a posteriori* from the velocity increments without any possibility to optimize it for given side conditions of the rendezvous.

The objective of the sequel is therefore to propose a new optimization algorithm for the general glideslope framework and extend the results to elliptic reference orbits, taking these two important features into account:

- Minimize the fuel consumption for a given set of initial and final rendezvous conditions and an *a priori* fixed time of transfer;
- Control the maximum guidance error by defining constraints on the humps profile.

The objective is therefore to identify a new formulation of the problem including useful degrees of freedom that allows to minimize the fuel consumption and helps to enclose the resulting trajectory segments between two successive maneuvers, usually referred to as hopping, in a user-defined approach corridor.

4.5. Guidance law #2: minimum-fuel fixed-time approach via Semidefinite Programming

In order to obtain a minimum-fuel solution to the glideslope guidance problem while controlling the guidance error, we propose a new controller based on a Semidefinite Programming (SDP) problem.

We first define the glideslope line tracking constraints according to the classical approach presented in Section 4.3 – reference [56] – or in [91]. Within this context, intermediate positions are free variables, as it will be shown hereafter. The maximum guidance error is addressed by defining constraints on the humps profile using a parametrization of the relative trajectory defined in [35] and results from polynomial optimization from the reference [89].

Finally, an SDP problem is proposed, whose solution leads to a general minimum-fuel multipulse glideslope guidance algorithm.

4.5.1. Glideslope line tracking constraint

In Hablani's glideslope algorithm in Section 4.4, the distance to go $\vec{\lambda}_k$ at each step k is directly known by applying Expression (4.26). However, in this new controller, the commanded profile is not fixed, releasing some degrees of freedom. For clarity purposes in the sequel, we re-write Expression (4.19), that parametrizes the commanded profile:

$$\vec{\rho}_k = \vec{\rho}_0 - \lambda_k\, \vec{u}_{gls},\ k = 0, 1, \cdots, N-1, \tag{4.28}$$

From Expression (4.8), we obtain a set of N equations of the form (4.21). Combining Equations (4.19) and (4.21a) enforces the requirement for the chaser to come back on the path after each maneuver period leading to:

$$[\vec{\rho}_0 - \lambda_{k+1}\, \vec{u}_{gls}] = \Phi_{rr}(t_{k+1}, t_k)\, [\vec{\rho}_0 - \lambda_k\, \vec{u}_{gls}] + \Phi_{rv}(t_{k+1}, t_k)\, \vec{v}_k^{\,+}, \tag{4.29}$$

such that:

$$-\lambda_{k+1}\, \vec{u}_{gls} + \Phi_{rr}(t_{k+1}, t_k)\, \lambda_k\, \vec{u}_{gls} - \Phi_{rv}(t_{k+1}, t_k)\, \vec{v}_k^{\,+} = [\Phi_{rr}(t_{k+1}, t_k) - I_3]\, \vec{\rho}_0, \tag{4.30}$$

for $k = 0, 1, \cdots, N-1$.

Since the reference orbit is considered to be elliptic, the transition matrix $\Phi(t_{k+1}, t_k)$ in (4.5) is not constant all over the orbit and needs to be updated for each maneuver. The time intervals for impulse control are input data, so that all transition matrices partitions $\Phi_{ij}(t_{k+1}, t_k)$ can be computed *a priori*.

The decision variables in (4.30) are composed by the sequence of scalar variables λ_k for $k = 1, 2, \cdots, N-1$ and by the sequence of vectors $\vec{v}_k^{\,+}$ for $k = 0, 1, \cdots, N-1$.

The sequence of impulses $\left\{\Delta\vec{V}_0, \Delta\vec{V}_1, \cdots, \Delta\vec{V}_k, \cdots, \Delta\vec{V}_{N-1}\right\}$ is deduced afterwards, computing the difference between the design variable $\vec{v}_k^{\,+}$ and the velocity vector $\vec{v}_k^{\,-}$ resulting from the previous maneuver and from the relative dynamics of the chaser in Equation (4.21b).

4.5.2. Final velocity constraint

It is also interesting for safety reasons to control the final velocity of the spacecraft. To this end, a last impulse $\Delta\vec{V}_N$ is needed and an additional equality constraint is defined. This $(N+1)^{th}$ impulse maneuver is given by evaluating Expressions (4.20) and (4.21b) at time t_N:

$$\Delta\vec{V}_N = \vec{v}_N^{\,+} - \Phi_{vr}(t_N, t_{N-1})\, \vec{\rho}_{N-1} - \Phi_{vv}(t_N, t_{N-1})\, \vec{v}_{N-1}^{\,+}. \tag{4.31}$$

Setting the vector $\vec{v}_N^+ = \vec{v}_f$ as the desired final velocity and $\Delta\vec{V}_N$ being a free variable, an extra equality constraint is appended once the term $\vec{\rho}_{N-1}$ is replaced by $\vec{\rho}_0 - \lambda_{N-1}\,\vec{u}_{gls}$:

$$-\Phi_{vr}(t_N, t_{N-1})\,\lambda_{N-1}\,\vec{u}_{gls} + \Phi_{vv}(t_N, t_{N-1})\,\vec{v}_{N-1}^+ + \Delta\vec{V}_N = \vec{v}_f - \Phi_{vr}(t_N, t_{N-1})\,\vec{\rho}_0. \tag{4.32}$$

The decision variables in (4.32) are composed by λ_{N-1}, $\vec{v}_{N-1}^+$ and $\Delta\vec{V}_N$.

4.5.3. Constraints on guidance error

The aim of this subsection is to give a numerically tractable formulation of the continuous constraints imposed on the spacecraft relative trajectory in order to bound the guidance error inherent to the impulsive glideslope approach.

In the spirit of the method developed in [35], the idea is to look for an equivalent finite description of the admissible relative trajectories using various tools from algebraic geometry and in particular, properties of non-negative polynomials.

The main steps of the method are:

1. define a piecewise linear envelope enclosing the admissible trajectory;
2. use a rational parametrization of the trajectory between each pulse to transform the previous continuous linear constraints into polynomials non negativity constraints;
3. apply representation theorems of cones of nonnegative polynomials from [89] to get a final SDP formulation of the constraints on guidance error.

4.5.3.1. Admissible trajectories envelope

First, a set of linear constraints on the chaser's relative trajectory is defined for each maneuver interval $[t_k\ t_{k+1}]$, defined as the elapsed time between the k^{th} impulse to the instant when the spacecraft is back on the glideslope line.

The input specifications regarding the maximal allowable excursion will define a rectangular corridor with four planes parallel to the glideslope direction $\vec{u}_{gls}$ bounding the trajectory at each step k. We define the parameters δ_{α_k} and δ_{β_k} to specify the distance from the glideslope line to each pair of planes, as shown in Figure 4.5a.

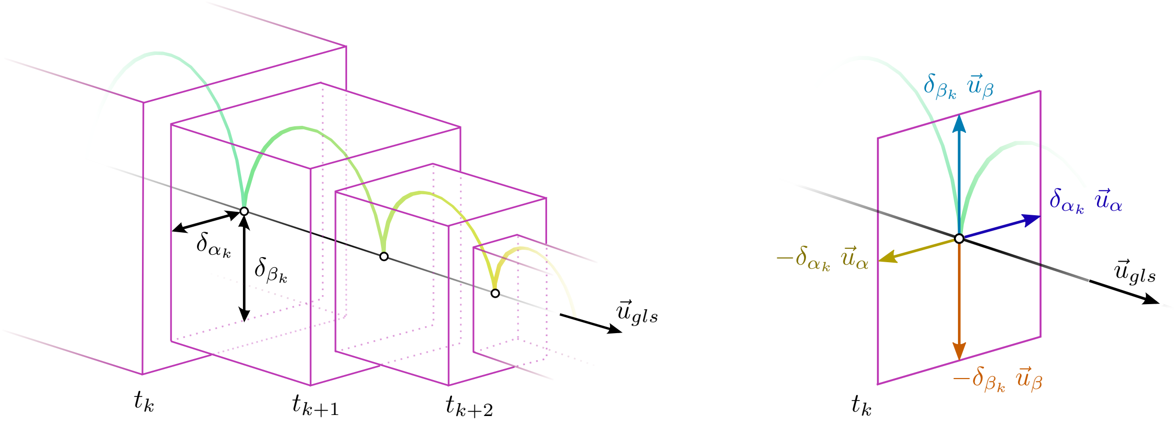

(a) Rectangular corridor bounding the trajectory.
(b) Orthonormal basis to vector $\vec{u}_{gls}$.

Figure 4.5: Glideslope corridor constraints.

A set of four linear constraints (upper and lower bounds for both parameters δ_{α_k} and δ_{β_k}) will be therefore necessary to define the maximum allowable excursion at each maneuver, represented by the following inequalities:

$$\begin{aligned} -\vec{u}_\alpha^{\,T}(\vec{\rho}_k - \delta_{\alpha_k}\,\vec{u}_\alpha) \le \vec{u}_\alpha^{\,T}\,\vec{\rho}(t) \le \vec{u}_\alpha^{\,T}(\vec{\rho}_k + \delta_{\alpha_k}\,\vec{u}_\alpha), \\ -\vec{u}_\beta^{\,T}(\vec{\rho}_k - \delta_{\beta_k}\,\vec{u}_\beta) \le \vec{u}_\beta^{\,T}\,\vec{\rho}(t) \le \vec{u}_\beta^{\,T}(\vec{\rho}_k + \delta_{\beta_k}\,\vec{u}_\beta), \end{aligned} \tag{4.33}$$

where $\vec{u}_\alpha$ and $\vec{u}_\beta$ are chosen as an orthonormal basis for the null space of $\vec{u}_{gls}^{\,T}$, as shown in Figure 4.5b.

The inequalities in Expression (4.33) can be recasted in a matrix form as:

$$A_k\,\vec{\rho}(t) \le b_k,\ \forall t \in [t_k\ t_{k+1}],\ \forall k = 0, 1, \dots, N-1 \tag{4.34}$$

where $A_k \in \mathbb{R}^{n_c \times 3}$ is a constant matrix, n_c denotes the number of scalar inequalities, each of which defines a plane bounding the trajectory ($n_c = 4$ in this case); and $b_k \in \mathbb{R}^{n_c}$ is a constant vector:

$$\underbrace{\begin{bmatrix} \vec{u}_\alpha^{\,T} \\ -\vec{u}_\alpha^{\,T} \\ \vec{u}_\beta^{\,T} \\ -\vec{u}_\beta^{\,T} \end{bmatrix}}_{A_k} \vec{\rho}(t) \le \underbrace{\begin{bmatrix} \vec{u}_\alpha^{\,T}(\vec{\rho}_k + \delta_{\alpha_k}\,\vec{u}_\alpha) \\ -\vec{u}_\alpha^{\,T}(\vec{\rho}_k - \delta_{\alpha_k}\,\vec{u}_\alpha) \\ \vec{u}_\beta^{\,T}(\vec{\rho}_k + \delta_{\beta_k}\,\vec{u}_\beta) \\ -\vec{u}_\beta^{\,T}(\vec{\rho}_k - \delta_{\beta_k}\,\vec{u}_\beta) \end{bmatrix}}_{b_k}, \tag{4.35}$$

where the inequalitites are considered term to term. Matrix A_k is constant $\forall k = 0, 1, \dots, N-1$. However, vector b_k might change according to the different distance specifications $\{\delta_{\alpha_k}, \delta_{\beta_k}\}$ associated to each maneuver k, as shown in Figure 4.5a.

We can express the inequalities for the corridor constraints in (4.34) parametrized in *tilde* coordinates, as shown in Chapter 2. By means of Equation (2.76), we obtain the expression of the relative position vector $\vec{\tilde{r}}(\nu)$ as:

$$\vec{\rho}(t) = T_{TH}^{-1}(\nu)\,\vec{\tilde{r}}(\nu), \tag{4.36}$$

such that Expression (4.34) becomes:

$$A_k\,\vec{\tilde{r}}(\nu) \le\ \kappa(\nu)\,b_k,\ \ \forall \nu \in [\nu_k\ \nu_{k+1}],\ \ \forall k = 0, 1, \dots, N-1. \tag{4.37}$$

Within these *tilde* variables, any relative trajectory is parametrized by K_i, $i = 1, \dots, 6$ as in Expressions (2.90) and (2.104), gathered hereafter:

$$\begin{cases} \tilde{x}(\nu) = K_3 - \cos(\nu)\,(\kappa(\nu)+1)\ K_4 + \sin(\nu)\,(\kappa(\nu)+1)\ K_5 + 3\,\kappa(\nu)^2 J(\nu,\nu_0)\ K_6, \\ \tilde{y}(\nu) = \cos(\nu)\ K_1 + \sin(\nu)\ K_2, \\ \tilde{z}(\nu) = \kappa(\nu)\sin(\nu)\ K_4 + \kappa(\nu)\cos(\nu)\ K_5 + (2 - 3\,e\sin(\nu)\ J(\nu,\nu_0))\ K_6, \end{cases} \tag{4.38}$$

for $\nu \in [\nu_0, \nu_f]$.

4.5.3.2. Transformation of the admissible trajectories constraints into polynomial non-negativity constraints

Expression (4.38) shows several trigonometrical terms. The following change of variable is used in order to transform the trigonometrical functions into rational functions:

$$w = \tan\frac{\nu}{2},\ \cos(\nu) = \frac{1-w^2}{1+w^2},\ \sin(\nu) = \frac{2w}{1+w^2}. \tag{4.39}$$

This transformation allows us to obtain a description of the relative trajectories containing terms of the same nature [31] such that the continuous linear constraints in (4.34) can be expressed into polynomial non negativity constraints that lead to a finite description of the admissible trajectories.

The propagation of the spacecraft relative motion in (4.38) can then be expressed as a function of w:

$$\begin{cases} \tilde{x}(w) = K_3 - \dfrac{1-w^2}{1+w^2}\left(\left(1+e\dfrac{1-w^2}{1+w^2}\right)+1\right) K_4 + \dfrac{2w}{1+w^2}\left(\left(1+e\dfrac{1-w^2}{1+w^2}\right)+1\right) K_5 + 3\left(1+e\dfrac{1-w^2}{1+w^2}\right)^2 J(\nu,\nu_0)\, K_6, \\ \tilde{y}(w) = \dfrac{1-w^2}{1+w^2}\, K_1 + \dfrac{2w}{1+w^2}\, K_2, \\ \tilde{z}(w) = \left(1+e\dfrac{1-w^2}{1+w^2}\right)\dfrac{2w}{1+w^2}\, K_4 + \left(1+e\dfrac{1-w^2}{1+w^2}\right)\dfrac{1-w^2}{1+w^2}\, K_5 + \left(2-3e\dfrac{2w}{1+w^2}J(\nu,\nu_0)\right) K_6. \end{cases} \tag{4.40}$$

These equations can be compactly written as:

$$\begin{cases} \tilde{x}(w) = R_{xyz}(w)\left[P_x(w) + 3P_{Jx}(w)J(w)\, K_6\right], \\ \tilde{y}(w) = R_{xyz}(w)(1+w^2)\, P_y(w), \\ \tilde{z}(w) = R_{xyz}(w)\left[P_z(w) + 2P_{Jz}(w)J(w)\, K_6\right]. \end{cases} \tag{4.41}$$

All $R_{xyz}(w)$ and $P_{(\cdot)}(w)$ functions are polynomials, whose expressions are detailed below once Expression (4.40) has been worked out:

$$R_{xyz}(w) = \frac{1}{(1+w^2)^2}. \tag{4.42}$$

The polynomials $P_{Jx}(w)$ and $P_{Jz}(w)$ are given by:

$$\begin{aligned} P_{Jx}(w) &= \left((1+e)+(1-e)w^2\right)^2, \\ P_{Jz}(w) &= -3e\left((1+e)w+(1-e)w^3\right). \end{aligned} \tag{4.43}$$

The coefficients of $P_x(w)$, $P_y(w)$ and $P_z(w)$ depend linearly on the vector K, as shown below:

$$P_x(w) = \sum_{i=0}^{4} p_{xi}w^i, \qquad P_y(w) = \sum_{i=0}^{2} p_{yi}w^i, \qquad P_z(w) = \sum_{i=0}^{4} p_{zi}w^i, \tag{4.44}$$

where the polynomial $P_x(w)$ is defined as:

$$\underbrace{\begin{bmatrix} p_{x0} \\ p_{x1} \\ p_{x2} \\ p_{x3} \\ p_{x4} \end{bmatrix}}_{p_x} = \begin{bmatrix} 0 & 0 & -1 & -2-e & 0 & 0 \\ 0 & 0 & 0 & 0 & 4+2e & 0 \\ 0 & 0 & 2 & 2e & 0 & 0 \\ 0 & 0 & 0 & 0 & 4-2e & 0 \\ 0 & 0 & 1 & 2-e & 0 & 0 \end{bmatrix} \begin{bmatrix} K_1 \\ K_2 \\ K_3 \\ K_4 \\ K_5 \\ K_6 \end{bmatrix}, \tag{4.45}$$

the polynomial $P_y(w)$ is:

$$\underbrace{\begin{bmatrix} p_{y0} \\ p_{y1} \\ p_{y2} \end{bmatrix}}_{p_y} = \begin{bmatrix} 1 & 0 & 0 & 0 & 0 & 0 \\ 0 & 2 & 0 & 0 & 0 & 0 \\ -1 & 0 & 0 & 0 & 0 & 0 \end{bmatrix} \begin{bmatrix} K_1 \\ K_2 \\ K_3 \\ K_4 \\ K_5 \\ K_6 \end{bmatrix}, \tag{4.46}$$

and the polynomial $P_z(w)$ is:

$$\underbrace{\begin{bmatrix} p_{z0} \\ p_{z1} \\ p_{z2} \\ p_{z3} \\ p_{z4} \end{bmatrix}}_{p_z} = \begin{bmatrix} 0 & 0 & 0 & 0 & e+1 & 2 \\ 0 & 0 & 0 & 2e+2 & 0 & 0 \\ 0 & 0 & 0 & 0 & -2e & 4 \\ 0 & 0 & 0 & 2-2e & 0 & 0 \\ 0 & 0 & 0 & 0 & e-1 & 2 \end{bmatrix} \begin{bmatrix} K_1 \\ K_2 \\ K_3 \\ K_4 \\ K_5 \\ K_6 \end{bmatrix}. \tag{4.47}$$

Before defining trajectory constraints, we first need to deal with the term $J(w)$ in the spacecraft relative motion (4.41). In [31], the integral term is given by its closed form solution:

$$J(w) = \left[\frac{2ew}{(e^2-1)(e+1+(1-e)w^2)} - \frac{2 \arctan h \left(\frac{\sqrt{e-1}}{\sqrt{e+1}} w \right)}{\sqrt{(e^2-1)^3}} \right]_{w_0}^{w}. \tag{4.48}$$

In order to have a rational expression for the motion, a polynomial approximation is derived to bound J over $w \in [w_0, w_f]$:

$$J(w) = \Theta_r(w) + \varepsilon(w) \Rightarrow \underbrace{\Theta_r(w) - \bar{\varepsilon}}_{\Theta_l(w)} \leq J(w) \leq \underbrace{\Theta_r(w) + \bar{\varepsilon}}_{\Theta_u(w)} \tag{4.49}$$

where $\Theta_r(w)$ is a polynomial of degree r and $\bar{\varepsilon}$ the maximum error due to the approximation.

The linear constraints (4.37) are transformed by the change of variables (4.39) into:

$$A_k \, \vec{\tilde{r}}(w) \leq \left(\frac{1+e+(1-e)w^2}{1+w^2} \right) b_k, \ \ \forall w \in [w_k \; w_{k+1}], \ \ \forall k = 0, 1, \ldots, N-1, \tag{4.50}$$

with $w_k = \tan \dfrac{\nu_k}{2}$. In matrix form, Equation (4.50) is given by:

$$\begin{bmatrix} A_{k_{1,1}} & A_{k_{1,2}} & A_{k_{1,3}} \\ A_{k_{2,1}} & A_{k_{2,2}} & A_{k_{2,3}} \\ A_{k_{3,1}} & A_{k_{3,2}} & A_{k_{3,3}} \\ A_{k_{4,1}} & A_{k_{4,2}} & A_{k_{4,3}} \end{bmatrix} \begin{bmatrix} \tilde{x}(w) \\ \tilde{y}(w) \\ \tilde{z}(w) \end{bmatrix} = \begin{bmatrix} b_{k_1} \\ b_{k_2} \\ b_{k_3} \\ b_{k_4} \end{bmatrix}, \tag{4.51}$$

such that the i^{th} row of this latter expression is:

$$A_{k_{i,1}} \tilde{x}(w) + A_{k_{i,2}} \tilde{y}(w) + A_{k_{i,3}} \tilde{z}(w) \leq b_{k_i}. \tag{4.52}$$

Replacing $\tilde{x}(w)$, $\tilde{y}(w)$ and $\tilde{z}(w)$ by their values in Expression (4.41), we obtain:

$$R_{xyz}(w)\left[A_{k_{i,1}}\left(P_x(w)+3P_{Jx}(w)J(w)\,K_6\right)+A_{k_{i,2}}\left(\left(1+w^2\right)P_y(w)\right)+A_{k_{i,3}}\left(P_z(w)+2P_{Jz}(w)J(w)\,K_6\right)\right]\leq \left(\frac{1+e+(1-e)w^2}{1+w^2}\right)b_{k_i}. \tag{4.53}$$

If we denote:

$$\begin{aligned}\Gamma_i^k(w)&=\left[(1+w^2)(1+e+(1-e)w^2)\right]b_{k_i}\\&\quad-A_{k_{i,1}}\left(P_x(w)+3P_{Jx}(w)J(w)\,K_6\right)-A_{k_{i,2}}\left(\left(1+w^2\right)P_y(w)\right)-A_{k_{i,3}}\left(P_z(w)+2P_{Jz}(w)J(w)\,K_6\right),\end{aligned} \tag{4.54}$$

we obtain:

$$\frac{\Gamma_i^k(w)}{R_{xyz}(w)}\geq 0. \tag{4.55}$$

Replacing the function $J(w)$ by the two extreme bounding polynomials Θ_l and Θ_u, the function in (4.55) becomes polynomial, leading to $\Gamma_{il}^k(w)$ and $\Gamma_{iu}^k(w)$, defined as:

$$\begin{aligned}\Gamma_{il}^k(w)&=\left[(1+w^2)(1+e+(1-e)w^2)\right]b_{k_i}-A_{k_{i,1}}\left(P_x(w)+3P_{Jx}(w)\Theta_l(w)\,K_6\right)\\&\quad-A_{k_{i,2}}\left(\left(1+w^2\right)P_y(w)\right)-A_{k_{i,3}}\left(P_z(w)+2P_{Jz}(w)\Theta_l(w)\,K_6\right),\\\Gamma_{iu}^k(w)&=\left[(1+w^2)(1+e+(1-e)w^2)\right]b_{k_i}-A_{k_{i,1}}\left(P_x(w)+3P_{Jx}(w)\Theta_u(w)\,K_6\right)\\&\quad-A_{k_{i,2}}\left(\left(1+w^2\right)P_y(w)\right)-A_{k_{i,3}}\left(P_z(w)+2P_{Jz}(w)\Theta_u(w)\,K_6\right).\end{aligned} \tag{4.56}$$

Hence, the inequality (4.55) becomes a pair of inequalities with $\Gamma_{il}^k(w)$ and $\Gamma_{iu}^k(w)$, that must be repeated for each i^{th} row of A_k (i.e. each constraint) and for each maneuver k. Finally, the whole constraint on the guidance error (4.55) is formulated as the polynomial non negativity constraints:

$$\begin{cases}\Gamma_{il}^k(w)\geq 0, & \forall i=1,2,\ldots,n_c,\quad \forall k=0,1,\ldots,N-1,\\ \Gamma_{iu}^k(w)\geq 0, & \forall w\in[w_k\ w_{k+1}].\end{cases} \tag{4.57}$$

4.5.3.3. Semidefinite formulation for the guidance error

The properties of non negative polynomials and representation theorems of cones of non negative polynomials given in [89] are now used to translate these inequalities defined on an infinite interval into a SDP problem involving a finite number of decision variables.

The full development of the SDP formulation may be obtained in the appendix of the reference [35] from where we have extracted the basic concepts based on [89], recalled hereafter.

If $\mathcal{K}_{a,b}$ is the convex, closed and pointed cone of the coefficients of polynomials that are non negative on a finite interval $[a,b]\in\mathbb{R}$:

$$\mathcal{K}_{a,b}=\left\{p\in\mathbb{R}^{n+1},\ P(w)=\sum_{i=0}^{n}p_iw^i,\ \forall w\in[a,b]\right\}. \tag{4.58}$$

a polynomial $P(w)$ represented through its vector of coefficients $[p_0\quad p_1\quad\cdots\quad p_n]^T$ belongs to $\mathcal{K}_{a,b}$ if and only if there exist two symmetric positive semidefinite matrices Y_1 and Y_2 such that:

$$p\in\mathcal{K}_{a,b}\Leftrightarrow\exists\,Y_1,\ Y_2\succeq 0\ \ s.t.\ \ p=\Lambda^*(Y_1,Y_2). \tag{4.59}$$

The definition of the linear operator Λ^* and the dimensions of Y_1, Y_2 depend on whether the polynomials $P(w)$ in Expressions (4.44) have an odd or even degree. In the three cases considered here, n is even, therefore $Y_1\in\mathbb{R}^{(m+1)\times(m+1)}\succeq 0$ and $Y_2\in\mathbb{R}^{m\times m}\succeq 0$, where $m=n/2$.

Now, let $H_{k,i} \in \mathbb{R}^{(k+1)\times(k+1)}$ be Hankel matrices that contain ones on the i^{th} anti-diagonal and zeros everywhere else:

$$H_{k,1} = \begin{bmatrix} 1 & 0 & 0 & \cdots & 0 \\ 0 & 0 & 0 & \cdots & 0 \\ 0 & 0 & 0 & \cdots & 0 \\ \vdots & \vdots & \vdots & \ddots & \vdots \\ 0 & 0 & 0 & \cdots & 0 \end{bmatrix}, \quad H_{k,2} = \begin{bmatrix} 0 & 1 & 0 & \cdots & 0 \\ 1 & 0 & 0 & \cdots & 0 \\ 0 & 0 & 0 & \cdots & 0 \\ \vdots & \vdots & \vdots & \ddots & \vdots \\ 0 & 0 & 0 & \cdots & 0 \end{bmatrix}, \quad H_{k,3} = \begin{bmatrix} 0 & 0 & 1 & \cdots & 0 \\ 0 & 1 & 0 & \cdots & 0 \\ 1 & 0 & 0 & \cdots & 0 \\ \vdots & \vdots & \vdots & \ddots & \vdots \\ 0 & 0 & 0 & \cdots & 0 \end{bmatrix}. \tag{4.60}$$

The linear operator Λ^* is then defined by:

$$\Lambda^*(Y_1, Y_2) = \begin{bmatrix} \text{tr}(Y_1 H_{m,1}) & + & \text{tr}(Y_2(-abH_{m-1,1})) \\ \text{tr}(Y_1 H_{m,2}) & + & \text{tr}(Y_2((b+a)H_{m-1,1} - abH_{m-1,2})) \\ \text{tr}(Y_1 H_{m,3}) & + & \text{tr}(Y_2((b+a)H_{m-1,2} - H_{m-1,1} - abH_{m-1,3})) \\ & \vdots & \\ \text{tr}(Y_1 H_{m,i}) & + & \text{tr}(Y_2((b+a)H_{m-1,i-1} - H_{m-1,i-2} - abH_{m-1,i})) \\ & \vdots & \\ \text{tr}(Y_1 H_{m,2m}) & + & \text{tr}(Y_2((b+a)H_{m-1,2m-1} - H_{m-1,2m-2})) \\ \text{tr}(Y_1 H_{m,2m+1}) & + & \text{tr}(Y_2(-H_{m-1,2m-1})) \end{bmatrix}. \tag{4.61}$$

The guidance constraints in Expression (4.57) can then be translated into:

$$\begin{cases} \exists\, Y_{1il}^k, Y_{2il}^k \succeq 0 \quad \text{s.t.} \quad \gamma_{il}^k = \Lambda^*(Y_{1il}^k, Y_{2il}^k), \\ \exists\, Y_{1iu}^k, Y_{2iu}^k \succeq 0 \quad \text{s.t.} \quad \gamma_{iu}^k = \Lambda^*(Y_{1iu}^k, Y_{2iu}^k), \end{cases} \tag{4.62}$$

for $i = 1, 2, \ldots, n_c$, $k = 0, 1, \ldots, N-1$ and where $\Gamma_{il}^k(w)$ and $\Gamma_{iu}^k(w)$ are represented by their vector of coefficients γ_{il}^k and γ_{iu}^k, respectively.

When considering a second order polynomial approximation, we have that $Y_{1il}^k \in \mathbb{R}^{4\times4}$, $Y_{2il}^k \in \mathbb{R}^{3\times3}$, $Y_{1iu}^k \in \mathbb{R}^{4\times4}$ and $Y_{2iu}^k \in \mathbb{R}^{3\times3}$. Vectors γ_{il}^k and γ_{iu}^k are the given vectors of coefficients of polynomials Γ_{il}^k and Γ_{iu}^k.

4.5.4. Definition of the cost function

Apart the control of the humps during the glideslope, the other main objective of the approach is to minimize the fuel consumption during the transfer. As 6 ungimbaled identical chemical thrusters are used, the cost function may be naturally defined as the 1-norm of the $N+1$ impulsive thrusts, as defined in Appendix F, Expression (F.5):

$$\begin{aligned} J &= \sum_{k=0}^{N} ||\Delta\vec{V}_k||_1, \\ &= ||\Delta\vec{V}_0||_1 + \sum_{k=1}^{N-1} \|\Delta\vec{V}_k\|_1 + \|\Delta\vec{V}_N\|_1, \end{aligned} \tag{4.63}$$

with $\Delta\vec{V}_k = \vec{v}_k^{\,+} - \vec{v}_k^{\,-}$. The formulation (4.63) is transformed in order to express the above criterion with respect to the different decision variables:

- $\vec{v}_k^{\,+}$, $k = 0, 1, \cdots, N-1$,
- λ_k, $k = 1, 2, \cdots, N-1$,
- $\Delta\vec{V}_N$.

If we develop Equation (4.63) by using Expressions (4.21b) and (4.19), we obtain:

$$J = \|\vec{v}_0^{\,+} - \vec{v}_0^{\,-}\|_1 + \sum_{k=1}^{N-1} \|\vec{v}_k^{\,+} - \Phi_{vr}(t_k, t_{k-1})\,(\vec{\rho}_0 - \lambda_{k-1}\vec{u}_{gls}) - \Phi_{vv}(t_k, t_{k-1})\,\vec{v}_{k-1}^{\,+}\|_1 + \|\vec{v}_N^{\,+} - \vec{v}_N^{\,-}\|_1. \tag{4.64}$$

This cost function involving absolute values can be transformed into a linear function with the introduction of new variables and inequality constraints, using a usual trick in linear programming [12]:

$$\begin{aligned} \vec{v}_0^{\,+} - \vec{v}_0^{\,-} &\leq d_0, \\ -\left(\vec{v}_0^{\,+} - \vec{v}_0^{\,-}\right) &\leq d_0, \\ \vec{v}_k^{\,+} - \Phi_{vr}(t_k, t_{k-1})\,(\vec{\rho}_0 - \lambda_{k-1}\vec{u}_{gls}) - \Phi_{vv}(t_k, t_{k-1})\,\vec{v}_{k-1}^{\,+} &\leq d_k, \\ -\left(\vec{v}_k^{\,+} - \Phi_{vr}(t_k, t_{k-1})\,(\vec{\rho}_0 - \lambda_{k-1}\vec{u}_{gls}) - \Phi_{vv}(t_k, t_{k-1})\,\vec{v}_{k-1}^{\,+}\right) &\leq d_k, \\ \vec{v}_N^{\,+} - \vec{v}_N^{\,-} &\leq d_N, \\ -\left(\vec{v}_N^{\,+} - \vec{v}_N^{\,-}\right) &\leq d_N, \end{aligned} \tag{4.65}$$

where d_k are extra decision variables. The cost function becomes then:

$$J = \sum_{k=0}^{N} [1 \quad 1 \quad 1]\; d_k. \tag{4.66}$$

4.5.5. A semidefinite programming problem

In order to achieve a compact SDP formulation, we just have to gather the different terms defined in the previous subsections.

Therefore, a solution to the initial minimum-fuel glideslope guidance problem may be obtained via the solution of the following SDP problem:

$$
\begin{aligned}
&\min\ c^T D \\
&\text{s.t.} \\
&\lambda_{k+1}\,\vec{u}_{gls} - \Phi_{rr}(t_{k+1},t_k)\,\lambda_k\,\vec{u}_{gls} - \Phi_{rv}(t_{k+1},t_k)\,\vec{v}_k^{\,+} = \left[\Phi_{rr}(t_{k+1},t_k) - I_3\right]\vec{\rho}_0, \\
&\qquad\qquad\qquad\qquad\qquad\qquad\qquad \lambda_1 u - \Phi_{rv}^{[0]}\vec{v}_0^{\,+} = (\Phi_{rr}^{[0]} - I_3)\vec{\rho}_0, \\
&\vec{v}_f - \Phi_{vr}(t_N,t_{N-1})\,\vec{\rho}_0 = \Phi_{vr}(t_N,t_{N-1})\,\lambda_{N-1}\,\vec{u}_{gls} + \Phi_{vv}(t_N,t_{N-1})\,\vec{v}_{N-1}^{\,+} + \Delta\vec{V}_N \\
&d_0 \geq \vec{v}_0^{\,+} - \vec{v}_0^{\,-}, \\
&d_0 \geq -\left(\vec{v}_0^{\,+} - \vec{v}_0^{\,-}\right), \\
&d_k \geq \vec{v}_k^{\,+} - \Phi_{vr}(t_k,t_{k-1})\,(\vec{\rho}_0 + \lambda_{k-1}\vec{u}_{gls}) - \Phi_{vv}(t_k,t_{k-1})\,\vec{v}_{k-1}^{\,+}, \\
&d_k \geq -\left(\vec{v}_k^{\,+} - \Phi_{vr}(t_k,t_{k-1})\,(\vec{\rho}_0 + \lambda_{k-1}\vec{u}_{gls}) - \Phi_{vv}(t_k,t_{k-1})\,\vec{v}_{k-1}^{\,+}\right),\ k = 1,\ldots,N-1, \\
&d_N \geq \vec{v}_N^{\,+} - \vec{v}_N^{\,-}, \\
&d_N \geq -\left(\vec{v}_N^{\,+} - \vec{v}_N^{\,-}\right), \\
&\gamma_{il}^k = \Lambda^*(Y_{1il}^k, Y_{2il}^k),\ i = 1,2,\ldots,n_c,\ k = 0,1,\ldots,N-1, \\
&\gamma_{iu}^k = \Lambda^*(Y_{1iu}^k, Y_{2iu}^k), \\
&Y_{1il}^k \succeq 0,\ Y_{2il}^k \succeq 0, \\
&Y_{1iu}^k \succeq 0,\ Y_{2iu}^k \succeq 0,
\end{aligned}
\tag{4.67}
$$

with $c = [1 \quad 1 \quad \ldots \quad 1]^T$ and $D = \left[d_0^T \quad d_1^T \quad \ldots \quad d_N^T\right]^T$. The decision variables of the SDP in Expression (4.67) are:

- d_k for $k = 0,1,\ldots,N$,
- λ_k for $k = 1,2,\ldots,N-1$,
- $\vec{v}_k^{\,+}$ for $k = 0,1,\ldots,N-1$,
- $\Delta\vec{V}_N$,
- Y_{1il}^k, Y_{2il}^k, Y_{1iu}^k and Y_{2iu}^k for $i = 1,2,\ldots,n_c$, for $k = 0,1,\ldots,N-1$.

4.5.6. Algorithm

```
Data: chaser's information:
        initial true anomaly $\nu_0$ and initial position and velocity in target's LVLH frame $\vec{\rho}_0$, $\vec{v}_0^{\,-}$;
        final desired position and velocity in target's LVLH frame $\vec{\rho}_f = \vec{\rho}_N$, $\vec{v}_f = \vec{v}_N^{\,+}$;
        number of maneuvers $N$;
        transfer time $T$;
        maximum allowable excursion $\delta_k$;
Initialization: initial distance to go $\lambda_0$;
                unit vector $\vec{u}_{gls}$;
                interval between consecutive impulses $\Delta t$;
                state transition matrices $\Phi_{rr}(t_{k+1}, t_k)$, $\Phi_{rv}(t_{k+1}, t_k)$, $\Phi_{vr}(t_{k+1}, t_k)$, $\Phi_{vv}(t_{k+1}, t_k)$;
Compute: cost matrix $c$ ;
         glideslope constraints ;
         final velocity constraints ;
         excursion constraints ;
         guidance constraints matrix $\Lambda^*(Y_{1il}^k, Y_{2il}^k)$ and $\Lambda^*(Y_{1ul}^k, Y_{2ul}^k)$ ;
Solve: SDP problem (4.67):
if solution found then
    extract: departure velocity from $k$, $\vec{v}_k^{\,+}$ ;
    for $k = 1, \cdots, N$ do
        compute: next relative position at $k+1$, $\vec{\rho}_{k+1}$ in (4.21a) ;
                 arrival velocity at $k+1$, $\vec{v}_{k+1}^{\,-}$ in (4.21b) ;
                 impulsive maneuver at $k$, $\Delta\vec{V}_k$ in (4.23);
    end
    compute: impulsive maneuver at $N$, $\Delta\vec{V}_N$ in (4.31);
else
    increase values $\delta_k$, update constraints, re-run solver.
end
```

Algorithm 2: Minimum-fuel SDP glideslope.

In this section, an SDP problem is proposed to find a fuel-optimal solution with a bounded guidance error in a general elliptical case, two desired characteristics for the glideslope problem. However, if we consider a circular orbit, and more precisely, either a V-bar or an R-bar approach defined in the local orbital plane $x - z$, the SDP problem is simplified and the controller design is based on the solution of an LP problem.

In the sequel of this chapter, we present these two particular cases of Guidance law #2 when the approach is either a V-bar, or R-bar approaches for a circular orbit. If the excursion constraint is eliminated, the SDP problem (4.67) simplifies to an LP problem, whose detailed developments are worth giving in the next sections.

4.6. Guidance law #3: minimum-fuel fixed-time V-bar and R-bar approaches via Linear Programming

The goal here is to show that when the direction of the glideslope is defined to be the V-bar or the R-bar directions and for a circular reference orbit, the previous SDP problem (4.67) may be simplified by using analytical developments to characterize the bounding corridor.

Indeed, the main development is the same as for Section 4.5: we first define the glideslope line tracking constraints according to the classical approach presented in Section 4.3. The maximum guidance error is then addressed by defining constraints on the humps profile and bounding them for both V-bar and R-bar cases.

Finally, we propose a linear programming formulation leading to the obtention of a minimum-fuel solution to the glideslope guidance problem while controlling the guidance error for both V-bar and R-bar approaches.

4.6.1. V-bar and R-bar

In the literature, we find several missions that were performed following the V-bar classic approach, such as the ESA's ATV program or the NASA's Space Shuttle mission. Among the R-bar approach, we distinguish Japan's HTV, SpaceX's Dragon mission or NASA's Cygnus program [85].

These two common approach strategies are based on the directions of approaching a target in the close range phase of the rendezvous mission in a circular reference orbit, as shown in Figure 4.6. This is mainly due to observability — LoS — constraints and safety reasons imposing the requirement of a trajectory belonging to a cone-shaped approach corridor.

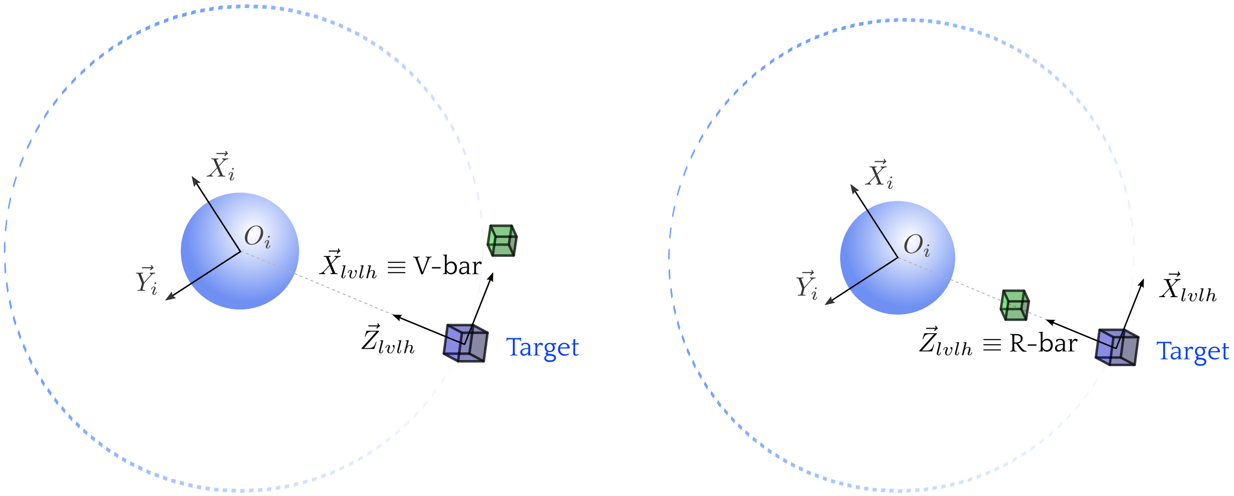

(a) V-bar approach.

(b) R-bar approach.

Figure 4.6: Chaser satellite following a V-bar and R-bar glideslope approach.

V-bar and R-bar approaches are specific motions by which the chaser approaches the target in the tangential direction (V-bar) or radial direction (R-bar), meaning that the motion is restricted to the target's orbital plane.

In the case of a circular orbit, the relative dynamics in Expression (4.5) can be simplified by taking advantage of the fact that the dynamic matrix is LTI.

By defining the relative position vector as $\vec{\rho}(t) = [x \;\; z]^T$ and the relative velocity as $\vec{v}(t) = [\dot{x} \;\; \dot{z}]^T$, the four partitions of $\Phi(t, t_0)$ in Expression (4.6) have a simpler expression by just selecting the appropriate rows and columns. Since the interval between two consecutive thrusts Δt is constant — given by Expression (4.17) —, the transition matrix is constant and depends only on that interval Δt. We have therefore $\Phi_{rr}(t,t_0) = \Phi_{rr}$, $\Phi_{rv}(t,t_0) = \Phi_{rv}$, $\Phi_{vr}(t,t_0) = \Phi_{vr}$ and $\Phi_{vv}(t,t_0) = \Phi_{vv}$, as:

$$\Phi_{rr} = \begin{bmatrix} 1 & 6\,(\omega\Delta t - \sin(\omega\Delta t)) \\ 0 & 4 - 3\cos(\omega\Delta t) \end{bmatrix}, \qquad \Phi_{rv} = \begin{bmatrix} (4/\omega)\sin(\omega\Delta t) - 3\Delta t & (2/\omega)(1-\cos(\omega\Delta t)) \\ -(2/\omega)(1-\cos(\omega\Delta t)) & \sin(\omega\Delta t)/\omega \end{bmatrix},$$
$$\Phi_{vr} = \begin{bmatrix} 0 & 6\,\omega(1-\cos(\omega\Delta t)) \\ 0 & 3\omega\sin(\omega\Delta t) \end{bmatrix}, \qquad \Phi_{vv} = \begin{bmatrix} -3 + 4\cos(\omega\Delta t) & 2\sin(\omega\Delta t) \\ -2\sin(\omega\Delta t) & \cos(\omega\Delta t) \end{bmatrix}, \tag{4.68}$$

with $\Delta t = t - t_0$.

4.6.2. Glideslope line tracking constraint

The glideslope objective is to perform the chaser's transfer from an initial position $\vec{\rho}_0$ to a final position $\vec{\rho}_f = \vec{\rho}_N$ in N maneuvers in a fixed time T, where the maneuvers are equally spaced in time according to (4.18).

According to wether we perform a V-bar approach or an R-bar approach, the relative position vectors will vary. If the approach is of the type V-bar, the component in z stays constant and equal to its initial value, z_0, leading to:

$$\vec{\rho}_0 = \begin{bmatrix} x_0 \\ z_0 \end{bmatrix}, \qquad \vec{\rho}_k = \begin{bmatrix} x_k \\ z_0 \end{bmatrix}, \qquad \vec{\rho}_f = \begin{bmatrix} x_f \\ z_0 \end{bmatrix}. \tag{4.69}$$

On the other hand, if the approach is of the type R-bar, we focus on maintaining x constant and equal to x_0:

$$\vec{\rho}_0 = \begin{bmatrix} x_0 \\ z_0 \end{bmatrix}, \qquad \vec{\rho}_k = \begin{bmatrix} x_0 \\ z_k \end{bmatrix}, \qquad \vec{\rho}_f = \begin{bmatrix} x_0 \\ z_f \end{bmatrix}. \tag{4.70}$$

For this controller, the intermediate positions $\vec{\rho}_k$ are not fixed, as for Guidance law #2 in Section 4.5. We have therefore extra degrees of freedom to exploit. After each maneuver, we impose to the chaser to be back on the glideslope. Such a requirement can be enforced by N equations of the form of Expression (4.21):

$$\vec{\rho}_{k+1} = \Phi_{rr}\,\vec{\rho}_k + \Phi_{rv}\,\vec{v}_k^{\,+}, \tag{4.71a}$$
$$\vec{v}_{k+1}^{\,-} = \Phi_{vr}\,\vec{\rho}_k + \Phi_{vv}\,\vec{v}_k^{\,+}. \tag{4.71b}$$

for $k = 0, 1, \dots, N-1$. The decision variables are the components x_k for the V-bar approach or z_k for the R-bar contained within the relative position vector $\vec{\rho}_k$, as well as the velocity vector $\vec{v}_k^{\,+}$. Hence, all positions on the glideslope, except the initial and final ones, are set free.

4.6.3. Final velocity constraint

As for Guidance law #2 in Section 4.5, it is interesting to control the final velocity of the spacecraft after the last impulse. This $(N+1)^{th}$ impulse maneuver is given by evaluating Expressions (4.20) and (4.21b) at N:

$$\Delta\vec{V}_N = \vec{v}_N^{\,+} - \Phi_{vr}\,\vec{\rho}_{N-1} - \Phi_{vv}\,\vec{v}_{N-1}^{\,+}. \tag{4.72}$$

By setting the vector $\vec{v}_N^{\,+} = \vec{v}_f$ as the desired final velocity, the decision variables of the above expression are then $\Delta\vec{V}_N$, $\vec{\rho}_{N-1}$ and $\vec{v}_{N-1}^{\,+}$.

4.6.4. Constraints on guidance error

In order to control the maximum guidance error by defining constraints on the humps profile, we first need to define the error in the orbital plane or *excursion* $\vec{\epsilon}$ in a general framework for both V-bar and R-bar approaches.

Let us define the point A in the $x-z$ plane (see Figure 4.7) as the orthogonal projection of the chaser position $\vec{\rho}_c$ on the glideslope straight line. The excursion $\vec{\epsilon}$ is given by the difference between vectors $\vec{\rho}(t)$ and $\vec{\rho}_{gls}(t)$:

$$\vec{\epsilon} = \vec{\rho}(t) - \vec{\rho}_{gls}(t). \tag{4.73}$$

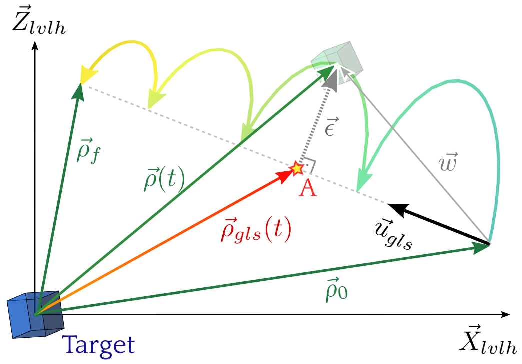

Figure 4.7: In-plane glideslope approach.

The auxiliary vector $\vec{\rho}_{gls}(t)$ can be itself expressed as:

$$\vec{\rho}_{gls}(t) = \vec{\rho}_0 + (\vec{w}^T\, \vec{u}_{gls})\, \vec{u}_{gls}, \tag{4.74}$$

where $\vec{w} = \vec{\rho}(t) - \vec{\rho}_0$ is also an auxiliary vector and $\vec{u}_{gls}$ is the unit vector defining the glideslope straight line, defined in Equation (4.15), but for the in-plane current case:

$$\vec{u}_{gls} = \begin{bmatrix} \dfrac{x_f - x_0}{||\vec{\lambda}_0||} & 0 & \dfrac{z_f - z_0}{||\vec{\lambda}_0||} \end{bmatrix}. \tag{4.75}$$

Hence, the excursion can be written as:

$$\vec{\epsilon} = (\vec{\rho}(t) - \vec{\rho}_0) - ((\vec{\rho}(t) - \vec{\rho}_0)^T\, \vec{u}_{gls})\, \vec{u}_{gls}. \tag{4.76}$$

If we note $\Delta\vec{\rho} = \vec{\rho}(t) - \vec{\rho}_0$, the excursion becomes:

$$\vec{\epsilon} = \Delta\vec{\rho} - (\Delta\vec{\rho}^{\,T}\, \vec{u}_{gls})\, \vec{u}_{gls}, \tag{4.77}$$

and the guidance error norm is then deduced as:

$$\begin{aligned} \|\,\vec{\epsilon}\,\|^2 &= \left[\Delta\vec{\rho} - (\Delta\vec{\rho}^{\,T}\vec{u}_{gls})\, \vec{u}_{gls}\right]^T \left[\Delta\vec{\rho} - (\Delta\vec{\rho}^{\,T}\vec{u}_{gls})\, \vec{u}_{gls}\right], \\ &= \Delta\vec{\rho}^{\,T}\Delta\vec{\rho} - (\Delta\vec{\rho}^{\,T}\vec{u}_{gls})^2, \\ &= \Delta r_x^2(1 - u_{gls_x}^2) + \Delta r_z^2(1 - u_{gls_z}^2) - 2u_{gls_x}u_{gls_z}\Delta r_x \Delta r_z, \end{aligned} \tag{4.78}$$

with $\Delta r_x = x - x_0$ and $\Delta r_z = z - z_0$.

4.6.4.1. Constraints on guidance error for V-bar

If the approach is performed along a line parallel to the x-axis, the unit direction vector is:

$$\vec{u}_{gls} = [1 \quad 0 \quad 0]^T. \tag{4.79}$$

Hence, the guidance error norm in Expression (4.78) is reduced to:

$$\|\,\vec{\epsilon}\,\|^2 = \Delta r_z^2. \tag{4.80}$$

If we develop the term z using Expression (4.68), we get:

$$\begin{aligned} \|\,\vec{\epsilon}\,\|^2 &= \left(4 - 3\cos(\omega\Delta t))\, z_0 + \frac{2}{\omega}(\cos(\omega\Delta t) - 1)\, \dot{x}_0 + \frac{1}{\omega}\sin(\omega\Delta t)\, \dot{z}_0 - z_0\right)^2, \\ &= \left(3(1 - \cos(\omega\Delta t))\, z_0 + \frac{2}{\omega}(\cos(\omega\Delta t) - 1)\, \dot{x}_0 + \frac{1}{\omega}\sin(\omega\Delta t)\, \dot{z}_0\right)^2. \end{aligned} \tag{4.81}$$

When the guidance error distance is maximal, the velocity vector $\vec{v}$ is parallel to the glideslope line. A maximum condition is then given by:

$$\dot{z} = 0 \;\Leftrightarrow\; 3\,\omega\;\sin(\omega\Delta t)\;z_0 - 2\;\sin(\omega\Delta t)\;\dot{x}_0 + \cos(\omega\Delta t)\;\dot{z}_0 = 0. \tag{4.82}$$

✳ **LEMMA 4:**
Let us define Δt_m the value of the time at which the guidance error is maximal and Δt_0 the value of the time when guidance error is zero, that is, when the satellite is back on the glideslope commanded path. Considering a single hump, we have the relationship:

$$\Delta t_0 = 2\;\Delta t_m, \tag{4.83}$$

meaning that the maximum occurs at the middle (in terms of time) of the hump.

Proof. The proof is presented only in cases for which $\omega\Delta t_0 \neq 2k\pi$, $k = 1, 2, \ldots$.

Consider Equation (4.82) on one hand and Equation $\|\vec{\epsilon}\| = 0$ on the other hand. In both cases, z_0 can be expressed as:

$$\begin{aligned} z_0 =& \frac{2}{3\,\omega}\dot{x}_0 - \frac{\cos(\omega\Delta t_m)}{3\,\omega\;\sin(\omega\Delta t_m)}\;\dot{z}_0, \\ z_0 =& \frac{2}{3\,\omega}\dot{x}_0 + \frac{\sin(\omega\Delta t_0)}{3\omega(\cos(\omega\Delta t_0)-1)}\;\dot{z}_0. \end{aligned} \tag{4.84}$$

Equalizing the two equations leads to

$$\sin(\omega\Delta t_0)\;\sin(\omega\Delta t_m) = -\cos(\omega\Delta t_m)\;\cos(\omega\Delta t_0) + \cos(\omega\Delta t_m), \Leftrightarrow\; \cos(\omega\Delta t_0 - \omega\Delta t_m) = \cos(\omega\Delta t_m). \tag{4.85}$$

Consequently, considering the range of the time only over a single hump, solutions of the above equation are $\Delta t_0 = 2\;\Delta t_m$ and $\Delta t_0 = 0$. ☐

From Equation (4.80), the guidance error distance can be readily upper-bounded with:

$$\begin{aligned} |\,\vec{\epsilon}\,| =& \left|(3 - 3\cos(\omega\Delta t))\;z_0 + \frac{2}{\omega}(\cos(\omega\Delta t) - 1)\;\dot{x}_0 + \frac{1}{\omega}\sin(\omega\Delta t)\;\dot{z}_0\right| \\ \leq& \left|(3 - 3\cos(\omega\Delta t_m))\;z_0 + \frac{2}{\omega}(\cos(\omega\Delta t_m) - 1)\;\dot{x}_0 + \frac{1}{\omega}\sin(\omega\Delta t_m)\;\dot{z}_0\right|. \end{aligned} \tag{4.86}$$

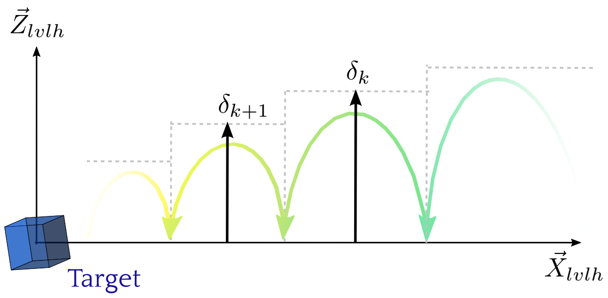

Figure 4.8: In-plane glideslope approach.

The analysis of Expression (4.86) provides an inequality that will be used to specify maximum conditions on guidance error for each hump, $k = 0, 1, \ldots, N-1$:

$$\left|(3 - 3\cos(\omega\Delta t_m))\;z_0 + \frac{2}{\omega}(\cos(\omega\Delta t_m) - 1)\;\dot{x}_k + \frac{1}{\omega}\sin(\omega\Delta t_m)\;\dot{z}_k\right| \leq \delta_k, \tag{4.87}$$

where δ_k is given and specifies the maximal allowable guidance error during the $(k+1)^{\text{th}}$ maneuver, as shown in Figure 4.8. Expression (4.87) is equivalently:

$$\begin{cases} (3-3\cos(\omega\Delta t_m))\,z_0+\dfrac{2}{\omega}(\cos(\omega\Delta t_m)-1)\,\dot{x}_k+\dfrac{1}{\omega}\sin(\omega\Delta t_m)\,\dot{z}_k\leq\delta_k, \\ -(3-3\cos(\omega\Delta t_m))\,z_0-\dfrac{2}{\omega}(\cos(\omega\Delta t_m)-1)\,\dot{x}_k-\dfrac{1}{\omega}\sin(\omega\Delta t_m)\,\dot{z}_k\leq\delta_k. \end{cases} \tag{4.88}$$

We recall that assuming that the interval Δt_0 is constant, the parameter Δt_m is constant too. Being aware of the fact that $\vec{v}_k^{\,+}=[\dot{x}_k \quad 0 \quad \dot{z}_k]^T$, the constraints (4.88) for the V-bar approach can be written in a matrix form as:

$$M_V\,\vec{v}_k^{\,+}\leq M_{V_k}, \tag{4.89}$$

where:

$$M_V=\begin{bmatrix} \dfrac{2}{\omega}(\cos(\omega\Delta t_m)-1) & \dfrac{1}{\omega}\sin(\omega\Delta t_m) \\ -\dfrac{2}{\omega}(\cos(\omega\Delta t_m)-1) & -\dfrac{1}{\omega}\sin(\omega\Delta t_m) \end{bmatrix}, \qquad M_{V_k}=\begin{bmatrix} \delta_k-(3-3\cos(\omega\Delta t_m))\,z_0 \\ \delta_k+(3-3\cos(\omega\Delta t_m))\,z_0 \end{bmatrix}. \tag{4.90}$$

4.6.4.2. Constraints on guidance error for R-bar

If the approach is performed along a line parallel to the z-axis, the unit direction vector is:

$$\vec{u}_{gls}=[0 \quad 0 \quad 1]^T. \tag{4.91}$$

Hence, the guidance error norm in Expression (4.78) is reduced to:

$$\|\,\vec{\epsilon}\,\|^2=\Delta r_x^2. \tag{4.92}$$

If we develop the term x using Expression (4.68), we get:

$$\begin{aligned} \|\,\vec{\epsilon}\,\|^2 &= \left(x_0+6(\omega\Delta t-\sin(\omega\Delta t))\,z_0+\frac{1}{\omega}(4\sin(\omega\Delta t)-3\omega\Delta t)\,\dot{x}_0+\frac{2}{\omega}(1-\cos(\omega\Delta t))\,\dot{z}_0-x_0\right)^2, \\ &= \left(6(\omega\Delta t-\sin(\omega\Delta t))\,z_0+\frac{1}{\omega}(4\sin(\omega\Delta t)-3\omega\Delta t)\,\dot{x}_0+\frac{2}{\omega}(1-\cos(\omega\Delta t))\,\dot{z}_0\right)^2. \end{aligned} \tag{4.93}$$

The following lemma will be used in the sequel to provide an inequality constraint on the excursion for each hump. Unlike the V-bar case, a simple relationship between the time Δt_m when the guidance error is maximal and the maneuver interval Δt_0 cannot be established. So, a conservative bound is introduced.

✻ **LEMMA 5:**

Let us define Δt_0 the value of the time when the guidance error is 0, that is, when the satellite is back on the glideslope commanded path. Considering a single hump such that $\omega\Delta t_0\in[0 \ \arccos\frac{3}{4}]$, a conservative upper-bound of the guidance error is given by:

$$|\,\vec{\epsilon}\,|\leq\alpha_1|\dot{x}_0|+\alpha_2|\dot{z}_0|+\alpha_3|z_0|, \tag{4.94}$$

with:

$$\begin{aligned} \alpha_1 &= \left|\frac{1}{\omega}(4\sin(\omega\Delta t_0)-3\omega\Delta t_0)\right|, \\ \alpha_2 &= \left|\frac{2}{\omega}(1-\cos(\omega\Delta t_0))\right|, \\ \alpha_3 &= \left|6(\omega\Delta t_0-\sin(\omega\Delta t_0))\right|. \end{aligned} \tag{4.95}$$

Proof. Let us apply the triangle inequality to Expression (4.93):

$$|\,\vec{\epsilon}\,| \leq \Big|6(\omega\Delta t - \sin(\omega\Delta t))\Big||z_0| + \Big|\frac{1}{\omega}(4\sin(\omega\Delta t) - 3\omega\Delta t)\Big||\dot{x}_0| + \Big|\frac{2}{\omega}(1-\cos(\omega\Delta t))\Big||\dot{z}_0|. \quad (4.96)$$

Then, each term needs to be analyzed:

- First term, $\frac{d}{d(\omega\Delta t)}(\omega\Delta t - \sin(\omega\Delta t)) = 1 - \cos(\omega\Delta t) \geq 0$, hence the 1st term $\leq \alpha_3$.
- Second term, $\frac{d}{d(\omega\Delta t)}(4\sin(\omega\Delta t) - 3\omega\Delta t) = 4\cos(\omega\Delta t) - 3 \geq 0$, if $\delta\nu \leq \arccos\frac{3}{4}$, hence the 2nd term $\leq \alpha_1$.
- Third term, $\frac{d}{d(\omega\Delta t)}(1-\cos(\omega\Delta t)) = \sin(\omega\Delta t) \geq 0$, if $\omega\Delta t \leq \pi$, hence the 3rd term $\leq \alpha_2$.

☐

Although in the above lemma the range of $\omega\Delta t_0$ is restricted to $[0 \;\; \arccos\frac{3}{4}]$, this result can be easily extended to a full revolution.

Being aware of the fact that $\vec{v}_k^{\,+} = [\dot{x}_k \;\; 0 \;\; \dot{z}_k]^T$, the constraints (4.96) for the R-bar approach can be written in a matrix form as:

$$M_R\,\vec{v}_k^{\,+} \leq M_{R_k}, \tag{4.97}$$

where:

$$M_R = \begin{bmatrix} \alpha_1 & \alpha_2 \\ -\alpha_1 & -\alpha_2 \end{bmatrix}, \qquad M_{R_k} = \begin{bmatrix} \delta_k - \alpha_3\, z_0 \\ \delta_k + \alpha_3\, z_0 \end{bmatrix}. \tag{4.98}$$

Note that the maximal allowable excursion at each step is denoted by δ_k, which can be seen in Figure 4.8 with the corresponding permutation between the X_{lvlh} and Z_{lvlh} axes.

4.6.5. Definition of the cost function

Apart the control of the humps during the glideslope, the other main objective of the approach is to minimize the fuel consumption during the transfer, as it was done in Guidance law #2 in Section 4.5. We define the cost function as the 1-norm of the $N+1$ impulsive thrusts, as defined in Expression (4.63), recalled again:

$$J = \sum_{k=0}^{N} ||\Delta\vec{V}_k||_1 = ||\Delta\vec{V}_0||_1 + \sum_{k=1}^{N-1} \|\Delta\vec{V}_k\|_1 + \|\Delta\vec{V}_N\|_1, \tag{4.99}$$

with $\Delta\vec{V}_k = \vec{v}_k^{\,+} - \vec{v}_k^{\,-}$. The formulation (4.99) is transformed in order to express the above criterion with respect to the decision variables:

- x_k or z_k, $k = 1, 2, \cdots, N-1$,
- $\vec{v}_k^{\,+}$, $k = 0, 1, \cdots, N-1$,
- $\Delta\vec{V}_N$.

If we develop Equation (4.99) by using Expression (4.71b), except for the last term $\Delta\vec{V}_N$, we obtain:

$$J = \|\vec{v}_0^{\,+} - \vec{v}_0^{\,-}\|_1 \; + \sum_{k=1}^{N-1} \|\vec{v}_k^{\,+} - \Phi_{vr}\,\vec{\rho}_{k-1} - \Phi_{vv}\,\vec{v}_{k-1}^{\,+}\|_1 \; + \|\Delta\vec{V}_N\|_1. \tag{4.100}$$

This cost function involving absolute values can be transformed into a linear function with the introduction of new variables $d_i \in \mathbb{R}^2$, $i = 0, 1, \ldots, N$ and inequality constraints [12], as it was previously done in Expression (4.65):

$$\begin{aligned} \vec{v}_0^{\,+} - \vec{v}_0^{\,-} &\leq d_0, \\ -\left(\vec{v}_0^{\,+} - \vec{v}_0^{\,-}\right) &\leq d_0, \\ \vec{v}_k^{\,+} - \Phi_{vr}\,\vec{\rho}_{k-1} - \Phi_{vv}\,\vec{v}_{k-1}^{\,+} &\leq d_k, \\ -\left(\vec{v}_k^{\,+} - \Phi_{vr}\,\vec{\rho}_{k-1} - \Phi_{vv}\,\vec{v}_{k-1}^{\,+}\right) &\leq d_k, \end{aligned} \tag{4.101}$$

where d_k are extra decision variables.

4.6.6. A linear programming problem

With the decision variables previously defined, the cost criterion (4.100) and gathering constraints on positions (4.71a), final velocity (4.72), and guidance errors (4.86) for V-bar and (4.96) for R-bar, the corresponding LP problem giving a solution to the initial minimum-fuel glideslope guidance problem may be readily obtained:

$$\begin{aligned} &\min\ c^T X \\ &\text{s.t. } A_{in} X \leq\ b_{in} \\ &\qquad A_{eq} X\ =\ b_{eq}. \end{aligned} \tag{4.102}$$

✍ **NOTE:**
Note that vector X in (4.102) *is not the same state vector as the one defined in Equation* (4.8). *To avoid confusions in the sequel, the state vector of the* LP *programming will have the subscript V or R whenever we consider the V-bar or R-bar approach respectively.*

4.6.6.1. LP problem for V-bar approach

The vector X_V is the vector where all the decision variables have been concatenated:

$$X_V = \left[\begin{array}{ccc|ccc|c|ccc} x_1 & \dots & x_{N-1} & \vec{v}_0^{\,+\,T} & \dots & \vec{v}_{N-1}^{\,+\,T} & \Delta\vec{V}_N^T & d_0^T & \dots & d_N^T \end{array}\right]^T. \tag{4.103}$$

The cost criterion in (4.102) is then reduced to the sum of d_i, $i = 0, 1, \dots, N$, and the vector c is defined as:

$$c^T = \left[\begin{array}{cccc} 0_{1\times(N-1)} & 1_{1\times 2N} & 1_{1\times 2} & 1_{1\times(2N+1)} \end{array}\right]. \tag{4.104}$$

The equality constraint $A_{eq} X_V = b_{eq}$ is built on Equations (4.71a) and (4.72) with:

$$A_{eq} = \left[\begin{array}{ccccc|cccccc|c|cccc} C_1 & 0 & 0 & \cdots & 0 & -\Phi_{rv} & 0 & 0 & \cdots & 0 & 0 & 0 & 0 & 0 & \cdots & 0 \\ -C_1 & C_1 & 0 & \cdots & 0 & 0 & -\Phi_{rv} & 0 & \cdots & 0 & 0 & 0 & 0 & 0 & \cdots & 0 \\ 0 & -C_1 & C_1 & \cdots & 0 & 0 & 0 & -\Phi_{rv} & \cdots & 0 & 0 & 0 & 0 & 0 & \cdots & 0 \\ \vdots & \vdots & \vdots & \ddots & \vdots & \vdots & \vdots & \vdots & \ddots & \vdots & \vdots & \vdots & \vdots & \vdots & \ddots & \vdots \\ 0 & 0 & 0 & \ddots & C_1 & 0 & 0 & 0 & \cdots & -\Phi_{rv} & 0 & 0 & 0 & 0 & \cdots & 0 \\ 0 & 0 & 0 & \cdots & -C_1 & 0 & 0 & 0 & \cdots & 0 & -\Phi_{rv} & 0 & 0 & 0 & \cdots & 0 \\ \hline 0 & 0 & 0 & \cdots & \Phi_{vr} C_1 & 0 & 0 & 0 & \cdots & 0 & \Phi_{vv} & I_2 & 0 & 0 & \cdots & 0 \end{array}\right], \tag{4.105}$$

$$b_{eq} = \left[\begin{array}{c} \Phi_{rr}\vec{\rho}_0 - C_2 z_0 \\ (\Phi_{rr} - I_2)C_2 z_0 \\ (\Phi_{rr} - I_2)C_2 z_0 \\ \vdots \\ (\Phi_{rr} - I_2)C_2 z_0 \\ \Phi_{rr}C_2 z_0 - \vec{\rho}_f \\ \hline \vec{v}_f - \Phi_{vr}C_2 z_0 \end{array}\right], \tag{4.106}$$

where $C_1 = [1 \quad 0]^T$ and $C_2 = [0 \quad 1]^T$.

The inequality constraint $A_{in}X_V \leq b_{in}$ is built on Equations (4.101) and (4.89) and additional inequalities are introduced to cope with the absolute values in the cost function. Matrices are defined in Expression (4.107).

✍ *REMARK.* Note that expressions of A_{in} and b_{in} matrices have been slightly simplified because we have $\Phi_{rr}C_1 = C_1$ and $\Phi_{vr}C_1 = [0 \quad 0]^T$.

$$A_{in} = \left[\begin{array}{cccccc|ccccccc|c|cccccc}
0 & 0 & 0 & \cdots & 0 & 0 & I_2 & 0 & 0 & 0 & \cdots & 0 & 0 & 0 & -I_2 & 0 & 0 & 0 & \cdots & 0 \\
0 & 0 & 0 & \cdots & 0 & 0 & -I_2 & 0 & 0 & 0 & \cdots & 0 & 0 & 0 & -I_2 & 0 & 0 & 0 & \cdots & 0 \\
0 & 0 & 0 & \cdots & 0 & 0 & -\Phi_{vv} & I_2 & 0 & 0 & \cdots & 0 & 0 & 0 & 0 & -I_2 & 0 & 0 & \cdots & 0 \\
0 & 0 & 0 & \cdots & 0 & 0 & \Phi_{vv} & -I_2 & 0 & 0 & \cdots & 0 & 0 & 0 & 0 & -I_2 & 0 & 0 & \cdots & 0 \\
-\Phi_{vr}C_1 & 0 & 0 & \cdots & 0 & 0 & 0 & -\Phi_{vv} & I_2 & 0 & \cdots & 0 & 0 & 0 & 0 & 0 & -I_2 & 0 & \cdots & 0 \\
\Phi_{vr}C_1 & 0 & 0 & \cdots & 0 & 0 & 0 & \Phi_{vv} & -I_2 & 0 & \cdots & 0 & 0 & 0 & 0 & 0 & -I_2 & 0 & \cdots & 0 \\
0 & -\Phi_{vr}C_1 & 0 & \cdots & 0 & 0 & 0 & 0 & -\Phi_{vv} & I_2 & \cdots & 0 & 0 & 0 & 0 & 0 & 0 & -I_2 & \cdots & 0 \\
0 & \Phi_{vr}C_1 & 0 & \cdots & 0 & 0 & 0 & 0 & \Phi_{vv} & -I_2 & \cdots & 0 & 0 & 0 & 0 & 0 & 0 & -I_2 & \cdots & 0 \\
\vdots & \vdots & \vdots & \ddots & \vdots & \vdots & \vdots & \vdots & \vdots & \vdots & \ddots & \vdots & \vdots & \vdots & \vdots & \vdots & \vdots & \vdots & \ddots & \vdots \\
0 & 0 & 0 & \cdots & -\Phi_{vr}C_1 & 0 & 0 & 0 & 0 & 0 & \cdots & -\Phi_{vv} & I_2 & 0 & 0 & 0 & 0 & 0 & \cdots & -I_2 \\
0 & 0 & 0 & \cdots & \Phi_{vr}C_1 & 0 & 0 & 0 & 0 & 0 & \cdots & \Phi_{vv} & -I_2 & 0 & 0 & 0 & 0 & 0 & \cdots & -I_2 \\
\hline
0 & 0 & 0 & \cdots & 0 & 0 & M_V & 0 & 0 & 0 & \cdots & 0 & 0 & 0 & 0 & 0 & 0 & 0 & \cdots & 0 \\
0 & 0 & 0 & \cdots & 0 & 0 & 0 & M_V & 0 & 0 & \cdots & 0 & 0 & 0 & 0 & 0 & 0 & 0 & \cdots & 0 \\
0 & 0 & 0 & \cdots & 0 & 0 & 0 & 0 & M_V & 0 & \cdots & 0 & 0 & 0 & 0 & 0 & 0 & 0 & \cdots & 0 \\
0 & 0 & 0 & \cdots & 0 & 0 & 0 & 0 & 0 & M_V & \cdots & 0 & 0 & 0 & 0 & 0 & 0 & 0 & \cdots & 0 \\
\vdots & \vdots & \vdots & \ddots & \vdots & \vdots & \vdots & \vdots & \vdots & \vdots & \ddots & \vdots & \vdots & \vdots & \vdots & \vdots & \vdots & \vdots & \ddots & \vdots \\
0 & 0 & 0 & \cdots & 0 & 0 & 0 & 0 & 0 & 0 & \cdots & M_V & 0 & 0 & 0 & 0 & 0 & 0 & \cdots & 0 \\
0 & 0 & 0 & \cdots & 0 & 0 & 0 & 0 & 0 & 0 & \cdots & 0 & M_V & 0 & 0 & 0 & 0 & 0 & \cdots & 0
\end{array}\right], \quad b_{in} = \left[\begin{array}{c}
\vec{v}_0^{\,-} \\
-\vec{v}_0^{\,-} \\
\Phi_{vr}\vec{\rho}_0 \\
-\Phi_{vr}\vec{\rho}_0 \\
\Phi_{vr}C_2 z_0 \\
-\Phi_{vr}C_2 z_0 \\
\Phi_{vr}C_2 z_0 \\
-\Phi_{vr}C_2 z_0 \\
\vdots \\
\Phi_{vr}C_2 z_0 \\
-\Phi_{vr}C_2 z_0 \\
\hline
M_0 \\
M_1 \\
M_2 \\
M_3 \\
\vdots \\
M_{N-2} \\
M_{N-1}
\end{array}\right] \tag{4.107}$$

4.6.6.2. LP problem for R-bar approach

The problem formulation for the R-bar approach follows the same process as in Subsection 4.6.6.1. The set of N motion equations (4.71a) allows the satellite to go along the glideslope line. For the R-bar approach, the z-component is changing while the x-component remains constant. Thus, Equations (4.71a), (4.72) and (4.100) are considered again and combined with the new appropriate vector of decision variables:

$$X_R = \left[\begin{array}{ccc|ccc|c|ccc} z_1 & \dots & z_{N-1} & \vec{v}_0^{+\,T} & \dots & \vec{v}_{N-1}^{+\,T} & \Delta\vec{V}_N^T & d_0^T & \dots & d_N^T \end{array} \right]^T . \tag{4.108}$$

The equality constraint $A_{eq}X_R = b_{eq}$ is built on equations (4.71a) and (4.72) with:

$$A_{eq} = \left[\begin{array}{ccccc|cccccc|c|cccc} C_2 & 0 & 0 & \cdots & 0 & -\Phi_{rv} & 0 & 0 & \cdots & 0 & 0 & 0 & 0 & 0 & \cdots & 0 \\ -\Phi_{rr}C_2 & C_2 & 0 & \cdots & 0 & 0 & -\Phi_{rv} & 0 & \cdots & 0 & 0 & 0 & 0 & 0 & \cdots & 0 \\ 0 & -\Phi_{rr}C_2 & C_2 & \cdots & 0 & 0 & 0 & -\Phi_{rv} & \cdots & 0 & 0 & 0 & 0 & 0 & \cdots & 0 \\ \vdots & \vdots & \vdots & \ddots & \vdots & \vdots & \vdots & \vdots & \ddots & \vdots & \vdots & \vdots & \vdots & \vdots & \ddots & \vdots \\ 0 & 0 & 0 & \ddots & 0 & 0 & 0 & 0 & \cdots & -\Phi_{rv} & 0 & 0 & 0 & 0 & \cdots & 0 \\ 0 & 0 & 0 & \cdots & C_2 & 0 & 0 & 0 & \cdots & 0 & -\Phi_{rv} & 0 & 0 & 0 & \cdots & 0 \\ \hline 0 & 0 & 0 & \cdots & \Phi_{vr}C_2 & 0 & 0 & 0 & \cdots & 0 & \Phi_{vv} & I_2 & 0 & 0 & \cdots & 0 \end{array} \right], \tag{4.109}$$

$$b_{eq} = \left[\begin{array}{c} \Phi_{rr}\vec{\rho}_0 - C_1 x_0 \\ (\Phi_{rr} - I_2)C_1 x_0 \\ (\Phi_{rr} - I_2)C_1 x_0 \\ \vdots \\ (\Phi_{rr} - I_2)C_1 x_0 \\ \Phi_{rr}C_1 x_0 - \vec{\rho}_f \\ \hline \vec{v}_f - \Phi_{vr}C_1 x_0 \end{array} \right], \tag{4.110}$$

where $C_1 = [1 \quad 0]^T$ and $C_2 = [0 \quad 1]^T$.

The inequality constraint $A_{in}X_R \leq b_{in}$ is built on Equations (4.101) and (4.97) and additional inequalities are introduced to cope with the absolute values in the cost function. Matrices A_{in} and b_{in} are defined in Expression (4.111).

$$A_{in} = \left[\begin{array}{cccccc|ccccccc|c|cccccc}
0 & 0 & 0 & \cdots & 0 & 0 & I_2 & 0 & 0 & 0 & \cdots & 0 & 0 & 0 & -I_2 & 0 & 0 & 0 & \cdots & 0 \\
0 & 0 & 0 & \cdots & 0 & 0 & -I_2 & 0 & 0 & 0 & \cdots & 0 & 0 & 0 & -I_2 & 0 & 0 & 0 & \cdots & 0 \\
0 & 0 & 0 & \cdots & 0 & 0 & -\Phi_{vv} & I_2 & 0 & 0 & \cdots & 0 & 0 & 0 & 0 & -I_2 & 0 & 0 & \cdots & 0 \\
0 & 0 & 0 & \cdots & 0 & 0 & \Phi_{vv} & -I_2 & 0 & 0 & \cdots & 0 & 0 & 0 & 0 & -I_2 & 0 & 0 & \cdots & 0 \\
-\Phi_{vr}C_2 & 0 & 0 & \cdots & 0 & 0 & 0 & -\Phi_{vv} & I_2 & 0 & \cdots & 0 & 0 & 0 & 0 & 0 & -I_2 & 0 & \cdots & 0 \\
\Phi_{vr}C_2 & 0 & 0 & \cdots & 0 & 0 & 0 & \Phi_{vv} & -I_2 & 0 & \cdots & 0 & 0 & 0 & 0 & 0 & -I_2 & 0 & \cdots & 0 \\
0 & -\Phi_{vr}C_2 & 0 & \cdots & 0 & 0 & 0 & 0 & -\Phi_{vv} & I_2 & \cdots & 0 & 0 & 0 & 0 & 0 & 0 & -I_2 & \cdots & 0 \\
0 & \Phi_{vr}C_2 & 0 & \cdots & 0 & 0 & 0 & 0 & \Phi_{vv} & -I_2 & \cdots & 0 & 0 & 0 & 0 & 0 & 0 & -I_2 & \cdots & 0 \\
\vdots & \vdots & \vdots & \ddots & \vdots & \vdots & \vdots & \vdots & \vdots & \vdots & \ddots & \vdots & \vdots & \vdots & \vdots & \vdots & \vdots & \vdots & \ddots & \vdots \\
0 & 0 & 0 & \cdots & -\Phi_{vr}C_2 & 0 & 0 & 0 & 0 & 0 & \cdots & -\Phi_{vv} & I_2 & 0 & 0 & 0 & 0 & 0 & \cdots & -I_2 \\
0 & 0 & 0 & \cdots & \Phi_{vr}C_2 & 0 & 0 & 0 & 0 & 0 & \cdots & \Phi_{vv} & -I_2 & 0 & 0 & 0 & 0 & 0 & \cdots & -I_2 \\
\hline
0 & 0 & 0 & \cdots & 0 & 0 & M_R & 0 & 0 & 0 & \cdots & 0 & 0 & 0 & 0 & 0 & 0 & 0 & \cdots & 0 \\
0 & 0 & 0 & \cdots & 0 & 0 & 0 & M_R & 0 & 0 & \cdots & 0 & 0 & 0 & 0 & 0 & 0 & 0 & \cdots & 0 \\
0 & 0 & 0 & \cdots & 0 & 0 & 0 & 0 & M_R & 0 & \cdots & 0 & 0 & 0 & 0 & 0 & 0 & 0 & \cdots & 0 \\
0 & 0 & 0 & \cdots & 0 & 0 & 0 & 0 & 0 & M_R & \cdots & 0 & 0 & 0 & 0 & 0 & 0 & 0 & \cdots & 0 \\
\vdots & \vdots & \vdots & \ddots & \vdots & \vdots & \vdots & \vdots & \vdots & \vdots & \ddots & \vdots & \vdots & \vdots & \vdots & \vdots & \vdots & \vdots & \ddots & \vdots \\
0 & 0 & 0 & \cdots & 0 & 0 & 0 & 0 & 0 & 0 & \cdots & M_R & 0 & 0 & 0 & 0 & 0 & 0 & \cdots & 0 \\
0 & 0 & 0 & \cdots & 0 & 0 & 0 & 0 & 0 & 0 & \cdots & 0 & M_R & 0 & 0 & 0 & 0 & 0 & \cdots & 0
\end{array}\right], \quad b_{in} = \left[\begin{array}{c}
\vec{v}_0^{\,-} \\
-\vec{v}_0^{\,-} \\
\Phi_{vr}\vec{\rho}_0 \\
-\Phi_{vr}\vec{\rho}_0 \\
\Phi_{vr}C_1x_0 \\
-\Phi_{vr}C_1x_0 \\
\Phi_{vr}C_1x_0 \\
-\Phi_{vr}C_1x_0 \\
\vdots \\
\Phi_{vr}C_1x_0 \\
-\Phi_{vr}C_1x_0 \\
\hline
M_0 \\
M_1 \\
M_2 \\
M_3 \\
\vdots \\
M_{N-2} \\
M_{N-1}
\end{array}\right] \tag{4.111}$$

4.6.7. Algorithm

This algorithm computes appropriate impulses to transfer the satellite from an initial position $\vec{\rho}_0$ to a final position $\vec{\rho}_f$ while minimizing the consumption. The algorithm is presented in a general setup for both V-bar and R-bar approaches.

```
Data: chaser's information:
        initial position and velocity in target's LVLH frame $\vec{\rho}_0$, $\vec{v}_0^{\,-}$;
        final desired position and velocity in target's LVLH frame $\vec{\rho}_f = \vec{\rho}_N$, $\vec{v}_f = \vec{v}_N^{\,+}$;
        number of maneuvers $N$;
Initialization: unit vector $\vec{u}_{gls}$;
                transfer time $T$;
                interval between consecutive impulses $\Delta t$, $\Delta t_0$, $\Delta t_m$;
                state transition matrices $\Phi_{rr}$, $\Phi_{rv}$, $\Phi_{vr}$, $\Phi_{vv}$;
for $k = 0, \cdots, N-1$ do
    compute: matrix $M_{V_k}$ or matrix $M_{R_k}$ from elements $\delta_k$ ;
end
Compute: Linear Programming matrices:
            cost matrix $c$ ;
            inequality matrices $A_{in}$, $b_{in}$;
            equality matrices $A_{eq}$, $b_{eq}$;
Solve: LP problem (4.102) and store solution in $X_V$ or $X_R$:
if solution found then
    extract from $X_V$ or $X_R$: departure velocity from $k$, $\vec{v}_k^{\,+}$ ;
                                 impulsive maneuver at $N$, $\Delta\vec{V}_N$ ;
    for $k = 0, \cdots, N-1$ do
        compute: next relative position at $k+1$, $\vec{\rho}_{k+1}$ in (4.21a) ;
                 arrival velocity at $k+1$, $\vec{v}_{k+1}^{\,-}$ in (4.21b) ;
                 impulsive maneuver at $k$, $\Delta\vec{V}_k$ in (4.23) ;
    end
else
    increase values $\delta_k$, update $M_{V_k}$ or $M_{R_k}$, re-run solver.
end
```

Algorithm 3: Minimum-fuel LP glideslope.

The fuel-optimal algorithm developed above is a way to address the V-bar and R-bar approaches as an LP problem, by minimizing the fuel consumption and taking into account the constraints on the guidance error.

4.7. Simulations

In this section, we present the numerical results obtained with the three controllers proposed in Sections 4.4, 4.5 and 4.6 in the context of the PRISMA mission already described in Subsection 3.9.1. All the results are obtained using the software *Matlab©* for a given orbital rendezvous scenario within the PRISMA mission.

4.7.1. Description of the simulations

The objective of the rendezvous is to perform a glideslope approach in a linear context from an initial state X_0 in the target's LVLH frame to a final state X_f in a given transfer time T. During the approach, the different impulsive maneuvers are separated by a constant interval Δt.

We aim at comparing the three different algorithms proposed for Guidance law #1 in 4.4, Guidance law #2 in 4.5 and Guidance law #3 in 4.6, which are addressed in a progressive way, corresponding to each of the next subsections:

- First, we present the results for the V-bar approach in a circular orbit. The objective is to present the general framework of the glideslope approach and show the evolution of different parameters (cost and excursion) when the number of impulses N varies. Within this context, we show the behavior of Guidance law #1 and Guidance law #3 in the specific case of a V-bar approach.
- Next, we continue with the numerical examples in an elliptical reference orbit for a V-bar approach. For the sake of comparison, we will present the direct extension based on Yamanaka-Ankersen equations of Guidance law #1 for an elliptical orbit, referred to as *elliptical GLS*, Guidance law #1 itself and Guidance laws #2 and #3.
- Finally, an example dedicated to a general glideslope approach in an elliptical orbit is presented.

According to the objectives of the simulation, two different initial conditions X_{0i}, $i = 1, 2$ have been used, which are chosen at different distances from the target satellite located at the origin of the LVLH frame, and summarized in Table 4.1.

Initial	**Position (m)**			**Velocity (m/s)**		
state	x	y	z	$\dot{x}$	$\dot{y}$	$\dot{z}$
X_{01}	-500	0	-20	0	0	0
X_{02}	-400	40	-50	0	0	0

Table 4.1: Values of the initial states X_{0i}, $i = 1, 2$.

The initial relative velocity for every initial state X_{0i} has been selected to be zero to account for the fact that the starting point of the rendezvous may be a holding point arising from a previous station keeping along the space mission.

In the same way, we set two different final states according to the type of approach, as shown in Table 4.2. For instance, to simulate a V-bar rendezvous, we would take initial condition X_{01} and final condition X_{f1}, where the z coordinate stays constant — the necessary condition for this kind of approach.

Final state	Position (m) x	 y	 z	Velocity (m/s) $\dot{x}$	 $\dot{y}$	 $\dot{z}$
X_{f1}	-100	0	-20	0	0	0
X_{f2}	-40	0	-20	0	0	0

Table 4.2: Values of the final states X_{fi}, $i = 1, 2$.

We also specify the upper bounds on the guidance error, i.e. the maximal allowable excursions δ_{α_k}, δ_{β_k} for Guidance law #2 and δ_k for Guidance law #3, as shown in Figures 4.5 and 4.8 respectively. All the excursion values for the k maneuver are set to the same value $\delta_{\alpha_k} = \delta_{\beta_k} = \delta_k$ in Table 4.3.

Maneuver k	1	2	3	4	5	6	7	8	9	10
$N = 2$	20	15	·	·	·	·	·	·	·	·
$N = 4$	10	5	2	0.5	·	·	·	·	·	·
$N = 10$	2	1.8	1.6	1.4	1.2	1	0.8	0.6	0.4	0.3

Table 4.3: Values of the maximal allowable excursion (m) for Guidance laws 4.5 and 4.6.

4.7.2. Results

In the following figures, we present the results through different graphs:

- **Trajectories:** representation of the chaser's trajectories exhibiting humps to approach the final state close to the target, in the LVLH reference frame.
- **Executed thrusts:** at each thrust location, we compute the *1-norm* to extract the consumption of that maneuver.

The idea is to illustrate the interest of the two Guidance laws #2 in 4.5 and #3 in 4.6 in terms of consumption reduction and admissibility of the trajectory in a corridor of visibility. It must be noted that the trajectories are considered in an open-loop setup in this manuscript, whereas real trajectories undergo orbital disturbances and therefore, have to be closed-loop controlled.

4.7.2.1. Results for V-bar approaches in a circular orbit

The following subsection shows the numerical examples for a circular orbit for a V-bar approach and for different values of N, varying between $N = 2$, $N = 4$ and $N = 10$, as shown in Figure 4.9. The initial state is X_{01} from Table 4.1 and the final state X_{f1} from Table 4.2.

The comparison is made with the classical glideslope algorithm oh Hablani: we observe the differences in the humps amplitude in both cases. The standard algorithm presented for Guidance law #1 in 4.4 shows an initial hump which is much higher than the next humps, with very low amplitude in the last maneuvers. The lower the number of maneuvers N is, the larger the first excursion is, as it can be seen in Figure 4.9 and in Table 4.4.

For the second algorithm concerning Guidance law #3 in 4.6, we have defined the maximum allowable excursions in Table 4.3. At each maneuver, the LP algorithm takes into account the guidance

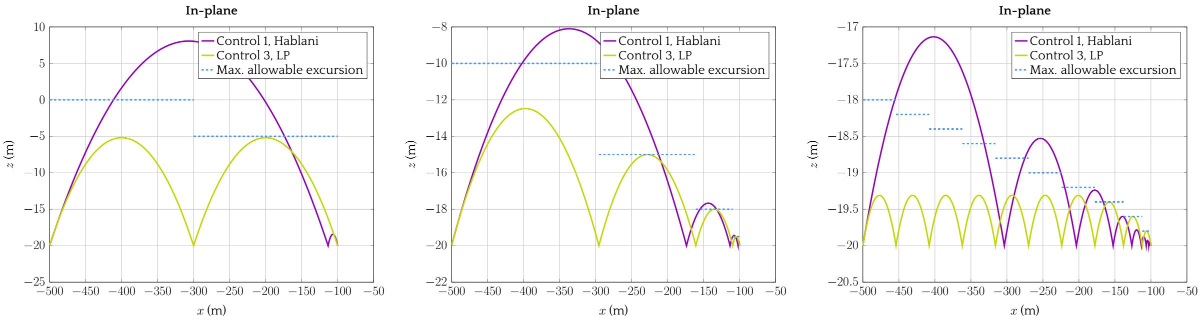

(a) $N = 2$.
(b) $N = 4$.
(c) $N = 10$.

Figure 4.9: V-bar circular glideslope trajectories for different values of N.

constraints defined therein and computes the optimal solution. In Figure 4.9 we see that the firsts humps do not arrive to their maximum allowable value, but they do as the maneuvers are sequenced, as shown in Table 4.4.

	Maneuver	1	2	3	4	5	6	7	8	9	10
$N = 2$	Control 4.4	28.06	1.56	·	·	·	·	·	·	·	·
	Control 4.5	14.81	14.81	·	·	·	·	·	·	·	·
$N = 4$	Control 4.4	11.90	2.33	0.56	0.23	·	·	·	·	·	·
	Control 4.5	7.52	5	2	0.5	·	·	·	·	·	·
$N = 10$	Control 4.4	2.86	1.47	0.76	0.40	0.22	0.12	0.07	0.05	0.04	0.03
	Control 4.5	0.69	0.69	0.69	0.69	0.69	0.69	0.69	0.6	0.4	0.2

Table 4.4: Excursion (m) for the Guidance law 4.4 vs Guidance law 4.6.

In the next figures we present the maneuver plan corresponding to the simulations in Figure 4.9.

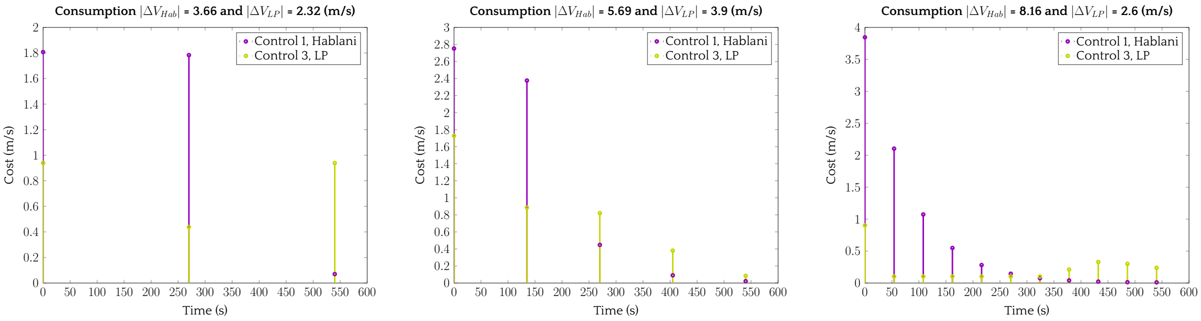

(a) $N = 2$.
(b) $N = 4$.
(c) $N = 10$.

Figure 4.10: V-bar circular glideslope impulses for different values of N.

What we notice first is the fact that both Guidance laws #1 and #3 have $N+1$ impulses. In the original standard glideslope methodology presented in Section 4.4, the algorithm computes N maneuvers to obtain a given final velocity, not chosen by the user, but coming out from the algorithm. On the other side, Guidance law #3 performs one more maneuver in order to set the final velocity to the desired one given by the user, implemented through the final velocity constraint defined in Subsection 4.6.3. For the sake of comparison, we have included in the Guidance law #1 an extra impulse to end up the maneuver with the same desired final velocity vector $\vec{v}_f$ as specified for Guidance law #3, leading to the $N+1$ maneuvers showing in Figures 4.10.

The sequences of impulsive maneuvers for the standard glideslope algorithm in Guidance law #1 and the minimum-fuel algorithm of Guidance law #3 are depicted in Figure 4.10 and detailed in Table 4.5.

Number of impulses	Control 4.4	Control 4.6
$N = 2$	3.66	2.32
$N = 4$	5.69	3.90
$N = 10$	8.16	2.60

Table 4.5: Consumption (m/s) for Guidance law #1 vs Guidance law #3.

Interesting phenomena appear for Guidance law #3, as shown in Figure 4.11, where an approach with $N = 6$ maneuvers is performed.

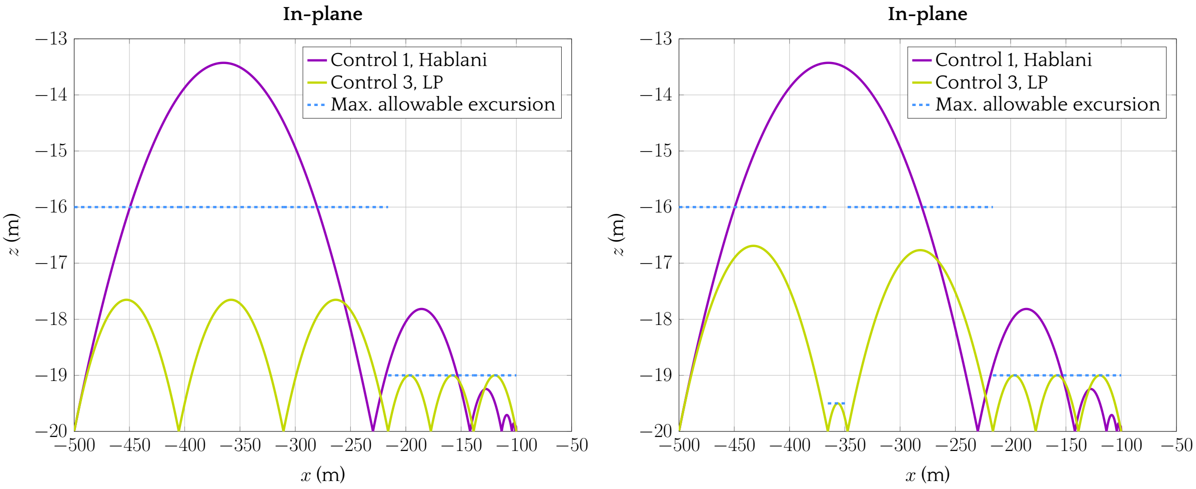

(a) Max. excursion on the 2^{nd} hump: $\delta_{k=2} = 4$ m.

(b) Max. excursion on the 2^{nd} hump: $\delta_{k=2} = 0.5$ m.

Figure 4.11: Effect of the maximum allowable constraint on the 2^{nd} hump over the whole trajectory.

We note that for a V-bar type of approach, the coordinates x_k, $k = 1, 2, \dots, N-1$ in (4.103) are not constrained and could be anywhere on the glideslope line. However, in 4.11a, we observe that the algorithm adjusts the pulses to be equally spaced, taking into account the maximum allowable excursions for each maneuver.

In addition, the three first humps in Figure 4.11a do not reach their maximum allowable excursion represented by the blue dashed line, but they do at the end of the corridor approach, in the last maneuvers. However, if one of the constraints is really tight at one of the maneuvers, as shown in 4.11b, where the maximum excursion for the second hump is set to 0.5 m instead of 4 m in 4.11a, the LP algorithm reshapes the rest of the maneuvers in order to respect all the constraints.

This in an interesting behavior, since we are able to set a user-defined profile of the desired approach to account for constraints related to the trajectory. On the other hand, this capacity does not come for free. The cost of the full maneuver plan increases from 2.99 m/s in 4.11a to 6.39 m/s in 4.11b. If all the maximum excursion values are set to 4 m, the cost falls to 2.37 m/s. In both cases, the cost is lower than the one obtained for Hablani: 6.88 m/s.

We can therefore conclude that tightening the constraints results in a desired profile path at the expense of an increased fuel consumption value, while changing the parameter N will not really affect the overall cost of the maneuver plan.

4.7.2.2. Results for V-bar approaches in an elliptical orbit

The following subsection shows the numerical examples for an elliptical orbit for a V-bar approach and for different values of N, varying between $N = 2$, $N = 4$ and $N = 10$, as shown in Figure 4.12. The initial state is X_{01} from Table 4.1 and the final state X_{f1} from Table 4.2.

Here, a specific case of V-bar approach in an elliptic orbit is studied. We have compared the three controllers presented in Sections 4.4, 4.5 and 4.6 plus a direct extension of Guidance law #1 for the elliptic case, based on the Yamanaka-Ankersen equations. The objective herein is twofold:

- first, we show how the standard algorithm of Guidance law #1 for a circular reference orbit is not a good approximation even in the case of reference orbit with a low eccentricity ($e = 0.004$ for PRISMA); but its extension to the elliptic orbit does the work;
- in this case of a V-bar approach, we are able to compare Guidance laws #2 and #3, and show that both algorithms give us the optimal solution in terms of consumption.

In Figure 4.12 we have represented the trajectory followed by the chaser for a V-bar approach in an elliptic reference orbit. We have represented the constraints on the guidance error by means of an admissible corridor for each maneuver k.

We aim at emphasizing the significant drift induced when using the glideslope control computed with the Guidance law #1 even when the reference orbit is quasi-circular and for all chosen N. This drift is increased when the number of maneuvers N increases, as shown in Figure 4.12c. However, the obtained trajectory for the extended glideslope algorithm in an elliptic orbit shows a better performance in terms of precision of the arrival point. Both Guidance laws #1 and its extended elliptic version have a similar behavior at the beginning of the maneuvers, but the differences show up at the end of the executed plan.

Regarding Guidance laws #2 and #3, we hardly distinguish them in Figure 4.12, since both algorithms return the optimal solution. We can see that, for any specific V-bar approach, Guidance law #3 is actually a specific case of Guidance law #2. In other words, Guidance law #2 generalizes Guidance law #3 to any type of approach.

Regarding the sequences of impulsive maneuvers in Figure 4.13 and Table 4.6, we observe that the Guidance laws #2 and #3 show the minimum values, which are almost identical. The elliptic glideslope and Guidance law #1 show higher consumption values in all cases, and the distribution of the thrusts is similar to the one shown in Figure 4.10: higher values at the beginning of the maneuvers and lower values at the end of the plan.

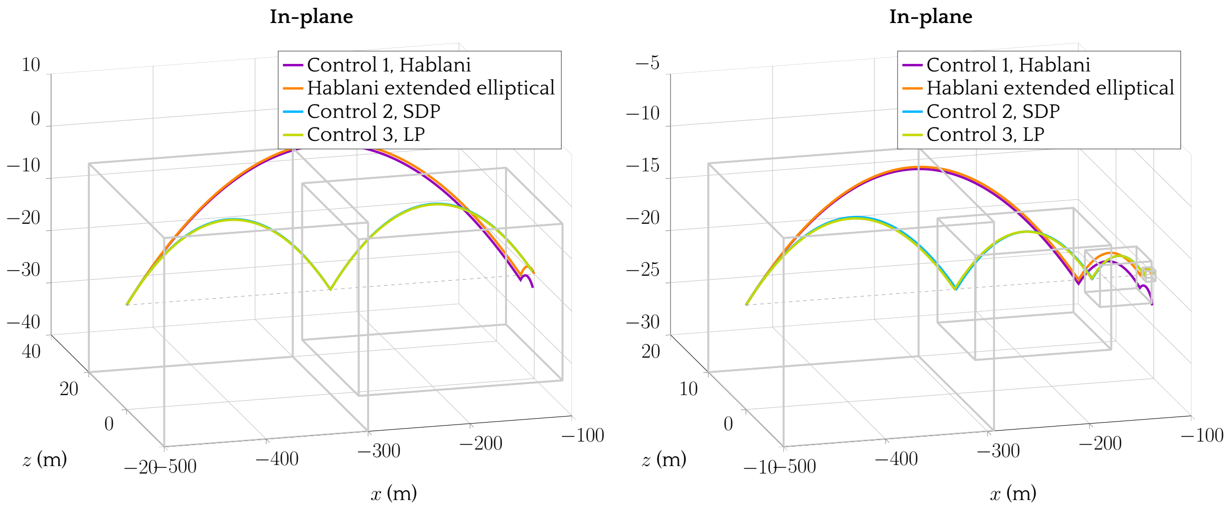

(a) $N = 2$.

(b) $N = 4$.

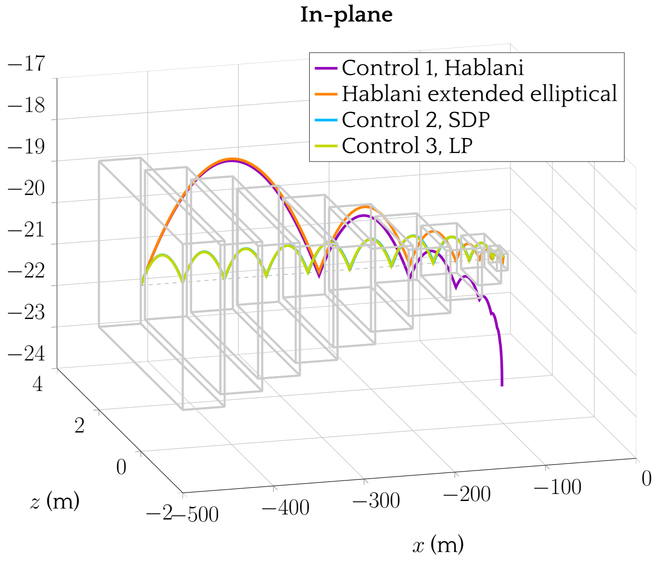

(c) $N = 10$.

Figure 4.12: V-bar elliptical glideslope trajectories for different values of N.

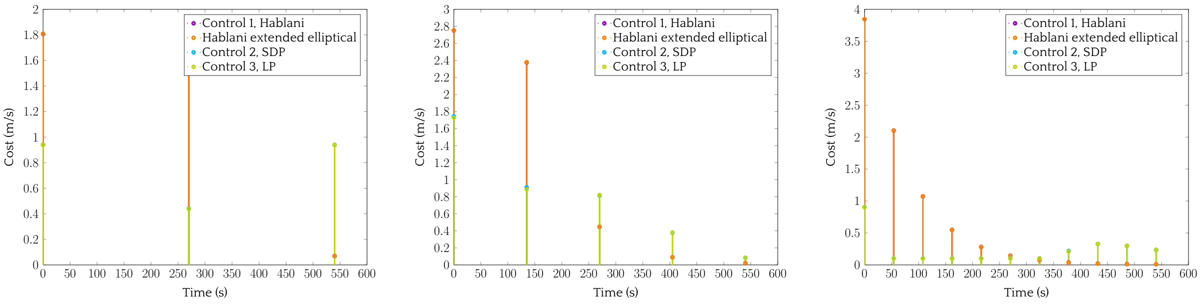

(a) $N = 2$.

(b) $N = 4$.

(c) $N = 10$.

Figure 4.13: V-bar elliptical glideslope impulses for different values of N.

Number of impulses	Control #1 in 4.4	Elliptical GLS	Control #2 in 4.5	Control #3 in 4.6
$N = 2$	3.66	3.67	2.32	2.32
$N = 4$	5.69	5.7	3.93	3.90
$N = 10$	8.16	8.17	2.61	2.60

Table 4.6: Consumption (m/s) for Guidance law #1, elliptical GLS, Guidance law #2 and Guidance law #3.

4.7.2.3. A general approach in an elliptical orbit

This last subsection addresses the numerical examples for an elliptical orbit when the approach is not performed *in plane*, for different values of N, varying between $N = 2$, $N = 4$ and $N = 10$, as shown in Figure 4.14. The initial state is X_{02} from Table 4.1 and the final state X_{f2} from Table 4.2.

Herein, we compare the elliptical controllers, i.e. the elliptical glideslope and Guidance law #2 in 4.5.

In Figure 4.14, the chaser's trajectories for the glideslope approach are represented. The elliptic glideslope shows strong first impulses in all cases, just as its original algorithm for the circular case in 4.4.

Guidance law #2 complies with all the guidance constraints, following the user-defined corridor. This controller gives us the minimum-fuel maneuver plan, as shown in Figure 4.15 and in Table 4.7.

Number of impulses	Elliptical GLS	Control #2 in 4.5
$N = 2$	3.63	2.27
$N = 4$	5.80	3.66
$N = 10$	8.61	2.55

Table 4.7: Consumption (m/s) for elliptical GLS vs Guidance law #2 in 4.5.

For the different values of N, we observe that Guidance law #2 in 4.5 performs much better in terms of fuel consumption. The value of this consumption lays within the same range, except for $N = 4$, which can be explained from the fact that the guidance constraints in Table 4.3 are too tight for this case, since we also obtain the same behavior in Tables 4.5 and 4.6.

Actually, by increasing one of the guidance constraints at maneuver $k = 3$ from 2m to 5m, we obtain a similar performace as shown in Figure 4.11, and a reduced cost of 2.75 m/s.

We obtain therefore the same conclusions regarding the admissible excursion at each maneuver: the tighter the constraint is, the higher the cost of the full maneuver plan will be.

We can therefore design the admissible corridor in order to have greater margins at the first maneuvers and reduce these margins as the chaser arrives to sensitive zones such as the proximity of the target.

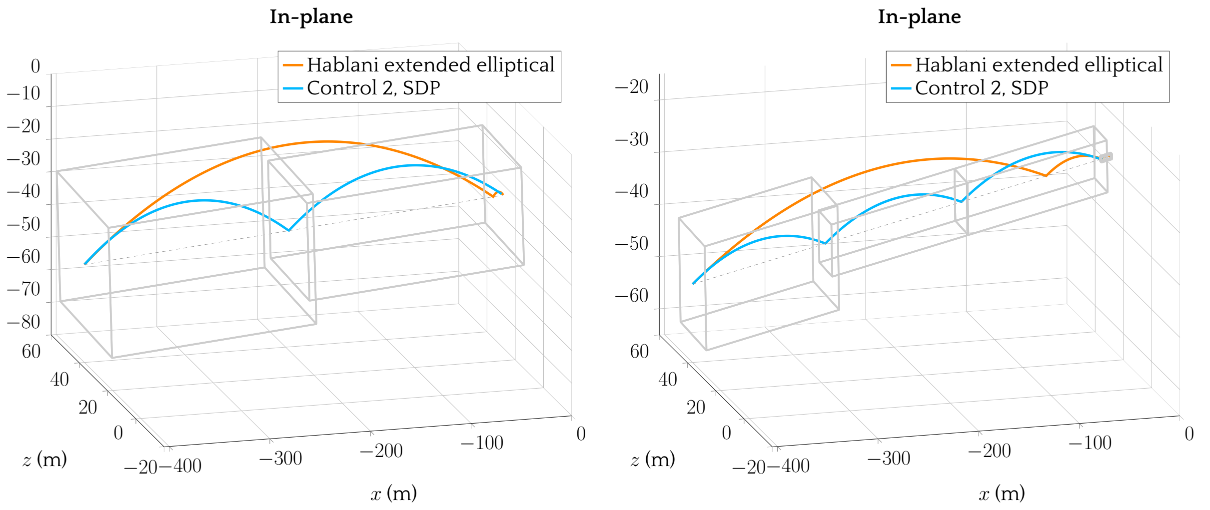

(a) $N = 2$.

(b) $N = 4$.

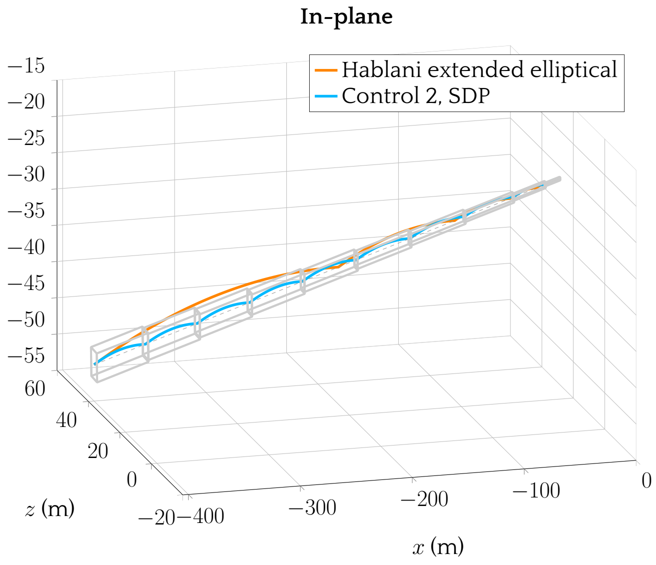

(c) $N = 10$.

Figure 4.14: Elliptical glideslope trajectories for different values of N.

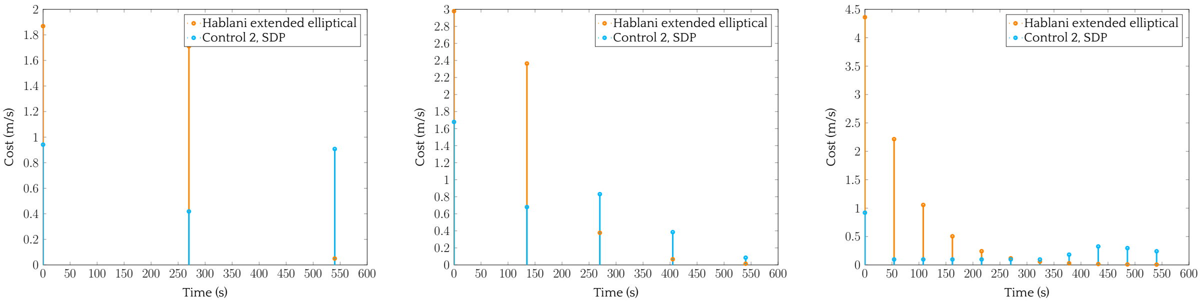

(a) $N = 2$.

(b) $N = 4$.

(c) $N = 10$.

Figure 4.15: Elliptical glideslope impulses for different values of N.

4.8. Conclusions

In this chapter, a revisited solution to the classical Hablani glideslope algorithm, [56], for the impulsive close range rendezvous is proposed, first for any type of approach in Guidance law #2, and later on, in the specific cases of the V-bar and R-bar approaches for Guidance law #3.

The motivations for the development of a new solution to the glideslope method come from two main issues regarding the standard algorithm: the lack of control on the bounds over the inherent guidance errors and the impossibility of minimizing the fuel consumption.

These shortcomings are tackled via a combination of simple techniques mainly borrowed from the field of non negative polynomials theory. For a fixed-time glideslope rendezvous with a pre-assigned number of maneuvers, a new problem formulation is developed, where the relative dynamics, the guidance error expressions and the identification of relevant decision variables are combined in order to derive an SDP programming problem in an elliptic orbit.

The main design features included in the new proposed glideslope algorithm are on one hand the minimization of the consumption and, on the other hand, the possibility to specify an admissible volume for each hump of the relative trajectory and therefore to control the guidance error all along the rectilinear path.

From this general case using an SDP formulation, we derived the solution via an LP problem for the specific cases of V-bar and R-bar approaches in a circular orbit, also showing an optimal consumption while respecting a user-defined bound profile on the maximum guidance error, which turns out to be very useful when dealing with visibility constraints while keeping a reasonable numerical complexity of computation.

The different numerical examples illustrate the usefulness of the new methods compared to the classical one when the approach corridor has to verify stringent geometrical restrictions such as LoS constraints. The consumption is also significantly reduced, mainly when the number of maneuvers increases.

CHAPTER 5

CONCLUSIONS AND PERSPECTIVES

In this thesis the problem of modeling and GNC design for proximity operations in space has been addressed. The focus is on the particular cases of the close-range approach and the observation phases by an active chaser satellite — fully actuated — of a non-cooperative target.

5.1. Summary of the contributions

In the context of proximity operations, where both satellites are close to each other, the challenge is to develop autonomous effective GNC systems with small computational effort by achieving a good knowledge of the relative dynamic model. These dynamics can be represented as the translation and rotation about the CoM of the spacecraft. However, in close proximity, the satellites cannot be considered as point masses and a more complete description of the dynamics becomes necessary.

This problem can be addressed by means of a relative dynamic model describing not only the translational or attitude motions independently, but taking into account the effects the translation has over the rotation and vice-versa, referred to as coupling. These features are met when considering a 6 DoF relative coupled model to describe the motion of the chaser with respect to the target.

The development of this coupled model is done progressively. First, the relative nonlinear translational model is presented for an elliptic orbit under Keplerian assumptions. This model is then linearized with respect to the target's orbit in order to obtain the linear relative translational model.

During this process, a particularly useful change of coordinates has been identified thanks to Lyapunov-Floquet theory. The resulting linearized model for the relative translational motion is simple enough to ease the characterization of bounded periodic trajectories of the chaser. This feature of particular value, has been exploited in the second chapter for the design of closed-loop control schemes.

Even if it has not been used later on in the manuscript, the dual quaternions formalism has been carried out for the joint modeling of both translational and attitude motions, leading to a compact representation of the 6 DoF coupled model. Though not completely original, these developments are still quite unusual and deserve to be more widely spread in the space community.

The fact of considering a chaser satellite equipped with chemical thrusters allows us to use the classical assumption of impulsive actuation leading to immerse the relative translational dynamics in the particular class of hybrid dynamical systems — systems showing continuous-time dynamics and discrete events.

We take advantage of the hybrid systems formalism to propose several hybrid closed-loop guidance control laws. The objective of the proposed hybrid guidance laws is to stabilize the chaser in a reference periodic (bounded) trajectory close to the target, for the observation phase and after a free approach trajectory. The use of well-established tools from the hybrid systems theory allows us to prove asymptotic stability of the relative motion as well as robustness properties, demonstrated by several numerical simulations.

Within Chapter 4, additional operational constraints, such as LoS restrictions are added to the requirements for the approach phase and open-loop guidance laws are proposed. These control laws impose the chaser satellite to follow a glideslope approach — an approach following a straight line in any direction of the target's reference frame. We have generalized the existing results in literature by proposing additional degrees of freedom to the classical problem. In particular, the capacity of minimizing the fuel consumption and enclosing the admissible trajectories within a user-defined corridor has been integrated into the design.

In the general elliptical case, the minimum-fuel glideslope approach restricted to a user defined corridor is recast as an SDP problem. We have also proposed another type of control law for two specific cases found recurrently in the literature: the V-bar and R-bar approaches. In these cases, the SDP problem is simplified and the guidance law design is based on the solution of an LP problem. Both of the proposed guidance laws show efficient numerical results, reducing the cost of the maneuvers and limiting the humps deviation with respect to the glideslope line when compared to the classical Hablani's glideslope approach.

5.2. Perspectives

Future work aspects regarding Chapter 2 concern the linear translational relative model. After the four different coordinate changes leading to a simplified model characterizing periodic chaser trajectories, we obtained an LTI dynamic matrix which is particularly convenient for control purposes design in the hybrid set-up. The state vector of the associated linearized model is composed of 6 components that are reminiscent of the 6 orbital parameters — all constant except one, but also from the cartesian coordinates (decoupling). It would be interesting to look for the physical meaning of any of this new set of parameters describing the linearized relative motion.

Another framework feature to study is the use of the 6 DoF relative coupled model in the hybrid formalism for the design of hybrid control laws dedicated to proximity maneuvers (inspection for instance). The 6 DoF coupled model being formally similar to a model for attitude control when using dual quaternions, the idea is to extend some preliminary results obtained from the hybrid comments [83] for attitude control to these particular models. By selecting a proper elapsed time between impulses and a given reference for both the translation and attitude motions, we can propose a 6 DoF guidance law.

When dealing with the particular glideslope approach, a way to add safety considerations to the designs proposed in this manuscript could be to impose bounded and periodic trajectories relating thrusts localization on the glideslope, allowing therefore to keep the chaser away from the target in case of failure of the propulsive actuation system. The methods developed in Chapter 2 seem to be easily customizable for this particular objective.

Finally, the simplicity of the control laws developed in this thesis prompt us to test their implementability on dedicated FPGAs via hardware-in-the-loop simulation as in the reference [50] for different control laws.

CONCLUSIONS ET PERSPECTIVES

Dans cette thèse, le problème de la modélisation et de la conception des systèmes GNC pour les opérations de proximité dans l'espace a été abordé. L'accent est mis sur les cas particuliers du rendez-vous proche et les phases d'observation par un satellite de chasseur actif — actionné — vers une cible non coopérative.

Sommaire des contributions

Dans le contexte des opérations de proximité, où les deux satellites sont proches l'un de l'autre, le défi est de développer des systèmes autonomes effectifs mais simples. Cela passe par l'obtention d'un modèle dynamique relatif suffisamment représentatif et limité de complexité, la dynamique relative complète comportant le mouvement de translation et de rotation du satellite autour de son centre de masse. En effet, quand les satellites sont très proches l'un de l'autre, ils ne peuvent plus être considérés comme des masses ponctuelles.

Ce problème ne peut être abordé en considérant indépendamment les mouvements de translation ou de rotation. Il est nécessaire de tenir compte des effets du couplage entre la translation et la rotation.

Le développement de ce modèle couplé à 6 degrés de liberté est réalisé progressivement. Tout d'abord, le modèle de translation non linéaire relatif est présenté pour une orbite elliptique sous des hypothèses Kepleriennes. Ce modèle est ensuite linéarisé par rapport à l'orbite de la cible afin d'obtenir le modèle linéaire relative en translation.

Au cours de ce processus, un changement de coordonnées particulièrement utile a été identifié grâce à la théorie de Lyapunov-Floquet. Il a permis de générer un modèle linéarisé à temps invariant pour un phénomène naturellement périodique. Ce modèle permet de caractériser des trajectoires périodiques bornées du satellite chasseur. Cette propriété a été exploitée dans le deuxième chapitre pour la conception de schémas de contrôle en boucle fermée.

Afin de proposer une modélisation compacte du mouvement couplé, le formalisme des quaternions duaux a été utilisé dans ce manuscrit. Bien qu'ils ne soient pas complètement originaux, ces développements sont encore assez inhabituels et méritent d'être plus diffusés dans la communauté spatiale.

L'utilisation de la propulsion chimique nous pousse à considérer l'hypothèse classique de commande impulsionnelle conduisant à immerger la dynamique de translation relative dans la classe par-

ticulière de systèmes dynamiques hybrides — systèmes présentant des dynamiques en temps continu et des événements discrets.

Nous profitons du formalisme des systèmes hybrides pour proposer plusieurs lois hybrides de contrôle de guidage en boucle fermée. L'objectif des contrôleurs hybrides proposés est de stabiliser le chasseur dans une trajectoire périodique (et donc bornée) de référence proche de la cible, pour la phase d'observation et après une trajectoire d'approche libre. L'utilisation d'outils bien établis à partir de la théorie des systèmes hybrides nous permet de prouver la stabilité asymptotique du mouvement relatif ainsi que les propriétés de robustesse. Nous illustrons ces propriétés à travers de plusieurs simulations numériques.

Dans le chapitre 4, des contraintes opérationnelles supplémentaires telles que les contraintes de visibilité sont ajoutées aux exigences de la phase d'approche et des contrôleurs de guidage en boucle ouverte sont proposés. Une approche de type glideslope pour laquelle le satellite chasseur s'astreint à suivre une ligne droite est étudiée. Nous avons généralisé les résultats existants dans la littérature en proposant des degrés supplémentaires de liberté au problème classique. En particulier, nous avons intégré à la conception de ces lois de contrôle la capacité de minimiser la consommation de carburant et d'inclure les trajectoires admissibles dans un corridor défini par l'utilisateur.

Dans le cas elliptique général, l'approche de glideslope à consommation minimale restreinte à un couloir d'approche défini par l'utilisateur est synthétisée en tant que problème SDP. Nous avons également proposé un autre type de loi de contrôle pour deux cas spécifiques trouvés fréquemment dans la littérature: les approches V-bar et R-bar dans le cas d'une orbite circulaire. Dans ces cas, le problème SDP est simplifié et la conception du contrôleur est basée sur la solution d'un problème LP. Les deux contrôleurs proposés montrent des résultats numériques efficaces, réduisant le coût des manœuvres et limitant l'écart des sauts par rapport à la ligne glideslope en comparaison à l'approche classique du glideslope de Hablani.

Perspectives

Des potentiels travaux futurs concernent le modèle linéaire relatif en translation. Après les quatre changements de coordonnées différents conduisant à un modèle LTI, nous avons obtenu une matrice dynamique invariante dans le temps, particulièrement pratique pour la conception d'algorithmes de contrôle dans le contexte hybride. Le vecteur d'état du modèle linéarisé associé est composé de six éléments rappelant les six paramètres orbitaux: tous sont constants sauf un, et ils autorisent un découplage du mouvement cartésien. Il serait intéressant de chercher le sens physique d'un des ces nouveaux jeux de paramètres décrivant le mouvement relatif linéarisé.

Une autre caractéristique à étudier est l'utilisation du modèle couplé relatif à 6 degrés de liberté dans le formalisme hybride pour la conception de lois de contrôle hybrides dédiées aux manoeuvres de proximité (inspection par exemple). Le modèle couplé à 6 degrés de liberté étant formellement similaire à un modèle de contrôle d'attitude lors de l'utilisation de quaternions duaux, l'idée est d'étendre certains résultats préliminaires obtenus dans [83] pour le contrôle d'attitude à ces modèles particuliers. En sélectionnant un temps approprié entre les impulsions et une référence donnée pour les mouvements de translation et d'attitude, nous pouvons envisager un contrôleur mêlant contrôle d'orbite et d'attitude de manière couplée.

En ce qui concerne l'approche particulière du glideslope, un moyen d'ajouter des restrictions de sécurité aux modèles proposés dans ce manuscrit pourrait être d'imposer des trajectoires bornées *et périodiques concernant la localisation des poussées sur le glideslope, ce qui permet de garder le chasseur loin de la cible en cas de défaillance du système propulsif. Les méthodes développées dans le chapitre 2 semblent être adaptables a ce nouvel objectif.*

Enfin, la simplicité des lois de contrôle développées dans cette thèse nous invite à tester leur mise en œuvre sur des FPGA dédiés via la simulation hardware-in-the-loop comme dans la référence [50] pour les différentes lois de contrôle.

APPENDIX A

ORBITAL PARAMETERS

In order to perfectly define the motion of a spacecraft in space, we need six coordinates, out of which three correspond to the position and the other three to the velocity of the spacecraft. The motion of a spacecraft is therefore defined by these six cartesian elements (ce):

$$X_{ce} = (x,\ y,\ z,\ \dot{x},\ \dot{y},\ \dot{z}).$$

Current computation methods allow to numerically integrate the spacecraft centre of gravity's motion in cartesian coordinates. However, these coordinates neither allow to precise a more "physical" interpretation of the motion nor help simplifying the mathematical equations to obtain simpler analytical expressions [54].

The motion of the spacecraft can be expressed differently, through the orbital parameters: elements that allow representing the spacecraft's motion in a more geometrical way, within an orbital context.

A.1. Geometrical elements definitions

For this purpose, some geometrical elements are defined below, which can be spotted in Figures (A.1) and (A.2):

- *ecliptic*: imaginary plane containing the Earth's orbit around the sun [110];
- *equatorial plane*: plane containing the equator of the Earth;
- *perigee*: closest point of the orbit to the Earth;
- *apogee*: farthest point of the orbit to the Earth;
- *line of apsides*: virtual line that links the perigee and the apogee;
- *ascending node* ☊: point of the orbit in which the satellite passes from the southern to the northern hemisphere;
- *descending node* ☋: point of the orbit in which the satellite passes from the northern to the southern hemisphere;
- *line of nodes*: virtual line that links the ascending and descending nodes;
- *vernal equinox* ♈: intersection point between the ascending node of the sun's direction and the line of nodes.

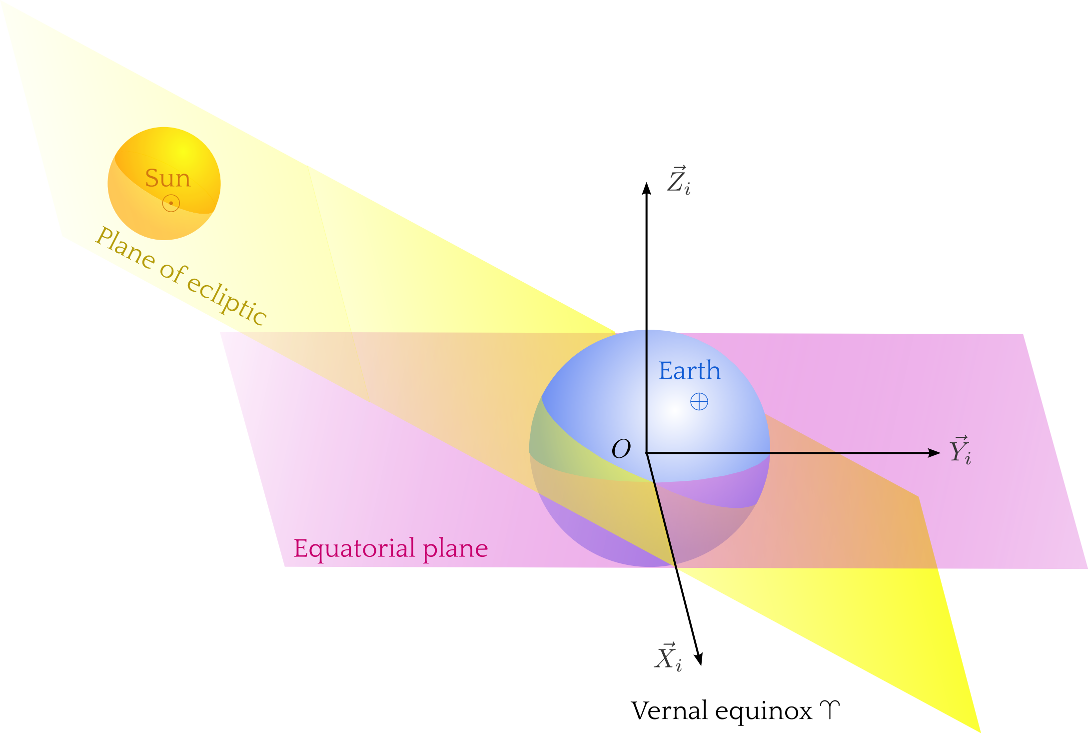

Figure A.1: Ecliptic and equatorial planes.

Once these geometrical elements have been defined, the orbital parameters can be introduced. For this purpose, three types of parameters are presented:

- parameters related to the orbit's orientation in space;
- parameters related to the spacecraft's orbit shape; and
- parameters related to the position of the spacecraft in the orbit.

These orbital elements are explained in the sequel.

A.2. Orbit's orientation in space

We can define three angles (analogue to the Euler's angles) that allow to place the orbital plane with respect to an inertial equatorial reference frame:

- i, **Inclination**: angle between the orbital plane and the equatorial plane (equivalent to the angle between vector $\vec{Z}_i$ and the kinetic moment vector $\vec{h}$).

- Ω, **Right Ascension of the Ascending Node (RAAN)**: angle between the $\vec{X}_i$ axis of the inertial frame (pointing towards the vernal equinox ♈) and the intersection line between the orbital plane and the equatorial plane (line of nodes), oriented towards the ascending node (☊).

- ω, **Argument of perigee**: angle between the ascending node (☊) and the perigee, contained in the orbital plane.

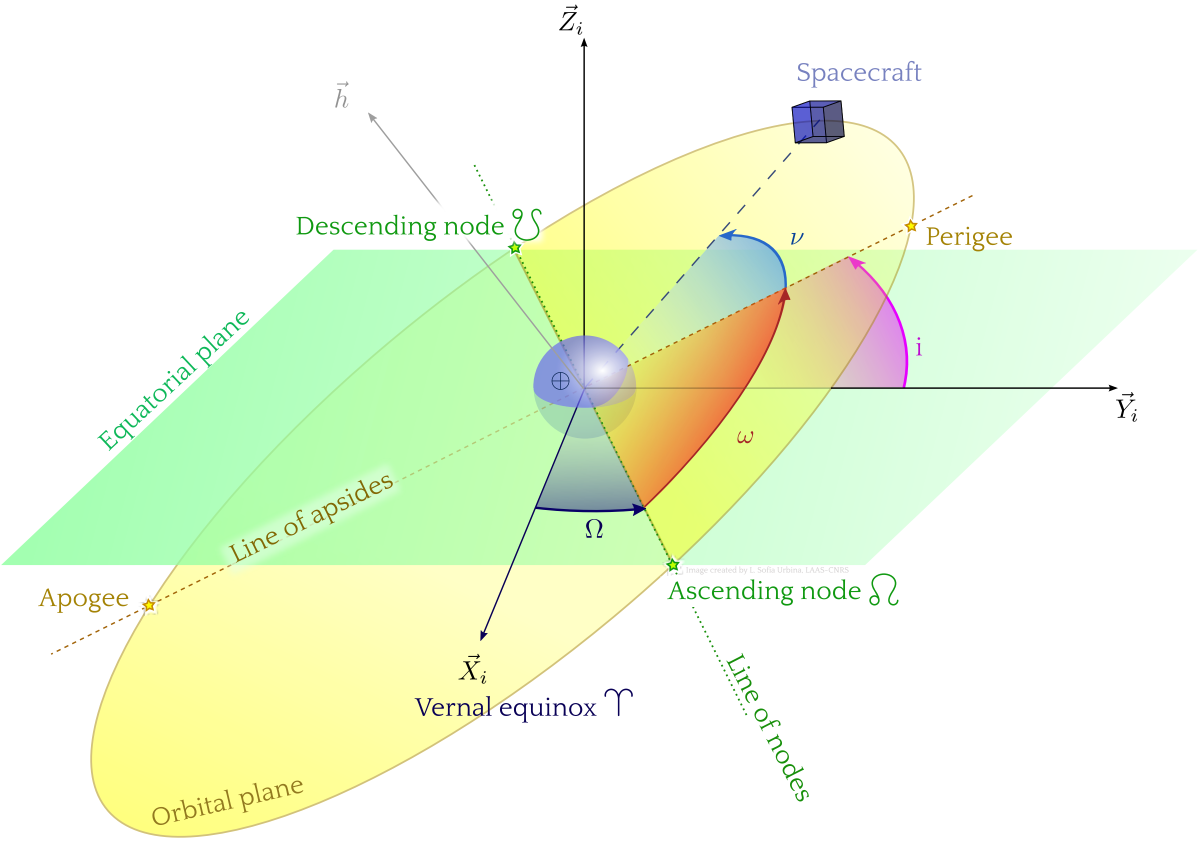

Image created by L. Sofía Urbina, LAAS-CNRS

Figure A.2: Orbital parameters.

A.3. Orbit's shape

Within the orbital plane, the ellipse itself is characterized by two parameters:

- a, **Semi-major axis**: half the ellipse's extent along the longest of its two principal axis.

- e, **Eccentricity**: fraction of the distance along the semi-major axis at which the focus lies $e = \frac{c}{a}$, where c is the distance from the center of the ellipse to the focus, as shown in Figure A.3.

A.4. Position of the spacecraft in the orbit

The last parameter regards the position of the spacecraft on the orbit, characterized by one of the three following angles:

- ν, **True anomaly**: angle of the spacecraft with respect to the perigee.

- E, **Eccentric anomaly**: anomaly once ν has been projected over the tangent circle (point S').

$$\tan\left(\frac{E}{2}\right) = \sqrt{\frac{1-e}{1+e}}\,\tan\left(\frac{\nu}{2}\right). \tag{A.1}$$

- M, **Mean anomaly**: defined by Kepler's equation:

$$M = E - e\,\sin(E) = M_0 + n\,(t - t_0) = \sqrt{\frac{\mu}{a^3}}\,(t - t_0) = \frac{2\pi}{T_{sat}}\,(t - t_0), \tag{A.2}$$

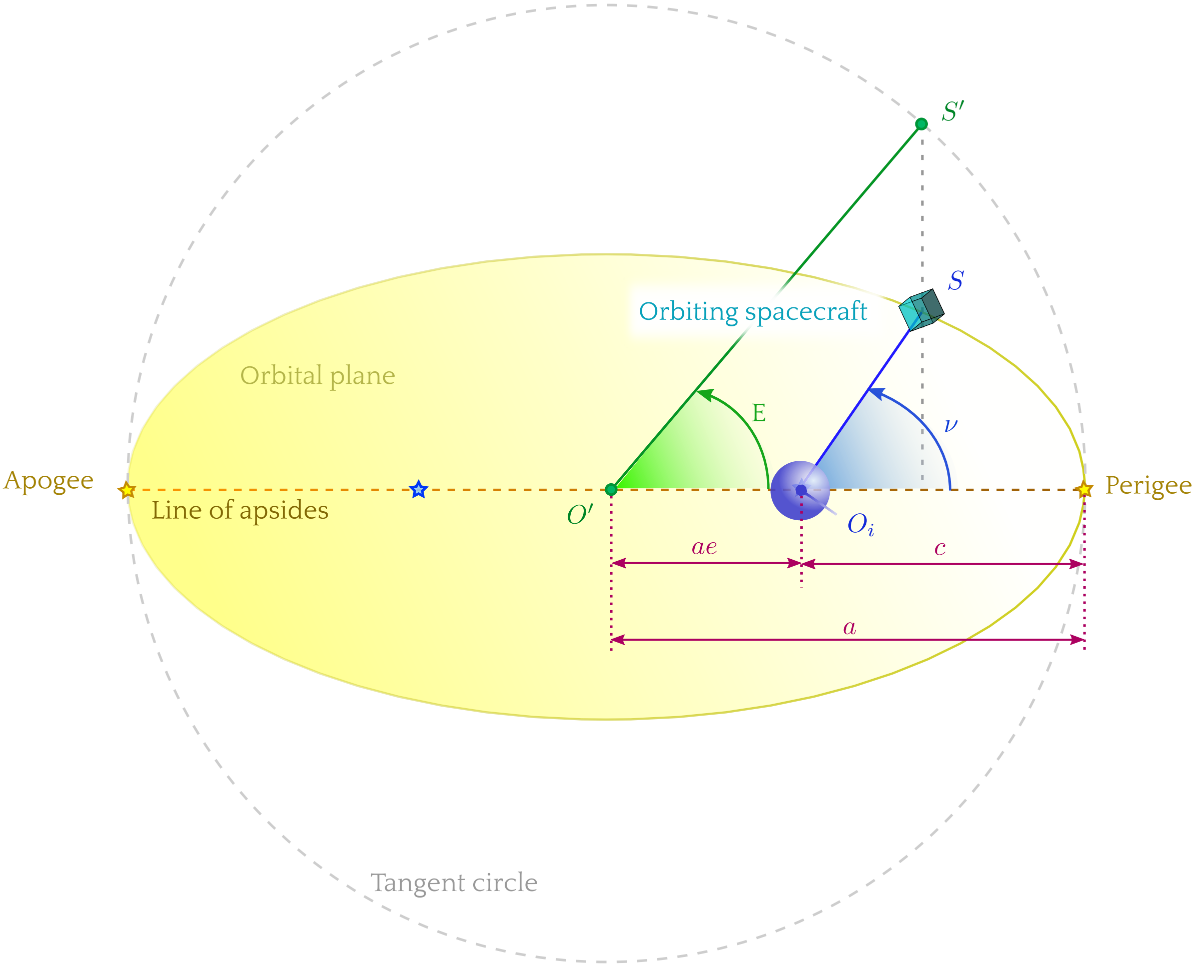

Figure A.3: Orbital parameters defined in the spacecraft's orbital plane.

where n is the mean motion, t_0 is the time at which the spacecraft passes through the perigee and μ is the Earth standard gravitational parameter.

Angles ν and E are represented in Figure A.3, where S is the spacecraft position on the orbit and S' is the orthogonal projection of S over the tangent circle to the orbital trajectory.

A.5. Synthesis of the orbital elements

The motion of a spacecraft is therefore defined by the six orbital elements (oe) presented previously:

$$X_{oe} = (a,\ e,\ i,\ \Omega,\ \omega,\ \nu \text{ or } E \text{ or } M).$$

APPENDIX B

COORDINATE REFERENCE FRAMES

B.1. Inertial / equatorial geocentric reference frame

Earth-centered pseudo-inertial reference frame $\mathcal{I} = \left(O_i, \vec{X}_i, \vec{Y}_i, \vec{Z}_i\right)$ is defined as a pseudo-inertial frame whose origin is the center of the Earth and whose basis is defined by vectors $B_i = [\vec{X}_i, \vec{Y}_i, \vec{Z}_i]$ where:

- $\vec{X}_i$ is pointing towards the vernal equinox ♈ (intersection point between the sun's ascendent node $\Omega_\odot$ and the line of nodes);
- $\vec{Z}_i$ defines the Earth's rotation axis with respect to the poles and pointing towards the north pole (in the same direction as the Earth's angular momentum);
- $\vec{Y}_i$ completes the right-handed coordinate system.

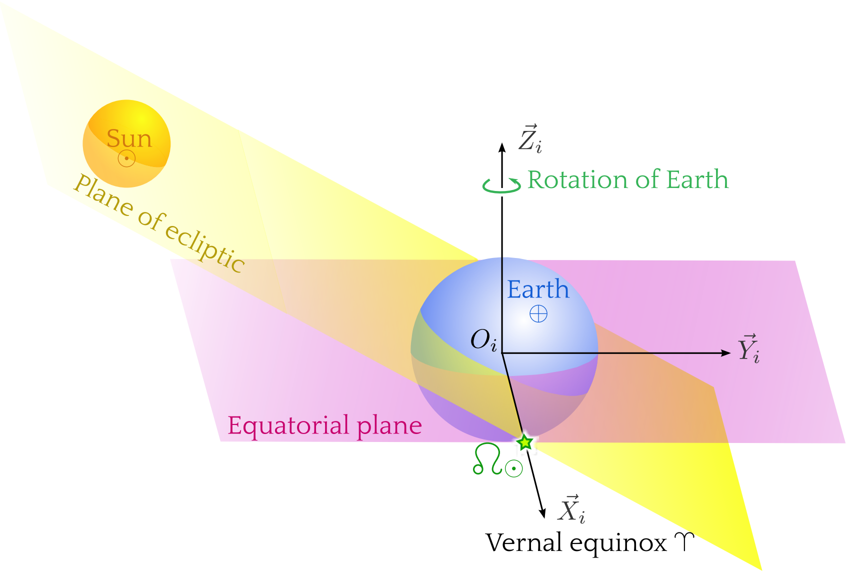

Figure B.1: Inertial reference frame.

B.2. Local orbital Hill / RSW reference frame

Local reference frames are adapted to represent the components of vectors, specifically the accelerations due to perturbations. These reference frames also allow to express the geometry of satellites' formations.

One of the local reference frames is the Hill's frame (also known as RSW coordinate frame) $\mathcal{O}_H = \left(O_S, \vec{X}_H, \vec{Y}_H, \vec{Z}_H\right) = \left(O_S, \vec{R}, \vec{S}, \vec{W}\right)$, centered at the CoM of the satellite and whose basis is defined by vectors $B_H = [\vec{X}_H, \vec{Y}_H, \vec{Z}_H]$ or $[\vec{R}, \vec{S}, \vec{W}]$ where:

- $\vec{X}_H$ or $\vec{R}$ is radial, oriented from the center of the Earth towards the spacecraft (orbit radius direction);
- $\vec{Z}_H$ or $\vec{W}$ is normal to the orbital plane defined by the position and velocity vectors (also known as cross-track direction) and parallel to the orbital angular momentum vector $\vec{h}$;
- $\vec{Y}_H$ or $\vec{S}$ completes the right-handed coordinate system.

The $(\vec{X}_H, \vec{Y}_H)$ coordinates define the relative orbital motion in the target orbit plane (known as *in-plane* motion), while $\vec{Z}_H$ coordinate defines the motion normal to the target orbital plane (also referred to as *out-of-plane* motion).

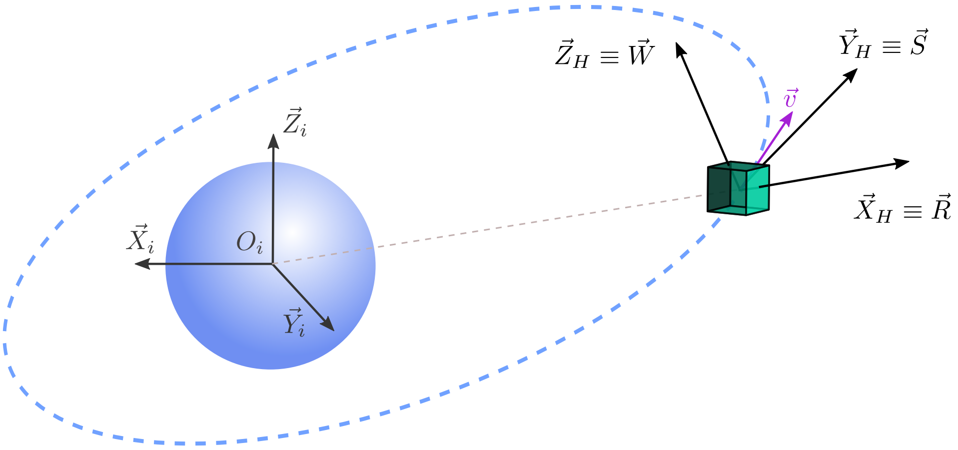

Figure B.2: Hill reference frame, 3D view.

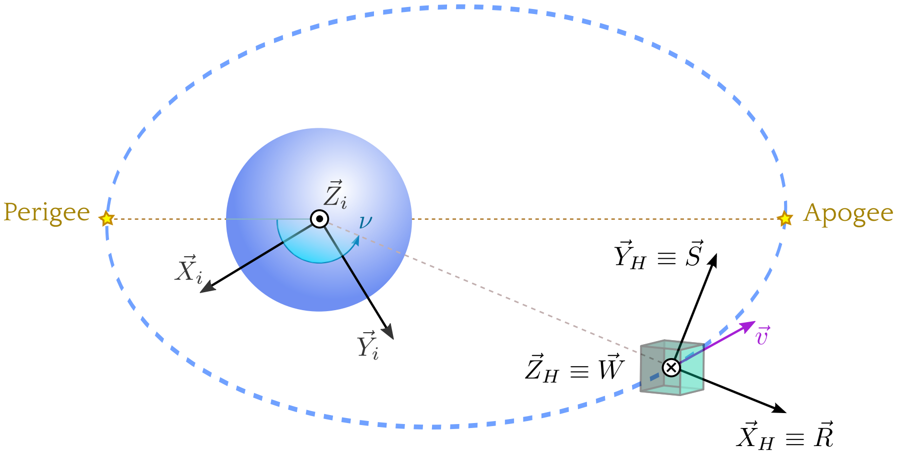

Figure B.3: Hill reference frame, 2D view.

B.3. Local Vertical Local Horizontal (LVLH) reference frame

The LVLH reference frame is linked to the spacecraft and must not be mixed up with the previous one. This local orbital frame $\mathcal{O}_o = \left(O_S, \vec{X}_o, \vec{Y}_o, \vec{Z}_o\right)$ is centered at the CoM of the satellite. Its basis is defined by vectors $B_o = [\vec{X}_o, \vec{Y}_o, \vec{Z}_o]$, where:

- Y_o (also known as *H-bar*) is orthogonal to the orbital plane and in the opposite direction of orbital angular momentum vector $\vec{h}$;
- Z_o (also known as *R-bar*) is radial, oriented from the CoM of the satellite towards the center of the Earth;
- X_o (also known as *V-bar*) completes the right-handed coordinate system.

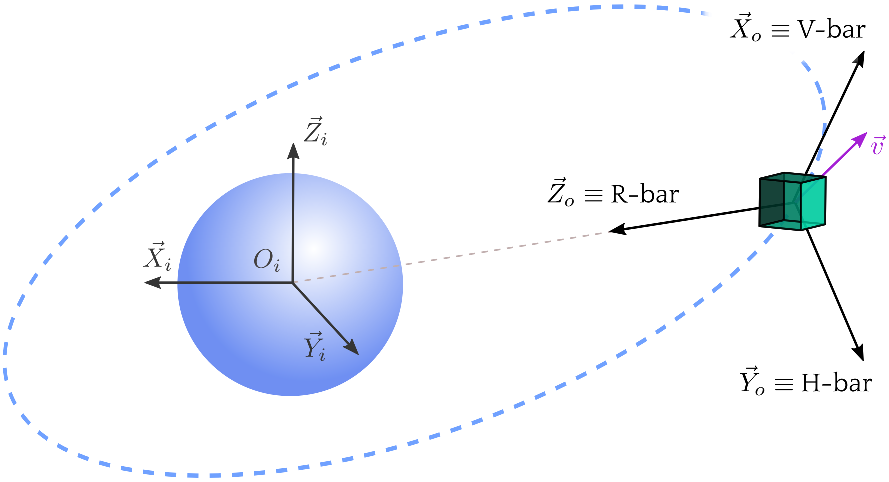

Figure B.4: Local Vertical Local Horizontal (LVLH) reference frame, 3D view.

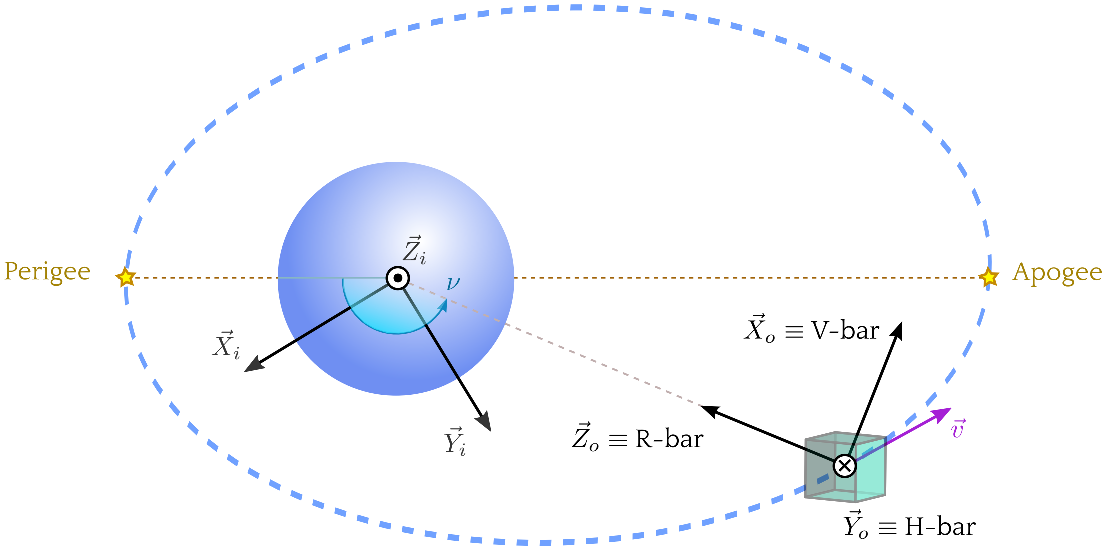

Figure B.5: Local Vertical Local Horizontal (LVLH) reference frame, 2D view.

B.4. Body reference frame

Coordinate reference frame centered at the CoM of the satellite $\mathcal{B} = \left(O_b, \vec{X}_b, \vec{Y}_b, \vec{Z}_b\right)$, whose basis is defined by vectors $B_b = [\vec{X}_b, \vec{Y}_b, \vec{Z}_b]$, where:

- X_b is coincident with the X principal inertia axis of the satellite;
- Y_b is coincident with the Y principal inertia axis of the satellite;
- Z_b is coincident with the Z principal inertia axis of the satellite.

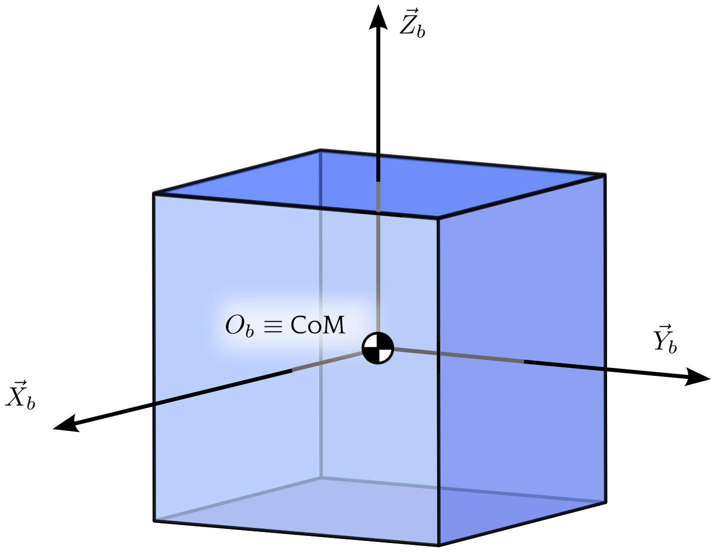

Figure B.6: Body reference frame.

APPENDIX C

ELEMENTS FOR RELATIVE TRANSLATIONAL MOTION LINEARIZATION

C.1. Computation of the differential acceleration for a keplerian reference orbit

In the particular case where the reference orbit is considered as following Keplerian assumptions (no external disturbance), then $\dot{\Omega} = \ddot{\Omega} = \dot{i} = \ddot{i} = 0$ and we can write [7]:

$$ {\vec{\omega}_t}^{\mathcal{O}_t} = -\dot{\nu}\vec{Y}_{lvlh} = \begin{bmatrix} 0 & -\dot{\nu} & 0 \end{bmatrix}^T , \tag{C.1} $$

$$ {\dot{\vec{\omega}}_t}^{\mathcal{O}_t} = -\ddot{\nu}\vec{Y}_{lvlh} = \begin{bmatrix} 0 & -\ddot{\nu} & 0 \end{bmatrix}^T . \tag{C.2} $$

The differential acceleration is given by Equation (2.14), reminded hereafter:

$$ \ddot{\vec{\rho}}^{\,\mathcal{I}} = \ddot{\vec{\rho}}^{\,\mathcal{O}_t} + {\vec{\omega}_t}^{\mathcal{O}_t} \wedge ({\vec{\omega}_t}^{\mathcal{O}_t} \wedge \vec{\rho}^{\,\mathcal{O}_t}) + {\dot{\vec{\omega}}_t}^{\mathcal{O}_t} \wedge \vec{\rho}^{\,\mathcal{O}_t} + 2{\vec{\omega}_t}^{\mathcal{O}_t} \wedge \dot{\vec{\rho}}^{\,\mathcal{O}_t} . \tag{C.3} $$

By developing each term of the right-handed part of this equation, we obtain the following acceleration components in the orbital frame $\mathcal{O}_t$:

- The relative acceleration:

$$ \ddot{\vec{\rho}}^{\,\mathcal{O}_t} = \begin{bmatrix} \ddot{x} & \ddot{y} & \ddot{z} \end{bmatrix}^T . \tag{C.4} $$

- The centrifugal acceleration:

$$ \vec{\omega}_t \wedge (\vec{\omega}_t \wedge \vec{\rho}) = \omega_t^{\times}\omega_t^{\times}\vec{\rho} = \begin{bmatrix} 0 & 0 & -\dot{\nu} \\ 0 & 0 & 0 \\ \dot{\nu} & 0 & 0 \end{bmatrix} \begin{bmatrix} 0 & 0 & -\dot{\nu} \\ 0 & 0 & 0 \\ \dot{\nu} & 0 & 0 \end{bmatrix} \begin{bmatrix} x \\ y \\ z \end{bmatrix} = \begin{bmatrix} -\dot{\nu}^2 x \\ 0 \\ -\dot{\nu}^2 z \end{bmatrix}^{\mathcal{O}_t} . \tag{C.5} $$

- Euler's acceleration:

$$\dot{\vec{\omega}}_t \wedge \vec{\rho} = \dot{\omega}_t^{\times} \vec{\rho} = \begin{bmatrix} 0 & 0 & -\ddot{\nu} \\ 0 & 0 & 0 \\ \ddot{\nu} & 0 & 0 \end{bmatrix} \begin{bmatrix} x \\ y \\ z \end{bmatrix} = \begin{bmatrix} -\ddot{\nu} z \\ 0 \\ \ddot{\nu} x \end{bmatrix}^{\mathcal{O}_t}. \tag{C.6}$$

- Coriolis' acceleration:

$$2\vec{\omega}_t \wedge \dot{\vec{\rho}} = 2\omega_t^{\times} \dot{\vec{\rho}} = 2 \begin{bmatrix} 0 & 0 & -\dot{\nu} \\ 0 & 0 & 0 \\ \dot{\nu} & 0 & 0 \end{bmatrix} \begin{bmatrix} \dot{x} \\ \dot{y} \\ \dot{z} \end{bmatrix} = \begin{bmatrix} -2\dot{\nu}\dot{z} \\ 0 \\ 2\dot{\nu}\dot{x} \end{bmatrix}^{\mathcal{O}_t}. \tag{C.7}$$

We have therefore:

$$\ddot{\vec{\rho}}^{\,\mathcal{I}} = \begin{bmatrix} \ddot{x} \\ \ddot{y} \\ \ddot{z} \end{bmatrix}^{\mathcal{O}_t} + \begin{bmatrix} -\dot{\nu}^2 x \\ 0 \\ -\dot{\nu}^2 z \end{bmatrix}^{\mathcal{O}_t} + \begin{bmatrix} -\ddot{\nu} z \\ 0 \\ \ddot{\nu} x \end{bmatrix}^{\mathcal{O}_t} + \begin{bmatrix} -2\dot{\nu}\dot{z} \\ 0 \\ 2\dot{\nu}\dot{x} \end{bmatrix}^{\mathcal{O}_t}. \tag{C.8}$$

C.2. Elements of the Jacobian matrix for the linearization of differential gravity

The linearized equation is given by Expression (2.50), which is reminded below:

$$\vec{g}(C) = \vec{g}(C)_0 + \left.\frac{\partial \vec{g}(C)}{\partial \vec{r}_c}\right|_{op} (\vec{r}_c - \vec{r}_{c_0}), \tag{C.9}$$

where $\vec{g}(C) = -\mu r_c^{-3} \vec{r}_c = -\mu (x^2 + y^2 + (z - r_t)^2)^{-3/2} \begin{bmatrix} x & y & z - r_t \end{bmatrix}^T$.

The Jacobian matrix is thus computed as:

$$\frac{\partial \vec{g}(C)}{\partial \vec{r}_c} = \begin{bmatrix} \frac{-\mu}{r_c^3}\left[1 - 3\frac{x^2}{r_c^2}\right] & 3\frac{\mu}{r_c^3}\frac{xy}{r_c^2} & 3\frac{\mu}{r_c^3}\frac{xz}{r_c^2} \\ 3\frac{\mu}{r_c^3}\frac{yx}{r_c^2} & \frac{-\mu}{r_c^3}\left[1 - 3\frac{y^2}{r_c^2}\right] & 3\frac{\mu}{r_c^3}\frac{yz}{r_c^2} \\ 3\frac{\mu}{r_c^3}\frac{zx}{r_c^2} & 3\frac{\mu}{r_c^3}\frac{zy}{r_c^2} & \frac{-\mu}{r_c^3}\left[1 - 3\frac{z^2}{r_c^2}\right] \end{bmatrix} = -\frac{\mu}{r_c^3} \begin{bmatrix} 1 - 3\frac{x^2}{r_c^2} & -3\frac{xy}{r_c^2} & -3\frac{xz}{r_c^2} \\ -3\frac{yx}{r_c^2} & 1 - 3\frac{y^2}{r_c^2} & -3\frac{yz}{r_c^2} \\ -3\frac{zx}{r_c^2} & -3\frac{zy}{r_c^2} & 1 - 3\frac{z^2}{r_c^2} \end{bmatrix}. \tag{C.10}$$

The linearization being around $\vec{r}_{c_0} = \vec{r}_t = [0 \quad 0 \quad -r_t]^T$, we find $x = 0$, $y = 0$, $z = -r_t$:

$$\left.\frac{\partial \vec{g}(C)}{\partial \vec{r}_c}\right|_{op} = -\frac{\mu}{r_t^3} \begin{bmatrix} 1 & 0 & 0 \\ 0 & 1 & 0 \\ 0 & 0 & -2 \end{bmatrix}. \tag{C.11}$$

C.3. Development of the translational linear equations

The objective of this section is to show step by step the development of the model given by Equation (2.64) when we replace the values of $\dot{\nu}$, $\ddot{\nu}$ and $\frac{\mu}{r_t^3}$ given by Equations (2.39), (2.41) and (2.67) respectively. In order to ease the reading, the expressions of these equations are recalled below.

The model is given by:

$$\begin{cases} \dot{\nu}^2 x'' + \ddot{\nu} x' = \left[\dot{\nu}^2 - \dfrac{\mu}{r_t^3}\right] x + \ddot{\nu} z + 2\dot{\nu}^2 z', \\ \dot{\nu}^2 y'' + \ddot{\nu} y' = -\dfrac{\mu}{r_t^3} y, \\ \dot{\nu}^2 z'' + \ddot{\nu} z' = -\ddot{\nu} x + \left[\dot{\nu}^2 + 2\dfrac{\mu}{r_t^3}\right] z - 2\dot{\nu}^2 x', \end{cases} \tag{C.12}$$

while the parameters $\dot{\nu}$, $\ddot{\nu}$ and $\frac{\mu}{r_t^3}$ are given by:

$$\dot{\nu} = k^2 \kappa(\nu)^2, \tag{C.13}$$

$$\ddot{\nu} = 2k^4 \kappa(\nu)^3 \kappa(\nu)', \tag{C.14}$$

$$\frac{\mu}{r_t^3} = k^4 \kappa(\nu)^3. \tag{C.15}$$

✍ **NOTE:**

The derivatives of the parameter $\kappa(\nu)$ *given in Equation* (2.33) *are written below, which will be used in the sequel.*

$$\kappa(\nu)' = \frac{d\kappa(\nu)}{d\nu} = -e\ \sin\nu, \tag{C.16a}$$

$$\kappa(\nu)'' = \frac{d^2\kappa(\nu)}{d\nu^2} = -e\ \cos\nu. \tag{C.16b}$$

The following relations will also be used:

$$\kappa(\nu) + \kappa(\nu)'' = 1, \tag{C.17a}$$

$$(\kappa(\nu)(\cdot))' = \kappa(\nu)'(\cdot) + \kappa(\nu)(\cdot)', \tag{C.17b}$$

$$(\kappa(\nu)(\cdot))'' = \kappa(\nu)''(\cdot) + 2\kappa(\nu)'(\cdot)' + \kappa(\nu)(\cdot)'', \tag{C.17c}$$

where $(\cdot)$ *is either* x*,* y *or* z*.*

For the sake of simplicity, the development will be done firstly for the expression in x'', then for y'' and finally for z''.

For the equation in x'' we have:

$$k^4\kappa(\nu)^4 x'' + 2k^4\kappa(\nu)^3\kappa(\nu)' x' = \left[k^4\kappa(\nu)^4 - k^4\kappa(\nu)^3\right] x + 2k^4\kappa(\nu)^3\kappa(\nu)' z + 2k^4\kappa(\nu)^4 z'. \tag{C.18}$$

Dividing each term by $k^4\kappa(\nu)^3$, we get:

$$\kappa(\nu)x'' + 2\kappa(\nu)'x' - \kappa(\nu)x + x = 2\kappa(\nu)'z + 2\kappa(\nu)z'. \tag{C.19}$$

By using Equation (C.17a) into the term in x and developing it, we get:

$$\kappa(\nu)x'' + 2\kappa(\nu)'x' - \kappa(\nu)x + \kappa(\nu)x + \kappa(\nu)''x = 2\kappa(\nu)'z + 2\kappa(\nu)z'. \tag{C.20}$$

Let's now apply Equations (C.17b) and (C.17c):

$$(\kappa(\nu)x)'' = 2\left(\kappa(\nu)z\right)'. \tag{C.21}$$

The procedure is simpler for equation in y'', which gives:

$$k^4\kappa(\nu)^4y'' + 2k^4\kappa(\nu)^3\kappa(\nu)'y' = -k^4\kappa(\nu)^3y, \tag{C.22}$$

$$\kappa(\nu)y'' + 2\kappa(\nu)'y' + y = 0, \tag{C.23}$$

$$\kappa(\nu)y'' + 2\kappa(\nu)'y' + \kappa(\nu)''y = -\kappa(\nu)y, \tag{C.24}$$

$$(\kappa(\nu)y)'' = -\kappa(\nu)y. \tag{C.25}$$

Finally, for the term in z, we have that:

$$k^4\kappa(\nu)^4z'' + 2k^4\kappa(\nu)^3\kappa(\nu)'z' = -2k^4\kappa(\nu)^3\kappa(\nu)'x + \left[k^4\kappa(\nu)^4 + 2k^4\kappa(\nu)^3\right]z - 2k^4\kappa(\nu)^4x', \tag{C.26}$$

$$\kappa(\nu)z'' + 2\kappa(\nu)'z' - \kappa(\nu)z - 2z = -2\kappa(\nu)'x - 2\kappa(\nu)x', \tag{C.27}$$

$$\kappa(\nu)z'' + 2\kappa(\nu)'z' - \kappa(\nu)z - 2\kappa(\nu)z - 2\kappa(\nu)''z = -2\kappa(\nu)'x - 2\kappa(\nu)x', \tag{C.28}$$

$$\kappa(\nu)z'' + 2\kappa(\nu)'z' - 2\kappa(\nu)''z = 3\kappa(\nu)z - 2\kappa(\nu)'x - 2\kappa(\nu)x'. \tag{C.29}$$

By adding the term $3\kappa(\nu)''z$ to both sides of this last equation, we get that:

$$\kappa(\nu)z'' + 2\kappa(\nu)'z' - 2\kappa(\nu)''z + 3\kappa(\nu)''z = 3\kappa(\nu)''z + 3\kappa(\nu)z - 2\kappa(\nu)'x - 2\kappa(\nu)x', \tag{C.30}$$

$$\kappa(\nu)z'' + 2\kappa(\nu)'z' + \kappa(\nu)''z = 3\kappa(\nu)''z + 3\kappa(\nu)z - 2\kappa(\nu)'x - 2\kappa(\nu)x'. \tag{C.31}$$

We use once more Expression (C.17a) to simplify this last equation:

$$\kappa(\nu)z'' + 2\kappa(\nu)'z' + \kappa(\nu)''z = 3z - 2\kappa(\nu)'x - 2\kappa(\nu)x'. \tag{C.32}$$

Finally, applying Equation (C.17c) to left-side term and Equation (C.17b) to the right-side term, we obtain:

$$(\kappa(\nu)z)'' = 3z - 2\left(\kappa(\nu)x\right)'. \tag{C.33}$$

The model written in Equation (C.12) is therefore:

$$\begin{cases} (\kappa(\nu)x)'' = 2\left(\kappa(\nu)z\right)', \\ (\kappa(\nu)y)'' = -\kappa(\nu)y, \\ (\kappa(\nu)z)'' = 3z - 2\left(\kappa(\nu)x\right)'. \end{cases} \tag{C.34}$$

APPENDIX D

PARAMETRIZATION OF ROTATIONS AND TRANSLATIONS

This appendix aims at presenting the mathematical elements of parametrization for rotational and translational motions of a rigid body. We focus on the parametrization of the rotational motion of a rigid body around its center of gravity at first. Secondly, the parametrization of rigid transformations will be exposed. In addition to conventional and usual parametrization of rotations, found in the literature of engineering sciences (axis and angle of rotation, rotation matrices, quaternions), we also present less common rigid transformations parametrizations, based on advanced algebraic structures. They consist of hyper-complex algebras over $\mathbb{R}$ defined by the general Dickson algebra [36], [37], obtained by the generalized Dickson duplication process, also known as the Cayley-Dickson method [112]. This method, proposed by Arthur Cayley and Leonard Eugene Dickson, allows builing a $2n$ dimensional algebra on the ring algebra basis, from an n dimensional algebra on this algebra, generalizing this way Hamilton's work on quaternions and on the extension of complex numbers. We will not introduce here the underlying theory of the algebraic constructions but the basic algebraic properties for understanding the necessary developments for the relative motion modelling.

D.1. Rotation parametrizations

The rotational motion of a rigid body around its center of mass can be described as the motion of a point on a nonlinear 3-dimensional variety [11]. This variety has a particular algebraic structure and is identified as the special Lie orthogonal group of vector rotations in the three-dimensional Euclidean space, noted $SO(3)$, [111], [106], [62]. In order to write the relative rotational motion equations of a rigid body, it is necessary to choose a parametrization, a set of coordinates $(\zeta_1, \cdots, \zeta_i, \cdots, \zeta_n)$, completely describing the orientation of the rigid body relative to a reference frame. Thus, we define an orthogonal coordinate system, denoted $\mathcal{B}$, linked to the rigid body and a reference frame, denoted $\mathcal{R}$. This parametrization problem is well known, going back to Euler's work in 1776 together with the work of Jacobi, Hamilton, Cayley, Klein, Rodrigues and Gibbs among others. The different parametrizations are mainly characterized by n, the number of parameters (parametrization redundant or not) and their properties (singularities, uniqueness). Currently, it does not seem to exist, a preferable parametrization but rather better uses and preferences according to the different scientific fields and areas of application [11], [100]. However, there are still some general results which are summarized as follows:

- The minimum number of parameters to describe the relative angular displacement between two reference frames $\mathcal{B}$ and $\mathcal{R}$ is 3 [100];

- it is topologically impossible to have a global parametrization of rotations without singularities with only 3 parameters [111];
- In 1950 showed that 5 is the minimum number of parameters to represent the group of rotations in a 1-1 correspondence (globality and unicity of the parametrization) [111];
- The quaternions representation (parametrization with $n = 4$) is sufficient for a representation of the group of rotations in a correspondence 1-2 (globality and non-unicity) [111].

The most frequently encountered parametrizations are:

- the rotation matrices ($n = 9$);
- the Euler axis-angle representation ($n = 4$);
- the symmetric parameters of Euler-Rodrigues (or quaternions) ($n = 4$);
- the Euler angles ($n = 3$);
- the classic Rodrigues parameters or Gibbs vector [106], [100], [126] ($n = 3$);
- the modified Rodrigues parameters [106], [100] ($n = 3$);
- the higher order Rodrigues parameters [100] ($n = 3$);
- the axis-azimuth representation [106] ($n = 4$);
- the coordinates (w, z) [120] ($n = 4$);
- the Cayley-Klein parameters [106], [100] ($n = 4$);

In this appendix, we present only the four first parametrizations which are the most common. In particular, we first define the parametrization by means of rotation matrices that is global and without singularities though redundant. Then we interpret the other three with the formalism defined by the rotation matrices.

D.1.1. Parametrization by means of rotation matrices

The set of attitudes of a rigid body can be identified to the set of orthogonal matrices 3×3 whose determinant is equal to 1. Thus, consider the rotation of an orthonormal basis $B_r = [\vec{r}_1, \vec{r}_2, \vec{r}_3]$ in an orthonormal basis $B_b = [\vec{b}_1, \vec{b}_2, \vec{b}_3]$. Each vector of the basis B_b is expressed in the basis B_r as (see Figure D.1):

$$\vec{b}_i = \sum_{j=1}^{3} \cos(\alpha_{ij})\, \vec{r}_j,\ i = 1, \cdots, 3. \tag{D.1}$$

The matrix equation is thus obtained as:

$$\begin{bmatrix} \vec{b}_1 \\ \vec{b}_2 \\ \vec{b}_3 \end{bmatrix} = [\cos(\alpha_{ij})]_{\substack{1 \le i \le 3 \\ 1 \le j \le 3}} \begin{bmatrix} \vec{r}_1 \\ \vec{r}_2 \\ \vec{r}_3 \end{bmatrix} = R^{\,b/r} \begin{bmatrix} \vec{r}_1 \\ \vec{r}_2 \\ \vec{r}_3 \end{bmatrix}, \tag{D.2}$$

where $R^{b/r}$ is called the *cosine director matrix* or *rotation matrix* of the reference frame $\mathcal{R}$ with respect to the frame $\mathcal{B}$. This matrix is also defined by:

$$\left[R_{ij}^{b/r}\right]_{\substack{1 \le i \le 3 \\ 1 \le j \le 3}} = \vec{b}_i^{\,T} \vec{r}_j,\ i, j = 1, \cdots, 3. \tag{D.3}$$

Any rotation matrix is an element of the special orthogonal Lie group $SO(3)$ whose group operation is the matrix multiplication, where the identity is I_3 and where the inverse of a rotation matrix is its transpose. Any rotation matrix satisfies the properties:

★ **PROPERTY 2** (Rotation matrices)**:**

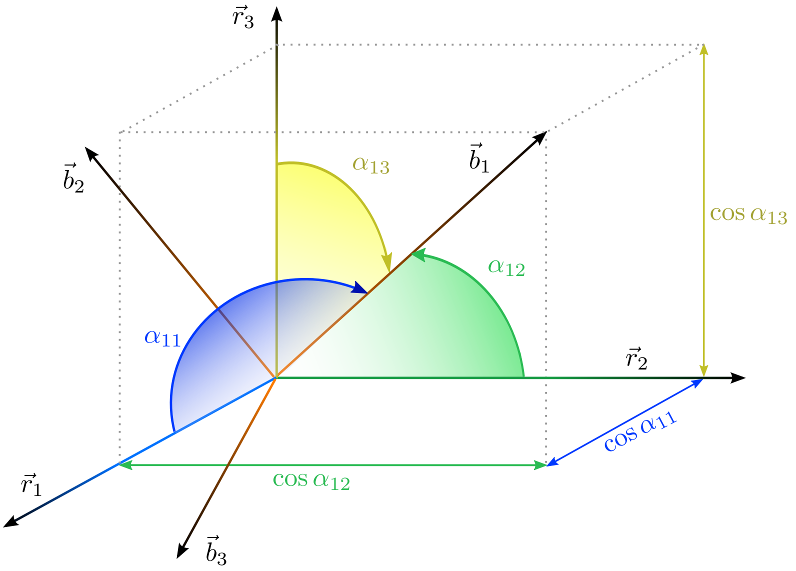

Figure D.1: Director cosines of $\vec{b}_1$ relative to $\mathcal{R}$.

- $R^{\,b/b} = I$;
- $(R^{\,b/r})^{-1} = (R^{\,b/r})^T$ *and* $\det(R^{\,b/r}) = 1$;
- *there is at least one eigenvector of* $R^{\,b/r}$ *whose associated eigenvalue is* 1. *This eigenvector whose coordinates are identical in* B_r *and in* B_b *and is a vector defining the axis of rotation;*
- $R^{\,r/b} = (R^{\,b/r})^T$.

In addition, the rotation matrix can be used to calculate the coordinates of a vector $\vec{v}$ in a basis B_b from the coordinates of this vector in a basis B_r.

$$\vec{v}^{\,\mathcal{B}} = R^{\,b/r}\,\vec{v}^{\,\mathcal{R}}, \quad \vec{v}^{\,\mathcal{R}} = (R^{\,b/r})^T\,\vec{v}^{\,\mathcal{B}}. \tag{D.4}$$

One of the interesting features of this parametrization is to exploit the matrix multiplication properties to perform composed rotations. Thus, if one takes a third basis $B_n = (\vec{n}_1, \vec{n}_2, \vec{n}_3)$ associated to a reference frame $\mathcal{N}$, we obtain:

$$\vec{v}^{\,\mathcal{B}} = R^{\,b/r}\vec{v}^{\,\mathcal{R}} = R^{\,b/r}R^{\,r/n}\,\vec{v}^{\,\mathcal{N}}. \tag{D.5}$$

This parametrization of a rigid body's relative orientation has the advantages of being global, without singularity, to allow easy composition of elementary rotations and to lead to a linear kinematic equation of the parameters for a given rotation vector $\vec{\omega}$ [126], [100].

$$\dot{R}^{\,b/r} = -\omega^{\times}R^{\,b/r}, \tag{D.6}$$

where $\omega^{\times}$ is the skew operator associated to the vector $\vec{\omega}^{\mathcal{B}}$. In return, this parametrization is redundant, which is evidenced by the algebraic constraint $R^{b/r}(R^{b/r})^T = I_3$.

D.1.2. Parametrization by means of the Euler axis-angle representation $(\vec{\Omega}, \Phi)$

This parametrization has its origin in the fundamental result of Euler on rigid rotations.

THEOREM 5 (Euler). *Any rigid body can be moved from an initial arbitrary orientation to another final arbitrary orientation by a single rigid rotation characterized by a main angle* Φ *and operating around a main axis, characterized by an axis rotation vector* $\vec{\Omega}$, *fixed for both orientations.*

Consider the rotation of a vector $\vec{X}_c$ into a vector $\vec{X}_t$ as defined in Figure D.2. According to Euler's theorem, this rotation is uniquely specified by the unit vector $\vec{\Omega}$ giving the direction of an axis (invariant under the rotation) and a scalar Φ specifying the angle of rotation around the axis.

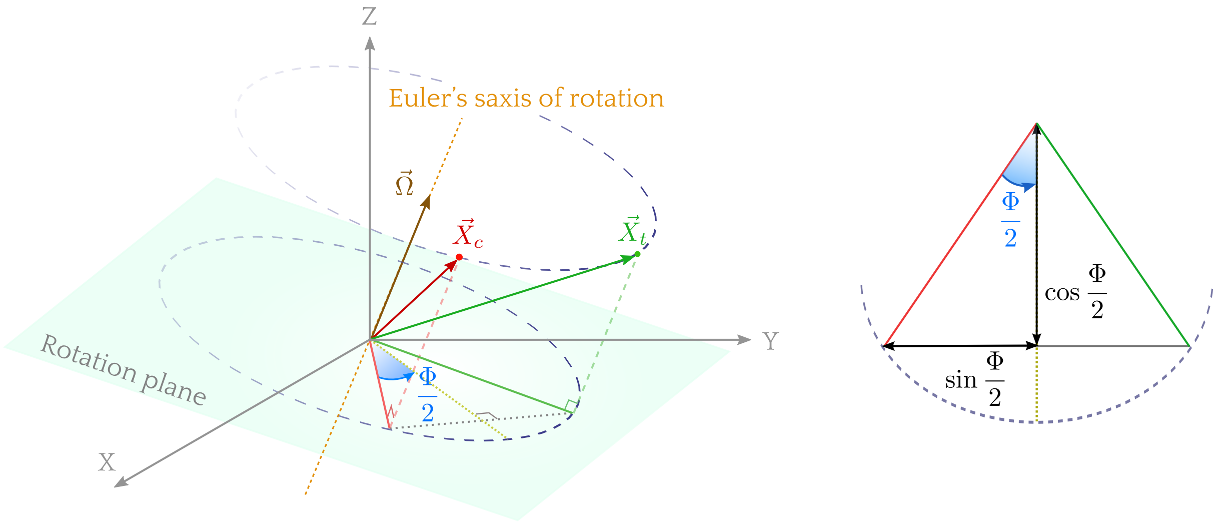

Figure D.2: Rotation of vector $\vec{X}_c$ into vector $\vec{X}_t$.

The expression of vector $\vec{X}_t$ as a function of vector $\vec{X}_c$ is given by Euler's formula:

$$\begin{aligned} \vec{X}_t &= \cos(\Phi)\vec{X}_c + (1-\cos(\Phi))(\vec{\Omega}^T\vec{X}_c)\vec{\Omega} + \sin(\Phi)\vec{\Omega}\wedge\vec{X}_c \\ &= \vec{X}_c + \sin(\Phi)\vec{\Omega}\wedge\vec{X}_c + (1-\cos(\Phi))\vec{\Omega}\wedge(\vec{\Omega}\wedge\vec{X}_c). \end{aligned} \tag{D.7}$$

By applying Euler's formula to the vectors of the basis B_r to transform it into the basis B_b, we get:

$$R_{ij}^{b/r} = \cos(\Phi)\delta_{ij} + (1-\cos(\Phi))(\vec{\Omega}^T\vec{b}_i)(\vec{\Omega}^T\vec{b}_j) + \sin(\Phi)(\vec{\Omega}\wedge\vec{b}_i)^T\vec{b}_j,\ i,j=1,\cdots,3. \tag{D.8}$$

(D.8) can be rewritten in a matrix form according to the Euler's vector and angle of rotation as:

$$R^{b/r} = \cos(\Phi)I + (1-\cos(\Phi))\vec{\Omega}\vec{\Omega}^T + \sin(\Phi)\Omega^\times. \tag{D.9}$$

Reciprocally, the Euler's vector and angle of rotation can be calculated as a function of the rotation matrix.

$$\begin{aligned} \Phi &= \arccos(\frac{1}{2}\left(\mathrm{trace}(R^{b/r})-1\right)), \\ \Omega^\times &= \frac{1}{2\sin(\Phi)}\left((R^{b/r})^T - R^{b/r}\right). \end{aligned} \tag{D.10}$$

The parametrization by *the Euler axis-angle representation* consists of defining this vector from $\vec{\Omega}$ and Φ as:

$$\vec{\gamma} = \Phi\vec{\Omega}. \tag{D.11}$$

This vector is therefore characterized by its amplitude (rotation angle Φ) and its orientation (unit vector $\vec{\Omega}$ of the axis of rotation). $\vec{\gamma}$ is the eigenvector of the rotation matrix, associated to the eigenvalue 1. It therefore satisfies the relationship:

$$(R^{b/r} - I_3)\,\vec{\gamma} = 0. \tag{D.12}$$

It is possible to infer the rotation matrix as a function of the Euler axis-angle representation.

$$R^{b/r} = \cos(\Phi)I + \frac{(1-\cos(\Phi))\,\vec{\gamma}\,\vec{\gamma}^T}{\|\vec{\gamma}\|^2} + \frac{\sin(\Phi)\,\gamma^\times}{\|\vec{\gamma}\|}. \tag{D.13}$$

The kinematic equation associated with this parametrization is derived as [100]:

$$\dot{\vec{\gamma}} = \left[I_3 + \frac{\gamma^\times}{2} + \frac{1}{\Phi^2}\left(1 - \frac{\Phi \sin\Phi}{2(1-\cos\Phi)}\right)[\gamma^\times]^2 \right]\vec{\omega}. \tag{D.14}$$

This 4-parameter parametrisation is global since it is not affected by singularities (if we exclude the trivial singularity associated with the zero angle of rotation $\Phi = 0$) but it is not unique. Indeed, two physical rotations about the same axis and different respective angles $2k\pi$, $k \in \mathbb{N}$ cannot be differentiated in this representation. Furthermore, due to the complex formulation of the associated kinematic equation, this parametrization is generally less attractive. Another widely used parametrization using 4 parameters in the satellite attitude control is given by the set of Euler's parameters or quaternions.

D.1.3. Parametrization by means of quaternions

The symmetrical parameters of Euler-Rodrigues or quaternions form a set of four global but not unique parameters characterizing a rotation and possessing some advantages over the parametrization by means of the main vector of rotation. They belong to a non-commutative $\mathbb{R}$-algebra of dimension 4 (isomorphic to $\mathbb{R}^4$ as a vectorial space), following the widespread Dickson process from the complex set.

They are defined by the relation:

$$\begin{aligned} \vec{q} &= \vec{\Omega}\sin\left(\frac{\Phi}{2}\right), \\ q_4 &= \cos\left(\frac{\Phi}{2}\right), \end{aligned} \tag{D.15}$$

where the quaternion q is written as:

$$q = q_1\mathbf{i} + q_2\mathbf{j} + q_3\mathbf{k} + q_4 = \vec{q} + q_4 = (\vec{q}, q_4), \tag{D.16}$$

with q_4 being the scalar part of the quaternion and $\vec{q} = q_1\mathbf{i} + q_2\mathbf{j} + q_3\mathbf{k}$, the vector part. **i**, **j**, **k** are the square roots of -1 and they are defined as hyper imaginary numbers. They allow defining the quaternion algebra and fundamental formulas initially proposed by William Rowan Hamilton [58] to represent points in space (dimension 3) identically to the representation of points in the plane (dimension 2) by the complex.

$$\mathbf{i}^2 = \mathbf{j}^2 = \mathbf{k}^2 = \mathbf{ijk} = -1. \tag{D.17}$$

The quaternion given by the Formula (D.15) is unitary and thus belongs to the unit sphere $\mathbb{S}^3$.

$$\mathbb{S}^3 = \left\{(q_1, q_2, q_3, q_4) \in \mathbb{R}^4 \ : \ \|(q_1, q_2, q_3, q_4)\| = 1\right\}. \tag{D.18}$$

DEFINITION D.1.1: *The set of quaternions, denoted $\mathbb{H}$ is a non-commutative entity which corresponds to the second level of the Dickson construction. It is defined by:*

$$\mathbb{H} = \{q_1\mathbf{i} + q_2\mathbf{j} + q_3\mathbf{k} + q_4 : q_1, q_2, q_3, q_4 \in \mathbb{R}\}. \tag{D.19}$$

The associativity and non-commutativity are the two main properties of the algebra of quaternions. The product of **i**, **j** and **k** is similar to the traditional vector product, as shown in Figure D.3.

Thus, the relations (D.17) and (D.20) represent the multiplication table that completely defines the algebra.

$$\begin{aligned} &\mathbf{ij} = \mathbf{k},\ \mathbf{ji} = -\mathbf{k}, \\ &\mathbf{jk} = \mathbf{i},\ \mathbf{kj} = -\mathbf{i}, \\ &\mathbf{ki} = \mathbf{j},\ \mathbf{ik} = -\mathbf{j}. \end{aligned} \tag{D.20}$$

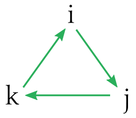

Figure D.3: Quaternion order multiplication.

The conjugate quaternion is given by:

$$q^* = -q_1\mathbf{i} - q_2\mathbf{j} - q_3\mathbf{k} + q_4. \tag{D.21}$$

Given two quaternions q_a and q_b:

$$\begin{aligned} q_a &= [q_{a1}, q_{a2}, q_{a3}, q_{a4}]\,, \\ q_b &= [q_{b1}, q_{b2}, q_{b3}, q_{b4}]\,, \end{aligned} \tag{D.22}$$

then the sum of these two quaternions is:

$$q_a + q_b = (q_{a1} + q_{b1})\mathbf{i} + (q_{a2} + q_{b2})\mathbf{j} + (q_{a3} + q_{b3})\mathbf{k} + (q_{a4} + q_{b4}), \tag{D.23}$$

and their product is:

$$\begin{aligned} q_a \odot q_b = {} & (q_{a4}q_{b4} - q_{a1}q_{b1} - q_{a2}q_{b2} - q_{a3}q_{b3}) + (q_{a4}q_{b1} + q_{a1}q_{b4} + q_{a2}q_{b3} - q_{a3}q_{b2})\mathbf{i} + \\ & + (q_{a4}q_{b2} - q_{a1}q_{a3} + q_{a2}q_{b4} + q_{a3}q_{b1})\mathbf{j} + (q_{a4}q_{b3} + q_{a1}q_{b2} - q_{a2}q_{b1} + q_{a3}q_{b4})\mathbf{k}. \end{aligned} \tag{D.24}$$

The product of two quaternions can also be expressed by means of the dot and cross products of the respective vector parts for the two quaternions:

$$q_a \odot q_b = q_{a4}\vec{q}_b + q_{b4}\vec{q}_a + \vec{q}_a \wedge \vec{q}_b + q_{a4}q_{b4} - \vec{q}_a^{\,T}\vec{q}_b. \tag{D.25}$$

It is also possible to write the product of two quaternions $q_a \odot q_b$ as the multiplication of an orthonormal matrix by a vector. This multiplication can be performed in two different ways according to which quaternion is selected first.

$$q_a \odot q_b = [M_l(q_a)]\, q_b^T = [M_r(q_b)]\, q_a^T\,, \tag{D.26}$$

where:

$$[M_l(q_a)]q_b^T = \begin{bmatrix} q_{a4} & -q_{a3} & q_{a2} & q_{a1} \\ q_{a3} & q_{a4} & -q_{a1} & q_{a2} \\ -q_{a2} & q_{a1} & q_{a4} & q_{a3} \\ -q_{a1} & -q_{a2} & -q_{a3} & q_{a4} \end{bmatrix} \begin{bmatrix} q_{b1} \\ q_{b2} \\ q_{b3} \\ q_{b4} \end{bmatrix} \quad , \quad [M_r(q_b)]q_a^T = \begin{bmatrix} q_{b4} & q_{b3} & -q_{b2} & q_{b1} \\ -q_{b3} & q_{b4} & q_{b1} & q_{b2} \\ q_{b2} & -q_{b1} & q_{b4} & q_{b3} \\ -q_{b1} & -q_{b2} & -q_{b3} & q_{b4} \end{bmatrix} \begin{bmatrix} q_{a1} \\ q_{a2} \\ q_{a3} \\ q_{a4} \end{bmatrix}. \tag{D.27}$$

The dot product of two quaternions q_a and q_b is defined by:

$$q_a \cdot q_b = \frac{1}{2}(q_a^* \odot q_b + q_b^* \odot q_a) = \frac{1}{2}(q_a \odot q_b^* + q_b \odot q_a^*) = (\vec{0}, q_{a4}q_{b4} + \vec{q}_a^{\,T}\vec{q}_b). \tag{D.28}$$

The cross product of two quaternions q_a and q_b is defined by:

$$q_a \times q_b = \frac{1}{2}(q_a \odot q_b - q_b^* \odot q_a^*) = (q_{b4}\vec{q}_a + q_{a4}\vec{q}_b + \vec{q}_a \wedge \vec{q}_b, 0). \tag{D.29}$$

The norm (magnitude) of a quaternion is defined by:

$$\|q\| = \sqrt{q \odot q^*} = \sqrt{q_1^2 + q_2^2 + q_3^2 + q_4^2} = q^* \odot q = q \cdot q = (\vec{0}, q_4^2 + \vec{q}^{\,T}\vec{q}). \tag{D.30}$$

The inverse of a quaternion is given by:

$$q^{-1} = \frac{q^*}{[\|q\|]^2}. \tag{D.31}$$

The multiplication by a matrix $M = \begin{bmatrix} M_{11} & M_{12} \\ M_{21} & M_{22} \end{bmatrix} \in \mathbb{R}^{4\times4}$ is defined identically to the multiplication of a matrix of $\mathbb{R}^{4\times4}$ by a vector of dimension 4:

$$M * q = (M_{11}\vec{q} + M_{12}q_4, M_{21}\vec{q} + M_{22}q_4). \tag{D.32}$$

Finally, similarly to the complex numbers, a real part and a complex part can be defined.

$$\Re(q) = \frac{q+q^*}{2}, \quad \Im(q) = \frac{q-q^*}{2}. \tag{D.33}$$

Quaternions are widely used to ease the representation of rotations in space. Thus, the expression of the vector $\vec{r}$ in the basis B_b and B_r are linked by the relationship:

$$\begin{bmatrix} \vec{r}^{\,\mathcal{B}_b} \\ 0 \end{bmatrix} = [q^{b/r}]^* \odot \begin{bmatrix} \vec{r}^{\,\mathcal{B}_r} \\ 0 \end{bmatrix} \odot q^{b/r}. \tag{D.34}$$

The relationships between a rotation matrix and the associated quaternion with the notation $(R^{b/r}(q^{b/r}))$ are given by:

$$\begin{aligned} \vec{q}^{\,b/r} &= \frac{1}{4{q_4}^{b/r}} \begin{bmatrix} R^{b/r}_{23} - R^{b/r}_{32} \\ R^{b/r}_{31} - R^{b/r}_{13} \\ R^{b/r}_{12} - R^{b/r}_{21} \end{bmatrix}, \\ {q_4}^{b/r} &= \pm\frac{1}{2}\sqrt{1 + \mathrm{trace}(R^{b/r})} \end{aligned} \tag{D.35}$$

and reciprocally (the notation b/r on the quaternion is left apart here to simplify the notation)

$$R^{b/r} = (q_4^2 - \vec{q}^{\,T}\vec{q})I + 2\vec{q}\,\vec{q}^{\,T} - 2q_4q^{\times}. \tag{D.36}$$

The composition of rotations can then be written in a simplified manner by using the identity:

$$R(q')R(q) = R(q' \odot q). \tag{D.37}$$

Thus, we get the following identity:

$$R^{b/r} = R^{b/i}(q^{b/i})R^{i/r}(q^{i/r}) = R^{b/i}(q^{b/i})(R^{r/i}(q^{r/i}))^T = R^{b/r}(q^{b/i} \odot (q^{r/i})^{-1}). \tag{D.38}$$

The kinematic equation associated to the classic Euler-Rodrigues parameters is easily obtained as [126], [100]:

$$\dot{q}^{b/r} = \frac{1}{2}Q(q^{b/r})\,\vec{\omega}^{\,\mathcal{B}}. \tag{D.39}$$

Despite the advantages of the algebra of quaternions, this parametrization remains non-unique since any physical attitude can be represented by a pair of unit quaternions $\pm q \in \mathbb{S}^3$.

D.1.4. Parametrization by means of the Euler angles

As mentioned in the introduction, the minimum number of parameters that allows to define a rotation from a basis B_r to a basis B_b is 3. Such rotation can be defined from the composition of three elementary rotations around one of the current coordinate axes. The sequence of necessary rotations is not unique since the order of the rotations can be inverted. Thus, for the first rotation, 3 axes choices are available then two possible axes choices for the two following rotations, leading to a possible choice of 12 sequences of elementary rotations. These sequences are identified by the triplet $(i-j-k),\ i,\ j,\ k = 1,\cdots,3$ defining the coordinate frame axis' number around which the rotation is performed. In order to define a rotation in this way, it is necessary to use four successive basis B_r, $B_{r'}$, $B_{r''}$ and B_b. The order of the sequence of elementary rotations completely determines the parametrization and its properties. The set of all 12 possible different sequences defines all the 12 possible sets of the *Euler angles*. The 6 anti-symmetric sequences ((1-2-3), (1-3-2), (2-3-1), (3-1-2), (3-2-1), (2-1-3)), referred to as *Cardan angles*, *Tait angles* or *Bryant angles*, can be distinguished from the 6 symmetric sequences ((1-2-1), (1-3-1), (2-3-2), (3-1-3), (3-2-3), (2-1-2)) [106]. The choice of the sequence to use depends on the domain of study and of the culture of the disciplinary field in question. Usually, the three Euler angles are identified as ϕ the angle of rotation (roll, spin), θ, the nutation angle (pitch) and ψ, the precession angle (yaw). We recall here that the parametrization generated by the anti-symmetric sequence (3-2-1), is the most widely used in the aerospace field. However, it must be noted that the symmetrical sequence (3-1-3) is also well known in the space field since it corresponds to the angles $(\Omega,\ i,\ \omega)$ defining the orientation of a satellite's orbital plane [100]. The sequence (3-2-1) is shown in Figure D.4 and it is written as $\psi \to \theta \to \phi$ with the basis sequence:

$$(\vec{r}_1,\ \vec{r}_2,\ \vec{r}_3) \xrightarrow{\psi} (\vec{r}_1{}',\ \vec{r}_2{}',\ \vec{r}_3{}' = \vec{r}_3) \xrightarrow{\theta} (\vec{r}_1{}'',\ \vec{r}_2{}'' = \vec{r}_2{}',\ \vec{r}_3{}'') \xrightarrow{\phi} (\vec{b}_1 = \vec{r}_1{}'',\ \vec{b}_2,\ \vec{b}_3). \tag{D.40}$$

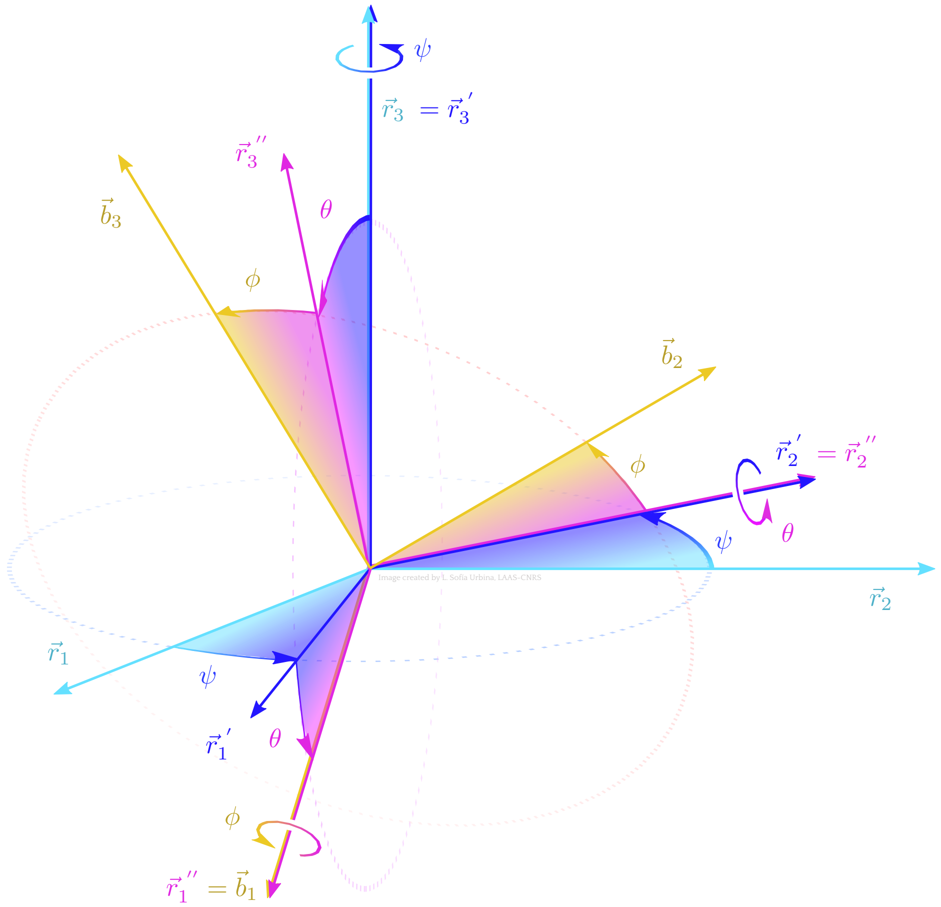

Figure D.4: Cardan angles.

In fact, each elementary rotation indexed by the axis around which it is produced and the current angle α can be characterized by a rotation matrix denoted $R_i(\theta)$ with:

$$R_1(\alpha) = \begin{bmatrix} 1 & 0 & 0 \\ 0 & \cos\alpha & \sin\alpha \\ 0 & -\sin\alpha & \cos\alpha \end{bmatrix}, \quad R_2(\alpha) = \begin{bmatrix} \cos\alpha & 0 & -\sin\alpha \\ 0 & 1 & 0 \\ \sin\alpha & 0 & \cos\alpha \end{bmatrix}, \quad R_3(\alpha) = \begin{bmatrix} \cos\alpha & \sin\alpha & 0 \\ -\sin\alpha & \cos\alpha & 0 \\ 0 & 0 & 1 \end{bmatrix}. \tag{D.41}$$

By composing these matrices of elementary rotations in the order of the selected sequence with the suitable angles, we obtain the rotation matrix of the complete rotation. Thus, for the sequence of interest (3-2-1), it yields:

$$R_{321}^{b/r} = R_1(\phi)R_2(\theta)R_3(\psi) = \begin{bmatrix} \cos\theta\cos\psi & \cos\theta\sin\psi & -\sin\theta \\ -\cos\phi\sin\psi + \sin\phi\sin\theta\cos\psi & \cos\phi\cos\psi + \sin\phi\sin\theta\sin\psi & \sin\phi\cos\theta \\ \sin\phi\sin\psi + \cos\phi\sin\theta\cos\psi & -\sin\phi\cos\psi + \cos\phi\sin\theta\sin\psi & \cos\phi\cos\theta \end{bmatrix}. \tag{D.42}$$

The rotation matrices from the 11 other parametrizations can be found in the reference [100], for example. It should be noted that to ensure the uniqueness of the anti-symmetrical Euler angles, one must have

$$0 \le \psi < 2\pi, \quad -\pi/2 \le \theta \le \pi/2, \quad 0 \le \phi < 2\pi, \tag{D.43}$$

since $R_{321}(\psi,\theta,\phi) = R_{321}(\psi+\pi, \pi-\theta, \phi-\pi)$. In addition, the parametrization by Euler angles has a singularity for $\theta = \pm 90$ deg. In this case, only the sum of the other two angles $\phi + \psi$ is uniquely determined.

Given the data of a rotation matrix $R^{b/r}$, the obtention of the Cardan angles for the sequence (3-2-1) is done from the following formulas:

$$\begin{aligned} \psi &= \arctan\left(\frac{R_{12}^{b/r}}{R_{11}^{b/r}}\right), \\ \theta &= -\arcsin\left(R_{13}^{b/r}\right), \\ \phi &= \arctan\left(\frac{R_{23}^{b/r}}{R_{33}^{b/r}}\right). \end{aligned} \tag{D.44}$$

For identical formulas associated with the 11 other sequences, the reader may refer to Appendix B of reference [100].

By using this rotation sequence (3-2-1) for the Euler angles, it is possible to obtain the kinematic equations by noting that the rotation vector $\vec{\omega}$ is written as:

$$\vec{\omega} = \omega_1\,\vec{b}_1 + \omega_2\,\vec{b}_2 + \omega_3\,\vec{b}_3 = \dot{\psi}\,\vec{r}_3 + \dot{\theta}\,\vec{r}_2\,' + \dot{\phi}\,\vec{b}_1. \tag{D.45}$$

Expressing the vectors $\vec{r}_2\,'$ and $\vec{r}_3$ in the basis B_b, we obtain the relationships:

$$\begin{aligned} \omega_1 &= -\dot{\psi}\sin\theta + \dot{\phi}, \\ \omega_2 &= \dot{\psi}\cos\theta\sin\phi + \dot{\theta}\cos\phi, \\ \omega_3 &= \dot{\psi}\cos\theta\cos\phi - \dot{\theta}\sin\phi. \end{aligned} \tag{D.46}$$

Thus, by reversing the previous relationships, the kinematic equations associated to the Cardan angles sequence (3-2-1) can be derived as:

$$\begin{aligned}
&\dot{\psi} = \frac{1}{cos\theta}[\omega_2 \sin\phi + \omega_3 \cos\phi], \\
&\dot{\theta} = \omega_2 \cos\phi - \omega_3 \sin\phi, \\
&\dot{\phi} = \omega_1 + [\omega_2 \sin\phi + \omega_3 \cos\phi] \tan\theta.
\end{aligned} \tag{D.47}$$

D.2. Joint parametrizations for rotation and translation

If we wish to represent the position and orientation (six degrees of freedom) of a reference frame $\mathcal{R}_f$ linked to a body with respect to an inertial reference frame $\mathcal{R}_e$, it is necessary to define a unit orientation quaternion $q^{f/e} \in \mathbb{H}$ and a translation vector $\vec{r}_{f/e} \in \mathbb{R}^3$. This problem is a particular case of the problem of representation of *rigid transformations*.

➻ **DEFINITION D.2.1:** *A rigid transformation is a transformation* $F : \mathbb{R}^n \to \mathbb{R}^n$ *preserving the distances (isometry) and the spatial orientation.*

$$F(\vec{x}) = R\vec{x} + \vec{t},\ \vec{x} \in \mathbb{R}^n,\ \vec{t} \in \mathbb{R}^n,\ R \in \mathbb{R}^{n\times n}, \tag{D.48}$$

with R *being an orthogonal matrix, i.e.* $R^T = R^{-1}$ *and* $\det(R) = 1$.

Rather than using the translation vector and the rotation matrix of the translation vector and the quaternion, it is possible to represent any rigid transformation by a single mathematical object that generalizes quaternions: *dual quaternions*.

D.2.1. The dual numbers

The dual numbers were introduced by W. Clifford in 1873 [22] and experienced various applications since then, including kinematics of rigid bodies [15], [123]. Dual numbers belong to one of the three hypercomplex algebra of dimension 2, also called set of parabolic complex numbers. Algebras based on dual numbers allow to link the rotation and translation.

➻ **DEFINITION D.2.2:** *The set of dual numbers is defined by:*

$$\mathbb{D} = \left\{\hat{z} = x + y\epsilon,\ (x, y) \in \mathbb{R}^2\right\}, \tag{D.49}$$

where x *is the real part,* y *is the dual part and* ϵ *is the dual operator or dual unit. The properties of* ϵ *are:*

$$\epsilon^2 = 0, \quad \epsilon \neq 0, \quad \epsilon.0 = 0.\epsilon = 0, \quad 1.\epsilon = \epsilon.1 = 1. \tag{D.50}$$

The relations (D.50) constitute the multiplication table defining the algebra of dual numbers. The dual conjugate number of a dual number $\hat{z}$ is given by:

$$\hat{z}^* = x - y\epsilon. \tag{D.51}$$

Given two dual numbers $\hat{z}_a = x_a + y_a\epsilon$ and $\hat{z}_b = x_b + y_b\epsilon$, then, the sum of these two dual numbers is:

$$\hat{z}_a + \hat{z}_{db} = x_a + x_b + (y_a + y_b)\epsilon, \tag{D.52}$$

and their product is:

$$\hat{z}_a\hat{z}_b = x_a x_b + (x_a y_b + x_b y_a)\epsilon. \tag{D.53}$$

The magnitude of a dual number is defined by:

$$\|\hat{z}\| = \sqrt{\hat{z}\hat{z}^*} = |x|, \tag{D.54}$$

and this is not a norm, even if it has the multiplicative property $|\hat{z}_a \hat{z}_b| = |\hat{z}_a||\hat{z}_b|$.

Due to the existence of divisors of 0, all dual numbers do not necessarily have an inverse.

DEFINITION D.2.3: *In the case of dual numbers, the set of divisors of 0 is the set of dual numbers, different from 0, whose magnitude is null:*

$$Z^*(\mathbb{D}) = \{\hat{z} \neq 0 \in \mathbb{D} \ : \ \|\hat{z}\| = 0\}\,. \tag{D.55}$$

The inverse of an invertible dual number is therefore given by:

$$\hat{z}^{-1} = \frac{\hat{z}^*}{[\|\hat{z}\|]^2} = \frac{1}{x} - \frac{y}{x^2}\epsilon. \tag{D.56}$$

Finally, as for complex numbers, a real part and a complex part can be defined.

$$\Re(\hat{z}) = \frac{\hat{z} + \hat{z}^*}{2}, \quad \Im(\hat{z}) = \frac{\hat{z} - \hat{z}^*}{2}. \tag{D.57}$$

The dual numbers can be naturally extended to define *the dual vectors* whose real and dual parts are vectors.

$$\hat{\vec{u}} = \vec{x} + \vec{y}\epsilon \in \mathbb{D}^n,\ \vec{x} \in \mathbb{R}^n,\ \vec{y} \in \mathbb{R}^n. \tag{D.58}$$

A dual vector can be used to represent a straight line in space by means of the Plücker coordinates. Let D be a straight line in space whose orientation is given by a unit vector $\vec{i}$ and which passes through the point P. Even more, let $\mathcal{R}$ be a reference frame whose origin is O and its basis is $\mathcal{B} = (\vec{x}, \vec{y}, \vec{z})$ (see Figure D.5). The Plücker coordinates of the straight line D in the reference frame $\mathcal{R}$ are given by the coordinates of the vector $\vec{i}$ in the direction of the line D in $\mathcal{R}$ and the coordinates of the *angular momentum* $\vec{m} = \vec{OP} \wedge \vec{i}$ of the line D in $\mathcal{R}$. A dual unit vector $\hat{\vec{u}}^{\,\mathcal{R}}$ can then be defined and it completely characterizes the straight line D by its Plücker coordinates in the basis $\mathcal{B}$:

$$\hat{\vec{u}}^{\,\mathcal{R}} = \vec{i}^{\,\mathcal{R}} + \epsilon\vec{m}^{\,\mathcal{R}} \in \mathbb{D}^3. \tag{D.59}$$

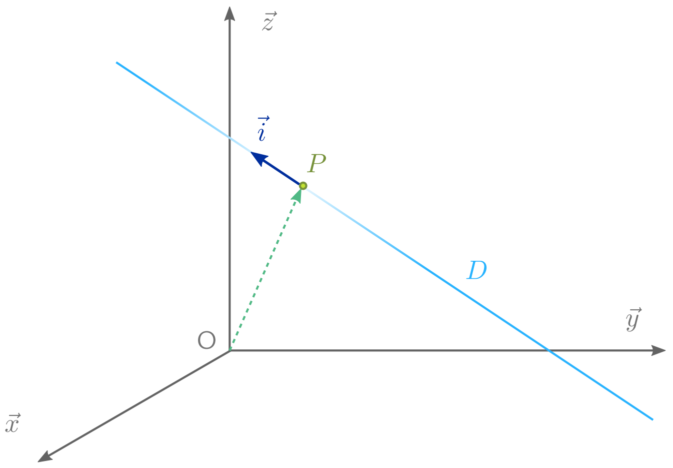

Figure D.5: Plücker coordinates of a line in space.

D.2.2. The dual quaternions

The set $\mathbb{H}(\mathbb{D})$ can be constructed as 8-dimensional algebra over $\mathbb{R}$, or as a 4-dimensional algebra over $\mathbb{D}$ or as a 2-dimensional algebra over $\mathbb{H}$. $\mathbb{H}(\mathbb{D})$ is an associative algebra defined as:

DEFINITION D.2.4:

$$\begin{aligned} \mathbb{H}(\mathbb{D}) &= \left\{\hat{q} = q_0 + q_1\epsilon,\ (q_0, q_1) \in \mathbb{H}^2\right\} \\ &= \left\{\hat{q} = d_1\mathbf{i} + d_2\mathbf{j} + d_3\mathbf{k} + d_4,\ (d_1, d_2, d_3, d_4) \in \mathbb{D}^4\right\}, \end{aligned} \tag{D.60}$$

where $q_0 \in \mathbb{H}$ *is the real part and* $q_1 \in \mathbb{H}$ *is the dual part of the dual quaternion.*

As 8-dimensional algebra, the basic elements are given by $(1, \mathbf{i}, \mathbf{j}, \mathbf{k}, \epsilon, \epsilon\mathbf{i}, \epsilon\mathbf{j}, \epsilon\mathbf{k})$ where the basis element ϵ of $\mathbb{D}$ commutes with the basis elements of $\mathbb{H}$ to give the following multiplication table:

$\odot$	1	$\mathbf{i}$	$\mathbf{j}$	$\mathbf{k}$	ϵ	$\epsilon\mathbf{i}$	$\epsilon\mathbf{j}$	$\mathbf{k}$
1	1	$\mathbf{i}$	$\mathbf{j}$	$\mathbf{k}$	ϵ	$\epsilon\mathbf{i}$	$\epsilon\mathbf{j}$	$\epsilon\mathbf{k}$
$\mathbf{i}$	$\mathbf{i}$	-1	$\mathbf{k}$	$-\mathbf{j}$	$\epsilon\mathbf{i}$	$-\epsilon$	$\epsilon\mathbf{k}$	$-\epsilon\mathbf{j}$
$\mathbf{j}$	$\mathbf{j}$	$-\mathbf{k}$	-1	$\mathbf{i}$	$\epsilon\mathbf{j}$	$-\epsilon\mathbf{k}$	$-\epsilon$	$\epsilon\mathbf{i}$
$\mathbf{k}$	$\mathbf{k}$	$\mathbf{j}$	$-\mathbf{i}$	-1	$\epsilon\mathbf{k}$	$\epsilon\mathbf{j}$	$-\epsilon\mathbf{i}$	$-\epsilon$
ϵ	ϵ	$\epsilon\mathbf{i}$	$\epsilon\mathbf{j}$	$\epsilon\mathbf{k}$	0	0	0	0
$\epsilon\mathbf{i}$	$\epsilon\mathbf{i}$	$-\epsilon$	$\epsilon\mathbf{k}$	$-\epsilon\mathbf{j}$	0	0	0	0
$\epsilon\mathbf{j}$	$\epsilon\mathbf{j}$	$-\epsilon\mathbf{k}$	$-\epsilon$	$\epsilon\mathbf{i}$	0	0	0	0
$\epsilon\mathbf{k}$	$\epsilon\mathbf{k}$	$\epsilon\mathbf{j}$	$-\epsilon\mathbf{i}$	$-\epsilon$	0	0	0	0

Table D.1: Multiplication table for the 8-dimensional algebra elements.

There exist many definitions of the dual quaternions conjugation [112]. We retain the one which is the most used in the references concerning the modelling of rigid transformations.

$$\hat{q}^* = q_0^* + q_1^*\epsilon,\ \forall\, \hat{q} \in \mathbb{H}(\mathbb{D}). \tag{D.61}$$

The classic operations over the dual quaternions are defined by:

- sum: $\hat{q}_a + \hat{q}_b = q_{a0} + q_{b0} + \epsilon(q_{a1} + q_{b1})$;
- multiplication by a scalar: $\lambda\hat{q} = (\lambda q_0) + \epsilon(\lambda q_1)$;
- multiplication: $\hat{q}_a \odot \hat{q}_b = (q_{a0} \odot q_{b0}) + \epsilon(q_{a0} \odot q_{b1} + q_{a1} \odot q_{b0})$;
- dot product: $\hat{q}_a \cdot \hat{q}_b = \dfrac{1}{2}(\hat{q}_a^* \odot \hat{q}_b + \hat{q}_b^* \odot \hat{q}_a) = \dfrac{1}{2}(\hat{q}_a \odot \hat{q}_b^* + \hat{q}_b \odot \hat{q}_a^*) = q_{a0} \cdot q_{b0} + \epsilon(q_{a1} \cdot q_{b0} + q_{a0} \cdot q_{b1})$;
- vectorial product: $\hat{q}_a \times \hat{q}_b = \dfrac{1}{2}(\hat{q}_a \odot \hat{q}_b - \hat{q}_b^* \odot \hat{q}_a^*) = q_{a0} \times q_{b0} + \epsilon(q_{a1} \times q_{b0} + q_{a0} \times q_{b1})$;
- module (dual norm): $\|\hat{q}\|_d^2 = \hat{q} \odot \hat{q}^* = \hat{q}^* \odot \hat{q} = \hat{q} \cdot \hat{q} = (q_0 \cdot q_0) + \epsilon(2q_0 \cdot q_1)$;
- exchange: $\hat{q}^s = q_1 + \epsilon q_0$;
- dual product: $\hat{q}_a \circ \hat{q}_b = q_{a0} \cdot q_{b0} + q_{a1} \cdot q_{b1}$;

- norm: $\|\hat{q}\| = \hat{q} \circ \hat{q}$;
- multiplication by a matrix: $M \star \hat{q} = (M_{11} * q_0 + M_{12} * q_1) + \epsilon(M_{21} * q_0 + M_{22} * q_1)$.

where $\hat{q},\ \hat{q}_a,\ \hat{q}_b \in \mathbb{H}(\mathbb{D})$, $\lambda \in \mathbb{R}$ and $M = \begin{bmatrix} M_{11} & M_{12} \\ M_{21} & M_{22} \end{bmatrix},\ M_{11},\ M_{12},\ M_{21},\ M_{22} \in \mathbb{R}^{4\times 4}$.

We deduce from these definitions the following properties:

★ **PROPERTY 3:**

1- $\hat{q}_a \circ (\hat{q}_b \odot \hat{q}_c) = \hat{q}_b^s \circ (\hat{q}_a^s \odot \hat{q}_c^*) = \hat{q}_c^s \circ (\hat{q}_b^* \odot \hat{q}_a^s) \in \mathbb{R}$;

2- $\hat{q}_a \circ (\hat{q}_b \times \hat{q}_c) = \hat{q}_b^s \circ (\hat{q}_c \times \hat{q}_a^s) = \hat{q}_c^s \circ (\hat{q}_a^s \times \hat{q}_b)$;

3- $\hat{q}_a \times \hat{q}_a = 0$;

4- $\hat{q}_a \times \hat{q}_b = -\hat{q}_b \times \hat{q}_a$;

5- $\hat{q}_a^s \circ \hat{q}_b^s = \hat{q}_a \circ \hat{q}_b$;

6- $\|\hat{q}_a^s\| = \|\hat{q}_a\|$;

7- $\|\hat{q}_a^*\| = \|\hat{q}_a\|$;

8- $|\hat{q}_a \circ \hat{q}_b| \leq \|\hat{q}_a\|\|\hat{q}_b\|$;

9- $\|\hat{q}_a \odot \hat{q}_b\| \leq \sqrt{3/2}\|\hat{q}_a\|\|\hat{q}_b\|$;

10- $(M \star \hat{q}_a) \circ \hat{q}_b = \hat{q}_a \circ (M^T \star \hat{q}_b)$.

The dual quaternions are particularly useful for the common representation of rotations and translations and especially suitable for helicoidal motions [130],[41], [42], [43].

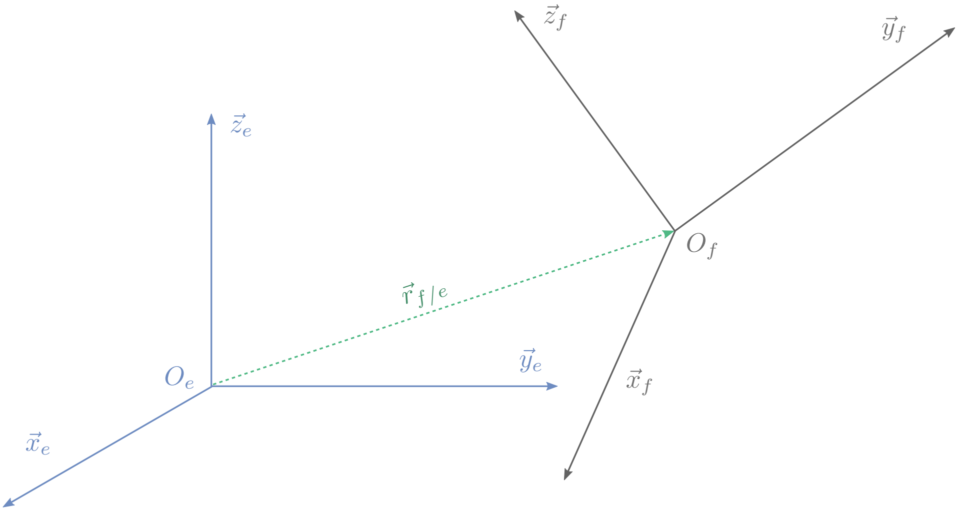

Figure D.6: Translation and rotation of a reference frame.

Consider for example the configuration of Figure D.6 where a reference frame $\mathcal{R}_f$ is derived from a reference frame $\mathcal{R}_e$ by the rigid transformation whose translation vector is $\vec{r}_{f/e}$ and the rotation quaternion is $q^{f/e}$. The position and attitude of the reference frame $\mathcal{R}_f$ with respect to frame $\mathcal{R}_e$ can then be represented by the dual quaternion defined by (D.62).

$$\hat{q}^{f/e} = q^{f/e} + \epsilon\frac{1}{2}\begin{bmatrix} \vec{r}^{\,\mathcal{O}_e}_{f/e} \\ 0 \end{bmatrix} \odot q^{f/e} = q^{f/e} + \epsilon\frac{1}{2}q^{f/e} \odot \begin{bmatrix} \vec{r}^{\,\mathcal{O}_f}_{f/e} \\ 0 \end{bmatrix}. \tag{D.62}$$

The more or less complete demonstration of this relationship uses the algebraic properties of quaternions and can be found in the reference [130].

APPENDIX E

ATTITUDE MODELING: DYNAMIC EQUATIONS

In this appendix, the dynamic equations of a satellite's rotational motion around its center of gravity are recalled in order to write an associated state space model. This is achieved by completing the last equations with the kinematic equations that were presented in Appendix D. We followed the references [127], [107], [100].

The satellite is modelled as a rigid body where a mobile reference frame $\mathcal{B}$ with basis vectors $B_b = (\vec{X}_b, \vec{Y}_b, \vec{Z}_b)$ is attached to its center of mass O_b. On the other hand an inertial reference frame $\mathcal{I}$ is defined for studying the rotational motion, with basis vectors $B_i = (\vec{X}_i, \vec{Y}_i, \vec{Z}_i)$.

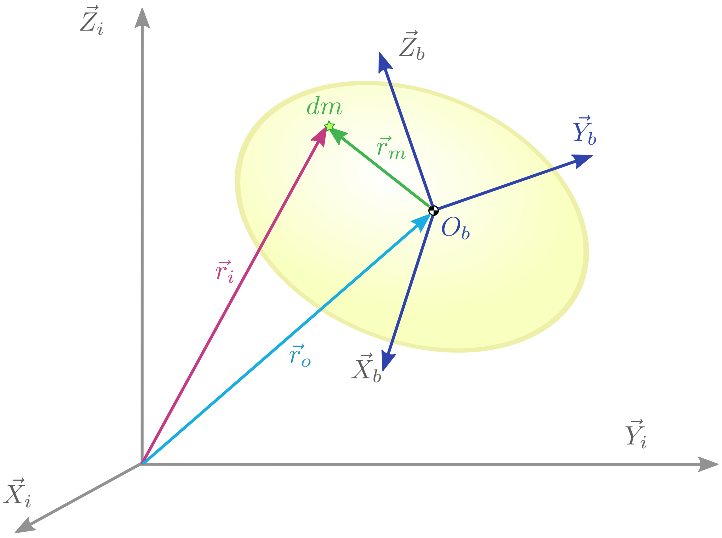

Figure E.1: Reference frames attached to the rigid body.

Using Figure 1.1, we recall the velocities composition law. We have $\vec{r}_i = \vec{r}_o + \vec{r}_m$ and noting $\vec{\omega}_{bi}$ the rotation vector of the frame $\mathcal{B}$ with respect to frame $\mathcal{I}$, it comes:

$$\left(\frac{d\vec{r}_i}{dt}\right)_{\mathcal{I}} = \left(\frac{d\vec{r}_o}{dt}\right)_{\mathcal{I}} + \left(\frac{d\vec{r}_m}{dt}\right)_{\mathcal{I}} = \left(\frac{d\vec{r}_o}{dt}\right)_{\mathcal{I}} + \left(\frac{d\vec{r}_m}{dt}\right)_{\mathcal{B}} + \vec{\omega}_{bi} \wedge \vec{r}_m = \left(\frac{d\vec{r}_o}{dt}\right)_{\mathcal{I}} + \vec{\omega}_{bi} \wedge \vec{r}_m. \tag{E.1}$$

By applying the second Newton's law (fundamental principle of dynamics) for the satellite's rotational motion *the Euler moments Equation* is written as:

$$\left(\frac{d\vec{H}}{dt}\right)_{\mathcal{I}} = \vec{T}, \tag{E.2}$$

where $\vec{H}$ is the angular momentum of the satellite and $\vec{T}$, the resultant of the moments applied to the satellite, calculated at the CoM O_b of the rigid body (see Figure 1.1). In order to express this relationship by using the properties of the angular momentum and the inertia matrix in the rigid body's reference frame, (1.2) is expressed in the $\mathcal{B}$ frame using the velocities composition law:

$$\left(\frac{d\vec{H}}{dt}\right)_{\mathcal{I}} = \left(\frac{d\vec{H}}{dt}\right)_{\mathcal{B}} + \vec{\omega}_{bi} \wedge \vec{H} = \vec{T}. \tag{E.3}$$

The next step is to express the angular momentum and its derivative with respect to the reference frame $\mathcal{B}$. The angular momentum of the rigid body is calculated by summation of the elementary masses composing the entire satellite:

$$\begin{aligned} \vec{H} &= \int \vec{r}_m \wedge \left(\frac{d\vec{r}_i}{dt}\right)_{\mathcal{I}} dm = \int \vec{r}_m \wedge \left(\frac{d\vec{r}_o}{dt}\right)_{\mathcal{I}} dm + \int \vec{r}_m \wedge (\vec{\omega}_{bi} \wedge \vec{n})\, dm \\ &= -\left(\frac{d\vec{r}_o}{dt}\right)_{\mathcal{I}} \wedge \int \vec{r}_m dm + \int \vec{r}_m \wedge (\vec{\omega}_{bi} \wedge \vec{r}_m)\, dm = \int \vec{r}_m \wedge (\vec{\omega}_{bi} \wedge \vec{r}_m)\, dm, \end{aligned} \tag{E.4}$$

since O_b is the CoM of the satellite, and therefore:

$$\int \vec{r}_m \, dm = 0. \tag{E.5}$$

It should be noted that the term (1.4) is valid regardless of the basis in which it is expressed but it will be even easier to calculate it if the chosen basis simplifies the expression of the integral's limits as it is the case for the basis B_b linked to the reference frame $\mathcal{B}$, where the mass distribution is invariant with respect to time.
By developing the second term of (1.4) and noting that $\vec{r}_m = x\vec{X}_b + y\vec{Y}_b + z\vec{Z}_b \; \vec{\omega}_{bi} = \omega_1\vec{X}_b + \omega_2\vec{Y}_b + \omega_3\vec{Z}_b$, we obtain in the B_b basis:

$$\vec{H}^{\mathcal{B}} = \begin{bmatrix} \omega_1 \int (y^2+z^2)\, dm - \omega_2 \int yx\, dm - \omega_3 \int zx\, dm \\ -\omega_1 \int yx\, dm + \omega_2 \int (x^2+z^2)\, dm - \omega_3 \int zy\, dm \\ -\omega_1 \int xz\, dm - \omega_2 \int yz\, dm + \omega_3 \int (y^2+x^2)\, dm \end{bmatrix}. \tag{E.6}$$

This last equation can be factorised as:

$$\vec{H}^{\mathcal{B}} = \int \begin{bmatrix} y^2+z^2 & -yx & -zx \\ -xy & x^2+z^2 & -zy \\ -xz & -yz & y^2+x^2 \end{bmatrix} dm \begin{bmatrix} \omega_1 \\ \omega_2 \\ \omega_3 \end{bmatrix}. \tag{E.7}$$

Using the definition of the rigid body's inertia matrix composed of the inertia matrix of the rigid body about its orthogonal axis as well and the inertia products, we obtain the matrix formulation as shown next:

$$\vec{H}^{\mathcal{B}} = I\, \vec{\omega}_{bi}^{\mathcal{B}}, \tag{E.8}$$

where I is the satellite's inertia matrix, denoted by:

$$I = \begin{bmatrix} I_{xx} & -I_{xy} & -I_{xz} \\ -I_{xy} & I_{yy} & -I_{yz} \\ -I_{xz} & -I_{yz} & I_{zz} \end{bmatrix}. \tag{E.9}$$

A physical interpretation of the equation (1.8) is that the relative velocity vector $\vec{\omega}_{bi}$ and the angular momentum are not generally aligned. As we have said before, the rigid body inertia matrix is constant in the satellite's body reference frame $\mathcal{B}$. By combining equations (1.3) and (1.8) we can write the *Euler's equation*:

$$I \left(\frac{d\,\vec{\omega}_{bi}}{dt} \right)_{\mathcal{B}} + \vec{\omega}_{bi}^{\,\mathcal{B}} \wedge I\,\vec{\omega}_{bi}^{\,\mathcal{B}} = \vec{T}^{\,\mathcal{B}}. \tag{E.10}$$

APPENDIX F

PERFORMANCE CRITERIA AND FUEL CONSUMPTION

One key requirement when designing a space mission is the fuel consumption — or cost.The most frequent way to evaluate the consumption is by means of the concept of characteristic velocity or $\Delta\vec{V}$, a measure of the needed impulse to perform a maneuver. The $\Delta\vec{V}$ is proportional to the propulsion force exerted by the spacecraft — thrust — per unit mass and burn time.

As stated in Section 3.1, we consider here a chaser satellite equipped with chemical thrusters, leading to an impulsive abstraction of the associated control problem, where the satellite's velocity changes instantaneously — jump discontinuity — while the position remains constant.

In a general context, the formulation of continuous dynamical systems can be described by the ordinary differential equation in Expression (2.56), rewritten below for simplicity:

$$\dot{X}(t) = A(t)X(t) + B\,U(t), \tag{F.1}$$

where $U(t) = \dfrac{\vec{F}_{prop_c}}{m_c} \in \mathbb{R}^m$ represents or is related to the applied thrust or acceleration of the spacecraft, as it was shown in Expression (2.59), where $\vec{F}_{prop_c}$ is the chaser's propulsion force and m_c its mass.

Considering Expression (2.3), we define the impulsive control input in terms of $\Delta\vec{V}$ for the chaser satellite as:

$$\Delta\vec{V}(t_k) = \Delta\vec{V}_k = \int_{t_k^-}^{t_k^+} \frac{\vec{F}_{prop_c}}{m_c}\,dt, \tag{F.2}$$

where t_k is a generic firing time, t_k^- is the time right before the thrust and t_k^+ is the time right after the thrust execution.

For linearized impulsive problems, the control function $U(t)$ in (F.1) is replaced by a finite set of generalized velocity jumps $\{\Delta\vec{V}_k \in \mathbb{R}^m, k = 1, \cdots, N\}$, where N is a positive integer [19]:

$$\dot{X}(t) = A(t)X(t) + \sum_{k=0}^{N} B\,\Delta\vec{V}_k. \tag{F.3}$$

The consumption or cost, noted J, is a magnitude directly related to the required mass of propellant for a given maneuver, given by the Tsiolkovsky rocket equation [88], which depends on parameters such as the equivalent exit velocity of the nozzle or the initial and final total mass of the chaser once the maneuver has been executed.

The cost J is directly related to the number of thrusters and their geometrical configuration [96]. The computation of the $\Delta\vec{V}$ is done by means of p-norms, as shown hereafter. We show three different configurations of the thrusters and their respective p-norm expressions.

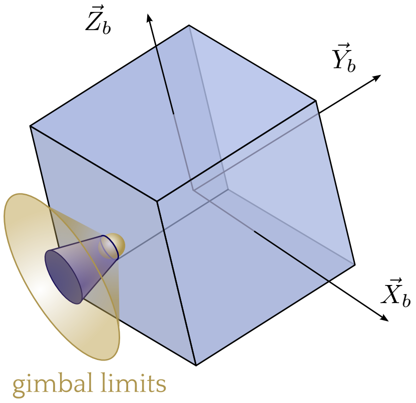

Figure F.1: Single gimbaled thruster.

Thrusters configuration:
Single thruster that steers the satellite by gimbaling, where the gimbal limits are given by the golden cone around the thruster.

Associated cost function:

$$J=\sum_{k=1}^{N}||\Delta\vec{V}_k||_2=\sum_{k=1}^{N}\sqrt{\Delta v_{x\ k}^2+\Delta v_{y\ k}^2+\Delta v_{z\ k}^2}. \tag{F.4}$$

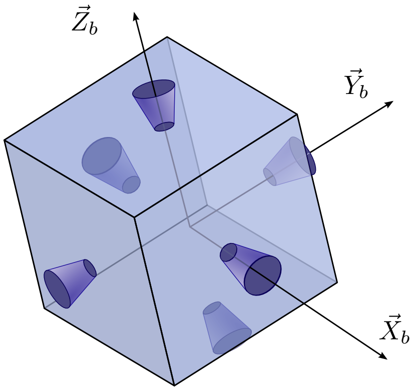

Figure F.2: Six identical ungimbaled thrusters.

Thrusters configuration:
Six identical ungimbaled thrusters are rigidly mounted on the body axes.

Associated cost function:

$$J=\sum_{k=1}^{N}||\Delta\vec{V}_k||_1=\sum_{k=1}^{N}\left(|\Delta v_{x\ k}|+|\Delta v_{y\ k}|+|\Delta v_{z\ k}|\right). \tag{F.5}$$

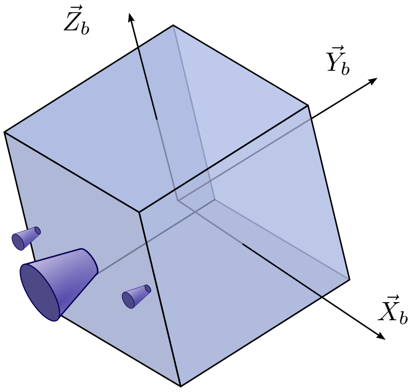

Figure F.3: Main thruster + vernier engines.

Thrusters configuration:
One main thruster used for guidance maneuvers and vernier engines used to steer the thrust vector.

Associated cost function:

$$J=\sum_{k=1}^{N}||\Delta\vec{V}_k||_\infty. \tag{F.6}$$

Bibliography

[1] S. AGHILI, *A prediction and motion-planning scheme for visually guided robotic capturing of free-floating tumbling objects with uncertain dynamics*, IEEE Transactions on Robotics, 28 (2012), pp. 634–649.

[2] K. ALFRIEND, S. VADALI, P. GURFIL, J. HOW, and L. BREGER, *Spacecraft Formation Flying*, elsevier, Burlington, MA, USA, 2010.

[3] K. T. ALFRIEND, S. R. VADALI, P. GURFIL, J. HOW, and L. BREGER, *Spacecraft Formation Flying - Dynamics, control and navigation*, Elsevier Astrodynamics Series, Butterworth-Heinemann, Elsevier, The Boulevard, Langford Lane, Kidlington, Oxford OX5 1GB, UK, first edition ed., 2010. ISBN 978-0-75-068533-7.

[4] K. T. ALFRIEND and H. YAN, *Evaluation and comparison of relative motion theories*, Journal of Guidance, Control and Dynamics, 28 (2005), pp. 254 – 261.

[5] F. ANKERSEN, *Guidance, Navigation, Control and Relative Dynamics for Spacecraft Proximity Maneuvers*, PhD thesis, Aalborg University, 2011.

[6] P. J. ANTSAKLIS and A. N. MICHEL, *Linear systems*, Springer Science & Business Media, 2006.

[7] D. ARZELIER, C. LOUEMBET, and A. THÉRON, *Etude bibliographique sur le problème du rendez-vous*, Note technique N.T. 2.2, version 2.1 Rapport 08552, LAAS-CNRS, 16 juin 2009.

[8] D. ARZELIER, A. THERON, and M. K. ZAITRI, *Etude bibliographique sur la modelisation du mouvement relatif pour le probleme du rendezvous*, convention cnes no.71372/00, EADS-Astrium / LAAS-CNRS / CNES, July 2008.

[9] D. ARZELIER, A. THÉRON, and M. KARA-ZAITRI, *Etude bibliographique sur la modélisation du mouvement relatif pour le problème du rendez-vous*, Note technique Rapport LAAS 08258, CNRS, Mai 2008.

[10] D. BAINOV and P. SIMEONOV, *Impulsive differential equations: periodic solutions and applications*, vol. 66 of Pitman Monographs and Surveys in Pure and Applied Mathematics, 1993.

[11] O. BAUCHAU and L. TRAINELLI, *The vectorial parametrization of rotation*, Nonlinear dynamics, 32 (2003), pp. 71–92.

[12] D. BERTSIMAS and J. TSITSIKLIS, *Introduction to Linear Optimization*, Athena Scientific, 1st ed., 1997.

[13] S. BITTANTI and P. COLANERI, *Periodic systems: filtering and control*, Springer, 2009. ISBN 978-1-84800-910-3.

[14] M. BRENTARI, *Controllo ibrido del rendezvous tra due veicoli spaziali in orbita ellittica*, Master's thesis, Università degli Studi di Trento, 2014. Dipartimento di Ingegneria Industriale.

[15] V. BRODSKY and M. SHOHAM, *Dual numbers representation of rigid body dynamics*, Mechanism and Machine Theory, 34 (1999), pp. 693–718.

[16] R. A. BROUCKE, *Solution of the elliptic rendezvous problem with the time as independent variable*, Journal of Guidance, Control and Dynamics, 26 (2003), pp. 615 – 621.

[17] T. CARTER, *New form for the optimal rendezvous equations near a keplerian orbit*, Journal of Guidance, Control, and Dynamics, 13 (1990).

[18] T. CARTER, *State transition matrices for terminal rendezvous studies: brief survey and new example*, Journal of Guidance, Control, and Dynamics, 21 (1998), pp. 148–155.

[19] T. CARTER and J. BRIENT, *Linearized impulsive rendezvous problem*, Journal of Optimization Theory and Applications, 86 (1995).

[20] T. CARTER and M. HUMI, *Clohessy-Wiltshire equations modified to include quadratic drag*, Journal of Guidance, Control and Dynamics, 25 (2002), pp. 1058–1063.

[21] N. CHATURVEDI, A. SANYAL, and N. McCLAMROCH, *Rigid-body attitude control*, IEEE Control Systems Magazine, 31 (2011), pp. 30 –51.

[22] W. CLIFFORD, *Preliminary sketch of biquaternions*, Proceedings of London Mathematical Society, 4 (1873), pp. 381–395.

[23] W. CLOHESSY and R. WILTSHIRE, *Terminal guidance system for satellite rendezvous*, Journal of the Astronautical Sciences, 27 (1960), pp. 653–658.

[24] W. H. CLOHESSY and R. S. WILTSHIRE, *Terminal guidance system for satellite rendevous*, Journal of the Aerospace Sciences, 27 (1960), pp. 653 – 658.

[25] CNES, *Atv: a resupply spacecraft for the iss*.

[26] CNES, *Prisma: testing new formation-flying technologies*.

[27] D. CONDURACHE and A. BURLACU, *A dual vectors based formalism for parametrization of rigid body displacement and motion*, in 5^th International Conference on Computational Mechanics and Virtual Engineering, Braov, Romania, 2013.

[28] D. CONDURACHE and A. BURLACU, *On 6 dof relative orbital motion parametrization using rigid bases of dual vectors*, in Proceedings of the Advances in the Astronautical Sciences, AAS 13-857, 2013.

[29] D. CONDURACHE and A. BURLACU, *On six dof relative orbital motion parameterization using rigid bases of dual vectors*, tech. rep., 2013.

[30] S. D'AMICO, J. ARDAENS, G. GAIAS, H. BENNINGHOFF, and B. SCHLEPP, *Noncooperative rendezvous using angles-only optical navigation: System design and flight results*, Journal of Guidance, Control and Dynamics, 36 (2013), pp. 1576–1595.

[31] G. I. DEACONU, *On the trajectory design, guidance and control for spacecraft rendezvous and proximity operations*, PhD thesis, Laboratoire d'Analyse et Architecture des Systèmes (LAAS-CNRS), Toulouse, France, 18th July 2013.

[32] G. I. DEACONU, C. LOUEMBET, and A. THERON, *Constrained periodic spacecraft relative motion using non negative polynomials*. LAAS-CNRS, supported by CNES and EADS Astrium, France, 2012.

[33] G. I. DEACONU, C. LOUEMBET, and A. THERON, *A two-impulse method for stabilizing the spacecraft relative motion with respect to a periodic trajectory*, in Decision and Control (CDC), 2012 IEEE 51st Annual Conference on, IEEE, 2012, pp. 6541–6546.

[34] G. I. DEACONU, C. LOUEMBET, and A. THÉRON, *Minimizing the effects of navigation uncertainties on the spacecraft rendezvous precision*, Journal of Guidance, Control, and Dynamics, 37 (2014), pp. 695–700.

[35] G. I. DEACONU, C. LOUEMBET, and A. THÉRON, *Designing continuously constrained spacecraft relative trajectories for proximity operations*, Journal of Guidance, Control, and Dynamics, 38 (2015), pp. 1208–1217.

[36] L. DICKSON, *Linear algebras*, Note technique Tracts-16, Cambridge University, Janvier 1914.

[37] L. DICKSON, *On the quaternions and their generalization in the history of the height square theorem*, Annals of Mathematics, 20 (1919), pp. 155–171.

[38] W. FEHSE, *Automated rendezvous and docking of spacecraft*, Cambridge aerospace series 16, Cambridge University Press, 2003.

[39] W. FEHSE, ed., *Automated rendezvous and docking of spacecraft*, Cambridge Aerospace Series, Cambridge University Press, Cambridge, UK, 2003.

[40] N. FILIPE and P. TSIOTRAS, *Adaptive position and attitude controller for satellite proximity operations using dual quaternions*, in Proceedings of the Astrodynamics Specialist Conference, AAS 13-858, Hilton Head, USA, 11-15 Août 2013.

[41] N. FILIPE and P. TSIOTRAS, *Adaptive position and attitude tracking controller for satellite proximity operations using dual quaternions*, in Proceedings of the Astrodynamics Specialist Conference, AAS 13-858, Hilton Head, SC, USA, 11-15 Août 2013.

[42] N. FILIPE and P. TSIOTRAS, *Rigid body motion tracking without linear and angular velocity feedback using dual quaternions*, in Proceedings of the European Control Conference, Zurich, Suisse, 17-19 Juillet 2013.

[43] N. FILIPE and P. TSIOTRAS, *Simultaneous position and attitude control without linear and angular velocity feedback using dual quaternions*, in Proceedings of the American Control Conference, Washington DC, USA, 17-19 Juin 2013.

[44] A. FRIAS, *Modeling and control of spacecraft systems with coupled orbital and attitude dynamics*, Master's thesis, Ryerson University, 2012.

[45] A. FRIAS, *Modelling and control of spacecraft systems with coupled orbital and attitude dynamics*, Master's thesis, Ryerson University, Toronto, Ontario, Canada, 2012.

[46] M. GANET-SCHOELLER, J. BOURDON, and G. GELLY, *Non linear and robust stability analysis for ATV rendezvous control*, in AIAA/AAS GNC Conference, Chicago Illinois, USA, Août 2009. AIAA paper 2009-5951.

[47] J. GARRISON, T. GARDNER, and P. AXELRAD, *Relative motion in highly elliptical orbits*, in Proceedings of the Advances in the Astronautical Sciences, AAS 95-194, 1995.

[48] S. GAULOCHER, J. CHÉTIEN, C. PITTET, M. DELPECH, and D. ALAZARD, *Closed-loop control of formation flying satellites: time and parameter varying framework*, in 2nd Int. Symposium on formation flying missions and technologies, Washington, DC, USA, 2004.

[49] P. R. A. GILZ, *A Matlab®/Simulink® non-linear simulator for orbital spacecraft rendezvous applications.*, Dec. 2016. A Matlab®/Simulink® non-linear simulator for orbital spacecraft rendezvous applications.

[50] P. R. A. GILZ, M. JOLDES, C. LOUEMBET, and F. CAMPS, *Model predictive control for rendezvous hovering phases based on a novel description of constrained trajectories*. To be published in IFAC2017 proceedings, Mar. 2017.

[51] D.-W. GIM and K. ALFRIEND, *The state transition matrix of relative motion for the perturbed non-cicular reference orbit*, Journal of Guidance, Control and Dynamics, 26 (2003), pp. 956–971.

[52] R. GOEBEL, R. SANFELICE, and A. TEEL, *Hybrid Dynamical Systems: modeling, stability, and robustness*, Princeton University Press, 2012.

[53] S. GONG, H. BAOYIN, and J. LI, *Coupled attitude–orbit dynamics and control for displaced solar orbits*, Acta Astronautica, 65 (2008), pp. 730–737.

[54] P. GOUDY, *Cours de technologie spatiale. techniques et technologies des véhicules spatiaux.*, CNES, 18 avenue Edouard Belin, Toulouse, September 2011. Volume 1: généralités et contraintes de développement.

[55] M. GUELMAN and M. ALESHIN, *Optimal bounded low-thrust rendezvous with fixed terminal-approach direction*, Journal of Guidance, Control and Dynamics, 24 (2001), pp. 378–385–864.

[56] H. B. HABLANI, M. L. TAPPER, and D. J. DANA-BASHIAN, *Guidance and relative navigation for autonomous rendezvous in a circular orbit*, Journal of Guidance, Control and Dynamics, Vol. 25 (2002).

[57] W. M. HADDAD, V. S. CHELLABOINA, and S. G. NERSESOV, *Impulsive and hybrid dynamical systems: stability, dissipativity, and control*, Princeton University Press, 2014.

[58] W. HAMILTON, *Lectures on quaternions*, McMillan and co. Ltd, Cambridge, UK, 1853.

[59] D. HAN, Q. WEI, Z. LI, and W. SUN, *Control of oriented mechanical systems: A method based on dual quaternion*, IFAC Proceedings Volumes, 41 (2008), pp. 3836–3841.

[60] D. P. HAN, Q. WEI, and Z. X. LI, *Kinematic control of free rigid bodies using dual quaternions*, International Journal of Automation and Computing, 5 (2008), pp. 319–324.

[61] L. HOLGUIN, S. VISWANATHAN, and A. SANYAL, *Guidance and control for spacecraft autonomous rendezvous and proximity maneuvers using a geometric mechanics framework*, in AIAA Guidance, Navigation, and Control Conference, Minneapolis, Minnesota, USA, 2012.

[62] A. IBRAHIMBEGOVI, *On the choice of finite rotation parameters*, Computer Methods in Applied Mechanics and Engineering, 149 (1997), pp. 49–71.

[63] S. in Images by ESA, *Prisma's tango and mango satellites*. `http://www.esa.int/spaceinimages/Images/2010/10/Prisma_s_Tango_and_Mango_satellites`.

[64] G. INALHAN, M. TILLERSON, and J. HOW, *Relative dynamics and control of spacecraft formations in eccentric orbits*, Journal of Guidance, Control and Dynamics, 25 (2002), pp. 48–59.

[65] D. IRVIN, *A study of linear vs nonlinear control techniques for the reconfiguration of satellite formations*, Master's thesis, Air Force Institute of Technology, Wright-Patterson Air Force Base, Ohio, USA, 2001.

[66] S. KIM, J. CRASSIDIS, Y. CHENG, A. FOSBURY, and J. JUNKINS, *Kalman filtering for relative spacecraft attitude and position estimation*, Journal of Guidance, Control and Dynamics, 30 (2007), pp. 133–143.

[67] M. KOBILAROV and S. PELLEGRINO, *Trajectory planning for cubesat short-time-scale proximity operations*, Journal of Guidance, Control and Dynamics, 37 (2014), pp. 566–579.

[68] A. KOMANDURI and D. BINKEL, *Guidance and control strategies for a spacecraft to rendezvous wit a noncooperative spacecraft*, in 61^{st} International Astronautical Congress, Prague, République Tchèque, 2010.

[69] R. KRISTIANSEN, E. GRØTLI, P. NICKLASSON, and J. GRAVDAHL, *A model of relative translation and rotation in leader-follower spacecraft formations*, Modeling, Identification and Control, 28 (2007), pp. 3–13.

[70] R. KRISTIANSEN and P. NICKLASSON, *Spacecraft formation flying: A review and new results on state feedback control*, Acta Astronautica, 65 (2009), pp. 1537–1552.

[71] R. KRISTIANSEN, P. NICKLASSON, and J. GRAVDAHL, *Spacecraft coordination control in 6dof: Integrator backstepping vs passivity-based control*, Automatica, 44 (2008), pp. 2896 – 2901.

[72] R. KRISTIANSEN, P. NICKLASSON, and J. GRAVDAHL, *Spacecraft coordination control in 6dof: Integrator backstepping vs passivity-based control*, Automatica, 44 (2008), pp. 2896 – 2901.

[73] M. R. LAPOINTE, *Formation flying with shepherd satellites*, phase i final report, NASA Institute for Advanced Concepts, December 2001.

[74] D. LAWDEN, *Optimal trajectories for space navigation*, Butterworth, London, England, 1963.

[75] D. LEE and H. BANG, *Coupled position and attitude control of a spacecraft in the proximity of a tumbling target*, in IAA-AAS-DyCoSS, September 2007.

[76] D. LEE and H. BANG, eds., *Coupled position and attitude control of a spacecraft in the proximity of a tumbling target*, Porto, Portugal, 2012.

[77] T. LEE, ed., *Relative attitude control of two spacecraft on SO(3) using line-of-sight observations*, Montréal, Canada, 2012.

[78] M. D. LEMMON, K. X. HE, and I. MARKOVSKY, *A tutorial introduction to supervisory hybrid systems*, ISIS, 98 (1998), p. 004.

[79] J. LI, *Intelligent control of satellite formation flying*, PhD thesis, Ryerson University, 2012.

[80] Y. LIAN, Y. MENG, G. TANG, and L. LIU, eds., *Constant-thrust glideslope guidance algorithm for rendezvous in multi-body realm*, Istanbul, Turquie, 2011.

[81] Y. LIAN, Y. MENG, G. TANG, and L. LIU, *Constant-thrust glideslope guidance algorithm for time-fixed rendezvous in real halo orbit*, Acta Astronautica, 79 (2012), pp. 241–252.

[82] W. LU, Y. GENG, X. CHEN, and F. ZHANG, *Relative position and attitude coupled control for autonomous docking with a tumbling target*, International Journal of Control and Automation, 4 (2011).

[83] C. G. MAYHEW, R. G. SANFELICE, and A. R. TEEL, *Robust global asymptotic attitude stabilization of a rigid body by quaternion-based hybrid feedback*, in Decision and Control, 2009 held jointly with the 2009 28th Chinese Control Conference. CDC/CCC 2009. Proceedings of the 48th IEEE Conference on, IEEE, 2009, pp. 2522–2527.

[84] R. MELTON, *Time-explicit representation of relative motion between elliptical orbits*, Journal of Guidance, Control and Dynamics, 23 (2000), pp. 604–610.

[85] P. MIOTTO, L. BREGER, I. MITCHELL, B. KELLER, and B. RISHIKOF, *Designing and validating proximity operations rendezvous and approach trajectories for the cygnus mission*, in AIAA Guidance, Navigation, and Control Conference, Toronto, Ontario, Canada, 2009, AIAA.

[86] MIT, *Readings on dynamic systems and control*. `https://ocw.mit.edu/courses/electrical-engineering-and-computer-science/6-241j-dynamic-systems-and-control-spring-2011/readings/MIT6_241JS11_chap11.pdf`.

[87] B. NAASZ, M. BERRY, H. KIN, and C. HALL, *Integrated orbit and attitude control for a nanosatellite with power constraints*, in Proceedings of the Advances in the Astronautical Sciences, AAS 03-100, 2013.

[88] NASA, *Ideal rocket equation*. `https://spaceflightsystems.grc.nasa.gov/education/rocket/rktpow.html`.

[89] Y. NESTEROV, *Squared functionals systems and optimization problems*, in High Performance Optimization, H. Frenck, K. Roos, T. Terlaky, and S. Zhang, eds., Springer US, Boston, MA, USA, 2000, ch. 17, pp. 405–440.

[90] L. NEUSTADT, *A general theory of minimum-fuel space trajectories*, SIAM Journal of Control, 3 (1965), pp. 317–356.

[91] M. OKASHA and B. NEWMAN, *Guidance, navigation and control for satellite proximity operations using tschauner-hempel equations*, in AIAA Guidance, Navigation and Control Conference, Portland, Oregon, USA, 2011.

[92] H. PAN and V. KAPILA, *Adaptive nonlinear control for spacecraft formation flying with coupled translational and attitude dynamics*, in Proceedings of the 40th IEEE Conference on Decision and Control, Orlando, Florida, USA, Décembre 2001.

[93] D. PEARSON, *The glideslope approach*, Advances in Astronautical Sciences, 69 (1989), pp. 109–123.

[94] S. PERSSON, B. JACOBSSON, and E. GILL, *Prisma - demonstration mission for advanced rendezvous and formation flying technologies and sensors*, in 56th International Astronautical Congress, October 2005. Fukuoka, Japan.

[95] X. REN, L. YANG, and Y. ZHANG, *Optimal trajectory for GEO satellite proximity inspection based on HP-adaptive pseudospectral method*, in Proceedings of the 62nd International Astronautical Congress, Cape Town, South Africa, 2010.

[96] I. ROSS, *6 space trajectory optimization and l1-optimal control problems*, Elsevier Astrodynamics Series, 1 (2007), pp. 155–188.

[97] R. G. SANFELICE, *Robust hybrid control systems*, PhD thesis, University of California, September 2007.

[98] A. SANYAL, L. HOLGUIN, and S. VISWANATHAN, *Guidance and control for spacecraft autonomous chasing and close proximity maneuvers*, in IFAC Symposium on Robust Control Design – ROCOND12, Aalborg, Denmark, 2012.

[99] H. SCHAUB and J. JUNKINS, *Analytical mechanics of aerospace systems*, Texas A&M University, (2001).

[100] H. SCHAUB and J. JUNKINS, *Analytical mechanics of space systems*, Education Series, AIAA, Reston, Virginia, USA, 2003.

[101] S. SEGAL, A. CARMI, and P. GURFIL, *Stereovision-based estimation of relative dynamics between noncooperative satellites: Theory and experiments*, IEEE Transactions on Control Systems Technology, 22 (2014), pp. 568–584.

[102] S. SEGAL and P. GURFIL, *Effect of kinematic rotation translation coupling on relative spacecraft translational dynamics*, Journal of Guidance, Control and Dynamics, 32 (2009), pp. 1045 – 1050.

[103] S. SEGAL and P. GURFIL, *Effect of kinematic rotation-translation coupling on relative spacecraft translational dynamics*, Journal of Guidance, Control and Dynamics, 32 (2009), pp. 1045–1050.

[104] P. SENGUPTA, *Dynamics and control of satellite relative motion in a central gravitational field*, PhD thesis, Texas A%M University, December 2006.

[105] P. SENGUPTA and S. R. VADALI, *Relative motion and the geometry of formations in keplerian elliptic orbits.*, Journal of Guidance, Control and Dynamics, 30 (July - August 2007), pp. 953 – 964.

[106] M. SHUSTER, *A survey of attitude representation*, Journal of the Astronautical Sciences, 41 (1993), pp. 439–517.

[107] M. SISI, *Spacecraft dynamics and control*, Cambridge University Press, New York, USA, 1997.

[108] M. SIVA, R. PANDIYAN, D. GHOSE, M. BHAT, and M. RAMACHANDRAN, *Coordinated 6-dof control of dual spacecraft formation*, in 5th International Conference on Spacecraft Formation Flying Missions and Technologies, Munich, Allemagne, Mai 2013.

[109] R. E. SKELTON, T. IWASAKI, and D. E. GRIGORIADIS, *A unified algebraic approach to control design*, CRC Press, 1997.

[110] Y. SMITH, *Image of the day gallery*, 2008.

[111] J. STUELPNAGEL, *On the parametrization of the three-dimensional rotation group*, SIAM Review, 6 (1964), pp. 422–430.

[112] J. TAMBOUR, *Ensemble de nombres*, note technique, Forum Futura-Science, Septembre 2011.

[113] F. TERUI, *Position and attitude control of a spacecraft by sliding mode control*, in Proceedings of the American Control Conference, Philadelphia, PE, USA, Juin 1998.

[114] F. TERUI, *Model based visual relative motion estimation and control of a spacecraft utilizing computer graphics*, in Proceedings of the International Symposium on Space Flight Dynamics, Toulouse, France, Septembre 2009.

[115] F. TERUI and S. NISHIDA, *Relative motion estimation and control to a failed satellite by machine vision*, in Proceedings of the IFAC-ACA Symposium, Toulouse, France, Juin 2007.

[116] A. THÉRON, F. JOUHAUD, and J. CHRÉTIEN, *Modélisation du mouvement orbital relatif entre deux satellites*, Note technique 1/08282, ONERA, Janvier 2004.

[117] D. S. O. . A. Training, *Prisma formation flying mission*. `http://www.dlr.de/rb/en/desktopdefault.aspx/tabid-10749/10535_read-23364/`.

[118] J. TSCHAUNER, *Elliptic orbit rendezvous*, AIAA Journal, 5 (1967), pp. 1110–1113.

[119] J. TSCHAUNER and P. HEMPEL, *Optimale beschleunigungs-programme fur des rendezvous manover*, Astronautica Acta, 5-6 (1964), pp. 296–307.

[120] P. TSIOTRAS and J. LONGUSKI, *A new parametrization of the attitude kinematics*, Journal of the Astronautical Sciences, 46 (1996), pp. 242–262.

[121] B. UDREA, M. NAYAK, and F. ANKERSEN, *Analysis of the pointing accuracy of a 6u cubesat for proximity operations and rso imaging*, in 5th International Conference on Spacecraft Formation Flying Missions and Technologies, Munich, Allemagne, 2013.

[122] S. UEDA, T. KASAI, and H. UEMATSU, *HTV rendezvous technique and gnc design evaluation based on 1st flight on-orbit operation result*, in AIAA/AAS Astrodynamics Specialist Conference, Toronto, Canada, Août 2010. AAS paper 2010-7664.

[123] G. VELDKAMP, *On the use of dual numbers, vectors and matrices in instantaneous, spatial kinematics*, Mechanism and Machine Theory, 11 (1978), pp. 141–156.

[124] F. WANG, X. CAO, and X. CHEN, *Guidance algorithms for the near-distance rendezvous of on-orbit-servicing spacecraft*, Transactions of Japanese Society for Aeronautical and Space Sciences, 50 (2007), pp. 9–17.

[125] J. WANG and Z. SUN, *6-dof robust adaptive terminal sliding mode control for spacecraft formation flying*, Acta Astronautica, 73 (2012), pp. 76–87.

[126] J. WERTZ, *Spacecraft attitude determination and control*, Reidel Publications, (1997).

[127] W. WIESEL, *Spaceflight dynamics*, Aeronautical and Aerospace Technology, McGraw-Hill, New York, New York, USA, 1997.

[128] Y. WU, X. CAO, Y. XING, and P. ZHENG, *Relative motion decoupled control for spacecraft formation with coupled translational and rotational dynamics*, in Proceedings of the International Conference on Computer Modeling and Simulation, ICCMS'09, Macau,, 2009, pp. 63–68.

[129] Y. WU, X. CAO, Y. XING, P. ZHENG, and S. ZHANG, *A survey of coupled control for spacecraft formation flying*, in Proceedings of the 3rd International Symposium on Formation Flying, Missions and Technologies, Noordwijk, The Netherlands, 2008, pp. 63–68.

[130] Y. WU, X. HU, D. HU, T. LI, and J. LIAN, *Strapdown inertial navigation systems algorithms based on dual quaternions*, IEEE Transactions on Aerospace and Electronic Systems, 41 (2005), pp. 110–132.

[131] R. XIANHAI, Y. LEPING, and Y. ZHANG, *Optimal trajectory for geo satellite proximity inspection based on hp-adaptive pseudospectral method*, in 62nd International Astronautical Congress, Cape Town, SA, 2010.

[132] M. XIN and H. PAN, *Integrated control of position, attitude, and flexible motion for satellite proximity operations*, in Proceedings of the AIAA Guidance, Navigation, and Control Conference, Chicago, IL, USA, 2009.

[133] M. XIN and H. PAN, *Nonlinear optimal control of spacecraft approaching a tumbling target*, in Proceedings of the 2009 conference on American Control Conference, IEEE Press, 2009, pp. 4818–4823.

[134] M. XIN and H. PAN, *Integrated nonlinear optimal control of spacecraft in proximity operations*, International Journal of Control, 83 (2010), pp. 347–363.

[135] M. XIN and H. PAN, *Nonlinear optimal control of spacecraft approaching a tumbling target*, Aerospace Science and Technology, 15 (2011), pp. 79–89.

[136] Y. XING, X. CAO, S. ZHANG, H. GUO, and F. WANG, *Relative position and attitude estimation for satellite formation with coupled translational and rotational dynamics*, Acta Astronautica, 67 (2010), pp. 455 – 467.

[137] Y. XING, X. CAO, S. ZHANG, H. GUO, and F. WANG, *Relative position and attitude estimation for satellite formation with coupled translational and rotational dynamics*, Acta Astronautica, 67 (2010), pp. 455 – 467.

[138] A. Y., D. ARZELIER, L. S. URBINA, and C. LOUEMBET, *V-bar and r-bar glideslope guidance algorithms for fixed-time rendre-vous: a linear programming approach*, in IFAC Symposium on Automatic Control in Aerospace (ACA), Sherbrooke (Canada), 2016.

[139] K. YAMANAKA and F. ANKERSEN, *New state transition matrix for relative motion on an arbitrary elliptical orbit*, Journal of Guidance, Control and Dynamics, 25 (2002).

[140] R. ZANETTI, *Optimal glideslope guidance for spacecraft rendezvous*, Journal of Guidance, Control and Dynamics, 34 (2011), pp. 1593–1597.

[141] F. ZHANG, G. DUAN, and M. HOU, *Integrated relative position and attitude control of spacecraft in proximity operation missions with control saturation*, International Journal of Automation and Computing, 9 (2012), pp. 342–351.